HOT DEFORMATION BEHAVIOR OF Zr-Nb ALLOYS

Ph.D. THESIS

by

KULDEEP KUMAR SAXENA

**DEPARTMENT OF METALLURGICAL AND MATERIALS ENGINEERING
INDIAN INSTITUTE OF TECHNOLOGY ROORKEE
ROORKEE-247 667 (INDIA)
FEBRUARY, 2018**

HOT DEFORMATION BEHAVIOR OF Zr-Nb ALLOYS

A THESIS

Submitted in partial fulfilment of the
requirements for the award of the degree
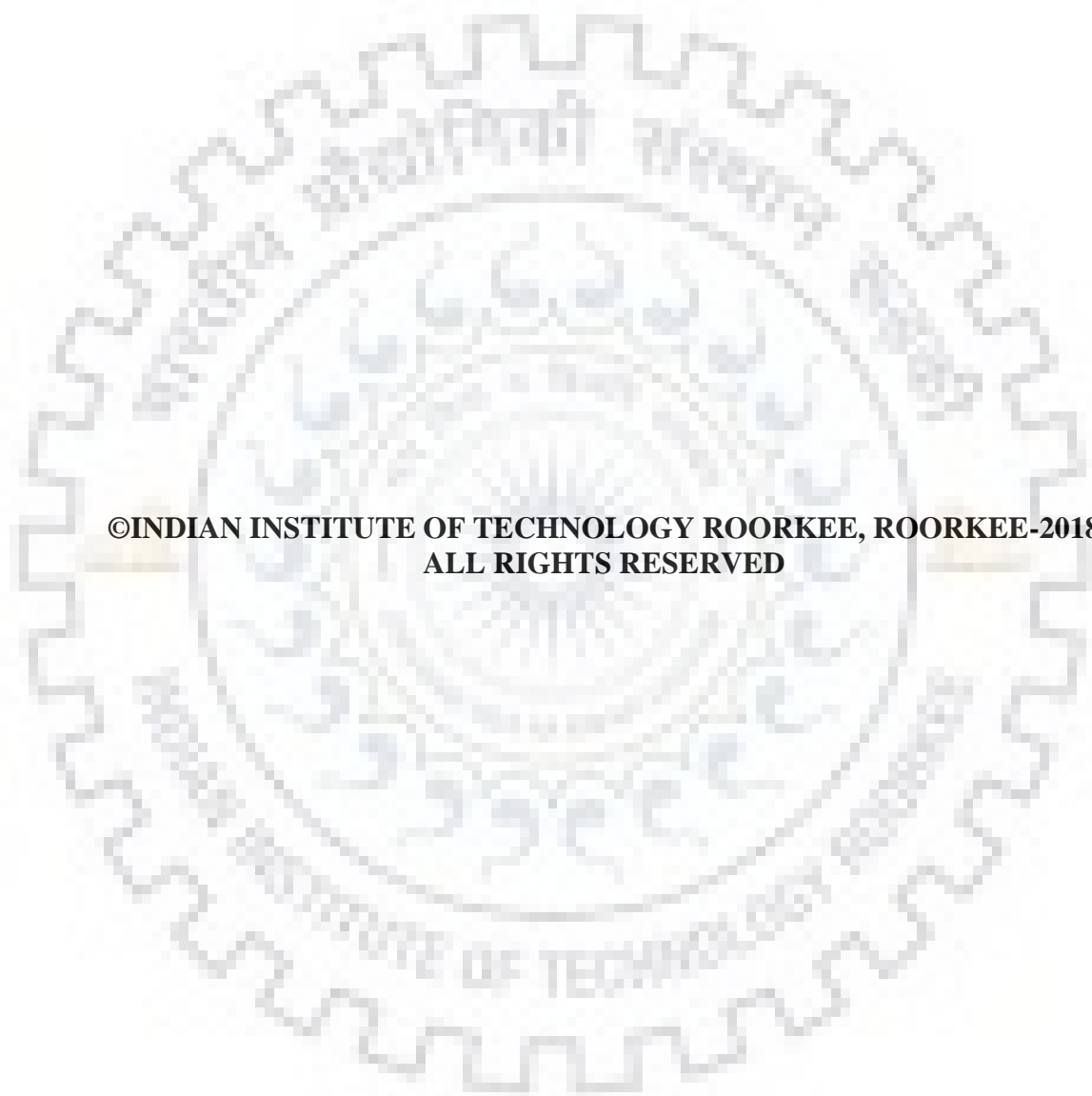*of*

DOCTOR OF PHILOSOPHY
in

METALLURGICAL AND MATERIALS ENGINEERING

by

KULDEEP KUMAR SAXENA

DEPARTMENT OF METALLURGICAL AND MATERIALS ENGINEERING
INDIAN INSTITUTE OF TECHNOLOGY ROORKEE
ROORKEE-247 667 (INDIA)
FEBRUARY, 2018

INDIAN INSTITUTE OF TECHNOLOGY ROORKEE
ROORKEE

CANDIDATE'S DECLARATION

I hereby certify that the work which is being presented in the thesis entitled "**HOT DEFORMATION BEHAVIOR OF Zr-Nb ALLOYS**" in partial fulfilment of the requirements for the award of Degree of Doctor of Philosophy and submitted in the Department of Metallurgical and Materials Engineering of the Indian Institute of Technology Roorkee, Roorkee is an authentic record of my own work carried out during a period from January, 2013 to February, 2018 under the supervision of Dr. Vivek Pancholi, Associate Professor and Dr. G.P. Chaudhari, Associate Professor, Department of Metallurgical and Materials Engineering, Indian Institute of Technology Roorkee, Roorkee.

The matter presented in the thesis has not been submitted by me for the award of any other degree of this or any other Institute.

(KULDEEP KUMAR SAXENA)

This is to certify that the above statement made by the candidate is correct to the best of our knowledge.

Dr. Vivek Pancholi   Dr. G.P. Chaudhari
(Supervisor)   (Supervisor)

The Ph. D. Viva-Voce Examination of **KULDEEP KUMAR SAXENA**, Research Scholar, has been held on 6th July, 2018.

Dr. S.K. Nath   Dr. V. Subramanya Sarma
(Chairman, SRC)   (External Examiner)

This is to certify that the student has made all the corrections in the thesis.

Dr. Vivek Pancholi   Dr. G.P. Chaudhari   Dr. Anjan Sil
(Supervisor)   (Supervisor)   (Head of the Department)

Date: **July 6th, 2018**

ABSTRACT

Zr-Nb alloys are used to fabricate structural components in nuclear power reactors. Zr-1Nb alloy is used to produce calandria tube with 60 mm diameter and 1 to 2 mm wall thickness for pressurized heavy water reactor (PHWR). Zr-2.5Nb alloy is used to fabricate pressure tube for CANDU water reactor having diameter less than 30 mm whereas, Zr-2.5Nb-0.5Cu is used to make garter spring. These components are exposed to corrosive and neutron radiation environment with surrounding temperature of $280 - 400^oC$. Therefore, it is essential to optimize mechanical properties in order to improve service life. Thermo-mechanical processing is one of the best route to enhance mechanical properties without altering chemical composition. The processing conditions such as strain, strain rate and temperature are optimized to get desired microstructure without introducing any instability. Fine equiaxed grains, obtained through process of dynamic recrystallization (DRX), is the desirable microstructure.

The Zr-Nb alloys exhibit α–phase (hcp) at lower temperatures, β–phase (bcc) at elevated temperatures and two phase region (i.e. α+β phase) in the intermediate temperature range. The flow stress curves exhibited phase dependent flow behavior. Most of the flow curves in single α–phase showed strain hardening behavior whereas, single β–phase showed steady-state behavior. On the other hand, in two phase region flow softening was observed. The degree of slow softening was quantified and plotted as a function of deformation temperature and strain rate. Most of the flow softening occurred in two phase region at lower strain rate (i.e. 10^{-2} s^{-1}) for different Zr-Nb alloys. The softening in two phase region could be due to DRX or microstructural instabilities, either in the α–phase or β–phase or both phases.

To identify and understand safe hot processing conditions and deformation mechanism, different processing map approaches were applied in the present work for different Zr-Nb alloys. The processing maps were developed using dynamic materials model (DMM), modified dynamic materials model (MDMM) and *α-parameter*. Among all the processing map approaches, DMM was found to be the most appropriate approach to delineate safe and unsafe processing conditions for Zr-Nb alloys. The predictions of the DMM were confirmed with microstructural analysis.

The processing map developed using DMM approach exhibited high power dissipation efficiency in two phase region for Zr-1Nb alloy. High power dissipation efficiency suggests that the hot deformation is accompanied by dynamic recrystallization. In the two phase region, flow curves also showed softening. Therefore, to clarify the cause of high power dissipation efficiency and flow softening in the two phase region, a novel approach was proposed wherein, calculated

flow stress was used to develop the processing map. Calculated flow stresses for the two phase region were obtained by incorporating phase information in the form of phase fractions of α and β–phases and, corresponding extrapolated flow stress values. The processing map developed using calculated flow stress data was able to reveal high dissipation efficiency domains whereas, processing map developed using experimental flow stress data could not. The superimposed dissipation efficiency maps of the individual phases in the two phase region revealed that the single α–phase has high power dissipation efficiency than β–phase. Hence, the dominant phase or the cause of flow softening in the two phase region was found to be the α–phase. Microstructural analysis of the samples deformed in the two phase region brought out that the α–phase has undergone DRX whereas, β–phase exhibited coarse elongated grains.

The constitutive equations were also developed for Zr-Nb alloys by relating flow stress with Zener–Hollomon parameter ($Z = \dot{\varepsilon}\exp(Q/RT)$), the terms have their usual meaning. Activation energy, Q and stress exponent, n are calculated during the development of a constitutive equation. Values of Q and n help to predict deformation mechanism operating during hot deformation. In the present work, activation energy of the two phase region was found to be close to that of individual α–phase. It brought out that the dominant phase in the two phase region of Zr-Nb alloy was the α–phase. The constitutive equation developed using calculated flow stress values for α (σ_{α}^{c}) and β–phases (σ_{β}^{c}) in two phase region (α+β) phase, clarified that the variation in the proportion of the two phases does not affect the predictability of the equation. Constitutive equations developed for the two phase (α+β) region and, for single phases α and β showed good agreement with the experimental values. However, the constitutive equation developed for the entire range of the deformation temperature (all the phases and phase mixture) predicted flow stress values with significant variation from experimental one. In this work, it was established that individual constitutive equation for each phase or phase mixture is expected to predict accurate results.

The developed constitutive equations were further validated by FEM simulation of hot extrusion process using the parameters obtained from the constitutive equations. The prediction of ram force by FEM for industrial hot extrusion process were compared with the actual shop floor data. In FEM simulation, input data were either in the form of flow stress data (look-up table, LUT) obtained from hot compression tests or the parameters of a constitutive equation. The FEM simulation showed that the phase-wise constitutive equation provide same ram force as provided by the look-up table and matched quite well with the shop floor data. However, single constitutive equation for all phases could not do so.

ii

Zr-Nb alloys are usually processed in the two phase region to get the desired microstructure and mechanical properties for structural applications in nuclear industries. The small punch test (SPT) was performed to evaluate mechanical properties of the samples after hot compression in the two phase region at different temperatures and strain rates. The microstructure after hot deformation was characterized by the size of primary α, secondary α lath size, prior β grain size and texture developed. In two phase region, samples deformed at low strain rate (0.01 s^{-1}) have undergone significant DRX and the fraction of DRX increases with temperature, while for samples deformed at 1 s^{-1}, prominent contribution from DRX was observed only from 850°C. The deformed samples were characterized with the formation of $<11\bar{2}0>$ fiber, which was found to strengthen with increase in the deformation temperature. The strengthening of fiber is attributed to the transformation aspects and deformation in the β–phase region. Recrystallized grains invariably found to have a weaker texture compared to the deformed grains. The yield load and maximum load was found maximum for sample deformed at 815°C/ 1 s^{-1} due to combined effect of higher dislocation density and finer α lath size.

ACKNOWLEDGEMENTS

TABLE OF CONTENTS

LIST OF TABLES

LIST OF FIGURES

xvii

xxiii

LIST OF ABBREVIATIONS AND SYMBOLS

Zr	Zirconium
CANDU	CANadian Deuterium Uranium
Nb	Niobium
Sn	Tin
Fe	Iron
Cr	Chromium
Ni	Nickel
SMR	Small Modular Reactor
SGHWR	Steam Generating Heavy Water Reactor
BWR	Boiling Water Reactor
PWR	Pressurised Water Reactor
SPT	Small Punch Test
FEM	Finite Element Method
FE-SEM	Field Emission Scanning Electron Microscopy
SEM	Scanning Electron Microscopy
EBSD	Electron Backscatter Diffraction
RT	Room Temperature
HCP	Hexagonal Close Packed
BCC	Body Centered Cubic
Cu	Copper
wt%	Weight Percent
ppm	Parts Per Million
PBWR	Pressurized Boiling Water Reactor
PHWR	Pressurized Heavy Water Reactor
RBMK	Reaktor Bolshoy Moschnosti Kanalniy
VVER	Voda Voda Energo Reactor
LBB	Leak Before Break
SPPs	Second Phase Particles
SR	Stress Relieved
RX	Recrystallized
TEM	Transmission Electron Microscopy
T_m	Melting Temperature

Q	Activation Energy
n	Strain Hardening
Z	Zener–Hollomon Parameter
R	Universal Gas Constant
T	Absolute Temperature
DDRX	Discontinuous Dynamic Recrystallization
CDRX	Continuous Dynamic Recrystallization
RRX	Rotational Recrystallization
GDX	Geometric Dynamic Recrystallization
DRV	Dynamic Recovery
HAGB	High Angle Grain Boundary
Qsd	Activation Energy of Lattice Self-diffusion
CP	Commercially Pure
GG	Grain Growth
DMM	Dynamic Materials Model
Co	Cobalt
Mo	Molybdenum
MDMM	Modified Dynamic Materials Model
DRX	Dynamic Recrystallization
m	Strain Rate Sensitivity
η	Efficiency of Power Dissipation
ξ	Instability Parameter
ε	True Strain
P	Total Power
J	Power Used in Microstructural Change
G	Power Used in Plastic Deformation
σ	Flow Stress
γ	Strain Hardening
ANN	Artificial Neural Network
BP	Bodner–Partom
RK	Rusinek–Klepaczko
ZA	Zerilli and Armstrong
PTW	Preston–Tonks–Wallace
VA	Voyiadjis–Almasri

CA	Cellular Automaton
VK	Voce–Kocks
JC	Johnson–Cook
KH	Khan–Huang
FB	Fields–Backofen
MR	Molinari–Ravichandran
TMP	Thermomechanical Processing
ABI	Automatic Ball Indentation
SOS	State of Stress
LVDT	Linear Voltage Differential Transducer
UTM	Universal Testing Machine
P	Typical Load
δ	Central Deflection
P_y	Yield Load
P_m	Maximum Load
GOS	Grain Orientation Spread
LAGB	Low Angle Grain Boundary
ATR	Adiabatic Temperature Rise
ΔT	Rise in Temperature
T_{actual}	Actual Temperature
$\Delta\sigma$	Change in Flow Stress
IPF	Inverse Pole Figure
GDRX	Geometric Dynamic Recrystallization
IQ	Image Quality
D-1	Domain-1
D-2	Domain-2
D-3	Domain-3
GROD	Grain Reference Orientation Deviation-Angle
$\sigma_\alpha^c, \sigma_\beta^c$	Flow Stress of Individual α Phase and β Phase in Two Phase Region, Calculated from Experimental Data
$\sigma_{(\alpha+\beta)}^{Cal}$	Calculated Flow Stress of (α+β) Phase in Two Phase Region
ZNC	Zr-2.5Nb-0.5Cu
AARE	Average Absolute Relative Error

A, A_1, A_2	Materials Constants
n, n'	Stress Exponent in Power Law and Sine Hyperbolic Constitutive Equation
ε_p	True Strain Corresponding to Peak Flow Stress
σ_p	Peak Flow Stress
$\dot{\varepsilon}$	Strain Rate
AE1	Activation Energy for Deformation Temperature Range 700°C to 815°C, Related to $(\alpha+\beta)$ Phase
AE2	Activation Energy for Deformation Temperature 815°C to 925°C Related to β Phase
AE3	Activation Energy for Entire Range of Deformation Temperature i.e. 700°C to 925°C Related to $(\alpha+\beta)$ and β Phase
AE4	Activation Energy for Two Phase Range Obtained Using the Calculated Flow Stress Values
$\sigma_\alpha^c, \sigma_\beta^c$	Flow Stress of Individual α Phase and β Phase in Two Phase Region, Calculated from Experimental Data
$\sigma^E, \sigma_P^E, \sigma_\beta^E$	Experimental Flow Stress, Experimental Peak Flow Stress and Experimental Flow Stress in Single Phase β (MPa)
f_α, f_β	Volume Fraction of α and β Phase Respectively in (α+β) Phase Range at Constant Temperature
Q_α^c, Q_β^c	Activation Energy of Individual α Phase and β Phase in Two Phase Region (kJ/mol)
$\sigma_{(\alpha+\beta)}^E$	Experimental Flow Stress of (α+β) Phase (MPa)
$Q_{two\,phase\,range}^c$	Activation Energy of (α+β) Phase Calculated from the Activation Energy of Individual Phase (i.e. Q_α, Q_β) in Two Phase Region (kJ/mol)
FEA	Finite Element Analysis
LUT	Look-Up Table
NFC	Nuclear Fuel Complex
ALE	Arbitrary Lagrangian Eulerian

<div style="text-align: right">

1

</div>

INTRODUCTION

1.1 GENERAL INTRODUCTION

The zirconium was discovered as an element in 1789 by Klaproth. In 1925, it was refined as zirconium and produced in high purity "crystal bar". In 1947, Krolls process was developed to produce Zr sponge. In 1949 it was observed that it has combined properties of low neutron absorption cross section and good mechanical properties, which made it a primary structural material for the nuclear reactors [1, 2]. Admiral Rickover of Pennsylvania, USA was the first person to use Zr in nuclear application for the water cooled reactor of the submarine Nautilus [3]. An upward swing took place when neutron absorption was a major consideration for CANDU nuclear reactor (developed by Canadian scientists) and therefore, uranium was replaced by zirconium. Thus, Zr became attractive and necessary material in the structural components of reactor core due to its low neutron absorption cross section **(Figure 1.1)**.
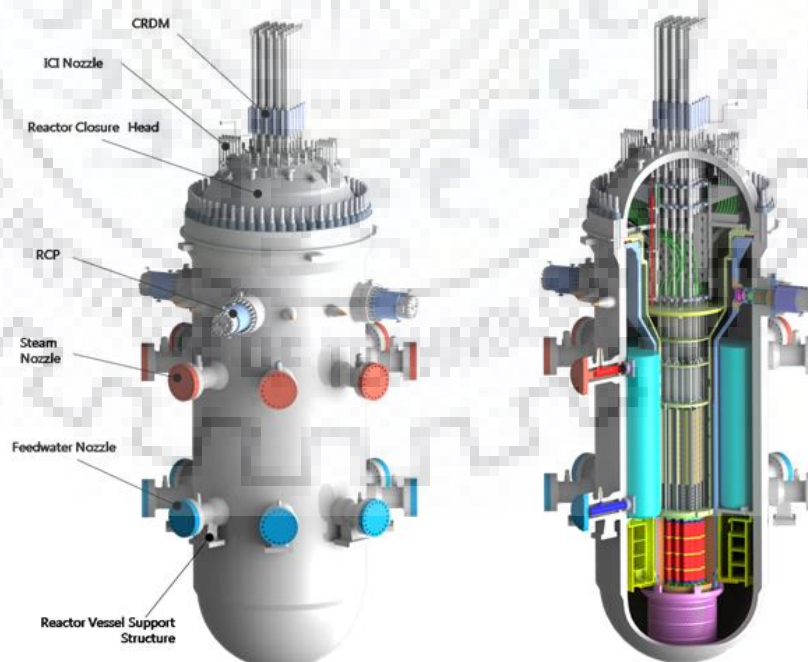
Figure 1.1: Small Modular Reactor (SMR) Showing Core of a Nuclear Reactor (ref: http://ansnuclearcafe.org/)

1.2 APPLICATION OF ZIRCONIUM IN NUCLEAR INDUSTRY

In early days of zirconium application in nuclear reactors, scientists tried to produce zirconium with maximum purity but the problem of corrosion at high temperature and heavy water was not resolved. Finally, they found that zirconium exhibit better corrosion resistance when, it was alloyed with Nb, Sn, Fe, Cr and Ni. Therefore, different zirconium alloys were developed for specific application in nuclear reactors. For nuclear applications, Zircaloy-2, Zircaloy-4, Zr-1Nb, Zr-2.5Nb and Zr-2.5Nb-0.5Cu are used to make various components as listed in **Table 1.1**. The typical compositions of these alloys are shown in **Table 1.2**.

Table 1.1: Applications of zirconium alloys in nuclear applications [1-3]

Reactor System	Fuel Cladding	Pressure Tubes	Calandria Tubes	Garter Springs
Heavy Water				
(a) CANDU	Zircaloy-4	Zircaloy-2 (initially) Zr-2.5Nb (currently)	Zircaloy-2 Zr-1Nb	Zr-2.5Nb-0.5Cu
(b) SGHWR	Zircaloy-2	Zircaloy-2	Zircaloy-2 (for commercial reactors)	
Light Water				
(a) BWR	Zircaloy-2 or 4			
(b) PWR	Zircaloy-4 or 2 Zr-Nb alloy (Zr-1Nb in certain Russian Reactors)			

CANDU → CANadian Deuterium Uranium
SGHWR → Steam Generating Heavy Water Reactor
BWR → Boiling Water Reactor
PWR → Pressurised Water Reactor

Table 1.2: Typical compositions of zirconium alloys used in nuclear applications [1]

Element	Zircaloy-2	Zircaloy-4	Zr-1Nb	Zr-2.5Nb	Zr-2.5Nb-0.5Cu
Tin	1.5	1.5	–	–	–
Iron	0.1	0.2	–	–	–
Chromium	0.1	0.1	–	–	–
Nickel	0.1	–	–	–	–
Niobium	–	–	1	2.5	–
Copper	–	–	–	–	0.5
Oxygen	1400	1400	900-1300	900-1300	900-1300
Balance	Zirconium plus impurities				

1.3 CHARACTERISTICS OF Zr-Nb ALLOYS IN NUCLEAR APPLICATION

In reactor, heavy water flow through the tubes which are made up of Zr-Nb alloys therefore, these alloys undergo the plastic deformation during the service life. To reduce the plastic deformation, these alloys must have possessed with appropriate mechanical properties. The mechanical properties of these alloys are based on the chemical compositions, thermo-mechanical processing history and their final microstructures. The thermo-mechanical treatment affects the final microstructure based on hot deformation conditions, deformation mechanism, and dominant phase during the hot deformation, specially in two phase region and the constitutive behavior of material during the hot deformation.

During thermo-mechanical treatment, hot deformation conditions provide the microstructures, with no instabilities. These conditions are referred as safe processing conditions. In literature, different approaches were proposed to predict the safe and unsafe processing conditions of a material. For Zr-Nb alloys, limited studies were reported to predict the safe processing conditions using different approaches. Each approach has its limitations to predict accurately safe processing conditions for a particular material [4-10].

The Zr-Nb alloys exhibits allotropic behavior, i.e. it exhibits two phase ($\alpha+\beta$) region at some temperature range. In industries, the hot deformation of these alloys usually performed in the two phase region. The proportion of individual phases in two phase region vary with temperature. Each phase behaves differently to the external stimuli, which depends on its crystal structure and other material properties. Therefore, it is important to understand the dominating phase and dominating deformation mechanism during the hot deformation in two phase region. Many studies were conducted to understand the deformation mechanism of Zr-Nb alloys for a range of deformation temperatures covering all the phases, i.e. single α–phase, single β–phase and two phase ($\alpha+\beta$) using processing map approaches and microstructure analysis [4-8].

Limited literature is available on hot deformation of Zr-Nb alloys, specially in two phase region. Hence, the present work has been envisaged to identify compatible approach to predict the safe processing conditions for Zr-Nb alloys. Processing map approach, microstructural analysis and constitutive equation development were used to identify the hot deformation mechanism and dominating phase during hot deformation in two phase region. The effect of microstructural features obtained after hot deformation in two phase region, mechanical properties were investigated using SPT, Optical images, FE-SEM/EBSD and texture analysis. The analysis revealed that the higher values of yield strength was due to the combined effect of higher dislocation density of the material and finer α lath size. The hot compression data and

3

parameters of constitutive equations were used to simulate a FEM model for hot extrusion, to help process industry in terms of expected load and power requirements.

1.4 OUTLINE OF THESIS

The outline and contents of various chapters of the thesis are summarized as follows:

Brief description of zirconium and its properties, different Zr alloys and their application in nuclear industries, characteristics of high temperature deformation and their effect on mechanical properties, and FEM simulation using hot compression data followed by literature review are summarized in **Chapter 2.** Based on literature review, formulation of the problem for present research work with research gap and research objectives are listed in **Chapter 3**. Materials processing condition, experimental procedures and their parameters, methodology pertaining to their microstructural characterization, texture analysis and mechanical testing are discussed in detail in **Chapter 4.**

Different investigations performed on Zr-Nb alloys after hot compression deformation at different temperatures and strain rates are presented in **Chapter 5.** The chapter contains; i) flow curves of different Zr-Nb alloys with their softening maps, ii) processing maps developed using different approaches, iii) constitutive analysis and validation using FEM simulation. The chapter also deals with application of hot deformation data and parameters of developed constitutive equations for FEM simulation in order to predict expected load required for hot extrusion. Rigorous microstructural analysis using optical images and EBSD analysis for different Zr-Nb alloys are presented to understand the effect of hot deformation conditions. Results obtained after mechanical testing using small punch test are also presented in this chapter.

Identification of suitable processing map approach for Zr-Nb alloys, dominant phase during hot deformation, interpretation of activation energy and processing map are discussed in detail in **Chapter 6**. Evaluation of various processing maps with microstructural analysis to identify suitable processing map approach is discussed in **subsection 6.1.1** of Section 6.1. Identification of dominant phase in two phase region using processing map developed using calculated flow stress data is discussed in **subsection 6.1.2** of Section 6.1. The findings discussed in subsection 6.1.2 are validated with microstructural analysis in **subsection 6.1.3** of Section 6.1. The significance of, activation energy of individual phases in two phase region and stress exponent in deformation behavior are discussed in **Section 6.2**. The mechanical properties after hot deformation are correlated with microstructural parameters such as phase fraction, grain size, and texture in **Section 6.3.**

The final conclusions are summarized in **Chapter 7** followed by future scope.

LITERATURE REVIEW

In this chapter, a brief description of zirconium and its alloys, various deformation processes, restoration mechanisms and dominant mechanism controlling hot deformation in single phase region and/ or in two phase (α+β) region are discussed. Literature pertaining to different heat treatments and thermo-mechanical treatments (hot deformation) of Zr-Nb alloys, understanding of operating deformation mechanism using various approaches with microstructural analysis and relevant effect of hot deformation on the mechanical properties are discussed. Based on existing literature reviewed in this chapter, the problem for the present dissertation work has been defined in the next Chapter.

2.1 ZIRCONIUM AND ITS PHYSICAL PROPERTIES

The name zirconium comes from the Persian word zargun, which means gold like metal. Klaproth discovered it in 1789, and it was placed as 40th metallic element in the periodic table, bearing atomic number of 40 and belongs to sub group of IVB, where titanium and hafnium are also placed. Zirconium occurs naturally in the form of five different isotopes with the mass numbers of 90, 91, 92, 94 and 96, and the natural abundances of 51.46%, 11.23%, 17.11%, 17.40% and 2.80% respectively. It is a grey-white, lustrous, ductile metal and exists in solid form at room temperature (RT). Zirconium readily reacts with oxygen and forms stable oxide [11].

At room temperature, pure zirconium is a hexagonal close packed (HCP) metal with anisotropic mechanical properties. The stress-free lattice spacing at room temperature is 0.323 nm and 0.515 nm in 'a' and 'c' directions respectively. Therefore, the c/a ratio is 1.59271 [12], and it approaches the ideal ratio at elevated temperatures. The melting of pure zirconium (α–Zr) occurs at 1860°C, and the boiling point is 4371°C. Thus, zirconium can be considered as a refractory metal. At higher temperature of 865°C, zirconium undergoes an allotropic transformation from low temperature HCP α–phase to BCC β–phase with lattice parameter of a=0.36090 nm [13]. Zirconium exists in the β-phase until the melting point. Upon cooling, β–phase transforms into plates of α–phase by martensitic transformation. The thickness of the plates of α–phase depends on cooling rate [14]. The martensitic transformation occurs with the following orientation

relationship $(000l)_\alpha$ // $(110)_\beta$ and $<1120>_\alpha$ // $<111>_\beta$. The transformation gives rise to basket weave or parallel plate microstructure [15].

Kaufman and Untermeyer discovered that the zirconium has a very low thermal neutron absorption cross section of 1×10^{-24} cm^2, which is 30 times lower than iron and hence, imparts nuclear reactor with high thermal efficiency [2]. Some of the physical properties of Zr and Zr-alloys are given in **Table 2.1**.

2.2 ALLOYING ELEMENTS AND THEIR EFFECT

Pure zirconium is rarely used in nuclear reactors due to its low corrosion resistance and insufficient strength and creep resistance. Therefore, zirconium is alloyed with tin and niobium to improve mechanical properties and corrosion resistance. Tin improves corrosion resistance while niobium improves creep resistance and mechanical strength. However, alloying elements should not affect neutron absorption capability of zirconium. Transition metals (Fe, Cr, Sn, Cu and Ni) are added to zirconium at very low concentrations to improve corrosion resistance and mechanical properties. Effect of different alloying elements is explained in the following sections [16, 17].

Table 2.1: Basic physical properties of some Zr and Zr-alloys used as structural materials in nuclear reactor [12, 18]

Reference Materials	Atomic mass, amu	Thermal neutron capture cross section, 10^{-24} cm^2	Concentration of nuclei, 10^{22} cm^{-3}	Melting point, $^\circ$C	Density, Kg/m^3	Heat capacity, kJ/(Kg.K)	Thermal conductivity, W/(mK)	Linear expansion coefficient, 10^{-6} 1/K	Electrical resistivity, 10-8 Ω.m
Zirconium 99.99%	91.22	0.185	4.29	1855	6520	0.278	24	5.7	40
Zr-1%Nb	91.24	0.178	4.32	1837	6550	0.320	18	5.8	70.0
Zr-2.5%Nb	91.26	0.191	4.33	1827	6570	0.315	19	5.2	72.0
Zircalloy–2	91.37	0.1806	4.31	1845	6550	0.290	17	5.8	74.0
Zircalloy–4	91.38	0.1812	4.34	-	6580	0.293	14.1	5.8	-

2.2.1 Tin: Tin (*Sn*) is an α–phase stabilizer, and forms substitutional solid solution with both α and β–phases. Addition of *Sn* up to 1.2- 1.7wt% provides substantial improvement in corrosion resistance over pure zirconium, without seriously affecting the neutron absorption capability. Addition beyond this concentration reduce yield strength of the alloy [19]. The addition of *Sn* lowers stacking fault energy of Zr, which is expected to have significant influence on its workability.
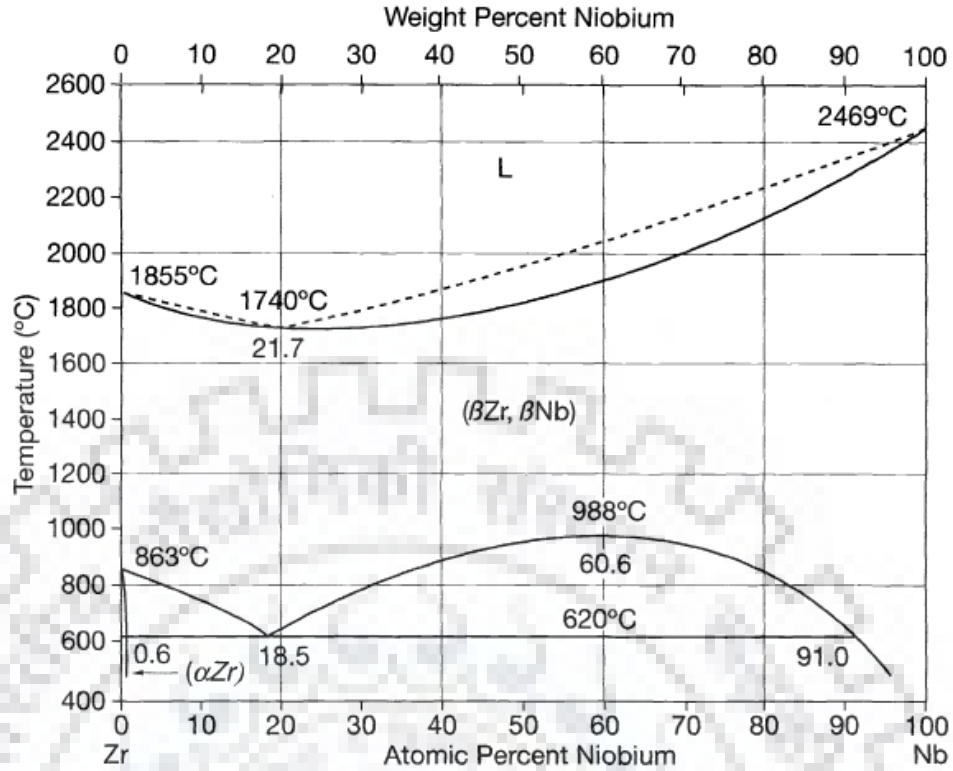
Figure 2.1: Zr-Nb phase diagram [20]

2.2.2 Niobium: Niobium (Nb) is a β stabilizer and improves strength and corrosion resistance of the alloy. Addition of Nb decreases the β transus temperature. **Figure 2.1** represents phase diagram of Zr-Nb alloy wherein, a monotectoid phase transformation occurs at the temperature of 620°C and concentration of 18.5 wt% of Nb. Upon water quenching from single β–phase or upper region of two phase (i.e. α+β phase), the β–niobium rich grains transform by martensitic decomposition to supersaturated α' HCP phase. Subsequent heat treatment below monotectoid temperature leads to precipitation of Nb (β') at the boundaries of α' needles or α–phase, as shown in **Figure 2.2** [21].

2.2.3 Copper: Addition of Copper (*Cu*) in Zr increases the ductility and strength of the alloy and reduces the corrosion rate. The addition of *Cu* results in lowering the (α+β) transition temperature. *Cu* modifies the deformation characteristics of β–phase in (α+β) region [22]. The addition of *Cu* changes the ageing kinetics of the alloy.

7
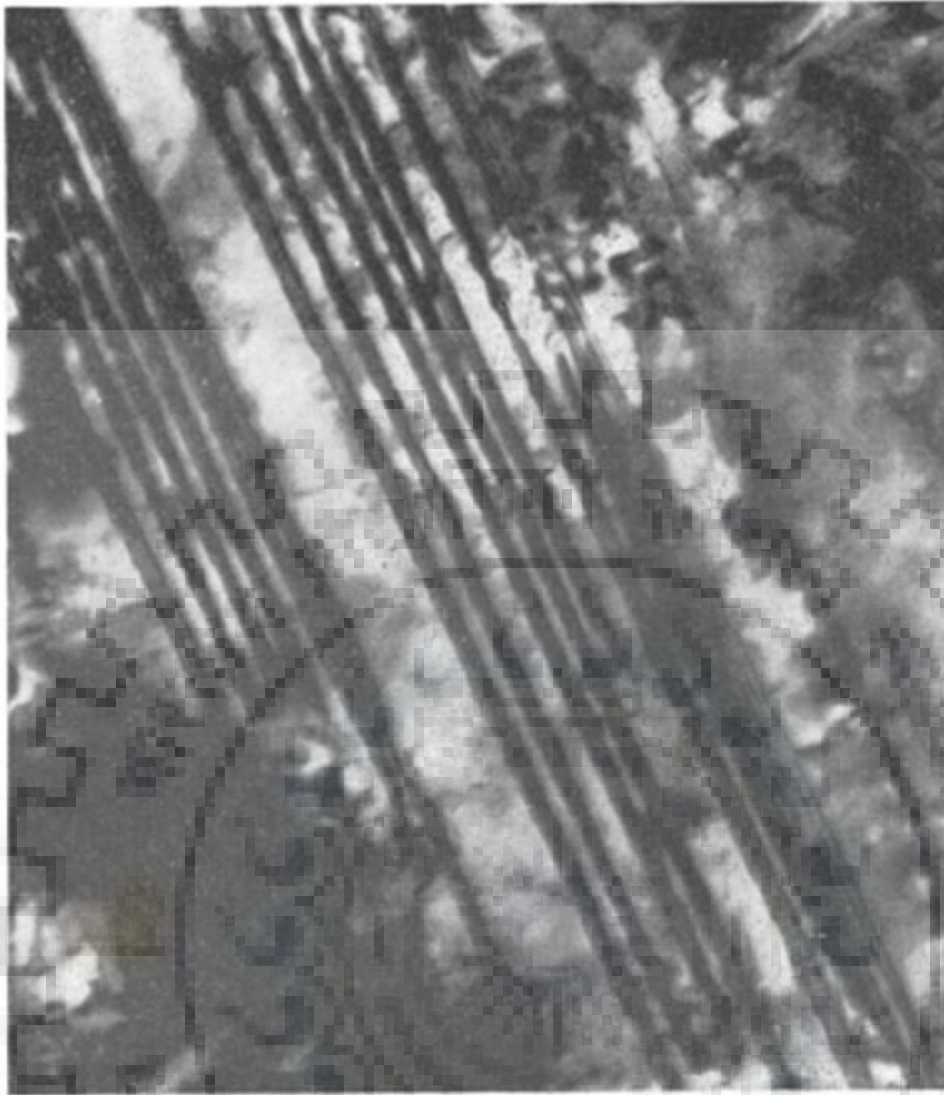
Figure 2.2: Zr-2.5 wt% Nb alloy quenched from β–phase (1000ºC) showing martensitic needles. Magnification 50,000X [21]

2.2.4 Oxygen and Hydrogen: Oxygen (O) is an α–stabilizer, and considered as an alloying element, rather than an impurity. Addition of oxygen expands the α–phase region in phase diagram, which approaches liquidus temperature on addition of higher oxygen content [23]. The concentration of oxygen is in the range of 800 – 1600 ppm. Oxygen forms an interstitial solid solution with Zr and helps to increase yield strength by solution strengthening. An addition of 1,000 ppm oxygen content in zirconium, increases yield strength by 150 MPa at room temperature [14]. Hydrogen is not an alloying element and is a cause of corrosion when absorbed from water. The solubility of hydrogen is 15 ppm at temperature of 200ºC and increases to 200 ppm at 400ºC. At higher cooling rate, a metastable body centered tetragonal γ phase (ZrH) is formed [24]. Precipitation of hydride causes volume expansion and hydrogen embrittlement [25, 26].

8

2.2.5 Iron, Chromium and Nickel: These elements are considered as "β–eutectoids", as they are the cause of eutectoid decomposition of β–phase. These elements dissolved in β–zirconium at the temperature range of 835 to 845°C, i.e. upper (α+β) region [27]. The solubility of Fe and Cr in α–phase is very low, i.e. in the range of 120 to 200 ppm [28]. For Zr-Cr and Zr-Ni binary alloys, $ZrCr_2$ and Zr_2Ni are the stable forms of the second phase [27].

2.3 Zr ALLOYS, THEIR APPLICATION AND REQUIRED PROPERTIES IN NUCLEAR APPLICATION

Zirconium alloys are mainly used in two different sectors: (i) industrial application and, (ii) nuclear application. In the nuclear applications, zirconium alloys are used as structural materials of all water cooled nuclear power reactors, particularly in fuel channels (boxes, wrappers), cladding tubes (also called as fuel tubes), pressure tubes (coolants tube), calandria tubes and fuel spacer grids (garter springs) [14]. **Figure 2.3** shows different parts of heating system in CANDU reactor core. The zircaloys and Zr–1-2.5%Nb alloys are extensively used in water cooled reactors. The zircaloys were first to put in application as cladding materials, pressure tubes and calandria tube in PWR, PBWR and PHWR respectively. In the development of zircaloys, corrosion resistance was the major consideration than the mechanical properties. It was then reported by Russian workers, that zirconium containing 1-5 wt.% Nb have better mechanical strength and adequate corrosion resistance [18].
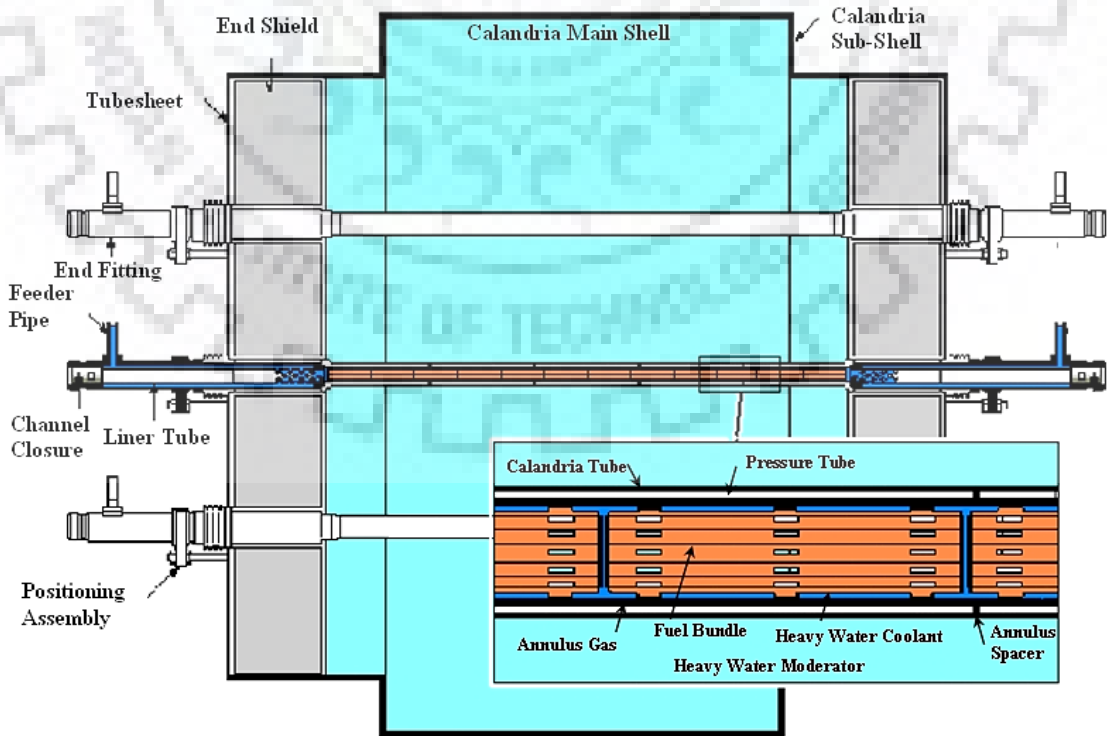
Figure 2.3: Schematic illustration of a CANDU reactor core and its primary heat transport system [29]

Therefore, nowadays Zr-2.5Nb alloy is used as pressure tube material for PHWR, CANDU reactor and RBMK reactor, whereas Zr-1Nb alloy is used as cladding tube in RBMK, VVER and submarine reactors.

2.3.1 Effect of Nb addition in Zr: In general, addition of Nb increases the strength and corrosion resistance of the Zr alloys. In nuclear applications, Zr-1Nb alloy is used to produce thin pressure tubes for PHWR, BWR and PWR. These thin tubes are used to encapsulate fuel pellets to prevent its contact with coolant in water cooled reactors. On the other hand, in PHWRs, Zr-1Nb alloy is used as calandria tube. The schematic diagram shows the position of calandria tube in **Figure 2.4**. It is clear from **Figure 2.4** that a concentric calandria tube surrounds the hot pressure tube and it is surrounded by unpressurized heavy water moderator.
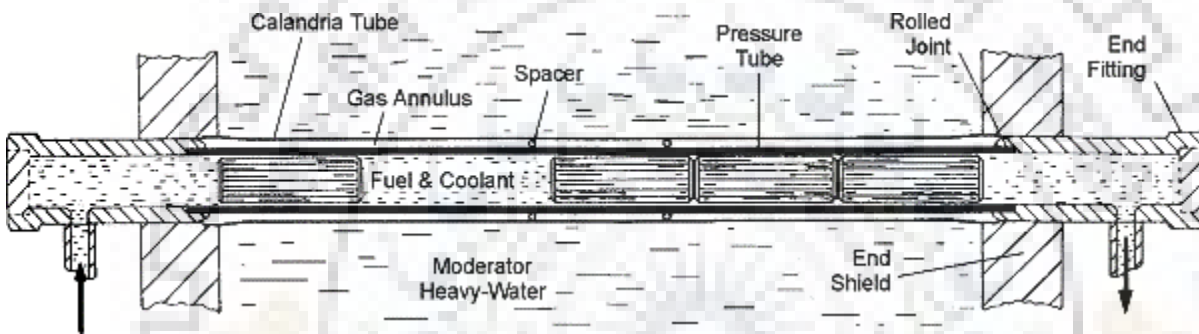
Figure 2.4: Schematic illustration of fuel channel [30]

Zr-2.5Nb alloy is used to produce pressure tubes (also called coolant tubes). These tubes experience hot pressurized heavy water coolant, fuel bundle weight and irradiation. Therefore, pressure tube materials should have good high temperature and corrosion properties and a stable microstructure under operating conditions. In PHWRs, reactor operation and safety demands that leak before break (LBB) criteria is satisfied. This could be achieved by retaining a minimum level of fracture toughness of pressure tube during service in the reactor.

The enhanced strength and better corrosion resistance in the pressure tube, cladding tube and calandria tube are achieved by the addition of Nb in Zr. These improved properties depend upon the Nb content, annealing temperature and the manufacturing process. Low content (0.2-0.3wt%) of Nb is soluble in the matrix without formation β–phase or precipitate and unaffected by annealing [31, 32], whereas middle range (0.5-0.8wt%) of Nb content exhibits precipitation of Nb in the matrix. The high range (1.0-2.0 wt%) of Nb content and subsequent annealing leads to formation of β Zr.

2.3.2 Effect of Cu addition in Zr-Nb alloy: The addition of Cu in Zr-2.5%Nb alloy i.e. Zr-2.5Nb-0.5Cu, is used to make garter spring (sometimes refer as spacer) for nuclear reactors.

The main role of garter spring is to avoid contact of hot pressure tube with the cooler calandria tubes, as shown in **Figure 2.4**. Addition of Cu provides adequate strength and ductility and retains sufficient crushing strength during service life. Fine distribution of Zr_2Cu precipitates is observed in Zr-Nb-Cu alloy [33], which is responsible for better mechanical properties at elevated temperatures. Moreover, it is found that the addition of Cu to Zr-Nb alloy reduces flow instability in two phase ($\alpha+ \beta$) region during hot deformation [8].

2.4 PRIMARY PROCESSING OF Zr-Nb ALLOYS

To get desired microstructure for end products, Zr-Nb alloys are subjected to different thermo-mechanical processing routes, as shown in **Figure 2.5**. After ingot melting, different thermo-mechanical processing routes are summarized as follows:

1) Hot forging and β–processing.
2) Intermediate temperature (upper α–range) forging and rolling, or extrusion for tubes.
3) A series of cold temperature rolling/pilgering followed by intermediate and a final anneal at temperatures between 450 – 600°C in vacuum furnaces.

2.4.1 Hot forging and β–processing: The hot forging (hot rolling for flat products) is done in the β–phase (900 to 1070oC) to break the cast structure. In this process material is heated and subsequently forging is performed in a number of steps. Before each forging step, the workpiece needs to be reheated to restore its ductility.
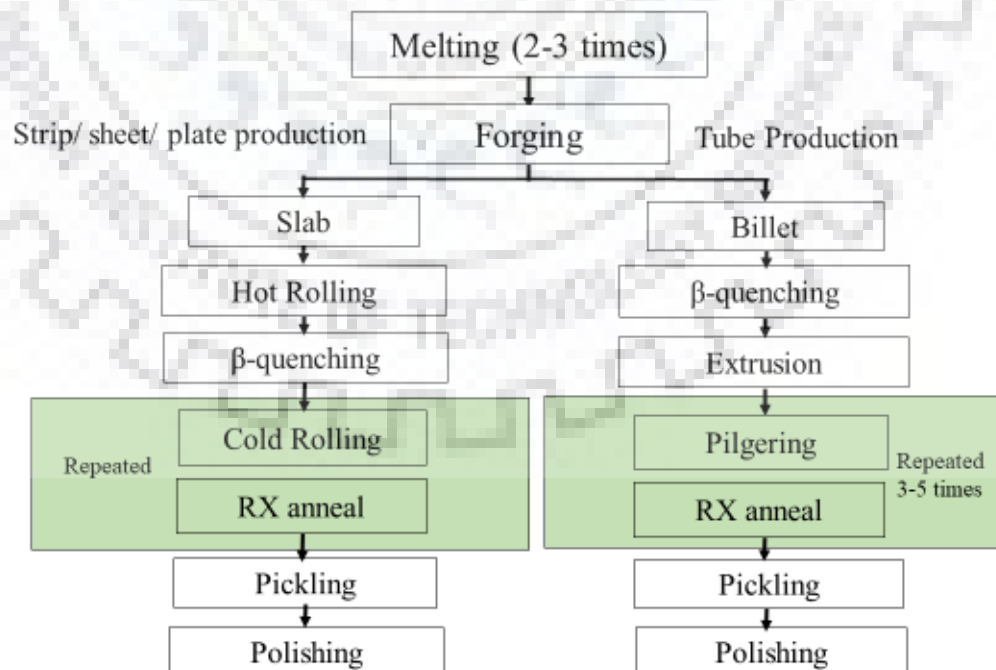
Figure 2.5: Outline for thermo-mechanical processes of Zr-Nb materials from the ingot stage [34]

Phase Transformation in Zr-Nb Alloys

B$_{Zr}$ (bcc)

Slow cooling **Rapid cooling**

α (hcp) + β$_{Nb}$

| α' (hcp) martensitic < 8% Nb Diffusionless | B$_{Zr}$ + ω 8-17% Displacive | Retained β$_{Zr}$ >17% Nb | B$_{Zr}$ + ω 30-60% Nb |

Ageing

| α (hcp) + β$_{Nb}$ | α (hcp) + β$_{Nb}$ | β$_{Zr}$ + ω or α (hcp) + β$_{Nb}$ | Spinodal β$_{Zr}$ + β$_{Nb}$ |
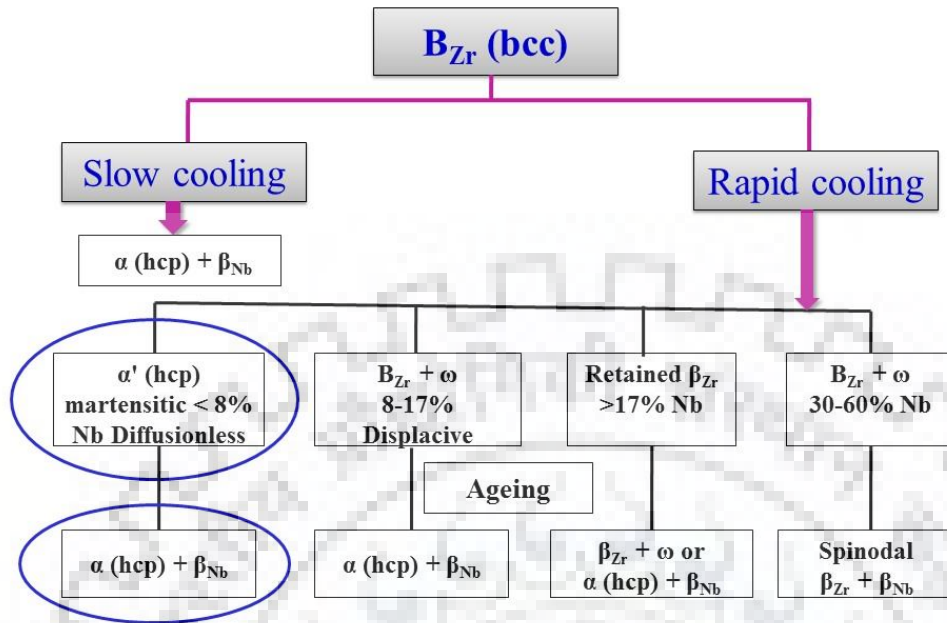
Figure 2.6: Phase transformation in Zr-Nb alloys during cooling from higher temperature of single β–phase

The β–processing is done in three steps: (a) furnace heating for α–β phase transformation (1000 to 1050°C), (b) homogenization in the β–phase for complete dissolution of all the second phase particles (SPPs) and, (c) β–α phase transformation (β–quenching) by rapid cooling in water or by gas cooling and transformation to different phases, as shown in **Figure 2.6** [35, 36]. Quenching leads to martensitic structures with supersaturation. At intermediate cooling rates, the grain structure consists of sheaves of α–Zr platelets and, β–phase located at the plate boundaries, as shown in **Figures 2.7 (a)** and **(b)** [37].
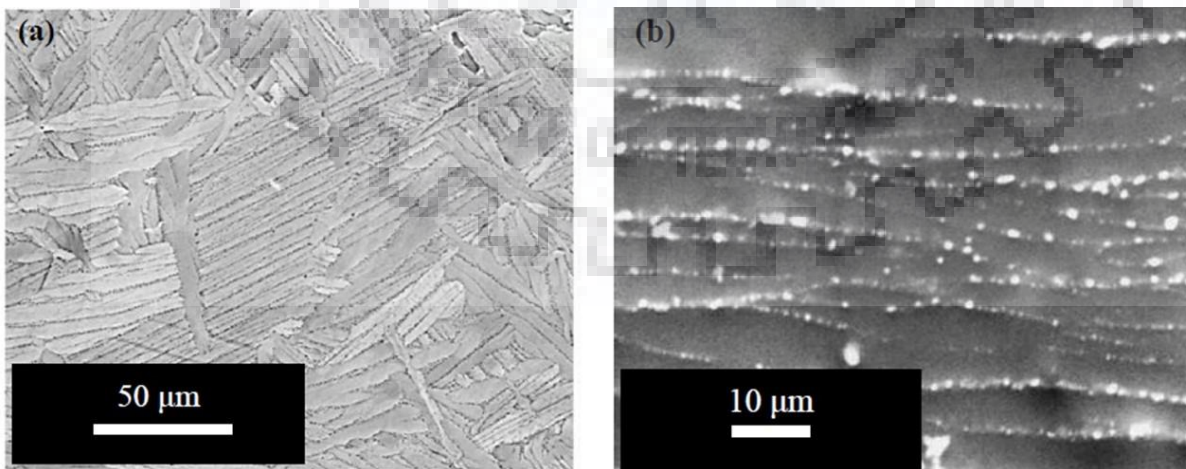
Figure 2.7: Typical SEM images of β–quenched condition showing; (a) lamellar grain structure [36], (b) SPPs precipitating on grain boundaries [35]

2.4.2 Hot Extrusion: For fabrication of pressure tubes, β–quenched material is subjected to extrusion in (α+β) phase (~760–850°C) region followed by cold-working (25–30% reduction) to final size. After cold working, a final stress-relief at 400°C for 24 hr is carried out. Variables such as the holding time in the furnace prior to extrusion and the extrusion ratio affect the microstructure of the final tube and its mechanical properties.

2.4.3 Annealing:

2.4.3.1 Annealing in α–phase: The annealing in α–phase or α–annealing is done at temperatures below the (α+β) phase region. It helps to produce mainly two types of microstructures: (i) stress relieved (SR) and, (ii) recrystallized (RX). Annealing for stress relieving is conducted at around 475°C in vacuum or protective atmosphere. During this process, the dislocation density reduces without recrystallization. The recrystallization is observed at 550°C to 600°C for both zirconium-niobium alloys and zircaloys [38]. During recrystallization process, new grains form and dislocation density obtained during deformation reduces dramatically. The nucleation and growth phenomena is strongly related to annealing temperature, time and the amount of deformation originally introduced into the material [39]. The annealing of Zr-1Nb alloy for 1 hour at 580°C exhibits fully recrystallized microstructure, as shown in **Figure 2.8**.
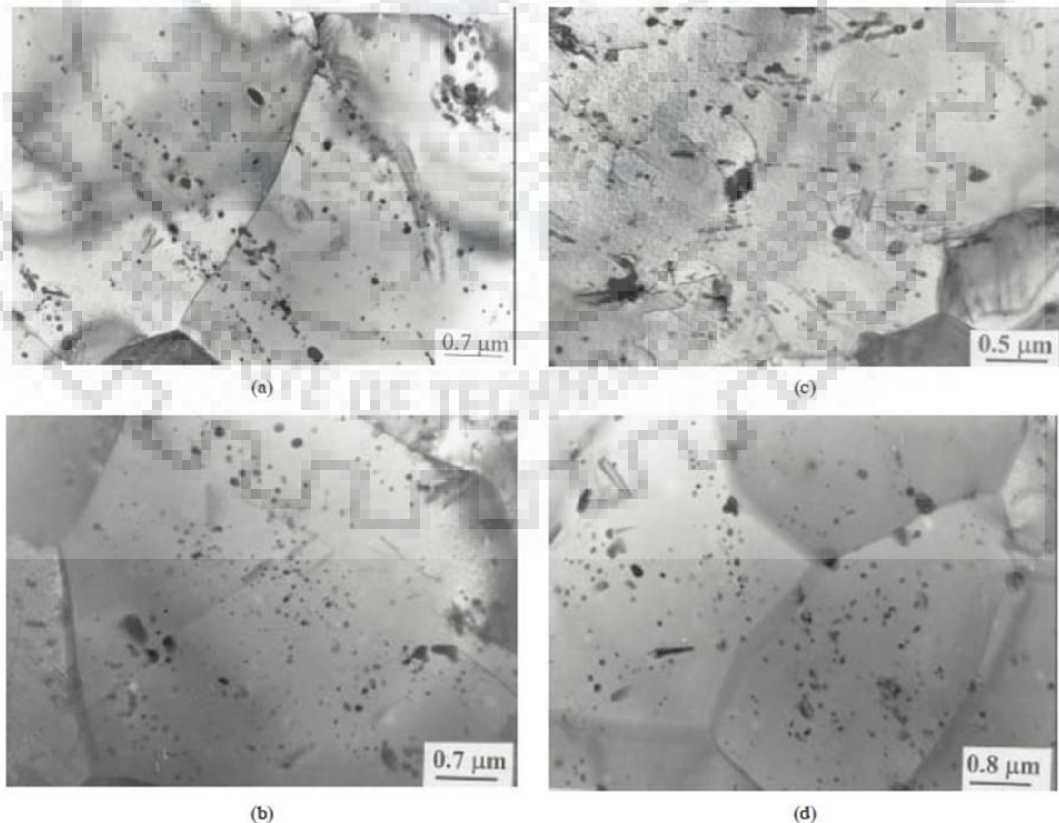
Figure 2.8: Bright field TEM micrographs of Zr-1Nb alloy annealed at; (a) 580ºC/1h, (b) 580ºC/4h, (c) 630ºC/1h and (d) 630ºC/4h [9]
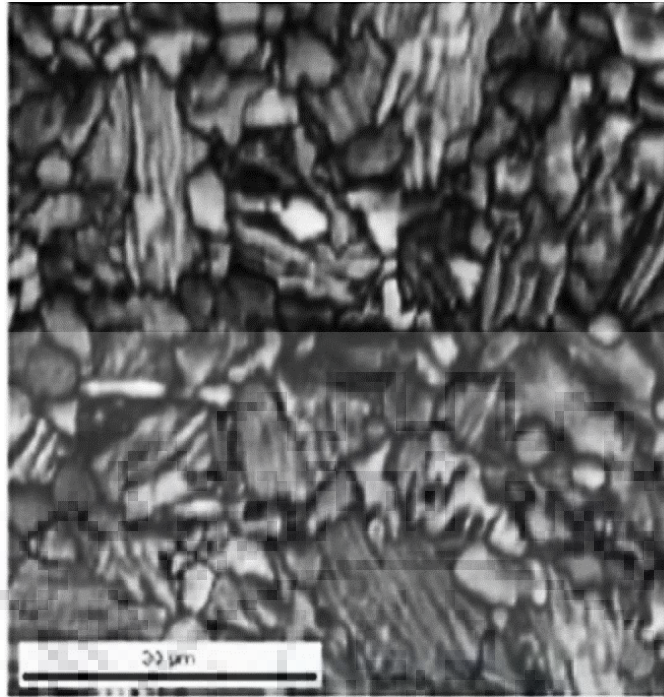
Figure 2.9: Bimodal microstructure of Zr-1Nb alloy, annealed at 883ºC and quenched at a rate of 0.5ºC/s [40]

2.4.3.2 Annealing in (α+β) or β–phase: Annealing in two phase region provides a bimodal grain size microstructure. These bimodal type microstructures are clearly visible in Figure 2.9. During heating, β–phase content increases sharply as the temperature goes just above the α/(α+β) transus (i.e. 610oC) and reaches 100% at nearly (α+β)/β transus temperature, while cooling from corresponding temperature it transforms to α plates, as shown in **Figure 2.10**. The shape and size of these transformed α plates depend on cooling rate. **Figure 2.10** shows microstructures based on different cooling rates. From **Figure 2.10**, it is clear that the size of α plates increases as cooling rate decreases. For instance, a slow cooling rate of 10oC/min provides the microstructure consisting with Widmanstätten α plates (**Figure 2.10b**), whereas fast cooling as 100oC/min provides very fine α plates (**Figure 2.10e**). The nucleation of these α plates starts at the prior β grain boundaries, as shown in **Figure 2.11**.

14
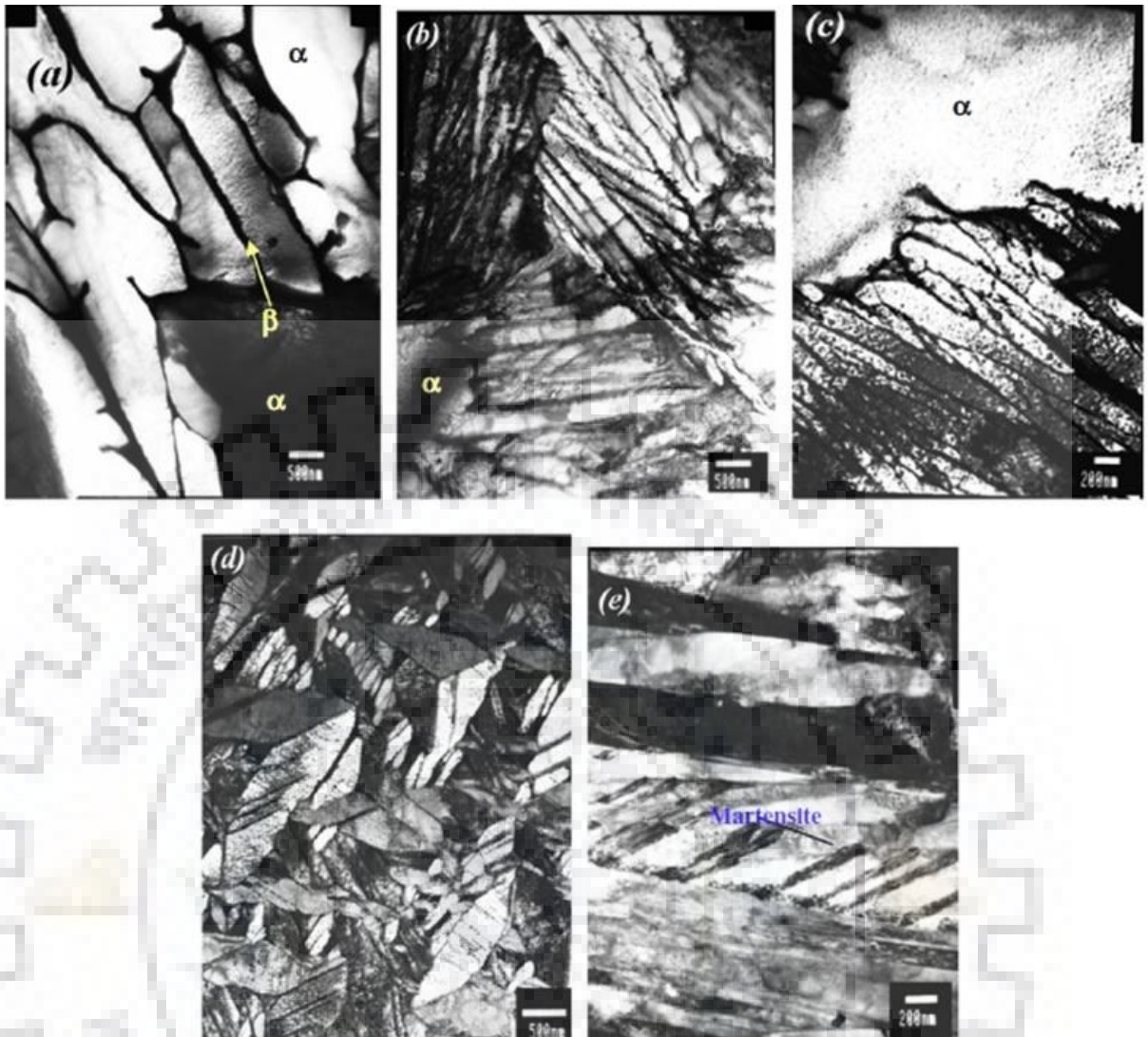
Figure 2.10: Bright field TEM images showing the effect of cooling rate, as the samples were soaked at 883°C (i.e. two phase region) and quenched at a rate of; (a) 0.5°C/s, (b) 10°C/s, (c) 25°C/s, (d) 50°C/s and (e) 100°C/s [41]
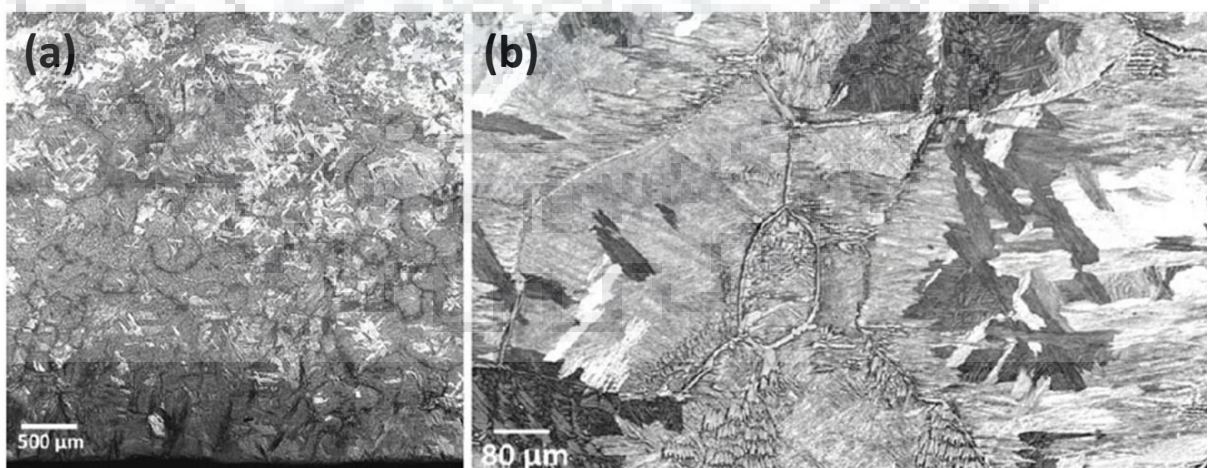
Figure 2.11: Microstructure of Zr-2.5Nb alloy after heating to β–phase (i.e. 1050°C) and cooling to α–phase. Rate of heating and cooling is constant as 20°C/s. **Figure 2.11b** is magnified image of **Figure 2.11a**, showing Widmanstätten α–plates surrounded by prior β–grain boundaries [13]

2.5 HOT DEFORMATION

The deformation carried out at a temperature of above $0.5T_m$ (T_m is the absolute melting temperature) is usually referred as hot deformation. Extrusion, forging and rolling are the primary processes wherein, deformation is carried out at temperatures exceeding $0.5T_m$. These hot deformation processes are very important in breaking the cast structure and giving shape to the ingot. Dominant deformation mechanism depends on relative ease with which following processes occur; dislocation generation and glide, cross slip and climb and, diffusion. The effect of all these processes can be understood by analysis of flow stress at different temperatures and strain rates and/or microstructural evolution after deformation. Increase in flow stress as a function of strain indicates strain hardening (dislocation generation) whereas, flow softening means decrease in dislocation density with strain. However, flow softening may also a result of instability in the material. Decrease in dislocation density can takes place due to recovery or recrystallization. Between recovery and recrystallization, which process will dominate the deformation process is decided by deformation condition and/or material properties like stacking fault energy. For example, usually recovery process is dominant mechanism at lower deformation temperatures and for materials with high stacking fault energy.

Temperature and strain rate are the two processing conditions that affect deformation processes significantly. However, effect of these two conditions on flow stress is quite different. Increase in strain rate increases flow stress whereas increase in temperature, decreases it. Temperature and strain rate can be represented by one single parameter called Zener Hollomon parameter $Z = \dot{\varepsilon} \exp\left(Q/RT\right)$. As the equation suggests, increase in Z value indicate increase in strain rate and decrease in temperature and vice versa. Therefore, flow stress can be related to Z parameter, which helps to develop constitutive equation. Activation energy, Q and stress exponent, n are calculated during the development of constitutive equation. These Q and n values help to predict the deformation mechanism operating during hot deformation. Another popular approach to identify the different deformation mechanisms operating during hot deformation is by generating processing maps. By taking help of microstructural analysis, the deformation mechanisms can be identified for a set of temperature and strain rate.

For zirconium alloys bulk metalworking is done in a series of steps. Each step of metalworking plays significant role in order to acquire the desired microstructure and properties in the final product. In the processing route of zirconium alloy (see **Figure 2.5**), melting and hot deformation are primary steps, and cold working and annealing are secondary steps. The process of forging, hot extrusion and helical rolling are usually done in (α+β) or in the β–phase region of

zirconium alloys. Dynamic recrystallization (RDX) is most desirable restoration mechanism, as it helps to improve the mechanical properties. The deformation conditions that favour dynamic recrystallization in Zr-alloys are dependent on the type of alloying elements (i.e. α stabilizer or β stabilizer).

However, in the conventional industrial hot working processes, it is difficult to identify deformation conditions that promote dynamic recrystallization in Zr-alloys. Hot compression tests under laboratory conditions proved quite successful in simulating the deformation conditions of the industrial processes, in order to identify the deformation mechanism and to obtain the desired microstructure [42].

2.5.1 Restoration mechanisms in hot deformation: The possible restoration mechanisms reported in literature for different alloys are discontinuous dynamic recrystallization (DDRX), continuous dynamic recrystallization (CDRX), rotational recrystallization (RRX), geometric dynamic recrystallization (GDX), dynamic recovery (DRV) accompanied by grain growth (GG) [43]. In DDRX, formation and growth of dislocation free nuclei surrounded by high angle grain boundaries occur in the highly strained matrix. However, continuous dynamic recrystallization (CDRX), rotational recrystallization (RRX) and geometric dynamic recrystallization (GDX) are based on DRV process [44]. In CDRX, sub-grain boundaries form during the initial stages of deformation. As strain increases, misorientation of sub boundaries gradually increases by dislocation recovery and eventually leads to significant increase in fraction of HAGBs. The rotational recrystallization (RRX) is a form of CDRX in which the cell walls and sub-grains rotate to increase the boundary misorientation [45]. GDX has also been observed in high stacking fault energy materials, where pronounced recovery takes place. Recovery of dislocation by climbing process which leads to annihilation of dislocation in the high angle grain boundaries results in serrated grain boundaries. As deformation increases, the original grains become flattened and eventually small crystallites form by interpenetration of the original serrated high angle grain boundaries [46].

Other than the microstructural analysis, some parameters of constitutive analysis (activation energy, Q and strain hardening, n) also provide some details about deformation mechanism occurring during hot deformation. If the calculated activation energy is similar to that of lattice self-diffusion, Q_{sd}, then dislocation climb is the rate controlling mechanism. The Q_{sd} values for Zr and Zr-alloys change significantly with temperature [36]. At temperature higher than 650°C the Q_{sd} varies in between 90 to 140 kJ/mol whereas, it is about 270 kJ/mol at lower temperatures [37, 38]. At higher temperatures, discrepancy in Q value may be due to additional

17

restoration mechanisms other than dynamic recovery (DRV) taking place. The possibility of additional restoration mechanisms at higher temperature can also arise due to increase in fraction of high angle grain boundaries [39].

2.5.2 Hot deformation behavior of Zr-Nb alloys: The hot deformation by hot compression tests of different Zr-Nb alloys provide significant information about deformation mechanisms [47]. In general, it is found that the deformation parameters, i.e. strain, strain rate and temperature influence the dominant deformation mechanism and final grain size. Based on strain rate sensitivity maps (**Figure 2.12**), it is reported that the addition of Nb shifts the DRX domain of commercially pure Zr (CP-Zr) towards lower strain rates whereas, addition of Sn does not influence the DRX domain of CP-Zr. In these alloys, DRX is essentially a nucleation and growth process, i.e. DDRX. [47-49]. This effect can be understood more clearly by considering the α stabilizers or β stabilizers. It is found that α stabilizers have limited influence on the deformation behavior of the α–phase (hcp phase) whereas, deformation characteristics of β–phase altered dramatically by adding β stabilizers [50, 51]. Addition of Nb lowers the strain rate of DRX by two orders of magnitude in Zr-Nb alloys, compared to pure Zr [49]. Moreover, the stacking fault energy is the primary factor that decides the DRX process in Zr-Nb, CP-Zr and Zr-Sn alloys.

2.5.2.1 Deformation behavior in single α–phase: The deformation in α–phase exhibits strain hardening similar to room temperature deformation and produce high strengthening with relatively lower ductility and low deformability [52]. In α–phase at very low strain rate deformation, commercially pure reactor grade α–zirconium exhibits texture-induced dynamic recovery at the temperature of 650ºC and strain rate of 10^{-3} s^{-1}. It does not exhibit superplasticity when deformed in α–phase due to lower diffusivity compared to β–Zr [53, 54]. It also exhibits microstructural instabilities in the form of localized shear bands, when deformed at strain rate higher than 1 s^{-1} [50]. The deformation of Zr-alloy in α–phase is not commercially useful. Therefore, the literature on hot deformation in α–phase is very limited.

2.5.2.2 Deformation behavior in single β–phase: In zirconium, β–phase appears first from the liquid phase during cooling [15, 37, 56, 57]. The hot working in β–phase is favorable compared to α–phase due to higher diffusion rate of alloying elements along with the lower values of flow stresses [4, 53]. The hot deformation in single β–phase of Zr-1Nb alloy with β–quenched initial microstructure, exhibited elongated prior β grain morphology, as shown in **Figure 2.13** [58]. Elongated prior β grain morphology is a clear evidence of dynamic recovery that is considered to be the deformation mechanism in β–phase of Zr-1Nb alloy.
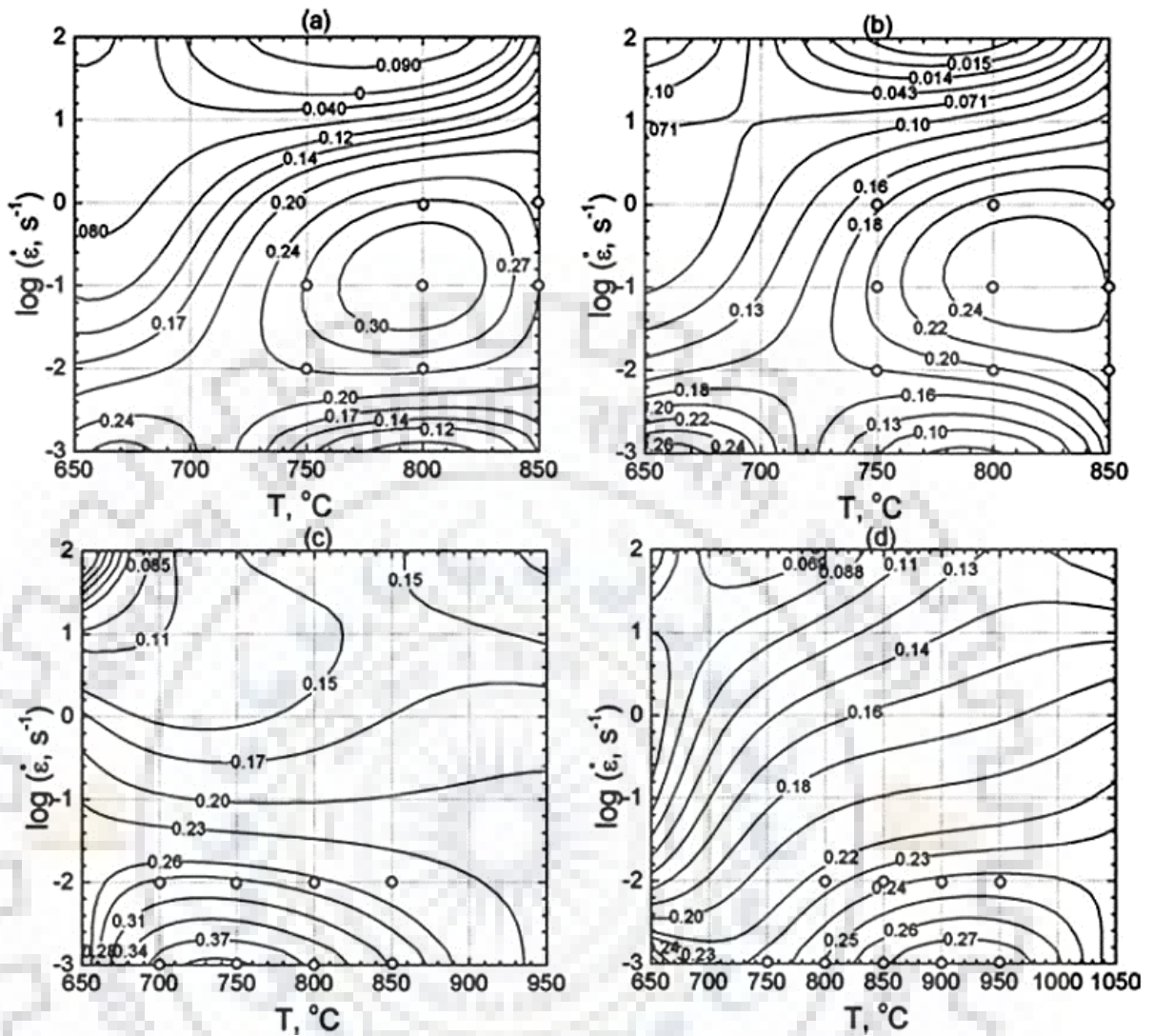
Figure 2.12: Strain rate sensitivity maps at a strain of 0.4 for different Zr-alloys; (a) CP-Zr (b) Zr–Sn (c) Zr–Nb and (d) Zr–Nb–Sn–Fe [55]
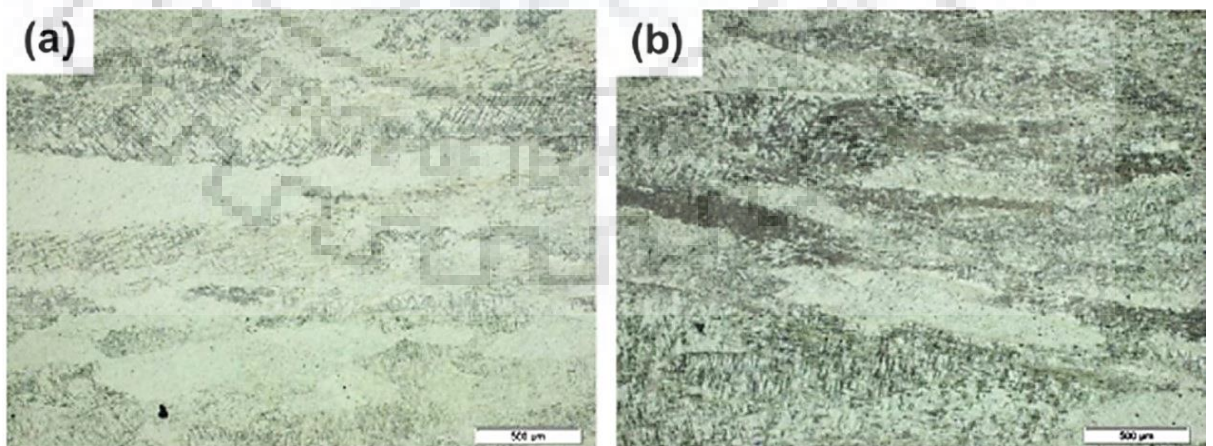
Figure 2.13: Optical micrograph of the sample deformed in β–phase of Zr-1Nb alloy at; (a) 900°C, 0.1 s^{-1} and (b) 950°C, 0.1 s^{-1} [58]

The tensile tests on different equiaxed microstructures of Zr-2.5Nb alloy at elevated temperatures exhibited superplastic behaviour [59]. The superplastic behavior was studied in the

19

temperature range of 730 – 830°C and at strain rates below 10^{-3} s^{-1}. As the grain size increases, superplastic deformation condition shifts towards higher temperature and lower strain rates. The apparent activation energy (Q) and stress exponent (n) suggest that the superplastic behavior of this material is controlled by the grain boundary diffusion of Zr and Nb in the β–phase. The superplastic deformation was also studied in β–quenched Zr-1Nb-1Sn alloy at temperature of 910°C and strain rates lower than 10^{-2} s^{-1} [55]. Calculated apparent activation energy for this alloy suggest that the rate controlling mechanism in single β–phase is non-conservative movement of jogs. The deformation of Zr-2.5Nb alloy and Zr-2.5Nb-0.5Cu in β–phase with β–quenched starting microstructure exhibited large grain superplasticity at higher temperature and lower strain rate, while elongated grains appeared at lower temperatures and higher strain rates representing dynamic recovery [4, 8]. The superplasticity in β–phase is associated with large grain size and attributed to newly formed stable sub-grains [8, 60]. During hot deformation in β–phase, unstable features in microstructures of Zr-Nb alloys have been reported at strain rate higher than $10\,s^{-1}$ [4, 8], whereas addition of Cu in Zr-Nb alloy increases the strain rate of unstable features from $10\,s^{-1}$ to $30\,s^{-1}$. There is no change in hot deformation behavior in β–phase by the addition of alloying elements like Sn or Nb.
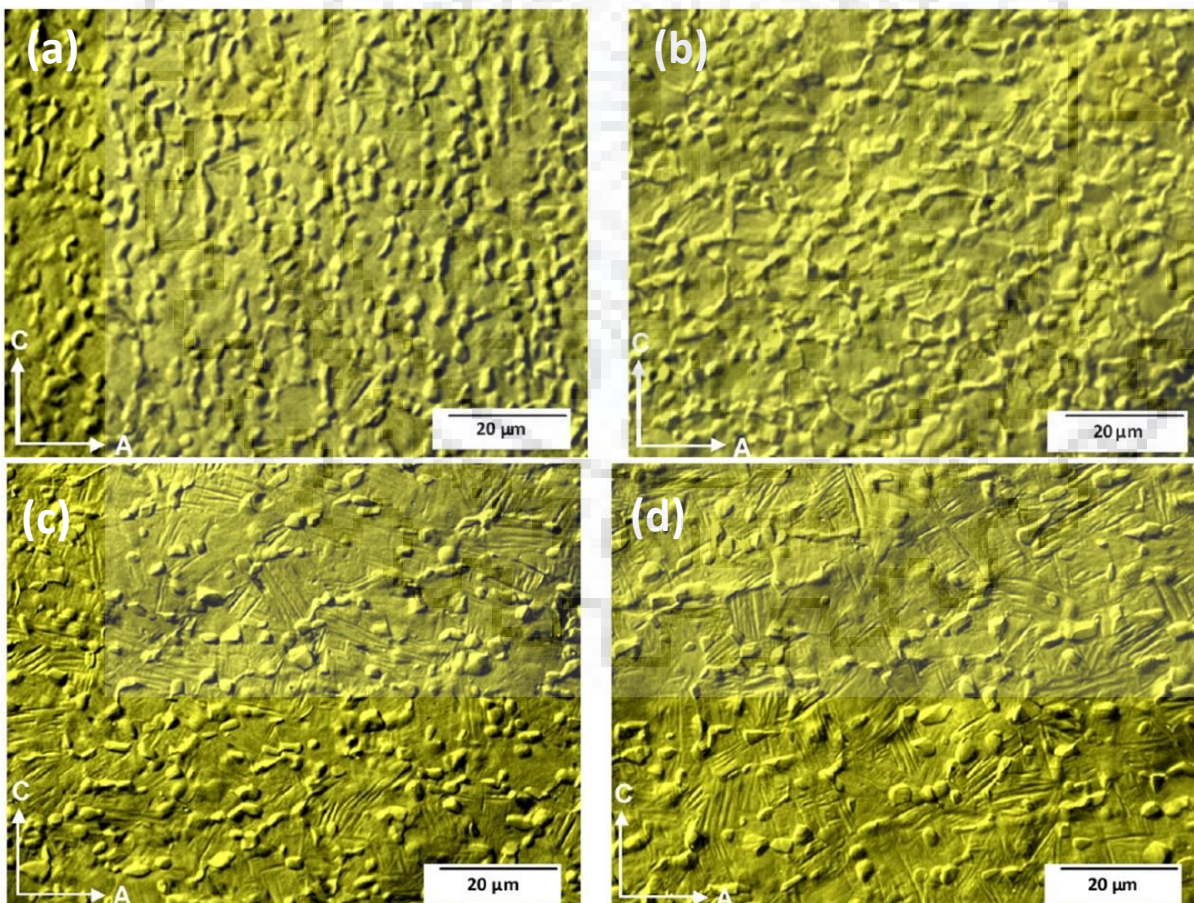
Figure 2.14: Optical micrograph of Zr-2.5Nb alloy showing primary α and α' (martensite) phase, when heated to two phase region and soaked at 850°C for; (a) 15 mins., (b) 30 mins., and at 870°C for; (c) 15 mins., (d) 30 mins. followed by water quenching [61].

2.5.2.3. Deformation behavior in two phase (α+β) region: Any Zr-Nb alloys heated up to two phase region and soaked for a certain time in two phase region and then quenched, produces two phase microstructure consisting of "primary α" and α' (β transformed) phase. Moreover, the volume fraction of α' increases with increasing soaking temperature as shown in **Figure 2.1**4 [61].

The hot compression of Zr-1Nb alloy in two phase region with β quenched starting microstructure reveals DRX as dominating deformation mechanism on the basis of equiaxed morphology and high angle grain boundaries. The equiaxed morphology with high angle grain boundaries is due to reorientation of initial Widmanstätten morphology of α–phase after hot compression. The calculated apparent activation energy and stress exponent suggests that the cross-slip (mechanical recovery) of screw dislocations in α–phase may be involved in the appearance of DRX [58].

Bocharov et al. [52] conducted compression and tension tests on Zr-1Nb alloy in two phase region (650 – 850°C) and found intensive dynamic polygonization process, which in turn stabilized the microstructure. The optimum parameters for hot deformation in two phase (α+β) region of Zr-1Nb-1Sn alloy with β–quenched starting microstructure was found in the temperature range of 750 – 950°C and in the lower strain rate range i.e. $< 10^{-2}\,\mathrm{s}^{-1}$. For this alloy, DRX in two phase region was reported at temperature of 910°C and strain rate of $10^{-3}\,\mathrm{s}^{-1}$. Flow instabilities in two phase region were also found at temperatures lower than 850°C and strain rates higher than $10^{-2}\,\mathrm{s}^{-1}$ [55]. Neogy et al. [9] performed hot compression test to understand hot deformation behaviour of Zr-1Nb-1Sn-0.1Fe alloy with β quenched and tempered starting microstructure. They reported both DRV and DRX in two phase (α+β) region in which DRV occurred at starting of two phase, whereas DRX exhibited at the end of two phase region at temperature of 850°C and strain rate of $10^{-3}\,\mathrm{s}^{-1}$. During DRX, initial microstructure having Widmanstätten morphology of α–phase was changed to an equiaxed microstructure. Chakravartty et al. [49] studied the hot deformation characteristic of Zr-2.5Nb alloy with two different starting microstructures; one is β–quenched and other equiaxed (α+β) using hot compression tests. They reported continuous flow softening and steady state behavior in stress–strain curves at strain rates lower than $1\mathrm{s}^{-1}$ for β–quenched and equiaxed (α+β) respectively. The DRX was reported at a strain rate of $10^{-3}\,\mathrm{s}^{-1}$ and temperature of 750°C for β–quenched, and at temperature of 850°C for equiaxed (α+β) starting microstructure, and considered these as the optimum hot working conditions. The DRX process in β–quenched microstructure initiates after 50% strain, whereas in equiaxed microstructure, it is controlled by the cross-slip of screw dislocations [8]. Both the starting microstructure exhibited instability in the form of localized shear bands at temperatures lower than 700°C and strain rates higher than 10 s^{-1}. The continuous flow softening in stress-strain curves

and DRX microstructure in two phase ($\alpha+\beta$) region was observed in the hot deformation of β–quenched Zr-2.5Nb-0.5Cu alloy. The DRX microstructure in two phase region was attributed as the shearing and spheroidization of α–platelets [8]. In hot deformation of commercially pure reactor grade α–zirconium, DRX was reported in the temperature range of 730 to 850°C (two phase region) and the strain rate range of 10^{-2} to 1 s^{-1}. It was concluded, that the optimum safe hot working conditions were at temperature of 800°C and strain rate of 10^{-1} s^{-1}, where dynamically recrystallized microstructure was observed in the deformed sample [50].

2.6 PREDICTION AND UNDERSTANDING OF DEFORMATION BEHAVIOR

2.6.1 Processing map approach: The optimization of the processing parameters is required to obtain safe deformation conditions without any instability. Therefore, it is essential to have understanding of hot deformation behavior and controlling mechanism. It is well established that the processing map technique is a powerful approach for process optimization and prediction of deformation behavior with controlling mechanism [62-65]. Processing map approach provides better results than other expensive and time-consuming trial and error methods [66, 67]. A processing map is developed using flow stress data as a function of strain, strain rate and temperature. The processing maps are sub-divided in to domains, which are classified as "safe" and "unsafe" domains for the hot deformation of materials [62, 68].

Processing maps are shown on the axes of temperature and strain rate for a particular strain. Initial development in the field of processing map saw pioneering attempts made by Ashby [69] and Raj [70]. They proposed deformation processing maps which are useful to establish relationship between processing parameters, deformation mechanism and flow behavior, but their applicability was limited for simple alloys or for low strain rate range (i.e. creep).

To analyze the constitutive behavior of material at high temperature in wide range of strain rates, a "systems approach" concept was introduced, which is based on the continuum mechanics of large plastic flow, modeling of physical system and irreversible thermodynamics. Gegel [71] introduced a model named as Dynamic Materials Model (DMM) to generate processing map, which act like a bridge between continuum mechanics and microstructural mechanics during hot deformation. This approach made it possible not only to optimize hot workability but also to sketch out the regimes of flow instability that should strictly be avoided during the processing. The first extension of DMM was proposed by Prasad et al. [62, 67, 71, 72] and later modified by Murty and Rao [73, 74] (named as Modified dynamic materials models, MDMM). These models were applied successfully in the optimization of processing parameters for a wide range of materials such as austenitic stainless steel, titanium alloys, zirconium alloys,

super-alloys like Co-Ni-Cr-Mo etc. [50, 62, 68, 73, 75-78]. Another model based on strain hardening (or flow softening) was introduced by Jonas et al. [79] that defined a flow localization *α–parameter*.

The different developed materials models can be classified based on material properties. DMM and MDMM are based on the strain rate sensitivity *(m)* of flow stress. However, DMM assumes power law dependence of flow stress on strain rate (constant strain rate sensitivity) whereas, MDMM considers variable strain rate sensitivity *(m)* and therefore provides a generalized model. On the other hand, *α-parameter* considers both strain rate sensitivity *(m)* and the strain hardening to define safe processing conditions.

2.6.1.1 Based on strain rate sensitivity:

2.6.1.1.1 Power law (Dynamic Material Model, DMM): In DMM, Prasad et al. [62] assumed that the material under hot deformation does not store energy during the deformation and suggested that at any instant during the plastic deformation process, the total power, *P* dissipated by a unit volume of a visco-plastic material specimen may be distributed into two parts. One part of the power is dissipated in deformation work, *G,* and other part of power is dissipated in microstructural change, *J.* Microstructural change, *J* may be contributed by metallurgical processes such as dynamic recrystallization, dynamic recovery, internal fracture (wedge cracking or void formation), dynamic spheroidization of acicular structures, dissolution or growth of particles or phases under dynamic conditions, and deformation induced precipitation or phase transformation under dynamic condition. *G* and *J* can be represented by following equations:

$$P_{T,\varepsilon} = G + J = \sigma\,\dot{\varepsilon} = \int_0^{\dot{\varepsilon}} \sigma\,d\dot{\varepsilon} + \int_0^{\sigma} \varepsilon\,d\sigma$$

where (2.1)

$$G = \int_0^{\dot{\varepsilon}} \sigma\,d\dot{\varepsilon} \quad and \quad J = \int_0^{\sigma} \varepsilon\,d\sigma$$

Efficiency of power dissipation, η and instability parameter, ξ can be described on basis of power partition. Power partitioning between *G* and *J* is decided by the strain rate sensitivity parameter, *m*.

$$\frac{\partial J}{\partial G} = \frac{\dot{\varepsilon}\,\partial\sigma}{\sigma\,\partial\dot{\varepsilon}} = \frac{\partial(\ln\sigma)}{\partial(\ln\dot{\varepsilon})} = m$$

(2.2)

In case of ideal linear power dissipater, strain rate sensitivity parameter, *m* becomes unity. Therefore, *J* acquires its maximum value, J_{max} and can be represented as:

$$J_{\max} = \frac{\sigma \dot{\varepsilon}}{2} = \frac{P}{2} \tag{2.3}$$

The efficiency of power dissipation, η is:

$$\eta_{Prasad} = \frac{J}{J_{\max}} = \frac{2J}{P} = \frac{2m}{m+1} \tag{2.4}$$

The value of power dissipation efficiency is associated with consequent microstructural evolution. Higher value of η_{Prasad} indicates deformation processes like dynamic recrystallization (DRX) or dynamic recovery (DRV), which can be easily interpreted by microstructural observations. However, processes like adiabatic heating and localized shear deformation are also highly efficient but lead to instability. Instability can be calculated according to the following:

$$\xi_{Prasad} = \frac{\partial \ln\left(m/m+1\right)}{\partial \ln \dot{\varepsilon}} + m < 0 \tag{2.5}$$

At constant strain, ε, the variation of efficiency, η and instability, ξ as a function of T and $\dot{\varepsilon}$, provides a power dissipation map and instability map respectively. These map show "valleys", "hills" and "plateaus", which may relate to certain deformation mechanism. Superimposition of power dissipation map and instability map represents the processing map. Processing map reveals additional information as safe domain and unsafe domain for processing. The safe domain is a representation of good processing conditions whereas, unsafe domain indicates that processing in this domain is not favorable and should be avoided during the processing.

2.6.1.1.2 Generalized model based on variable m (Modified Dynamic Material Model, MDMM): Widely used DMM model was modified by Murty and Rao [73, 74, 80], and they proposed a modified model, known as MDMM. In MDMM, they eliminated the use of constant strain rate sensitivity (or power law behavior) during the calculation of the efficiency of power dissipation. They suggested a different procedure to compute power dissipation efficiency (η) from the curve of flow stress versus strain rate, which provides more appropriate results.

In the MDMM [81, 82], integral for J should be evaluated carefully in **Equation 2.1**, along with the limits of integration from zero to σ. Flow stresses, sometimes do not increase monotonically with increasing strain rate due to its oscillatory nature. The differential form for the dissipator power co-content, J in **Equation 2.1** can be rewritten as:

$$dJ = \dot{\varepsilon}\, d\sigma = \dot{\varepsilon}\frac{\sigma}{\dot{\varepsilon}}\, d\dot{\varepsilon} = \frac{\dot{\varepsilon}}{\sigma}\frac{d\sigma}{d\dot{\varepsilon}}\, d\varepsilon = m\,\sigma\, d\varepsilon \tag{2.6}$$

$$or \;\; J = \int_0^{\dot{\varepsilon}} m\,\sigma\, d\dot{\varepsilon} \tag{2.7}$$

At any strain rate $\dot{\varepsilon}$ in **Equation 2.6**, if the strain rate sensitivity becomes zero ($m=0$), J will be zero and the curve of $\sigma - \dot{\varepsilon}$ will not obey the power law (as per DMM consideration). As J is used to evaluate the behavior of materials up to $\dot{\varepsilon}$ (global), while strain rate sensitivity m provides the information at $\dot{\varepsilon}$ (local). Therefore, whenever m is equal to zero, it is not necessary that J will be zero. To improve the accuracy for the computation, J is initially expressed in the terms of P and G, as per **Equation 2.1** and therefore, simplified equation in the terms of σ and $\dot{\varepsilon}$ can be expressed as follows:

$$J = P - G = \sigma\dot{\varepsilon} - \int_0^{\dot{\varepsilon}} \sigma\, d\dot{\varepsilon} \tag{2.8}$$

The integral value of G in **Equation 2.8** is evaluated using flow stress data, and simplification of integral of G can be rewritten as:

$$G = \int_0^{\dot{\varepsilon}_{min}} \sigma\, d\dot{\varepsilon} + \int_{\dot{\varepsilon}_{min}}^{\dot{\varepsilon}} \sigma\, d\dot{\varepsilon} = \left(\frac{\sigma\dot{\varepsilon}}{m+1}\right)_{\dot{\varepsilon}=\dot{\varepsilon}_{min}} + \int_{\varepsilon_{min}}^{\varepsilon} \sigma\, d\varepsilon \tag{2.9}$$

The calculation of efficiency according to MDMM:

$$\eta_{Murty\&Rao} = \frac{2J}{P} = \frac{2(P-G)}{P} = \frac{2\left(\sigma\dot{\varepsilon} - (\sigma\dot{\varepsilon}/m+1)_{\dot{\varepsilon}=\dot{\varepsilon}_{min}} + \int_{\varepsilon_{min}}^{\dot{\varepsilon}} \sigma\, d\varepsilon\right)}{\sigma\dot{\varepsilon}} = 2\left\{\frac{1-\int_0^{\dot{\varepsilon}} \sigma\, d\dot{\varepsilon}}{\sigma\varepsilon}\right\} \tag{2.10}$$

In the **Equation 2.9**, $\dot{\varepsilon}_{min}$ is the minimum strain rate tested and the strain rate sensitivity, m has its usual meaning (as in DMM), but considered only at lowest strain rate. The instability parameter in MDMM can be calculated using following expression:

$$\kappa_{Murty\&Rao} = \frac{2m}{\eta} - 1 < 0 \tag{2.11}$$

2.6.1.2 Based on both strain rate sensitivity and strain hardening

2.6.1.2.1 α–parameter approach: This approach was proposed by Jonas et al. [79] to determine unstable processing conditions. It is based on both, strain hardening and strain rate hardening properties of the material [79, 83]. It is given by following equation:

$$\alpha = \frac{-\gamma}{m} \tag{2.12}$$

where

$$\gamma = \frac{1}{\sigma}\frac{\partial \sigma}{\partial \varepsilon} = \frac{\partial \ln \sigma}{\partial \varepsilon} \tag{2.13}$$

where 'γ' is the strain hardening coefficient and m is strain rate sensitivity (**Equation 2.12**). The strain rate sensitivity has its usual meaning as defined in **Equation 2.2**. Flow softening during hot deformation may occur due to microstructural changes (DRX) or instability (flow localization, which may arise from structural instabilities such as generation of a softer texture during deformation, adiabatic heating, spheroidization or grain coarsening). The value of m provides clarity about whether DRX is responsible for flow softening or instability. Flow softening accompanied by high value of m indicates stable process whereas, low value of m indicates unstable process. This forms the basis for applicability of α–*parameter* to determine stable hot deformation conditions. However, value of α–*parameter* to indicate instability in a material is specific to that material. On the basis of microstructural observation of titanium alloys, it is reported that the instability occurs if the α-*parameter* is greater than 5 [81], which is similar to zirconium alloys.

2.6.1.3 Reported literature on processing maps for Zr-Nb alloys: Among all the processing map approaches, DMM was used to understand the deformation behaviour of Zr-2.5Nb alloy having two different microstructures; equiaxed ($\alpha+\beta$) and β–quenched microstructure. It was found that in the equiaxed microstructure safe deformation is at the temperature of 850°C and strain rate of 10^{-3} s^{-1}, whereas in β– quenched microstructure it is at 750°C and strain rate of 10^{-3} s^{-1} [49]. The safe processing conditions for hot deformation of α–zirconium using DMM approach were reported to be in the temperature range of 730 – 850°C and strain rate range of $10^{-2} – 1$ s^{-1}. The high peak efficiency of power dissipation was correlated with DRX in deformed microstructure [50]. The safe processing conditions of as cast Zr-2.5Nb alloy were obtained using processing map approach (i.e. DMM and strain rate sensitivity map), and it was found that the processing of cast Zr-2.5Nb alloy is safe in the temperature range of 800–1100°C and at strain rates lower than 10^{-1} s^{-1}. Moreover, unstable processing conditions were identified using different criteria, and it was found that at low temperature (i.e. 700 and 750°C) and high strain rate of 1 s^{-1} and 10 s^{-1}, as cast Zr-2.5Nb material is not safe for processing due to flow localization in microstructure [7]. Kapoor et al. [59] reported superplastic behaviour

26

in Zr-2.5Nb alloy at temperature range of 730 – 830°C and at strain rates below 10^{-3} s^{-1}, using strain rate sensitivity map **(Figure 2.15)** and microstructural analysis.
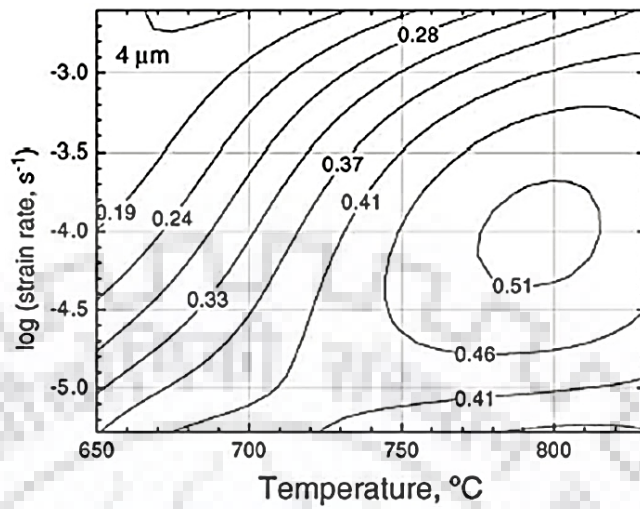
Figure 2.15: Iso-strain rate sensitivity map of Zr–2.5 wt.%Nb material [59]

Murty and Rao [77] observed safe domain for hot working of Zr-2.5Nb with equiaxed microstructure using modified dynamic material model (MDMM), and reported that the results obtained using DMM on same material are different from the MDMM results. Murty and Rao [73] worked on Zr-2.5Nb alloy to identify the unstable region in processing map using Ziegler criterion and found unstable domain different to DMM. A comparative table containing safe and unsafe processing conditions, deformation mechanism, approach used for different Zr-Nb alloys is shown in **Table 2.2**.
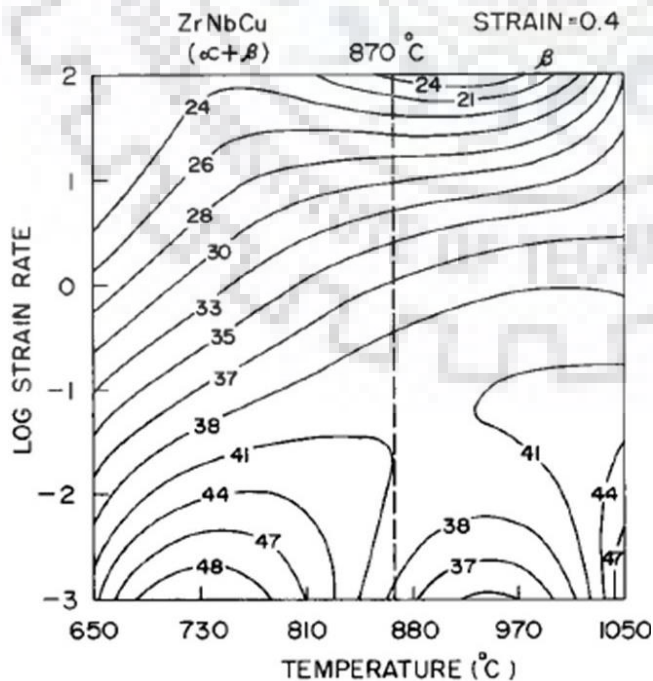
Figure 2.16: Processing map for β–quenched microstructure of Zr-2.5Nb-0.5Cu for a strain of 0.4. The dotted line represents (α+β) →β transition [8]

27

Table 2.2: Comparative study of safe and unsafe processing condition using different approach for Zr-Nb alloys

Alloy	As received condition	Approach used	Stable domain			Unstable domain		
			Processing condition	Peak efficiency (%)	Dominating mechanism	Approach used	Processing condition	Microstructural features
Zr-2.5Nb [49]	Equiaxed (α+β)	DMM	850°C/10⁻³ s⁻¹	45	DRX	DMM	700/> 1s⁻¹	Flow localization
Zr-2.5Nb [49]	β quenched	DMM	750°C/10⁻³ s⁻¹	54	Shearing of α plate	DMM	>670°C/ > 1s⁻¹	Localized shear band
α–zirconium [50]	Extruded, cold drawn and β-quenched	DMM	730 − 850°C/10⁻² − 1 s⁻¹	40	DRX	DMM	700/> 1s⁻¹	Flow localization
Zr-2.5Nb [7]	As cast	DMM, Strain rate sensitivity map	800 − 1100°C/ < 10⁻¹ s⁻¹	30	DRX	DMM, Lyapunov functions	700, 750°C/ 1 s⁻¹ and 10 s⁻¹	Flow instability
Zr-2.5Nb [59]	Extruded in (α+β) phase	Strain rate sensitivity map	730 − 830°C⁻¹/< 10⁻³ s⁻¹	50	Superplasticity	-	-	-
Zr-2.5Nb [49, 73]	β quenched	MDMM	800°C/10⁻³ s⁻¹	40	DRX	MDMM	650°C/ 10 and 100 s⁻¹	Flow localization
Zr-2.5Nb	Equiaxed (α+β)	MDMM	750°C/10⁻³ s⁻¹	30	DRX	MDMM	650°C/ 10 and 100 s⁻¹	Flow localization
Zr-2.5Nb-0.5Cu [8]	β-quenched	DMM	750, 1050°C/ 10⁻³ s⁻¹	48	spheroidization, DRX	DMM	> 800°C/ > 30 s⁻¹	Flow localization
			1050°C/ 10⁻¹ s⁻¹	47	Superplasticity			
			625 − 800°C/< 10⁻¹ s⁻¹	24	DRX			
Zr-1Nb [58]	Extruded and cold drawn	DMM	950°C/ 10⁻¹ s⁻¹	22	DRV	-	-	-

Only limited data is available on the hot deformation behaviour of Zr-2.5Nb-0.5Cu and Zr-1Nb alloys using processing map approach. DMM approach for processing map development was used to identify and understand the safe processing condition for Zr-2.5Nb-0.5Cu, as shown in **Figure 2.16** and two domains were found for safe processing; one is in two phase (α+β) phase and other is in β–phase. The safe processing in two phase region lie at the temperature of 750°C and strain rate of 10^{-3} s^{-1}, whereas in β–phase it is at 1050°C and strain rate of 10^{-3} s^{-1} [8]. The flow stress data of Zr-2.5Nb-0.5Cu was used by Murty et al. [63], who obtained different safe and unsafe regions using approach other than DMM and reported a lot of discrepancies. The strain rate sensitivity map **(Figure 2.17)** was used to understand hot deformation behavior of Zr-1Nb alloy having extruded and cold drawn conditions, and a safe DRX domain was found in the temperature range of 625 – 800°C and strain rate below 10^{-1} s^{-1}. Another domain was found in the β–phase region at temperature of 950°C and strain rate of 10^{-1} s^{-1} bearing dynamic recovery features [58].
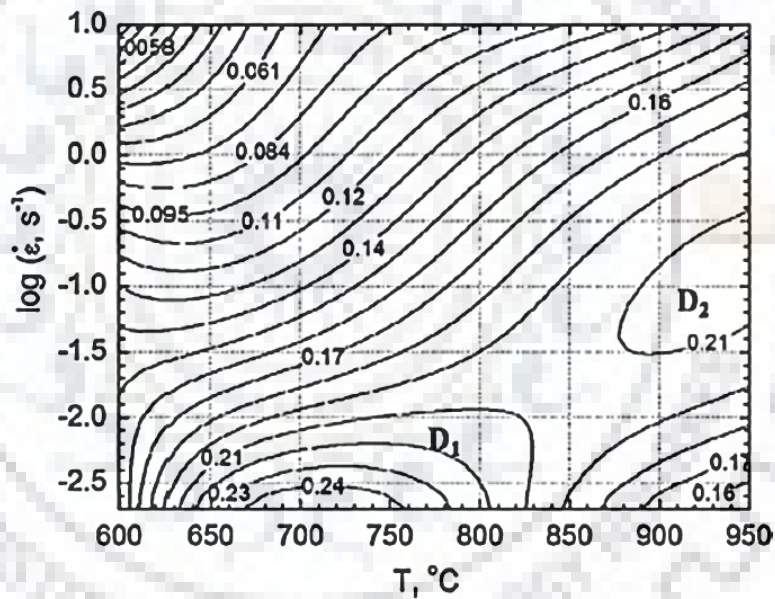
Figure 2.17: Iso-strain rate sensitivity contour map for a strain of 0.5. The values on the contours indicate the values of strain rate sensitivity (*m*) [58]

The above literature survey of processing maps for Zr-Nb alloys shows that there is discrepancy in the prediction of safe or unsafe processing domains/ regions, based on the approach used. Thus, it is necessary to identify as to which processing map approach is suitable to predict safe processing conditions for Zr-Nb alloys. Moreover, majority of safe processing conditions predicted by processing maps are in the two phase region, but the processing map is not able to define the role of individual phases in the two phase region.

2.6.2 Constitutive equation: Constitutive equation describes the relationship between stress, strain rate, and deformation temperature. It helps to calculate expected load and power

29

required for forming processes and also suggest material flow behavior [84]. Thus, it is necessary to develop an accurate constitutive equation for a given material.

2.6.2.1 Various constitutive equations/ models: The constitutive equations are classified into three different categories: physical-based constitutive model, phenomenological constitutive model and artificial neural network (ANN).

2.6.2.1.1 Physical-based constitutive model: These models are based on physical aspects of material behaviors, i.e. theory of thermodynamics, kinetics of slip and thermally activated dislocation movement. These models are applicable over a wide range of loading conditions. Few physical based models are Bodner-Partom (BP) model [85], Rusinek-Klepaczko (RK) model [86], Zerilli and Armstrong (ZA) model [87, 88] and its modification (m-ZA) [89], Preston-Tonks-Wallace (PTW) model [90] and Voyiadjis-Almasri (VA) model [91].

2.6.2.1.2 Phenomenological constitutive model: In these models, a description of flow stress is based on empirical observations using some mathematical functions. These models are suitable where an exact physical mechanism is not clear. However, these are applicable over a limited range of strain rate and temperature. Few phenomenological models are: Cellular Automation (CA) model [92, 93], Voce-Kocks (VK) model [94], Johnson-Cook (JC) model [95], and its modification (m-JC) [89], Khan-Huang (KH) [96], Fields-Backofen (FB) model [97], Molinari-Ravichandran (MR) model [98], Arrhenius type model with or without strain compensation [99-101], and its modification [102].

2.6.2.1.3 Artificial neural network (ANN): Lastly, ANN provides an alternative approach to predict flow behavior during hot deformation, and it is best suited to those problems for which material behavior is not clear at all. However, the successful application of ANN model is strongly based on error free data and characteristic variables.

Out of all the available approaches, phenomenological models are widely used models, because they offer a trade-off between knowing exact material behavior and "black box" approach of ANN. Sellars and Tegart [103] and Jonas et al. [104] have proposed a phenomenological approach, in which flow stress is related to the strain rate by sine-hyperbolic law in an Arrhenius type equation. Extensive work on constitutive analysis of hot deformation for different metals and alloys is reported by Lin and Chen [105], Cingara, and McQueen [106], Phaniraj and his group [107, 108], Kassam et al. [109], Mirzadeh and their co-workers [101, 110, 111], and Samantaray et al. [112]. The flow stress of a material depends upon both strain rate and temperature which can be combined in a single parameter known as Zener-Hollomon

parameter (Z) [113]. However, constitutive analysis of material having two phase region like that in Zr-Nb alloys (HCP/BCC) is not well understood.

2.6.2.2 Application of constitutive equations in two phase materials: Irrespective of the model used, development of a constitutive equation for a two phase material becomes even more complicated due to uncertainty in determining the dominant phase in the two phase region. Accurate determination of activation energy, stress exponent and pre-exponential factor is important to develop an accurate constitutive equation. Thus, it is essential to understand activation energies of individual phases in the two phase range. In literature, different approaches are used to calculate the activation energy for deformation of two phase materials. Kim et al. [114] considered activation energy on the basis of the strain rate range for deformation of the two phase Ti-6Al-4V alloy. Kotkunde et al. [102, 115], Yuan [116] and Chao et al. [117], compared constitutive models for various Ti alloys irrespective of the phases present. Chen et al. [118] developed constitutive models of Ti-6Al-4V alloy in the temperature range $20 - 900^{\circ}$C (below β transus temperature), without considering the effect of phases present. Wei et al. [119] reported a single activation energy of a dual-phase Mg−Li alloy for the entire range of deformation temperatures. Qin et al. [120] calculated common activation energy for TC11/Ti-22Al-25Nb dual phase alloy, without considering the effect of alloy as well as the phases present in the alloy. Balasundar et al. [121] calculated single activation energy of near-α titanium alloy IMI834 alloy having duplex microstructure, whereas Wanjara et al. [122] calculated two activation energies of the same alloy; one for the two phase (i.e. (α+β) phase) and another one for the single phase β. Seshacharyulu et al. [123], Porntadawit et al. [124] for Ti-6Al- 4V alloy, and Sarkar and Chakravartty [58] for Zr-1Nb alloy considered the activation energies of two phases and single phase separately and found that the activation energy of the two phase (α+β) is higher than the single phase β. To sum up, it can be said that there are two approaches used by researchers; i) a single activation energy for the entire range of deformation temperature covering both single and the two phase region or, ii) two activation energies according to the phases present, i.e. one for two phase (α+β) and another for single phase α or β.

From the above literature review, it is clear that the calculation of activation energy and other parameters of a constitutive equation for two phase materials require systematic approach.

2.7 INFLUENCE OF MICROSTRUCTURE ON MECHANICAL PROPERTIES

The microstructure is one of the most important factor influencing the mechanical properties such as tensile properties, fracture toughness and fatigue strength. The control of microstructure of any material is based on its response to heat treatment, hot or cold working and chemical composition.

Similarly, properties of zirconium alloy can be varied over a wide range by thermo-mechanical processing (TMP) or heat treatment process [41]. Based on the thermo-mechanical processing or heat treatment processes, microstructure of alloy can be changed from equiaxed to bimodal or fully lamellar. The fully lamellar structure is responsible for high fracture toughness and high fatigue crack propagation resistance whereas, bimodal microstructure favors higher yield stress, tensile stress, ductility and fatigue strength [125]. The important microstructural parameters for lamellar structure in Zr alloys, which affect mechanical properties are β grain size, thickness of the α lamellae, size of the colonies of α–phase lamellae and the nature of inter lamellar interface [40, 41, 126]. Slow and intermediate cooling rates lead to a diffusion controlled nucleation and growth process of α–lamellae in the β grains, whereas the martensitic transformation of the β–phase is the result of high cooling rates [127].

In case of pressure tube, the strength of tube increases from front to back-end. Towards the back-end, higher strength could be due to lower deformation temperature, higher volume fraction of α–phase, and finer α grain size. Higher radial-basal texture also helps to increase the back-end properties [128, 129]

Table 2.3: Ambient temperature tensile test properties of Zr-1Nb alloy, annealed at different conditions [10]

Treatment	Yield Strength (MPa)	Ultimate Tensile Strength (MPa)	Uniform Elongation (%)	Total Elongation (%)
As received	254.3	444.1	15.2	30.8
Cold worked	534	597	17	19
853 K/1 h	265	370.4	14	43
853 K/4 h	258	357	15.4	39
903 K/1 h	274	370	15.5	41
903 K/4 h	269.7	363	13	36

Neogy et al. [10] correlated the mechanical properties of Zr-Nb alloy with annealed microstructure, as shown in **Table 2.3**. They reported that the mechanical properties are dependent on microstructural parameters such as recrystallization of α–phase matrix, and nature and volume fraction of precipitate phase. They found higher hardness for cold worked material that reduced after the alloy was annealed at 580°C for 1 hour.

Kulkarni et al. [126] reported the effect of different heat treated microstructures on mechanical properties (yield load and maximum load) using conventional testing methods and automatic ball indentation (ABI) test, and found similar results. On the other hand, small punch test (SPT) showed contradictory results. This contradiction in results was probably due to biaxial deformation of disc samples in the later test. The increase in cooling rate improves the strength values

due to the finer morphology of Widmanstätten α and β. At even higher cooling rates fine plates of α formed due to martensitic transformation resulted in higher strength. In addition to cooling rate, soaking temperature also played important role due to two effects: solute-strengthening effect of Nb in β–phase and effectiveness of the barriers to the deformation front [41]. Kondo et al. [130] correlated the phase constituent, microstructure and the mechanical properties of cast Zr-(0-24) Nb alloy and found that α' formed with less than 6 mass% Nb showed high strength, moderate ductility, and a high Young's modulus. Liang et al. [131] investigated mechanical properties and microstructure of Zr–45Ti–5Al–3V alloy during heat treatment. They reported that the strength decreased from 1306 to 1188 MPa after annealing, however ductility showed an improvement. Liang et al. [132] evaluated mechanical properties and corresponding microstructure of Zr-45Ti-5Al-3V during annealing from 500 – 800ºC. The thickness of plates of α–phase and the relative fraction of β–phase increased with annealing temperature. They found increase in tensile and yield strengths, while the elongation decreased. Filip et al. [133] studied influence of heat-treated microstructural morphology on mechanical properties in two phase titanium alloy. They found maximum tensile elongation at intermediate cooling rates due to equiaxed α–phase. Lütjering [125] studied the effect of bi-modal type microstructural features and reported that the bi-modal type microstructures are better for mechanical properties of Ti-alloys.

The study related to the influence of microstructure on mechanical properties shows that sufficient work on mechanical properties has been reported on different heat-treated or annealed Zr-Nb alloys. However, either limited or no data is available regarding the effect of microstructural features on mechanical properties after thermo-mechanical treatment or hot compression on Zr-Nb alloys.

2.8 APPLICATION OF HOT COMPRESSION DATA AND CONSTITUTIVE EQUATION PARAMETERS IN FEM SIMULATION

The understanding of high temperature deformation or hot deformation of metals and alloys is very important to design industrial hot forming processes. Successful modelling of hot working process using numerical techniques, such as finite difference methods and finite element methods (FEM), is based on precise formulation of constitutive equations. A constitutive equation describes relationship between flow stress, strain, strain rate and deformation temperature. Different constitutive equations proposed to represent hot deformation behavior are already described in Section 2.6.2. For material exhibiting two phase region, a single constitutive equation covering whole temperature range of interest to deformation process in question, is in general difficult to frame with satisfactory results. Therefore, determination of activation energy,

stress exponent and pre-exponential factor for different temperature ranges (phase wise) are required to develop accurate constitutive equations, for different temperature regimes.

Additionally, hot deformation of metals and alloys in any industrial process involves two distinct stages, named as transient state at the beginning and steady state in the rest of the process cycle. These two are sequential steps in one extrusion cycle for which finite element method (FEM) is found to be appropriate model to simulate the process [134]. In case of hot extrusion simulation, the hot compression data can be used as an input for FEM simulation. But it is essential to convert compression data in to some other form, which is compatible with FEM simulation such as Look- Up table or parameters of constitutive equation.

In some studies [135-139], experimental hot compression flow stress data was used to develop the constitutive model, which further relate the flow stress with deformation temperature and strain rate. Additionally, they embedded the parameters of developed constitutive model in FEM simulation to simulate hot compression process. The simulated load-stroke values from FEM simulation were good in agreement with the measured force values of experiment. It indicates that the developed constitutive equation is accurate and provide good description of plastic deformation in hot forming process. Saibaba et al. [42], and Zhou and Duszczyk [140] investigated hot extrusion process to bring out the influence of ram velocity, extrusion temperature and extrusion ratio using finite element simulation. In simulation, they incorporated the results of hot compression test such as flow stress values in the form of Look-Up Table (LUT) due to difficulty in framing the constitutive equations for stress strain behavior. The difficulty was because of the phase transformation involved in the temperature regime under consideration. Their simulation predictions were found to be consistent with the measured values of extrusion load as a function of time.

Jang et al. [141], Liang et al. [142] and Li et al. [143] employed a finite element modeling to simulate hot forging using flow stress data, constitutive equation parameters and recrystallization model (microstructural results i.e. DRX and DRV) obtained through experimental hot compression test. They reported that the experimental measurements and FEM simulation results show a good agreement, and suggested that the implemented microstructure module in finite element model is an effective approach to analyze the hot working process. Similarly, Halici and Poletti [64] embedded experimental hot compression results to simulate 2D-finite element model to predict the flow localization of a titanium alloy during hot compression simulation. They reported that the flow localization obtained through simulation were in agreement with experimental findings of hot compression tests.

FORMULATION OF THE PROBLEM

3.1 RESEARCH GAPS

After comprehensive literature survey it was observed that considerable amount of research work exists on; hot deformation of different materials, processing maps and constitutive analysis. However, reported work on the development of constitutive equations and processing maps for Zr-Nb alloys is still limited. Understanding and analytical analysis of hot deformation in the two phase region is the other important issue which is not dealt in great detail. The gaps identified in the literature are summarized below:

1. For Zr-Nb alloys processing maps are developed using DMM and MDMM models in separate studies. However, there is no systematic work to identify suitable processing map for Zr-Nb alloys to predict safe and unsafe processing (deformation) conditions.

2. The processing of Zr-Nb alloy is usually carried out in two phase region. However, in the literature related to hot deformation of Zr-Nb alloy, there is no systematic attempt to identify hot deformation mechanism and dominant phase in two phase region. In development of processing maps and constitutive equations only input is flow stress data from different phases and phase mixtures.

3. There is hardly any attempt to relate hot compression tests, corresponding microstructural evolution and its effect on mechanical properties. In fact, in Zr-Nb alloys there is almost none. The evaluation of mechanical properties is required to understand expected material behavior during subsequent processing step. This information can be used for selecting process conditions, modelling of the process and design of the equipment.

3.2 RESEARCH OBJECTIVES

Based on the research gaps identified, the following objectives are proposed in the present work:

1. Identification of the most appropriate processing map for Zr-Nb alloys, using Zr-2.5Nb as candidate material, by validating predictions of the processing maps with microstructural analysis.

2. To understand the dominant phase and deformation mechanism in two phase region by incorporating phase information in development of processing maps and constitutive equations.

3. To correlate hot compression test data, microstructural information and mechanical properties obtained from small punch test.

4. To use constitutive equations developed using new approach in FEM simulation of hot extrusion process and validate its output with the actual industrial hot extrusion data.

EXPERIMENTAL DETAILS: MATERIAL AND METHODS

In the present chapter, material selected, experimental techniques used for hot deformation, mechanical testing and microstructural characterization are presented in detail.

4.1 MATERIALS AND THEIR PROCESSING CONDITIONS

Three different zirconium alloys were received from Nuclear Fuel Complex, Hyderabad, India. The chemical composition and processing conditions of each alloy is as follows:

4.1.1 Zr-1Nb Alloy: The chemical composition of as-received Zr-1Nb alloy is given in **Table 4.1**. The as-received Zr-1Nb alloy was received from two different processing routes: one was of extruded followed by β–quenched condition and other was in swaged conditions. The extruded material was in the form of billet, whereas swaged was in the form of rod.

Table 4.1: Chemical composition (wt. %) of Zr-1Nb alloy

Nb	Fe (ppm)	O (ppm)	Other impurities	Zr
1.04	500	946	< 1200	Balance

4.1.2 Zr-2.5Nb Alloy: The chemical composition of as-received Zr-2.5Nb alloy is given in **Table 4.2**. The as-received alloy was in forged followed by β–quenched condition and in the form of billet. The compression direction was kept parallel to the forging direction.

Table 4.2: Chemical composition (wt. %) of Zr–2.5Nb alloy

Nb	Fe (ppm)	O (ppm)	Other impurities (ppm)	Zr
2.59	1125	1062	< 800	Balance

4.1.3 Zr-2.5Nb-0.5Cu Alloy: The chemical composition of as-received Zr-2.5Nb-0.5Cu alloy is given in **Table 4.3**. The as-received alloy was in extruded followed by β–quenched condition and in the form of billet. The compression direction was kept parallel to the extrusion direction.

Table 4.3: Chemical composition (wt. %) of Zr-2.5Nb-0.5Cu alloy

Nb	Fe (ppm)	O (ppm)	Cu	Zr
2.51	820	1085	0.44	Balance

4.2 EXPERIMENTAL TECHNIQUES

4.2.1 Dilatometry Test: The dilatometry test was done to identify dimensional changes in a specimen as a function of temperature, which helped in identifying phase transition temperatures during heating or cooling.

4.2.1.1 Sample Preparation: The samples for dilatometry test were cylindrical in shape with the dimension of 10 mm diameter of and 15 mm height. The height of sample was kept parallel to extrusion, forging and swaging direction during the sample preparation.
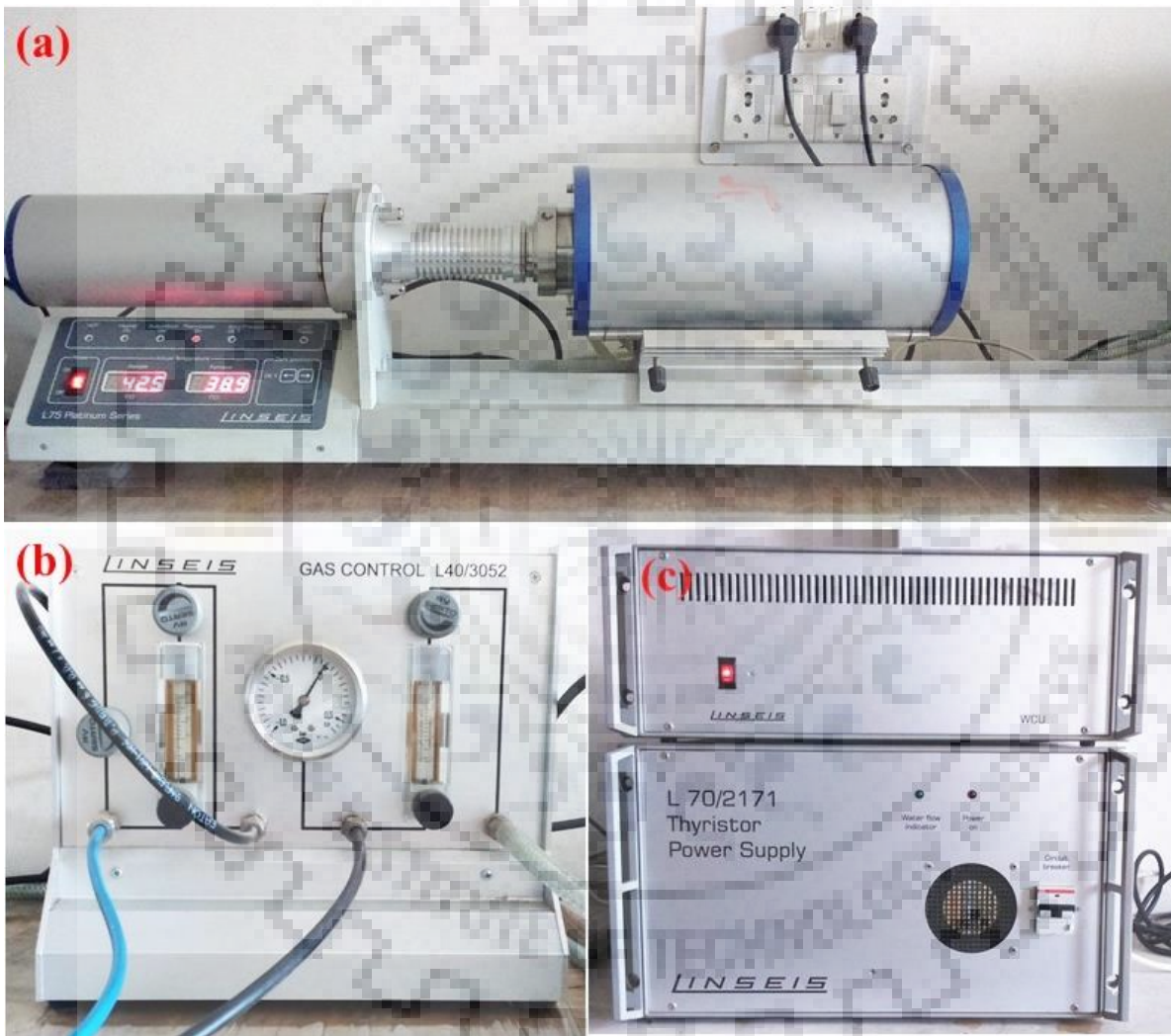
Figure 4.1: Set up for dilatometry test; (a) represents main part of connecting rod (push rod) dilatometer, where sample kept for testing, (b) equipment for gas controller to control the atmosphere around the sample, (c) power supply for dilatometer

4.2.1.2 Set-up of Dilatometry Test: Dilatometer instruments can precisely measure the dimensional changes of a specimen brought about by changes in its thermal environment. Usually, dilatometer instruments are capable to take measurements such as thermal expansion, determination of phase transitions, annealing studies, construction of phase diagrams and sintering studies etc. In the present research work, **LINSESIS®** L75 PT Horizontal Dilatometer

(DIL Dilatometer) was used to identify the phase transformation temperature of different Zr-Nb alloys.

In the dilatometer (see **Figure 4.1**) the specimen was positioned in a protective tube and heated in shielding gas atmosphere. The actual specimen temperature was measured with a thermocouple, positioned just above to sample. A quartz rod on an inductive displacement sensor relays information on the length change of the specimen. The measuring signal for the length change was fed into an XY writer synchronously with the temperature measuring signal.
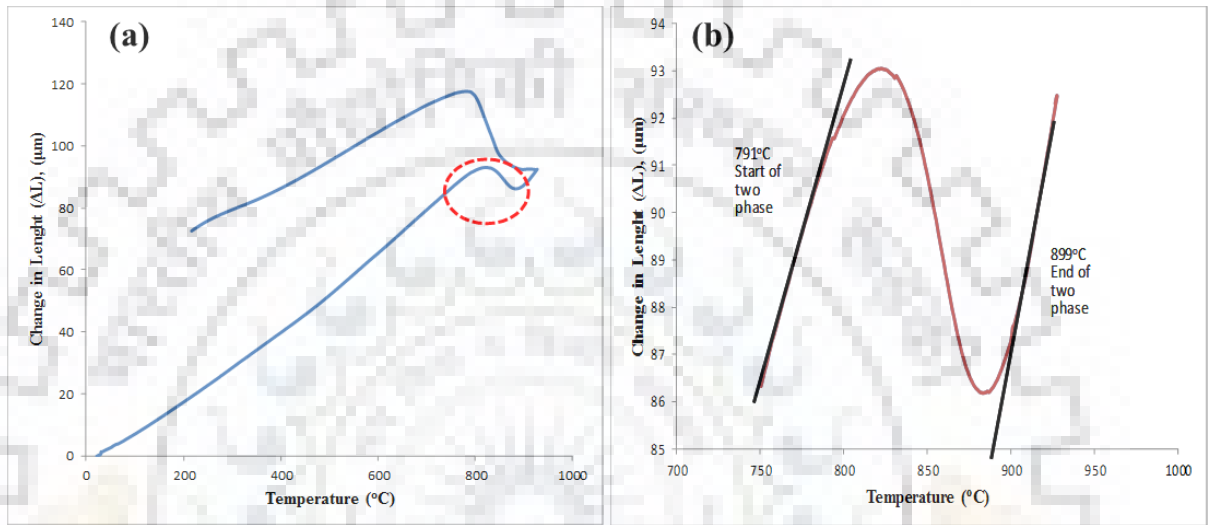
Figure 4.2: Representative results of dilatometry test to identify the start and end of two phase region for Zr-1Nb alloy, (a) change in length during heating and cooling, (b) magnified image to show start and end of two phase temperature

4.2.1.3 Output of Dilatometry Test: In dilatometry test, samples were heated and cooled with a constant or desired heating or cooling rate. In the present study samples were heated and cooled with a constant rate of 5°C/min. During heating and cooling, expansion and retraction of specimen's length was recorded with respect to temperature. The results of change in length was plotted with respect to temperature. The deviation in linear curve of 'change in length vs temperature' indicates the change in phase and the corresponding temperature will be phase change temperature. **Figure 4.2** shows a result of dilatometry test to identify the starting and ending of two phase for Zr-1Nb alloy.

4.2.2 Hot Compression Test:

4.2.2.1 Sample Details: The samples for hot compression test were prepared from the billet of corresponding alloy except swaged Zr-1Nb alloy. The samples were machined from the billet in such a manner that the extrusion or forged direction remain parallel to compression direction, whereas in the case of swaged Zr-1Nb alloy direction of compression was parallel to length of the rod. The dimension of all the samples were;10 mm in diameter and 15 mm in height

to maintain the standard aspect ratio (L/D) of hot compression samples within the range of 1.2 to 1.5 [144]. The geometry and physical appearance of compression sample is shown in **Figure 4.3**. Grooves were made at the end face of the samples to avoid friction between the anvils and the end face. Additionally, a chamfering of 45° was provided at the face edge of samples to avoid folding at the initial stage of deformation.
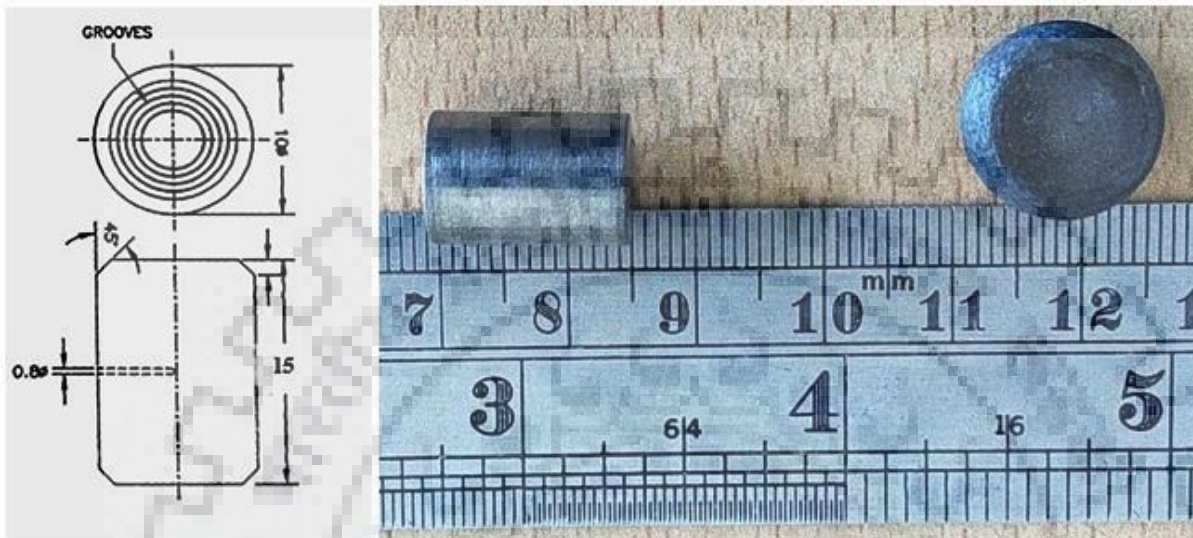
Figure 4.3: Sample for hot compression test. The geometry of sample is shown in left side and physical sample (before and after deformation) is shown right side

4.2.2.2 Set-up for Hot Compression Test: The hot compression tests were performed using Thermo-Mechanical Simulator (Gleeble® 3800). The Gleeble® 3800 is a fully integrated digital closed loop control thermal and mechanical testing system. It is a highly precise testing machine for physical simulation of hot deformation at very low and high strain rates, to study the hot deformation behavior of metals and alloys. It is a group of different units such as: main console, the hydraulic power unit, the vacuum pump unit and the testing unit. Gleeble® 3800, as shown in **Figures 4.4**, has various mobile conversion testing units, in which Pocket jaw and Hydrawedge are the main unites for hot compression. The Hydrawedge is the only commercial available machine that offers the capability to perform physical simulations of high-speed deformation, i.e. strain rate 1 s⁻¹ or higher with complete independent control on both strain and strain rate, whereas packet jaw is suitable for low speed deformation, i.e. lower than 1 s⁻¹. A brief specification of Gleeble® 3800 is given in **Table 4.4**.

In Gleeble 3800®, load cell and a linear voltage differential transducer (LVDT) is used to measure the force and displacement induced by hydraulic actuator. The LVDT is attached with actuator, and movable core is placed by the piston of the actuator. As the force applied, load cell provides an output voltage of proportional magnitude. The displacement of piston from its mid

40

stroke position increases output voltage linearly. The stroke has capability to inforce the constant strain rate during the deformation. The machine used for this work has 50 KN load cell capacity and 100 mm gauge length of LVDT.

Table 4.4: Brief Specification of Gleeble® 3800

Maximum heating rate	10,000°C per second
Cooling rate	up to 250°C per second (depending on material and sample size, quench media)
Atmospheric conditions	Rough/high vacuum, protective gasses (argon, nitrogen).
Other devices	Hot zone LVDT, Dilatometer LVDT, thermal couple spot welder, Digitally controlled force or displacement system
Maximum sampling rate	20,000Hz
Maximum stroke rate	2000 mm per second
Maximum stroke	100 mm
Maximum force	10 tones in tension and 20 tons in compression
Control methods	Stroke, force, diameter change, lengthwise change, stress and strain
Specimen sizes	Square 6 mm to 11 mm; round 5 mm to 10 mm diameter; flat strip 2 mm × 50 mm maximum size
Main Application	Small scale simulation of metal solidification, forming, heat-treatment and bonding processes. Physical and mechanical characterization of metals

4.2.2.3 Procedure and Output of Hot Compression Test: For the hot compression test, sample were kept in between the movable and fixed jaw (in case of pocket jaw unit). Movable jaw is operated by an integrated hydraulic–pneumatic system. The complete control of processing parameters in real time are managed by computer program, i.e. QuickSim which has interface with Gleeble main consol. The frequency of data acquisition should be in an appropriate range to record the data, in the quantity of at least 350 to 1000. A *K–type* thermocouple was spot welded on the mid span of the sample to acquire accurate temperature measurement. However, for higher temperature testing of Zr–alloys, spot welding was not found suitable due to detachment of thermocouple from the samples. Therefore, at higher temperature thermocouple was clamped into a hole of 1 mm diameter and 2 mm in depth, at the middle of the sample. The Gleeble has the facility to heat sample by resistance heating, therefore sample were resistance heated. The graphite foil of 5 or 10 mil thickness or tantalum foil along with nickel-based lubricant was used between sample and anvils to avoid welding, friction and to reduce the thermal gradient during the test. The selection of foil is based on the testing temperature and the sample material. The tests were conducted in the temperature range of 650 – 1050°C and the constant true strain rate range of 0.01 – 10 s^{-1}. The samples were heated up to desired temperature with a constant heating rate of 5°C per second and soaked at desired temperature for 300 seconds. In

41

prior work it was established that 300 s was sufficient for complete phase transformation. The schematic diagram to represent the hot compression test is shown in **Figure 4.5.** The samples were compressed to a true strain of 0.69 and then water quenched or slow cooled. During hot compression, the flow stress data were recorded automatically as a function of strain for each deformation temperature and strain rate from the computer interface of Gleeble® 3800.
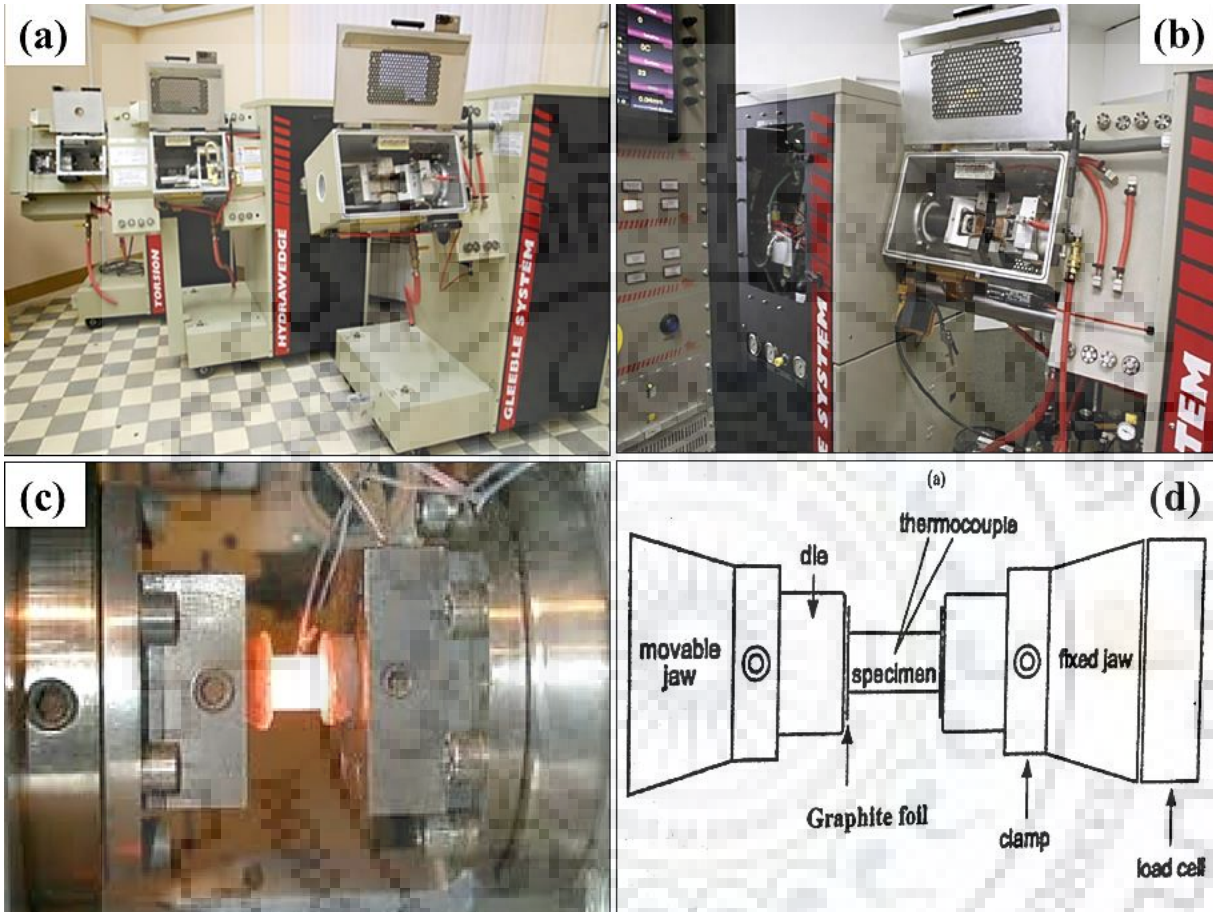
Figure 4.4: Gleeble 3800®; (a) an external view of different mobile conversion units, (b) close view of pocket jaw working chamber, (c) inside view of the working chamber during operation, and (d) schematic representation of sample, anvil and jaw arrangement

4.2.3 Mechanical Testing

4.2.3.1 Sample Preparation for Small Punch Test (SPT): The samples for small punch test (SPT) were prepared from the hot compressed samples. A slice of 0.5 mm thickness was cut parallel to compression direction from the middle of compressed sample. The samples were made flat and the thickness of slice were reduced to 0.26 mm (± 0.01), using conventional metallography techniques. From the slice, a circular disc of 3 mm diameter was punched from the middle of the slice, as shown in **Figure 4.6**.

42
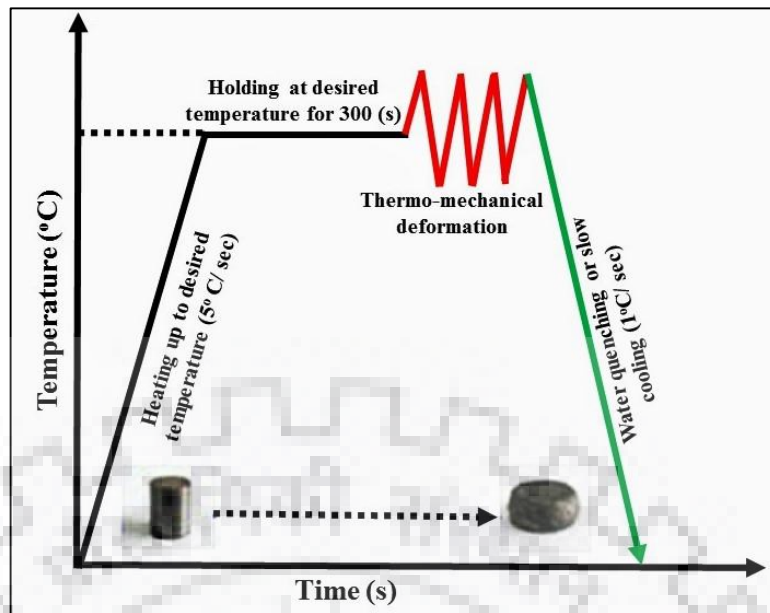
Figure 4.5: schematic diagram to represent hot compression test.
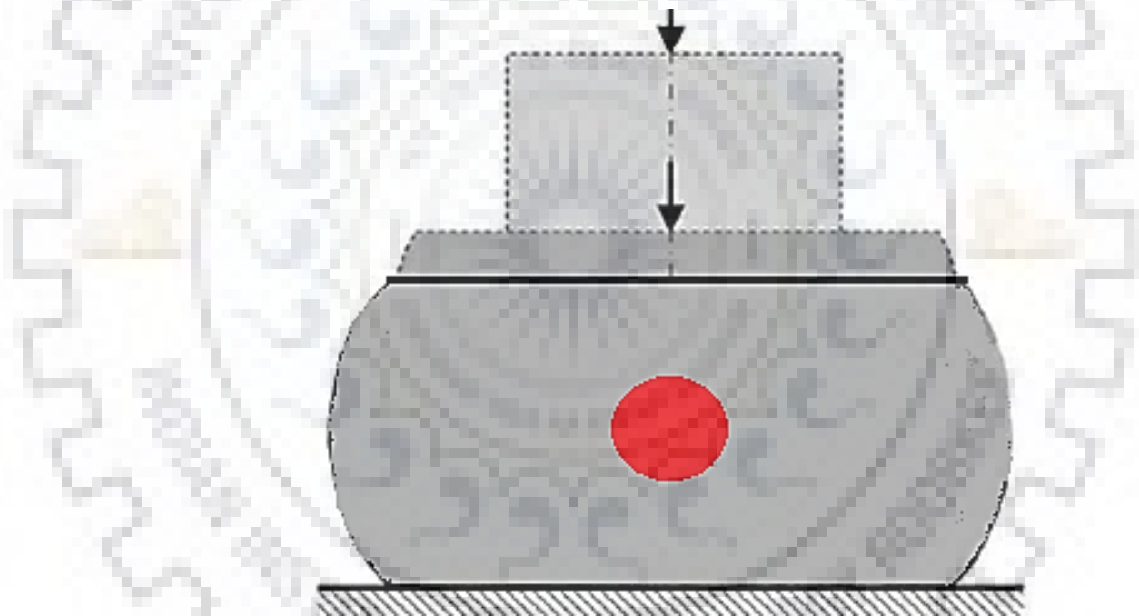
Figure 4.6: Schematic representation of small punch test (SPT) specimen. The downward arrow showing the compression direction. Red circle showing the location for SPT sample.

4.2.3.2 Set-up and Output of Small Punch Test: The SPT test on compressed samples was performed at room temperature as per guidelines provided for testing metallic materials, in the report JAERI-M-172 (1988) [145]. The Universal Testing Machine (UTM), make Instron, model TSET 28250 **(Figure 4.7)**, with a load cell capacity of 90 KN and Linearly Variable Differential Transducer (LVDT) with a resolution of 0.001 mm was used. The disc specimen was circumferentially gripped between the upper and lower dies of a jig and a 1.0 mm diameter hardened steel ball was positioned at the center of the test specimen. The steel ball was forced at a constant cross head velocity of 0.1 mm/s using a plunger. As the plunger pushed the steel ball,

a typical load (P) vs central deflection (δ) curve was recorded during the test until the specimen attains the fracture, as shown in **Figure 4.8a**. **Figure 4.8b** and **4.8c** represents the schematic diagram of the testing sample during the punching test. For each hot compression condition, at least three test were performed and the typical load (P) vs central deflection (δ) curve were analysed to evaluate the value of yield load (P_y) and the maximum load (P_m) incorporating the procedure recommended in ref. [146-149]. Using standard equations suggested by Mao and Takahashi [149], yield stress and maximum stress (UTS) were calculated from the obtained values of P_y and P_m.

Figure 4.7: External view of machine used for Small Punch Test (left) and die and pin used for holding the sample and pushing the steel ball (right)
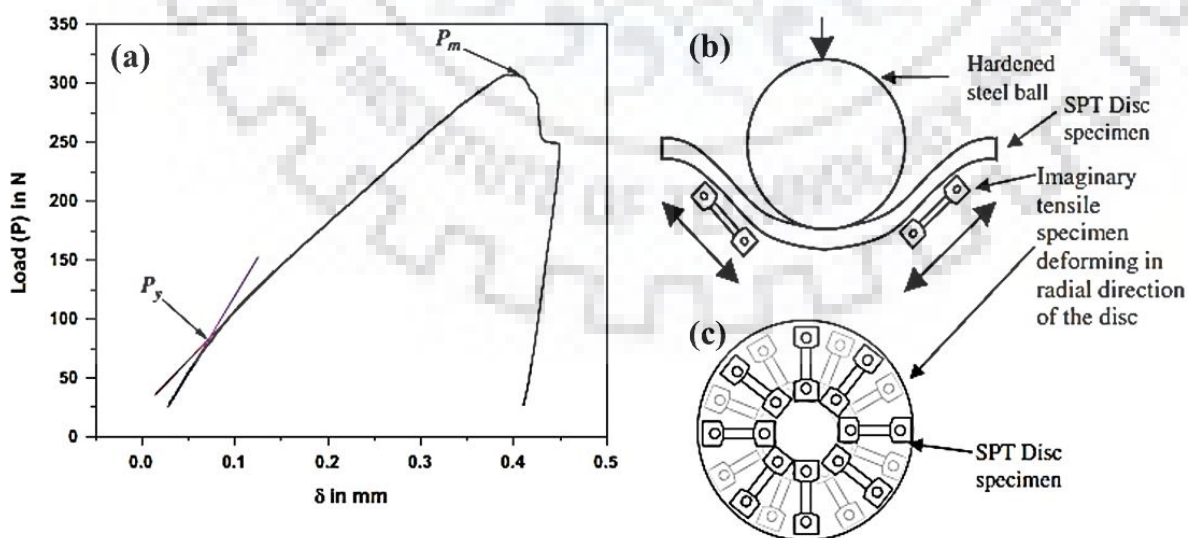
Figure 4.8: (a) Load vs deflection curves obtained during the test and showing the procedure to evaluate the P_y and P_m, (b) and (c) representation of forces applied on test specimen during the test [126]

4.3 CHARACTERIZATION TECHNIQUES

4.3.1 Optical Microscopy

4.3.1.1 Sample preparation: The samples for optical microstructural analysis were obtained from compressed samples after sectioning parallel to the compression direction. Cut samples were mounted in thermosetting resins such as PhenoCure® resin using hot mounting machine, Make Buehler SimpliMet® 1000 (shown in **Figure 4.9**). Mounted sample were mechanically polished using Buehler AutoMet® 250 (**Figure 4.10**). Buehler AutoMet® 250 is an automatic polishing machine set-up for mechanical polishing. After polishing, etching was done on the polished samples using a solution of 45% HNO_3, 10% HF and 45% distilled water. The etching time varied depending on hot deformation condition of the sample. Etched samples were washed in running water and dried with help of an air blower.

Figure 4.9: Buehler SimpliMet® 1000. An apparatus for hot mounting

4.3.1.2 Optical Microscope: The etched and dried sample were then observed in optical microstructure, using Leica DMI 5000M optical microscope (see **Figure 4.11**). It has inbuilt facility of five different magnifications such 50X to 1000X. To observed the effect of hot compression on microstructure, the middle portion of etched specimen (see **Figure 4.12**) was target to capture the optical images at different magnifications.

Figure 4.10: Buehler AutoMet 250. An automatic polishing machine

Figure 4.11: Leica DMI 5000M. An inverted optical microscope
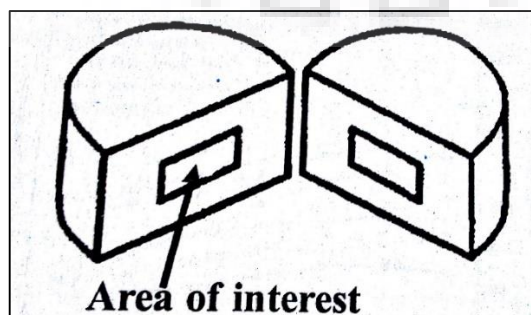
Figure 4.12: Schematic diagram to show area of interest for microstructural analysis

46

4.3.2 Electron Backscatter Diffraction (EBSD):

4.3.2.1 Sample Preparation: For EBSD analysis, the half part of compressed samples was selected (as shown in **Figure 4.12**), which was cut parallel to the compression direction. After mechanical polishing as described in **Section 4.3.1**, samples were electro-polished for EBSD scan. The samples were electro-polished using Buehler ElectroMet® 4 Polisher-Etcher (see **Figure 4.13**). To electro-polish, a common solution of Perchloric acid ($HClO_4$) and methanol (CH_3OH) in the ratio of 20: 80 by volume, was used. The parameters for electro-polishing were; time 20 second, voltage 20 V and temperature -40^oC. For EBSD scan, area of interest was same as in case of optical (see **Section 4.3.1** and **Figure 4.12**). The size of the scan area and step size were based on the microstructural features required. For each alloy, scan parameters are described individually, wherever it is required in the following chapters.

Figure 4.13: Buehler electro-polisher equipment; (a) main unit (left), (b) setup that contain solution and complete the circuit with electrode and specimen (middle), and (c) chiller to cool the solution temperature

4.3.2.2 Set-up for EBSD: For EBSD measurements, a scanning electron microscope FEI model Quanta™ 3D FEG (**Figure 4.14**), installed at National Facility of Texture & OIM, IIT Bombay (a DST-IRPHA facility)) was used. Quanta™ 3D FEG is equipped with FEG (Field Emission Gun). For EBSD measurements, beam of electrons is directed at a point of interest at 70° tilt, as shown in **Figure 4.15**, where the diffraction pattern follows the Bragg's law (see **Equation 4.1**).

$$2d \sin \theta = n\lambda \qquad\qquad\qquad (4.1)$$

where d is diffraction plate spacing, n is an integer, λ is the electron wavelength and θ represents the incident angle of beam or electron on the diffracting plane.

Figure 4.14: Set-up of FEI Quanta 3D FEG microscope for EBSD analysis

When the electron diffracts from each corresponding planes, a set of paired large angle cones are formed. When it is used to form an image on the fluorescent screen, the characteristic Kikuchi bands of the electron back scattered diffraction pattern are produced by the regions of the enhanced electron intensity between the cones. (see **Figure 4.16**).
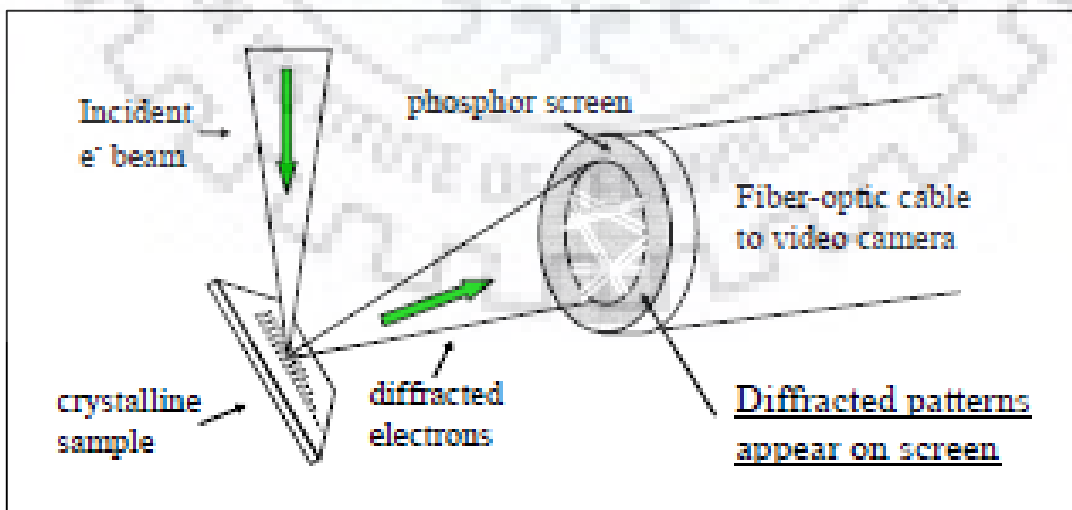
Figure 4.15: Schematic representation of scanning electron backscattered diffraction pattern [150]
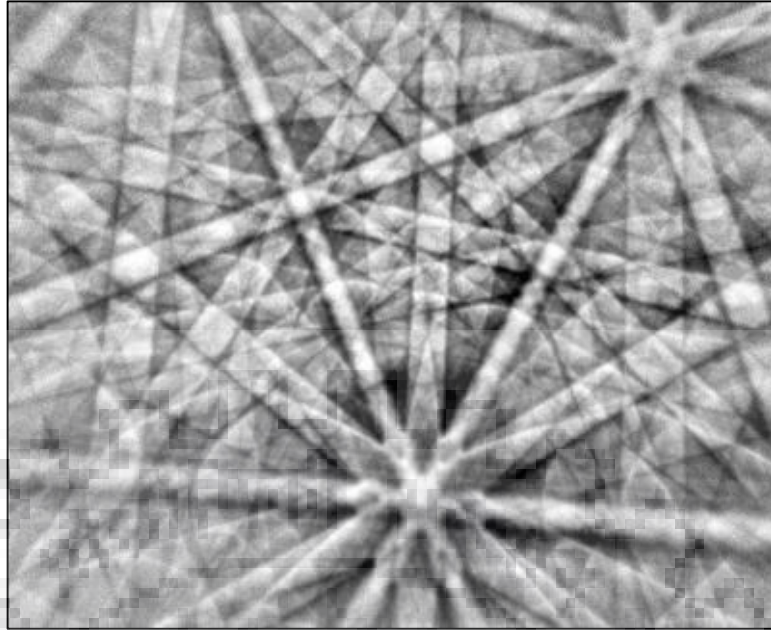
Figure 4.16: Characteristic Kikuchi bands of the electron backscatter diffraction pattern [150]

4.3.2.3 Post Processing of EBSD Data: The data obtained after EBSD scan was analyzed using TSL OIM software. At least a minimum of 2000 grains were selected for calculating the microstructural parameters such as grain size, distribution of grain boundaries misorientation, grain orientation spread, and texture. Grains are defined as regions that are bounded by boundaries of minimum misorientation of 5°. Grain orientation spread is the deviation between orientation of each pixel in a grain to the average orientation of the grain. To calculate the fraction of recrystallized grains, grain orientation spread (GOS) values were used. In literature [151, 152], it is reported that GOS < 1 is a suitable criterion to identify DRX grains in the deformed matrix and it was kept constant for each deformation conditions. Inverse pole figures were plotted using Harmonic series expansion method (with L=22) and are presented normal to compression axis. Boundaries with a misorientation angle between 1 to 15° were considered as low angle grain boundary (LAGB) and those with misorientation >15° were defined as high angle grain boundaries (HAGB).

RESULTS

In the present chapter, flow curves during the hot deformation, microstructural characterization of samples deformed at various conditions, development of constitutive equations, FEM simulation and results of mechanical testing are presented in detail.

5.1 FLOW CURVES:

Hot compression flow stress data was obtained from the hot compression test in Gleeble® 3800 thermo-mechanical simulator. The flow stress data was recorded automatically as a function of strain by the computer interface of Gleeble® 3800, where standard equations were used to convert load-stroke data to true stress – true strain data. In most of the samples, significant barrelling was not observed after deformation. However, samples which showed pronounced barrelling were not considered for further analysis. For high strain rate deformation (i.e. 1 s^{-1} or above), the flow data was affected by the adiabatic temperature rise (ATR) and was corrected accordingly. For ATR correction, rise in temperature (ΔT) was obtained by subtracting the desired temperature from the actual temperature (T_{actual}). The actual temperature (T_{actual}) as a function of strain was obtained using thermocouple welded on the sample and recorded by Gleeble® in real time. Correction in flow stress data ($\Delta\sigma$) due to ATR was calculated using **Equation 5.1**, in which $\dfrac{d\sigma}{dT}$ is the derivative of true stress vs. T_{actual} [153]. Finally, the corrected flow stress is the summation of experimental flow stress and $\Delta\sigma$.

$$\Delta\sigma = \Delta T \left.\frac{d\sigma}{dT}\right|_{\varepsilon,\dot{\varepsilon}} \tag{5.1}$$

5.1.1 Zr-1Nb alloys:

5.1.1.1 Extruded β-quenched: Figure 5.1 shows true stress-true strain curves at different strain rates and temperatures. The deformation temperatures from 650ºC to 750ºC lie in the single α–phase, from 815ºC to 885ºC in two phase (i.e. α+β) and from 925ºC to 1050ºC lie in single β–phase. True stress-true strain curves of deformation in α–phase (**Figure 5.1a – 5.1c**) exhibit transient hardening or softening and then steady state behaviour at higher strains.

Flow curve of deformation in two phase region and single β–phase (**Figure 5.1d – 5.1i**) exhibit steady state behaviour irrespective of the strain rate.
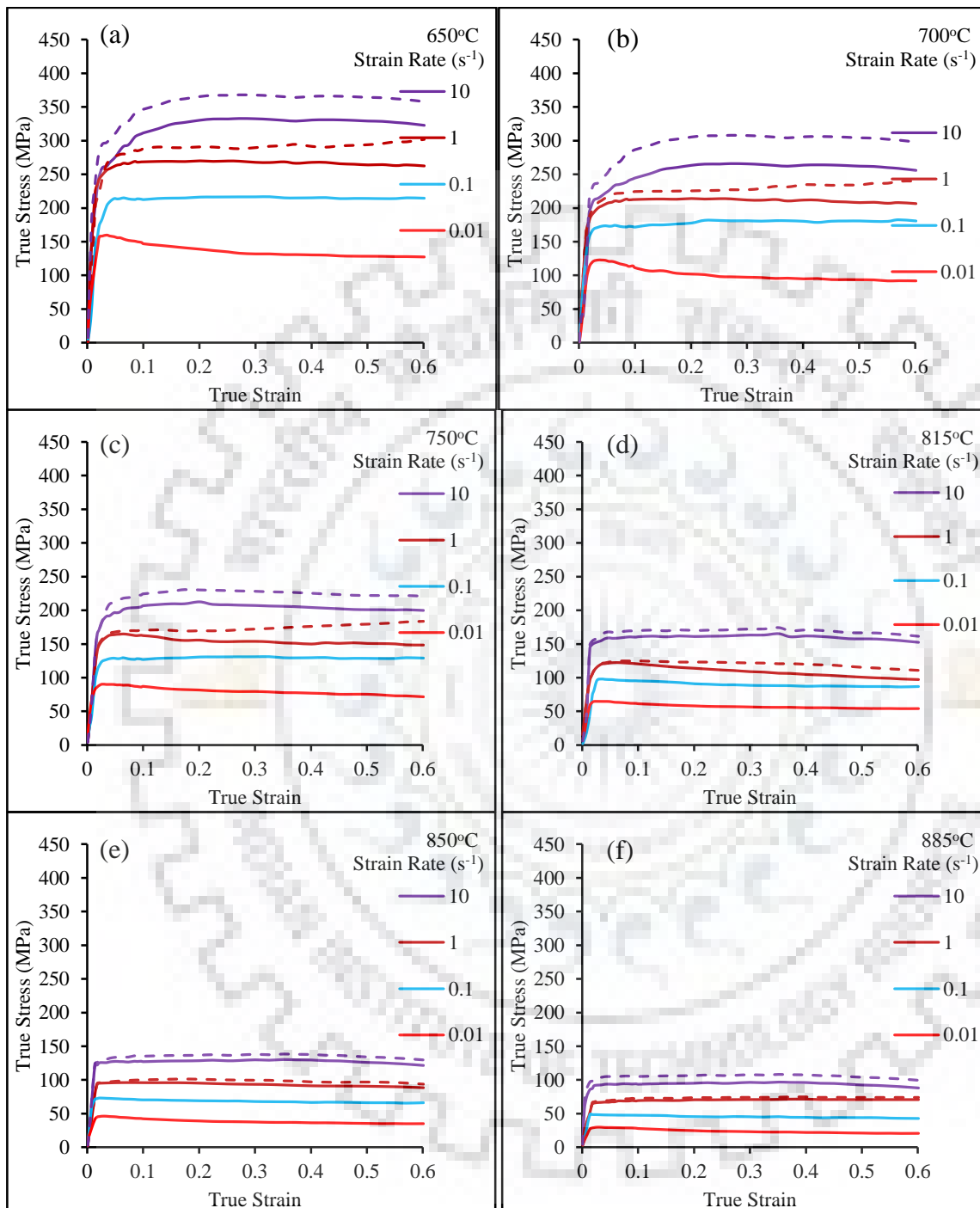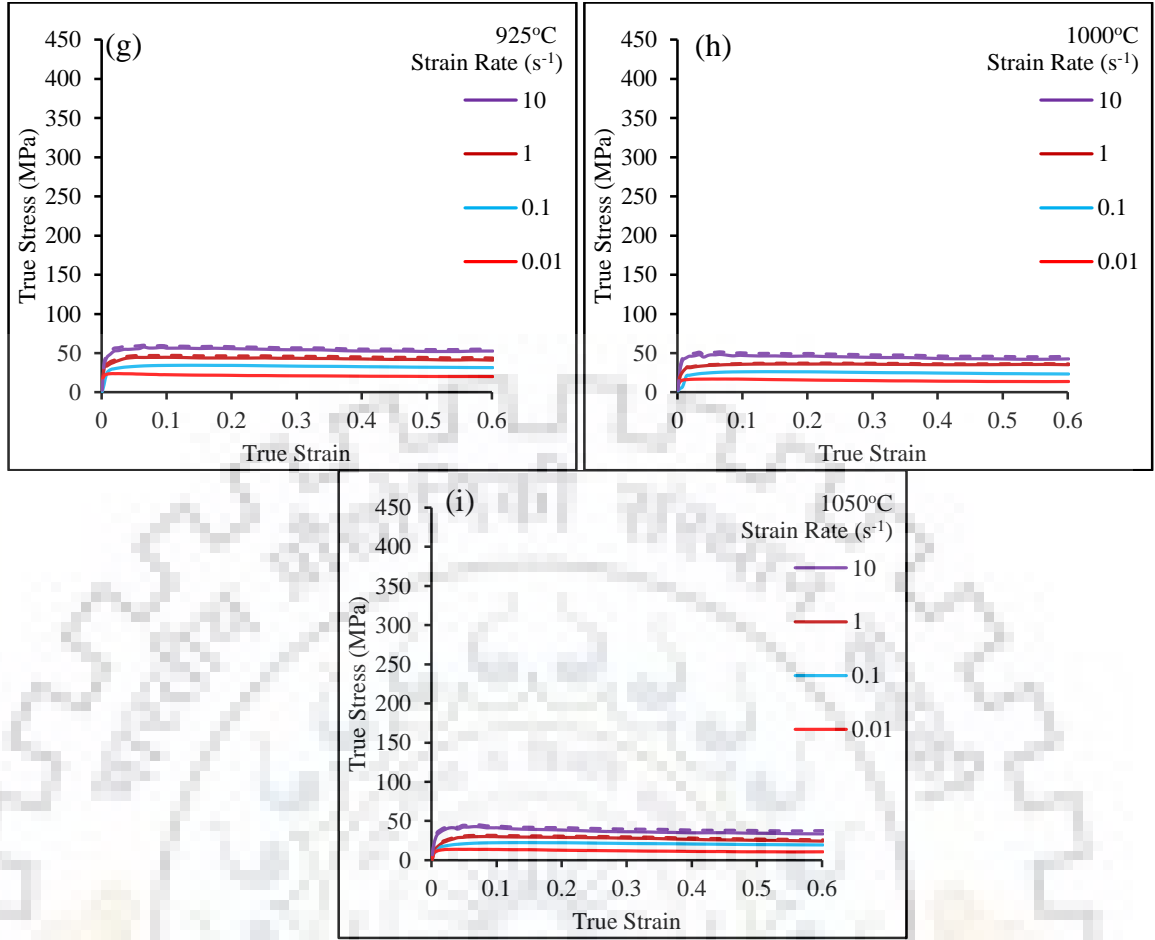
Figure 5.1: The true stress–true strain curves of Zr-1Nb alloy (extruded β-quenched condition) after uniaxial compression at different strain rates and deformation temperatures of (a) 650°C, (b) 700°C, (c) 750°C, (d) 815°C, (e) 850°C, (f) 885°C, (g) 925°C, (h) 1000°C and (i) 1050°C. All flow curves are adiabatic temperature rise (ATR) corrected. At higher strain rates of 1 s⁻¹ and 10 s⁻¹, solid lines are the experimental values of flow stress, while dashed lines are the adiabatic temperature rise (ATR) corrected flow stress.

It is difficult to comment on softening and steady state behaviour from the information provided in **Figure 5.1**, specially at higher temperatures due to use of single scale. Therefore, to quantify flow softening in flow curves, degree of softening, S_d (%) is introduced. The calculation of S_d is based on the value of flow stress at the end of deformation with respect to the corresponding peak stress value and normalised by peak stress $\left(S_d = \dfrac{\sigma_p - \sigma_s}{\sigma_p} \times 100 \right)$ where σ_s is flow stress value

at the end of the deformation (at a true strain of 0.6 in our study) and σ_p is peak stress value. The higher value of S_d indicates higher degree of flow softening. In hot deformation, flow curves are usually of three types; one is when flow stress increased up to peak and then becomes steady state, in second flow stress decreases from the peak value till the deformation ends and third is when flow stress continuously increases till the end of deformation [43]. In first two cases, a distinct peak stress is visible as the maximum value in the flow stress curve. But peak stress is

53

not clear when the flow stress continuously increases after the early stage of deformation (third case). In this case, the peak stress is identified as the tangent point on the flow stress curve by the extension of a line along the flow stress curve [154].
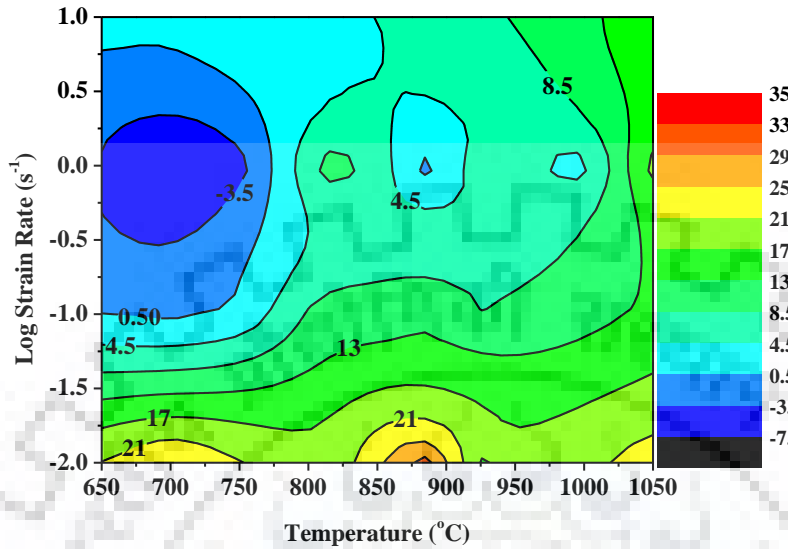
Figure 5.2: Degree of softening map for flow stress, S_d (%), as a function of deformation temperature and strain rate for Zr-1Nb alloy extruded β-quenched condition. Positive values represent the softening in stress-strain curve, whereas negative value represents strain hardening.

Figure 5.2 shows the degree of softening, S_d (%) as a function of deformation temperature and strain rate. Positive values indicate flow softening whereas negative values indicate flow hardening. Usually, with increase in strain rate S_d value is found to decrease, indicating a tendency for work hardening. On the other hand, lower strain rates and higher temperatures promote flow softening. **Figure 5.2** reveals that the maximum softening in flow curves occurs at lower strain rate (i.e. 10^{-2} s^{-1}) at temperature range of 650-750°C and 830-915°C. The deformation in single α–phase at higher strain rates, exhibit reduced values of S_d and at stain rate of 1 s^{-1} significant strain hardening is observed.

5.1.1.2 Swaged and annealed in single α–phase: The true stress-true strain curves of swaged and annealed Zr-1Nb alloy in single α–phase conditions are shown in **Figure 5.3**. In the single α–phase region (**Figure 5.3a – 5.3c**), all curves show hardening behaviour. In two phase region flow curves are showing steady state behaviour and flow softening in single β–phase (**Figure 5.3d – 5.3i**). In two phase region, at strain rate of 10^{-2} s^{-1}, flow curves at all three temperatures (i.e. 815, 850 and 885°C) seems to behave as steady state. At strain rate of 1 and 10 s^{-1} flow curves represent strain hardening (high flow stress) up to a true strain of 0.2 and thereafter they exhibit either softening (lower flow stress) or steady state behavior. Moreover, the shape of

true stress–true strain curves exhibit some features that help to identify the hot deformation mechanisms.
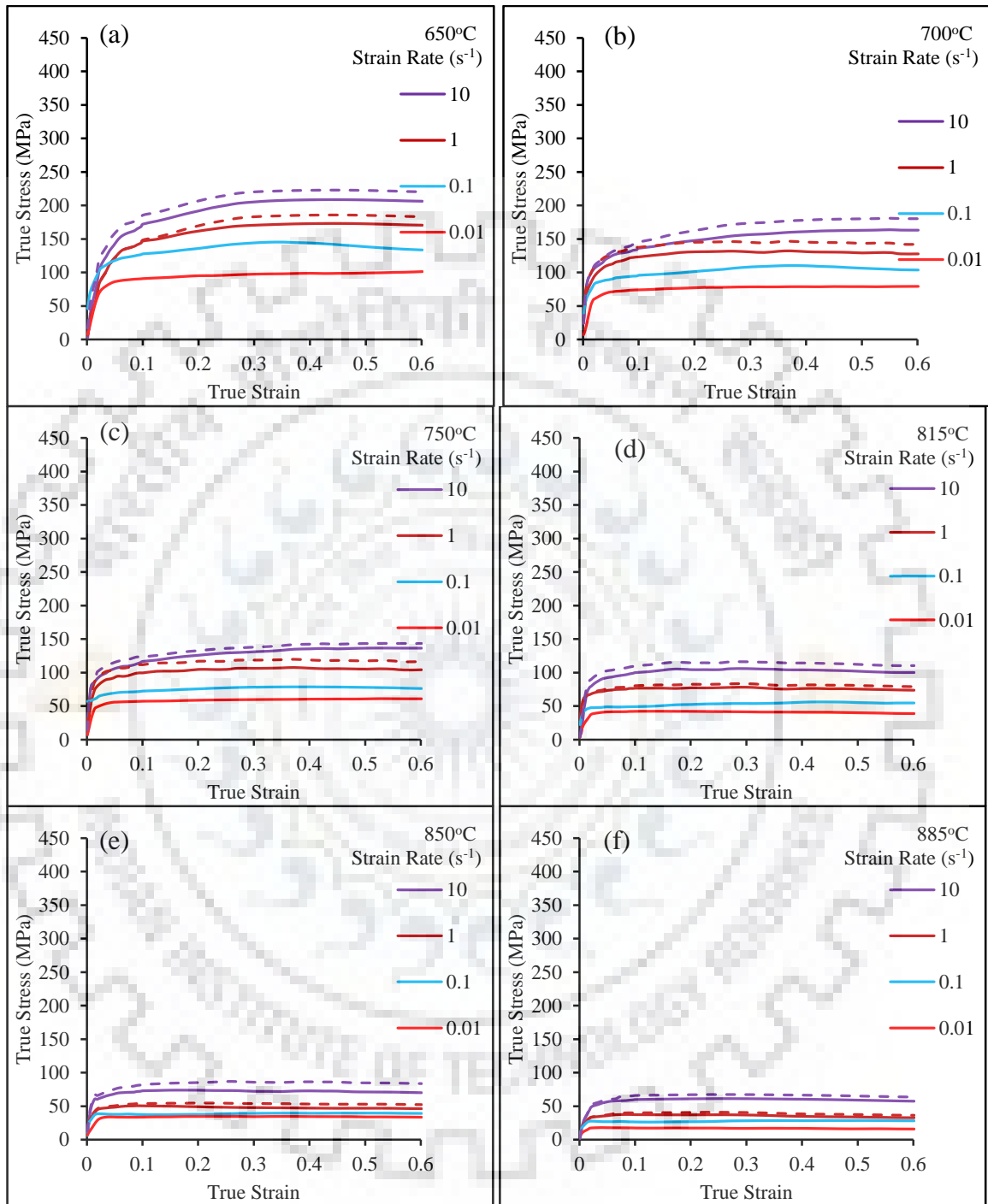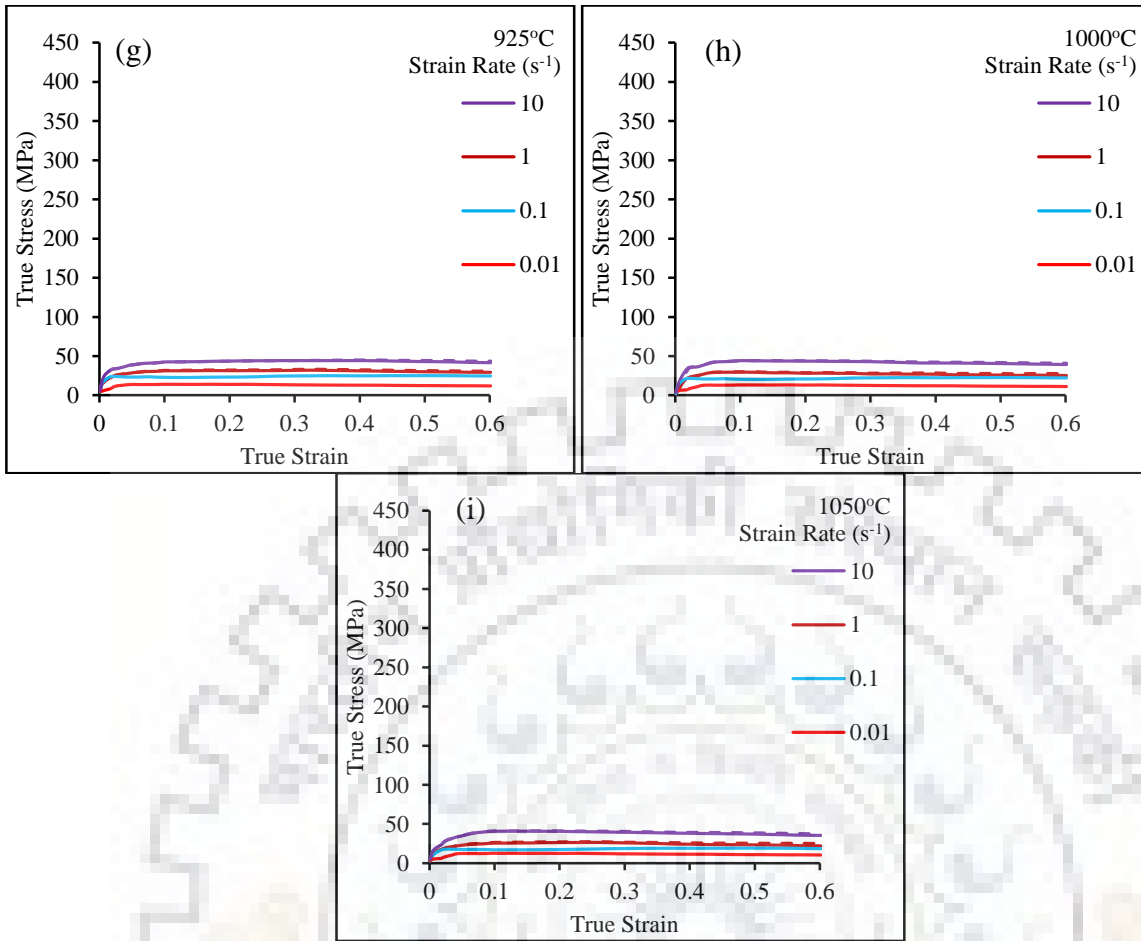
Figure 5.3: The true stress–true strain curves of Zr-1Nb alloy (swaged and annealed in single α–phase) after uniaxial compression at different strain rates and deformation temperatures of (a) 650ºC, (b) 700ºC, (c) 750ºC, (d) 815ºC, (e) 850ºC, (f) 885ºC, (g) 925ºC, (h) 1000ºC and (i) 1050ºC. All flow curves are adiabatic temperature rise (ATR) corrected. At higher strain rates of 1 s^{-1} and 10 s^{-1}, solid lines are the experimental values of flow stress, while dashed lines are the adiabatic temperature rise (ATR) corrected flow stress.

The degree of softening, S_d (%) was calculated to quantify the softening in flow curves. The method to calculate S_d is described in earlier **Section 5.1.1.1.** The map of S_d shown in **Figure 5.4** shows that the S_d values decreases as a function of strain rate, as characteristic of flow stress of hot deformation, except at strain rate of 1s^{-1} in the two phase region. The hardening behaviour of flow curves observed in single α–phase region (**Figure 5.3 a-c**) is validated in S_d map (**Figure 5.4**). Maximum softening (i.e. higher S_d value) is observed in single β–phase at lower strain rate (i.e. 10^{-2} s^{-1}) and at moderate strain rate (i.e. 1 s^{-1}) in the two phase region.

In the present study, the starting material has an equiaxed microstructure **(Figure 5.29)** with β–phase present along the grain boundaries of α. Therefore, the strain hardening processes at low temperature deformation (815ºC), could be mostly associated with dislocation interactions within the α–phase and pile-up at the grain and/or phase boundaries [155, 156]. Increase in the fraction of β–phase with deformation temperature, could effectively change the strain partitions

between the phases. At initial stages of deformation, the softer phase β accommodates more strain and subsequent strain hardening might increase its load bearing capacity to that of the α–phase. At this stage more fractions of α–phase accommodates the imposed strain. Therefore, competitive contribution from deformation of α and β–phase decides the strain hardening at higher temperatures (885°C). On the other hand, mechanisms of softening are able to balance rate of work hardening after true strain of 0.2 and may suggest that mechanisms like dynamic recrystallization and/or dynamic recovery are operating [156, 157]. Similar phenomenon of flow softening is also reported for Ti-6Al-4V alloy [158] and Zr-Nb alloys [47] in the two phase region.

Out of four strain rates reported here, only two strain rates i.e. 10^{-2} and 1 s^{-1} shows maximum softening and necessitate further analysis of microstructure and mechanical properties.
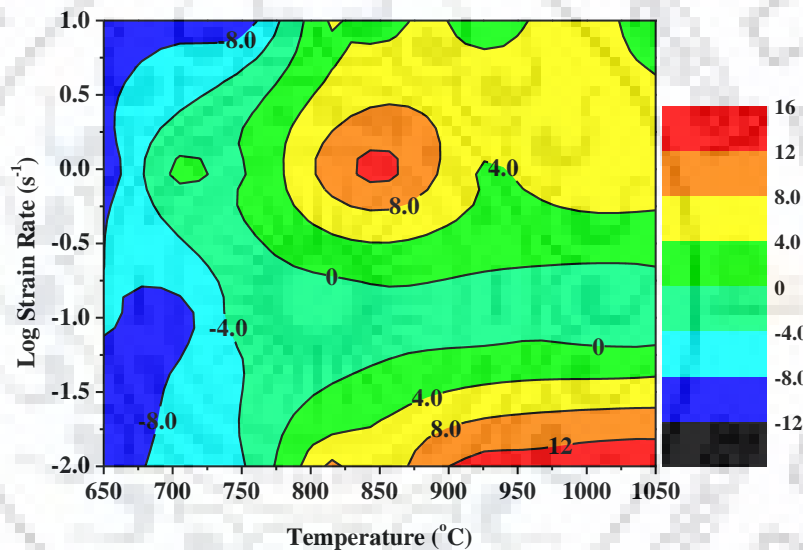
Figure 5.4: Degree of softening S_d (%) map – as a function of deformation temperature and strain rate for Zr-1Nb swaged and annealing in single α–phase.

5.1.2 Zr-2.5Nb alloy: The flow curves of Zr-2.5Nb alloy (forged β quenched condition) are shown in **Figure 5.5**. From true stress-true strain curves (**Figures 5.5**), it is clear that peak flow stress values are decreasing with the increase in temperature, and increasing with increase in strain rates, as a typical characteristics of stress-strain curves. The variation in flow stress represents the sensitivity of flow stress to strain rate and deformation temperature. At deformation temperatures of 700°C (**Figure 5.5a)** and 750°C (**Figure 5.5b),** the flow stress decreases monotonically towards a steady state regime with a varying softening rate (**Figure 5.6**). On the other hand, at higher temperatures {i.e. 850°C (**Figure. 5.5d)** and 925°C (**Figure 5.5e)**}; the flow stress remains more or less constant after attaining peak stress except at strain rate of 1 s^{-1}. At the strain rate of 1 s^{-1}, flow curve shows strain hardening behavior.

57
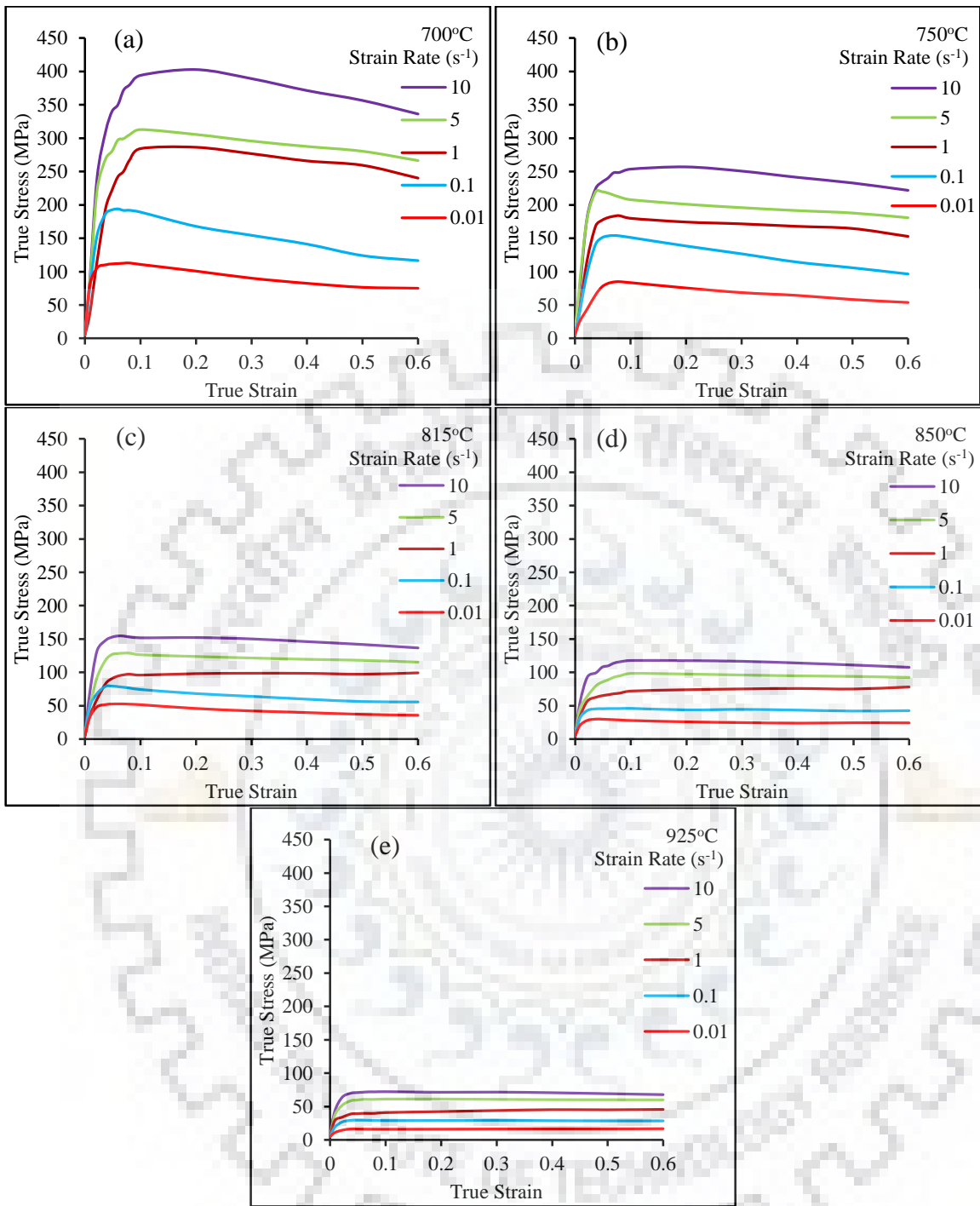
Figure 5.5: True stress-true strain plots of Zr-2.5Nb alloy at various strain rates and at temperatures of; (a) 700ºC, (b) 750ºC, (c) 815ºC, (d) 850ºC and (e) 925ºC. All flow curves are adiabatic temperature rise (ATR) corrected.
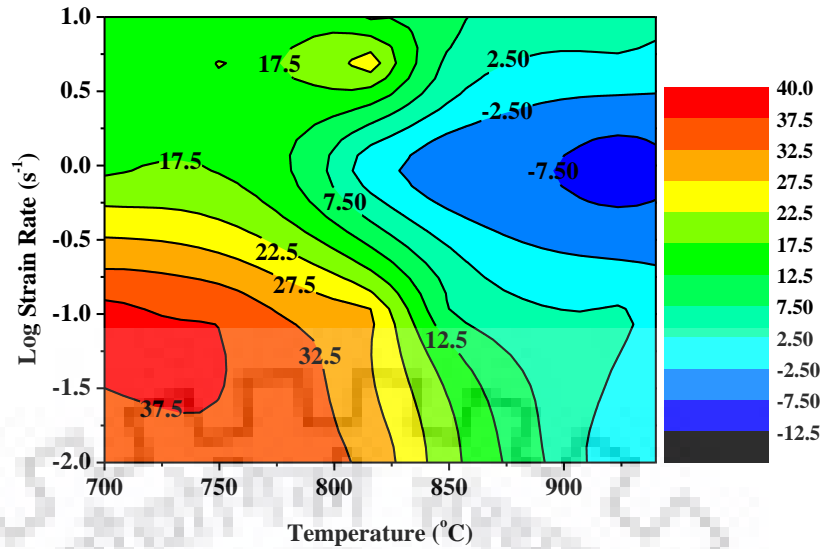
Figure 5.6: The curves in figure represent the flow softening at constant strain rates for entire deformation range of Zr-2.5Nb forged β quenched condition.

The true stress- true strain curves shown in **Figure 5.5** do not reveal degree of softening clearly. Therefore, to quantify softening in flow curves, degree of softening S_d was calculated for this material, too. The S_d values are then plotted as a function of deformation temperature and strain rate (**Figure 5.6**). The method to calculate S_d is already discussed in **Section 5.1.1.1**. **Figure 5.6** reveals that the maximum softening (higher S_d value) in flow curves is observed at lower deformation temperature and lower strain rates. As expected, S_d value decreases as function of strain rate for this material. But, at a strain rate of 1 s^{-1} for the temperature range of 815-925°C, S_d values are in the range of 5 to -5, which indicates that in this temperature range the flow curves change their behavior from softening (very less) to hardening. Similar, behavior was also noticed in the stress-strain curve at strain rate of 1 s^{-1}.

5.1.3 Zr-2.5Nb-0.5Cu (ZNC) alloy: The flow curves of ZNC alloy extruded β quenched conditions are shown in **Figure 5.7**.

Figure 5.7 shows the true stress–true strain curves of ZNC alloy for deformation temperatures of 700 – 925°C and strain rates of 10^{-2} – 10 s^{-1}. According to lever rule, proportion of α/β – phase should vary with the deformation temperature. Hence, flow behavior should reveal the dominance of a particular phase on the deformation mechanism at different temperatures. The flow curves at temperature range of 700-815°C have softening behavior for entire range of deformation strain rates, except at strain rate of 10^{-2} s^{-1} for 815°C. At 815°C/10^{-2} s^{-1}, curve shows steady state nature. In the temperature range of 850-925°C, the flow curves seem to have a steady state behavior (**Figure 5.7d-e**) for all strain rates used except at conditions of 850°C (5 and 10 s^{-1}) and 925°C (10 s^{-1}).
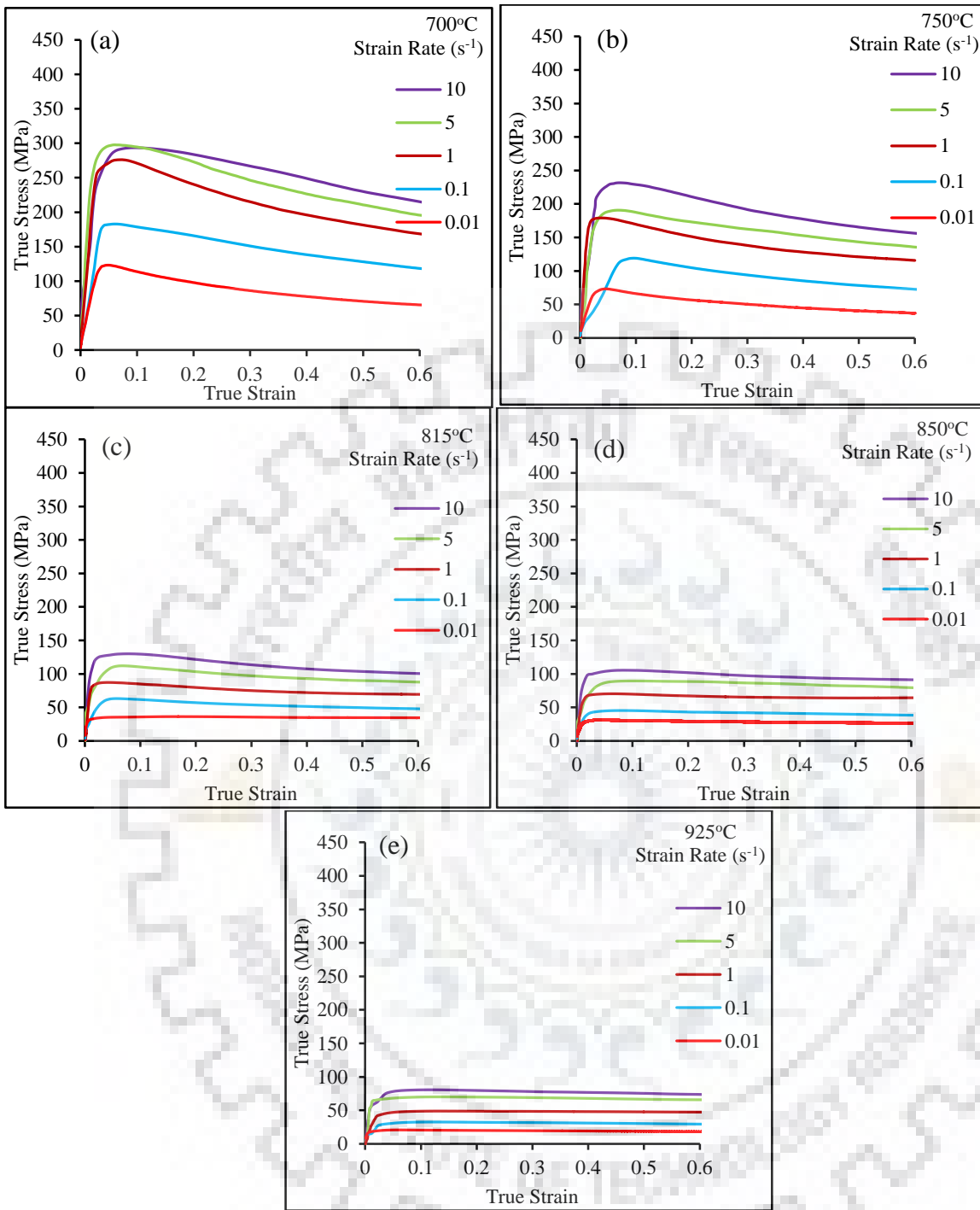
Figure 5.7: True stress- true strain curves of ZNC at different deformation temperatures of; (a) 700°C, (b) 750°C, (c) 815°C, (d) 850°C and (e) 925°C. All flow curves are adiabatic temperature rise (ATR) corrected.

To identify and quantify softening in ZNC flow curves, S_d map on the axis of deformation temperature and strain rate, is shown in **Figure 5.8**. From **Figure 5.8**, it is clear that the maximum degree of softening (maximum S_d value) occurred at lower deformation temperature (i.e. 700-815°C) and it reduces as function of deformation temperature and strain rate. The decrease in degree in softening may be due to decrease in α–phase proportion.

60
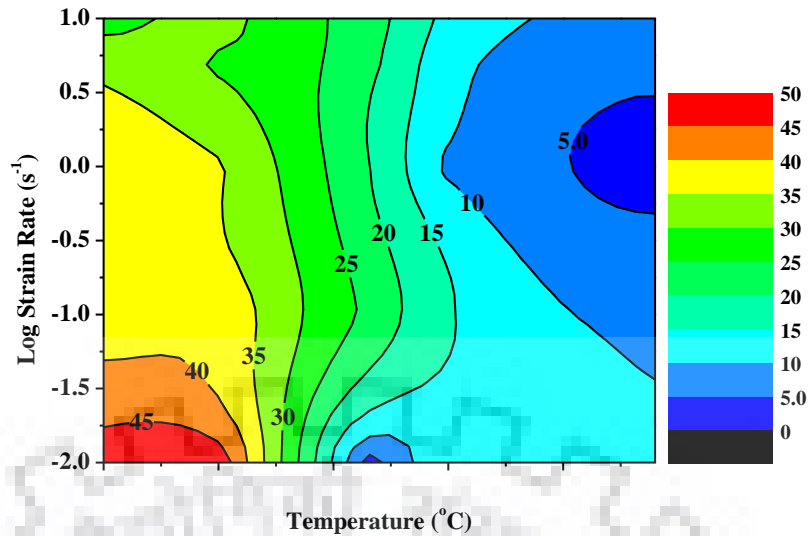
Figure 5.8: The curves in figure represents the flow softening at constant strain rates for entire deformation range of Zr-2.5Nb-0.5Cu extruded and β quenched condition.

Comparison of all true stress- true strain curves (**Figure 5.1, 5.3, 5.5 and 5.7**) of different Zr-Nb alloys reveals that the flow stresses increase with an increase in Nb content of alloys and are influenced by the processing conditions of the alloy. All three different categories of flow curves (i.e. hardening, steady-state and softening), obtained after hot deformation were observed in **Figure 5.1, 5.3, 5.5 and 5.7**. All flow stresses increased rapidly from the start of deformation, but some of them remain fairly constant or increase / decrease to some extent after the peak stress.

At an early stage of deformation, dislocations multiplied dramatically, and the work hardening process was predominant, thereby leading to a rapid increase in the flow stress [43]. As the dislocation density increased, dynamic softening occurred, which can offset the effect of work hardening [43]. Thus, the flow stress increased at a decreasing rate until the peak stress was reached. Subsequently, the flow stress either decreased with increasing strain or remained fairly steady. The former behavior is observed when the rate of dynamic softening is higher than that of work hardening. The latter behavior occurs as a result of a dynamic equilibrium between work hardening and dynamic softening [43]. In both cases, a distinct peak stress is visible as the maximum value in the flow stress curve. In some of the flow curves, the flow stress continuously increases after the early stage of deformation and is termed as strain hardening.

Furthermore, it is evident that the flow stress decreased with increasing deformation temperature and with decreasing strain rate. As the deformation temperature rises, the thermal activation, which favours overcoming an energy barrier to dislocation motion, is increased, while the stress needed to deform a material decreases [43, 44]. Besides, with the increase of temperature, the level of dynamic softening is improved, so that the dislocation density is reduced to facilitate the

61

further dislocation motion [45]. Hence, increasing temperature could substantially reduce the resistance to dislocation movement, which results in the reduction in flow stress. On the other hand, with the decrease of the strain rate, the dislocation multiplication rate is reduced, which leads to less tangled dislocation structures as barriers to the dislocation movement. In addition, a decreasing strain rate results in an increasing level of dynamic softening, due to the availability of more time for the proceeding of dislocation polygonization, which facilitates further movement of dislocation [43]. Therefore, decreasing the strain rate is expected to lower the stress, which is needed for dislocation movement, and leads to a decrease in flow stress.

From the all true stress – true strain curves, it is expected that the softening observed in flow stress curves during high temperature deformation is associated with dynamic recrystallization (DRX) or flow instability whereas, constant flow stress is usually associated with dynamic recovery (DRV) [43]. The strain hardening at higher strain rates represents the accumulation of dislocation during the hot deformation, which could be due to too less time of deformation at higher strain rates to annihilate themselves. It is also expected that the flow softening is due to DRX in α–phase [49] and its effect on flow behaviour is decreasing with an increase in the temperature (or increase in proportion of β–phase), more or less similar to Zr-2.5Nb alloy [159].

5.2 PROCESSING MAPS:

Processing maps are used to bring out effect of strain rate and temperature on the deformation behavior. It also helps in deducing dominant deformation mechanism like dynamic recrystallization, dynamic recovery, flow localization etc. Outs of these dynamic recrystallization and dynamic recovery are considered as efficient deformation mechanisms and flow localization is considered to introduce instability into the material. Details of processing map and explanation of efficiency and instability is provided in **Section 2.6.1**. Processing map contains superimposed power dissipation and instability maps in order to delineate high efficiency and unstable regions. Contours showed with solid lines in **Figure 5.9 – 5.12** represent the efficiency of power dissipation whereas shaded region indicates the instability domain. The higher values of dissipation efficiency are desirable for hot deformation. The unstable domains in processing maps are related to flow localization, adiabatic heating or shear band formation [62]. These domains suggest poor workability during hot deformation. All the processing maps were developed using experimental flow stress data (ATR corrected) at a true strain of 0.6. The maps were developed using different material models.

5.2.1 Zr-1Nb alloys: In this study, Zr-1Nb alloys obtained at two different starting conditions i.e. extruded β-quenched condition and swaged followed by annealed in single α–

62

phase, were used. The following sections describe the processing maps developed using different material models for the above two material conditions.

5.2.1.1 Extruded β-quenched: The processing maps of Zr-1Nb alloy obtained in extruded β-quenched condition are shown in **Figure 5.9**. **Figure 5.9a** shows the processing map developed using DMM, map in **Figure 5.9b** was developed using MDMM whereas, map in **Figure 5.9c** was developed using α-parameter approach.

From **Figure 5.9a**, it is quite clear that there are two domains of highest efficiency (i.e. 0.44) at the strain rate of 10^{-2} s^{-1}. First domain lies in the temperature range of 670 – 750°C (domain-1, D-1) and second domain lies in the range of 850 – 905°C (domain-2, D-2). Another domain of considerable high efficiency (i.e. 0.40) lies in the temperature range of 965 – 1050°C and the strain rate of 10^{-2} s^{-1} (domain-3, D-3). The domain D-1 lies in single α–phase region, D-2 in two phase region and D-3 in the single β–phase region. The instability prediction (**Figure 5.9a**) suggests that the instability may occur at higher strain rates of 10^{-1} s^{-1} or above for lower deformation temperature and, shifts to higher strain rates with rise in the deformation temperature.

Figure 5.9b, which is developed using MDMM approach, reveals two domain of highest efficiency of 0.48 at strain of 10^{-1} s^{-1} in the temperature range of 670 – 770°C and 835 – 915°C. The instability prediction (**Figure 5.9b**) suggests that the instability occurs at higher strain rates of 10^{-1} s^{-1} or above for entire deformation temperature range. In MDMM approach, high efficiency domains (**Figure 5.9b**) overlap with domain of unstable region of the processing map.

Comparison of processing maps (**Figure 5.9a – 5.9c**) developed using different materials models reveal different processing conditions for safe processing. It is expected due to different approaches and assumptions used in the development of these processing maps. However, both DMM and MDMM models predict same temperature range for higher efficiency processes though at different strain rates. A common unstable region is observed in all the maps at lower temperatures and higher strain rates.
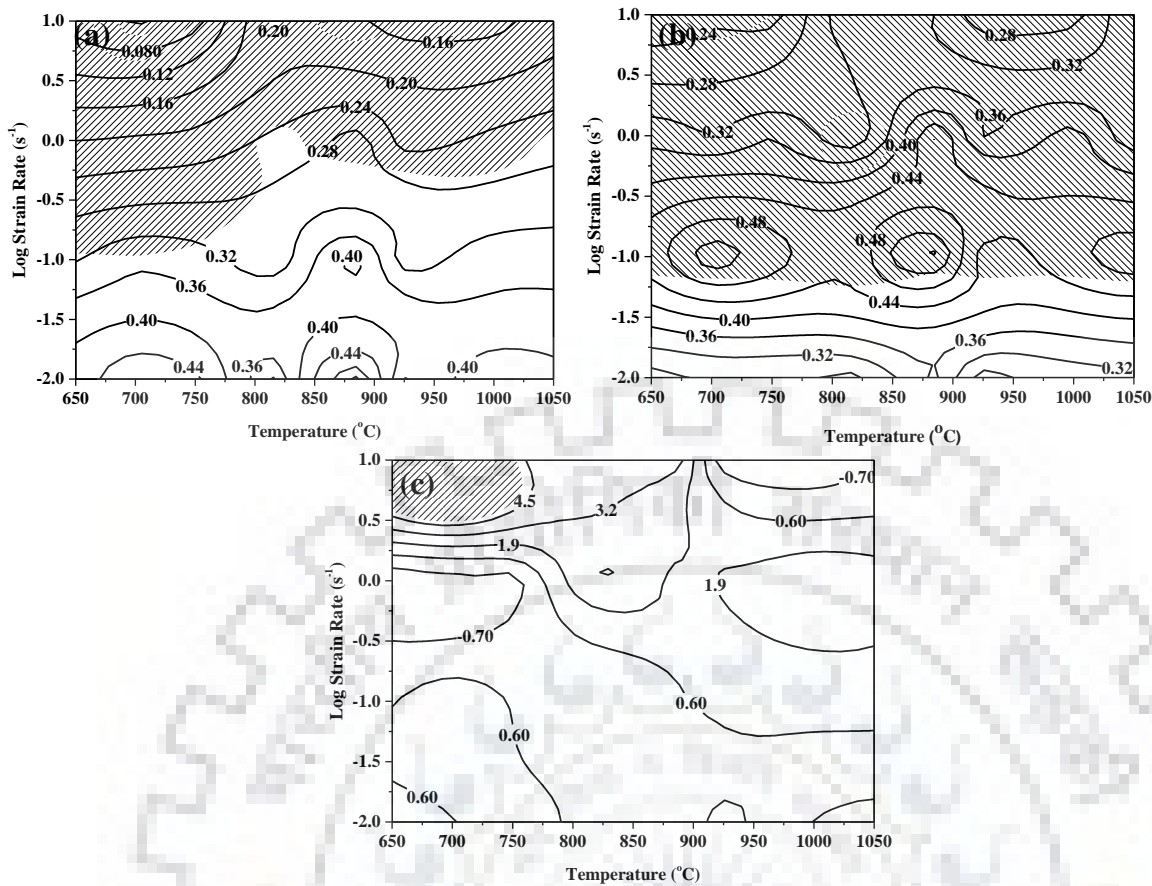
Figure 5.9: Processing maps of Zr-1Nb alloy (extruded β-quenched condition) at strain of 0.6; (a) developed using DMM, (b) developed using MDMM and (c) based on α-parameter. The contours of solid lines represent the efficiency of power dissipation and shaded regions are instability domains.

5.2.1.2 Swaged and annealed in α–phase region: The processing maps developed using different approaches for Zr-1Nb alloy swaged and annealed in α–phase conditions are shown in **Figure 5.10**.

The processing map shown in **Figure 5.10a** developed using DMM approach, reveals that the maximum power dissipation efficiency exists at higher temperature range (i.e. 885 – 1050°C) and lower strain rate of 10^{-2} s^{-1}. The unsafe domains predicting instability in the material are spread around three different processing conditions. The first one is at highest strain rate range of 1 – 10 s^{-1} and temperature range of 650 – 700°C; second at strain rate range of 10^{-2} – 10^{-1} s^{-1} and temperature range of 720 – 800°C, and third at a strain rate of 10^{-1} s^{-1} and temperature range of 900 – 1025°C. On the other hand, processing map (**Figure 5.10b**) developed using MDMM approach reveals maximum efficiency at more or less similar temperature range as in DMM, but at a strain rate of $5×10^{-2}$ s^{-1}. The instability domain in MDMM approach is spread unevenly. At lower temperature range, it is in the strain rate range of $5.6×10^{-2}$ – 10 s^{-1} and gradually strain rate range decreases as temperature increases. At the highest deformation temperature, the spread of

64

unstable region lies in the same range of strain rates as observed at lower temperatures. The processing map (**Figure 5.10c**) developed using α-parameter approach does not exhibit any instability domain and reveals that the processing of studied materials is safe for entire range of deformation temperatures and strain rates. The prediction obtained from α-parameter approach seems contradictory to that of DMM and MDMM approaches.
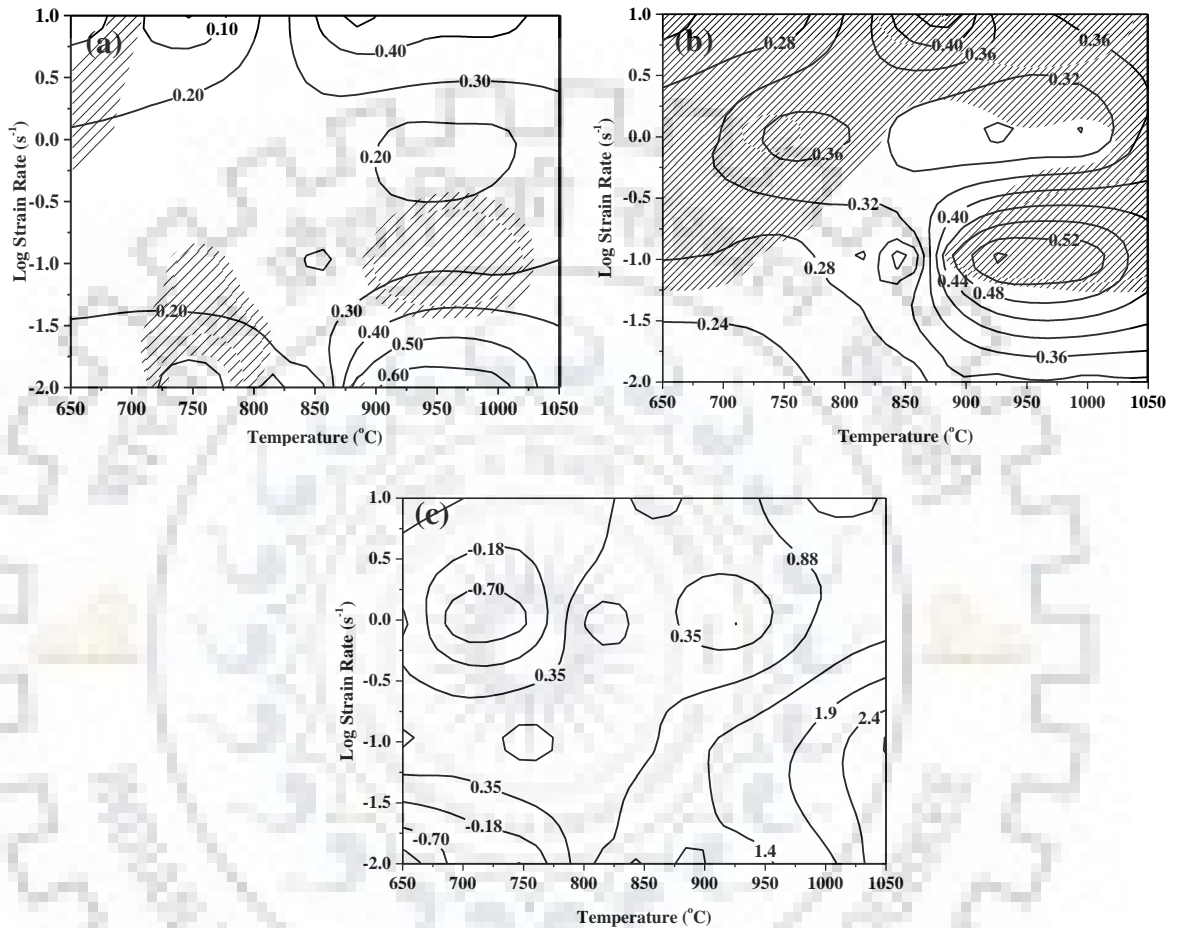
Figure 5.10: Processing maps of Zr-1Nb alloy (swaged and annealed in α–phase) at strain of 0.6; (a) developed using DMM, (b) developed using MDMM and (c) based on α-parameter. The contours of solid lines represent the efficiency of power dissipation and shaded regions are instability domains.

5.2.2 Zr-2.5Nb alloy: The processing maps developed using different approaches for Zr-2.5Nb alloy forged β quenched condition are shown in **Figure 5.11**. The processing map developed using DMM approach is shown in **Figure 5.11a**, using MDMM approach in **Figure 5.11b**, and **Figure 5.11c** shows the processing map developed using α-parameter approach.

The processing map at true strain of 0.6 **(Figure 5.11a)** using DMM approach shows two domains of similar high efficiency (i.e. 0.40). The first domain is observed at deformation temperature around 750°C and strain rate of $10^{-2}\,\text{s}^{-1}$. However, the second domain shifted towards the lower temperature (i.e. $840-920$°C) range and higher strain rates (i.e. around $10^{-1}\,\text{s}^{-1}$). Saxena

et al. [160] reported power dissipation map of Zr-2.5Nb alloy at strains of 0.2 and 0.5, too. From their work and present work, it is clear that with increase in strain, the size of high efficiency domain increases and shifts towards higher strain rates. On the other hand, three different instability domains are seen in **Figure 5.11a**. The first domain occurs at the lowest temperature of 700°C and strain rate of about 10 s^{-1}, the second in the temperature range of 775–925°C and strain rate range of 3×10^{-1} to 10 s^{-1}, and the third occurs at 900°C and strain rate of around 10^{-2} s^{-1}.
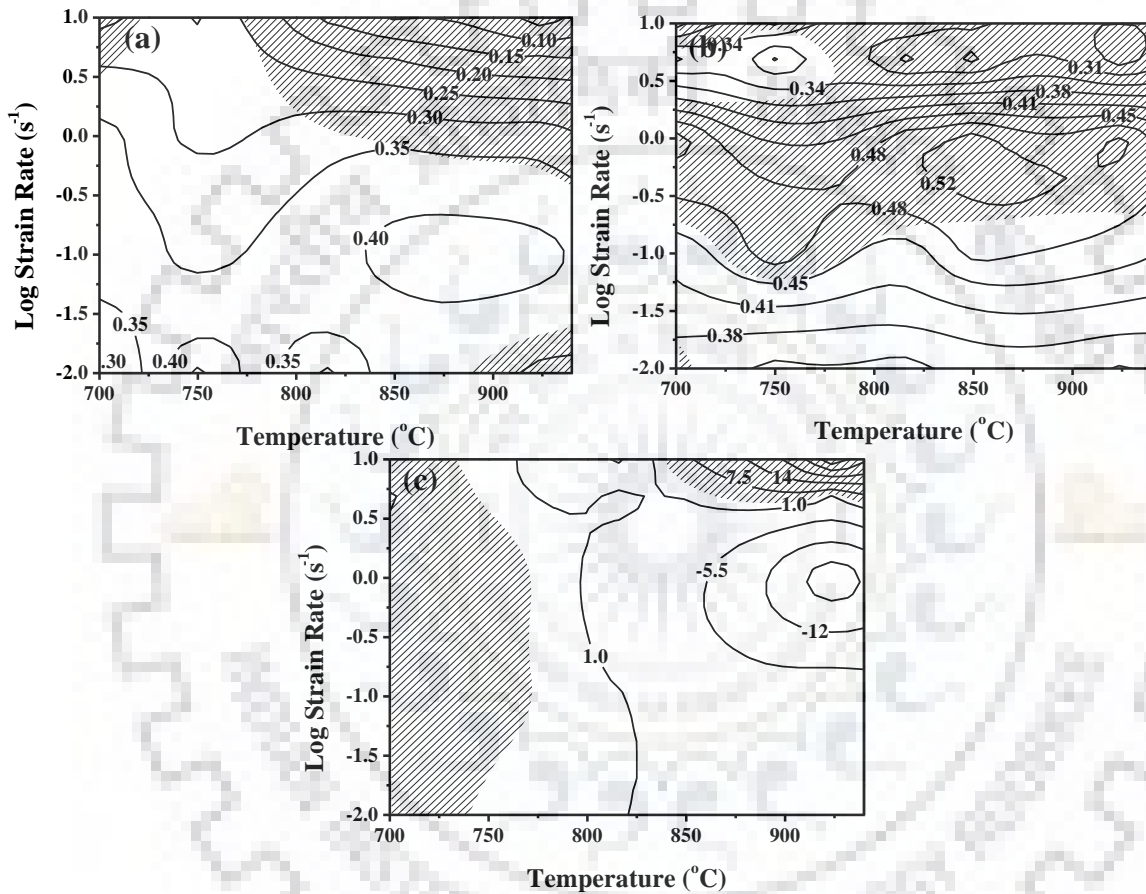
Figure 5.11: Processing maps of Zr-2.5Nb alloy at strain of 0.6; (a) developed using DMM, (b) developed using MDMM and (c) based on α-parameter. The contours of solid lines represent the efficiency of power dissipation and shaded regions are instability domains.

Figure 5.11b shows processing map developed using MDMM approach at a true strain of 0.6 with two different peak efficiencies: one is about 0.48 at a strain rate range of 10^{-1} to 1 s^{-1} for the entire temperature range whereas, second one is about 0.52 at a strain rate of about 5×10^{-1} s^{-1} and the temperature of about 850°C. The instability domain observed in **Figure 5.11b** exist for entire deformation temperature range and strain rate above 1×10^{-1} s^{-1}. Saxena et al. [160] also plotted instability at strain of 0.2 and 0.5 for the Zr-2.5Nb alloy, which makes it clear that with an increase in strain, the instability domains appear around or shift toward extreme deformation

conditions (temperature and/or strain rate), which may be attributed to the inefficient dynamic restoration mechanisms at these conditions.

Figures 5.11c shows the processing map developed using α-parameter approach at true strain of 0.6. The **Figures 5.11c** reveals two unsafe domains: one is below 750°C for entire range of deformation strain rates and other one is at temperature range of 840 – 925°C for highest strain rate.

On comparing the power dissipation efficiency evaluated using both the approaches (i.e. DMM and MDMM), it is clear that the values of peak efficiency of power dissipation obtained by MDMM is higher than DMM. However, deformation conditions showing peak efficiencies are different in both models. Domains of high efficiency obtained using DMM exist at the lower strain rate (0.01– 0.1 s^{-1}) whereas, in case of MDMM, these domains exist at a higher strain rate range (0.1–1 s^{-1}). The instability domain predicted by all three approaches coincides at a very small window of processing conditions (i.e. 840 – 925°C and strain rate of 10 s^{-1}).

5.2.3 Zr-2.5Nb-0.5Cu (ZNC) alloy: The processing maps developed using different approaches for Zr-2.5Nb-0.5Cu alloy extruded β quenched condition are shown in **Figure 5.12**. The processing map developed using DMM approach is shown in **Figure 5.12a**, MDMM approach in **Figure 5.12b** and **Figure 5.12c** shows the processing map developed using α-parameter approach.

The processing map (**Figure 5.12a)** at a strain of 0.6 reveals high power dissipation efficiency (i.e. 0.47) at lower temperature range of 700 – 750°C and strain rate of 10^{-2} s^{-1}. In this processing map, two different unstable domains are observed: one is at lower temperature of 700°C and strain rate range of 10^{-1} – 1 s^{-1} and other is at high strain rate of 10 s^{-1} and temperature around 815°C. The processing map developed using MDMM approach shown in **Figure 5.12b** reveals similar value of power dissipation efficiency at same deformation temperature range as of DMM but at higher strain rate of 10^{-1} s^{-1}. In this processing map approach, again two different unstable domains were observed: one is around temperature of 850°C and strain rate of 10^{-2} s^{-1} and other is for entire deformation temperature range at strain rate above 10^{-1} s^{-1}. While the processing map developed using α-parameter approach (**Figure 5.12c**) reveals two domains of unstable region different from DMM and MDMM approaches: one is at lower temperature of 700°C and strain rate range of 1 – 10 s^{-1} and other is strain rate around 10^{-1} s^{-1} for the temperature range of 825 – 900°C.
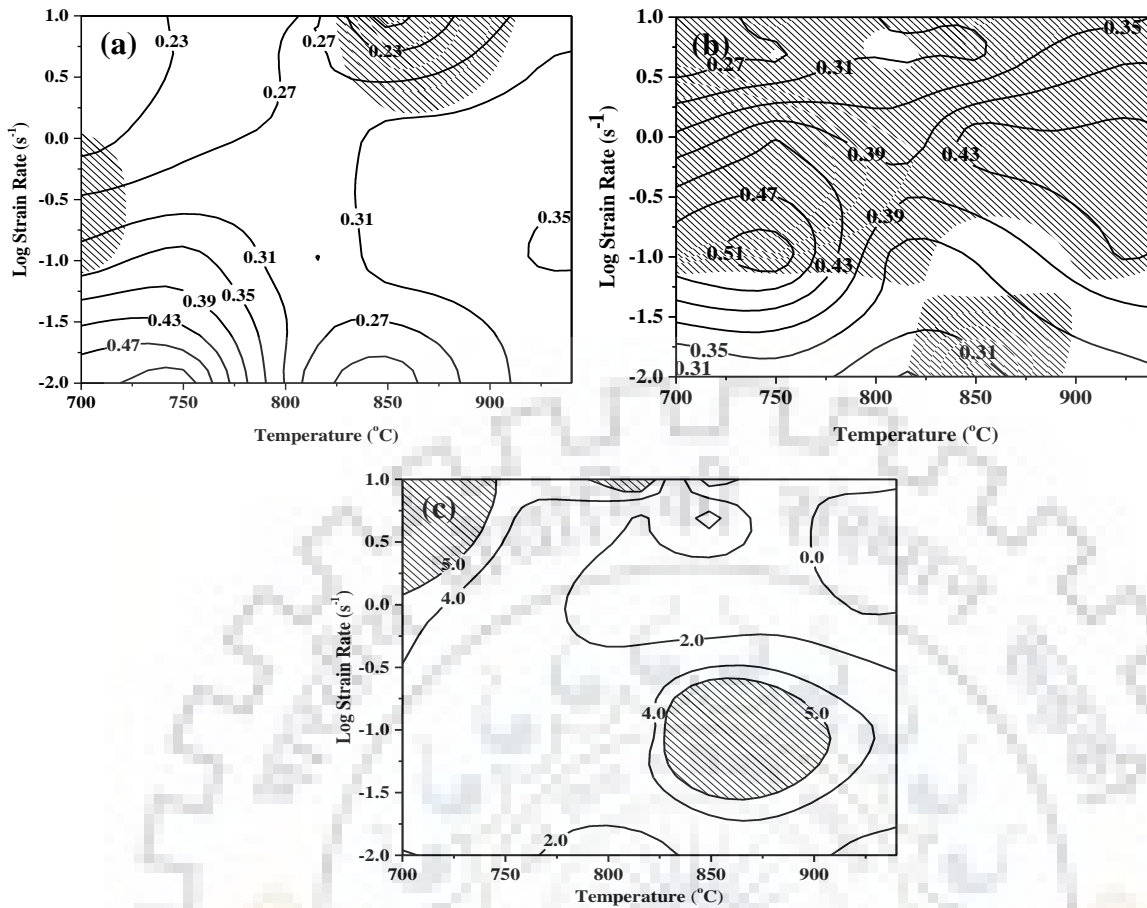
Figure 5.12: Processing maps of Zr-2.5Nb-0.5Cu alloy at strain of 0.6; (a) developed using DMM, (b) developed using MDMM and (c) based on α-parameter. The contours of solid lines represent the efficiency of power dissipation and shaded regions are instability domains

Comparison of the processing maps developed for Zr-1Nb alloys (**Figure 5.9** and **5.10**) reveals that the value of power dissipation efficiency is higher for the swaged and annealed alloy as compared to extrude β quenched alloy. Microstructures of the two materials (**Figure 5.19** and **5.29**) suggests that the grains of swaged and annealed alloy were finer and equiaxed, whereas alloy of extrude β quenched condition had coarse and plate like grains. The difference in size and morphology may be the reason for higher efficiency observed in swaged and annealed alloy. Moreover, the area of instability domain is also reduced in the swaged and annealed alloy.

The addition of Nb in Zr reduces the value of power dissipation efficiency and the domain of high efficiency shifts towards the high strain rates in processing maps. Whereas, addition of Cu in Zr-Nb alloys shifts the high efficiency domain towards the lower temperature and no significant difference in power dissipation efficiency were observed on Cu addition in Zr-Nb alloys.

Sarkar and Chakravartty [58] reported that the safe domain based on strain rate sensitivity map for Zr-1Nb alloy (extruded and cold drawn rods) is in the temperature range of 625 – 800°C and

68

strain rates lower than 10^{-1} s^{-1}. The results reported by Sarkar and Chakravartty [58] are similar to present work on Zr-1Nb alloys. For α–zirconium alloy, Chakravartty et al. [51] reported that the safe domain for hot workability occurs in the temperature range of 1003 – 1123 K (730°C to 850°C) and strain rate range of 10^{-2} to 1^{-1} s^{-1} with the peak efficiency of 0.40. In the two phase region of Zr-2.5Nb alloy, maximum peak efficiency was reported to be 0.45 with DRX like microstructural features [49]. The processing map for Zr-2.5Nb-0.5Cu (β–transformed microstructure) revealed two different domains of safe processing with high efficiency of 0.48 and 0.47 at 750°C and 10^{-3} s^{-1} and at 1050°C and 10^{-3} s^{-1} respectively [8]. At temperature of 750°C it is reported that the DRX is due to shearing of α-platelets followed by spheroidization. Therefore, the efficiency value and domains reported in this work are similar to the results reported in [8] for Zr-2.5Nb-0.5Cu alloy.

5.3 CONSTITUTIVE ANALYSIS AND VALIDATION:

The development of the constitutive equation allows extrapolation of flow stress data beyond the test window [161]. It is well reported that the deformation at high temperatures is a thermally activated process, and the flow stresses are significantly influenced by deformation conditions [113]. Based on the deformation conditions, flow stresses can be classified in terms of low and high stress levels. Zener and Hollomon [113] proposed a single parameter (Z) to express flow stress as a function of strain rate and temperature. Zener-Hollomon parameter (Z) can be defined in terms of temperature (T) and strain rate $(\dot{\varepsilon})$, as shown in **Equation 5.2** [112].

$$Z = \dot{\varepsilon} \exp(Q/RT) \tag{5.2}$$

In an Arrhenius equation, the strain rate is a common parameter to relate the deformation temperature and activation energy. Thus, the strain rate is generally expressed by one of the three different types of equations: the power law (**Equation 5.3**), the exponential law (**Equation 5.4**) and sine-hyperbolic law (**Equation 5.5**). Applicability of each equation depends upon the stress value. It is reported that the power law equation 'breaks down' at high stress, therefore it is valid for low stress values, i.e. ασ < 0.8 (**Equation 5.3**). On the other hand, the exponential law equation is valid at high stress values, i.e. ασ > 1.2 (**Equation 5.4**) [162]. However, a sine-hyperbolic law equation (**Equation 5.5**) is valid for a wider range of flow stresses and more commonly in use [103, 163].

$$\dot{\varepsilon} = A_1 \sigma^{n'} \exp\left(-\frac{Q}{RT}\right) \tag{5.3}$$

$$\dot{\varepsilon} = A_2 \exp(\beta\sigma) \exp\left(-\frac{Q}{RT}\right) \tag{5.4}$$

69

$$Z = \dot{\varepsilon} \exp\left(\frac{Q}{RT}\right) = A[\sinh(\alpha\sigma)]^n \tag{5.5}$$

whereas A, A_1, A_2, n, n' are material constants, Q is the activation energy for hot deformation (kJ/mol), R is the universal gas constant (8.314 J mol^{-1} K^{-1}) and T is the absolute temperature (K). One additional adjustable constant is α, known as stress multiplier. It brings $\alpha\sigma$ into the correct range to make $\ln\dot{\varepsilon}$ versus $\ln\left[\sinh\left(\alpha\sigma_p\right)\right]$ curves linear and parallel.

At a particular deformation condition of strain rate and temperature, flow stress is a function of strain. Therefore, for development of a constitutive equation either peak stress (strain can vary) or steady state stress value at a constant strain is considered. Stress values other than peak stress/ steady state stress may vary due to softening or hardening mechanisms and may not be obtained accurately [164]. Thus, it is better to use peak stress values/steady state valus to determine a constitutive equation [106, 165]. Also, peak stress/ steady state stress is uniquely related to Zener–Hollomon parameter (Z), for the entire range of deformation conditions [43]. Additionally, peak stress/ steady state stress is more important for industrial processes [166]. In this study, peak flow stress and steady state stress were considered in individual material to develop their sine-hyperbolic law equation (**Equation 5.5**). To develop the sine-hyperbolic law equation, it is required to determine few material constants, i.e. A, n, α and Q. These material constants can be obtained as follows:

Determination of α value: The value of α can be calculated by $\alpha\left(\approx \beta/n'\right)$ [162], where n' and β can be calculated from **Equations 5.3** and **5.4**. Taking natural logarithm on both sides of **Equations 5.3** and **5.4** yields **Equation 5.6** and **5.7**, respectively.

$$\ln\dot{\varepsilon} = \ln A_1 + n'\ln\sigma_p - \frac{Q}{R}(1/T) \tag{5.6}$$

$$\ln\dot{\varepsilon} = \ln A_2 + \beta\sigma_p - \frac{Q}{R}(1/T) \tag{5.7}$$

The partial differentiation of **Equations 5.6** and **5.7** with respect to peak flow stress (σ_p) at constant temperature yield to following equations.

$$n' = \left[\frac{\partial \ln \dot{\varepsilon}}{\partial \ln \sigma_p} \right]_T \tag{5.8}$$

$$\beta = \left[\frac{\partial \ln \dot{\varepsilon}}{\partial \sigma_p} \right]_T \tag{5.9}$$

where constant n' and β can be calculated using linear regression of the plot $\ln \sigma_p$ vs $\ln \dot{\varepsilon}$ and the plot of σ_p vs $\ln \dot{\varepsilon}$ respectively, at each temperature as shown in **Figures 5.13a** and **5.13b**. The final value of parameter n' and β are their average value calculated from the slope obtained at each temperature.

Determination of n: The value of n can be calculated using **Equation 5.5**. Simplification of **Equation 5.5** using natural logarithm on both side yields **Equation 5.10**. Partial differentiation of **Equation 5.10** with respect to peak flow stress at constant temperature results in **Equation 5.11**.

$$\ln \dot{\varepsilon} = \ln A + n \ln[\sinh(\alpha \sigma_p)] - \frac{Q}{RT} \tag{5.10}$$

$$\left[\frac{\partial \ln \dot{\varepsilon}}{\partial \ln \left[\sinh \left(\alpha \sigma_p \right) \right]} \right]_T = n \tag{5.11}$$

The relationship of $\ln \left[\sinh \left(\alpha \sigma_p \right) \right] - \ln \dot{\varepsilon}$ is plotted in **Figure 5.13c** at constant temperatures. Thereafter, the final value of n is an average slop value of all temperatures.

Determination of activation energy (Q): For high temperature deformation, activation energy *(Q)* can be obtained by rearranging **Equation 5.10** as follows:

$$\ln \left[\sinh \left(\alpha \sigma_p \right) \right] = \frac{Q}{nR} \frac{1}{T} + \frac{1}{n} \ln \dot{\varepsilon} - \frac{1}{n} \ln A \tag{5.12}$$

The partial differentiation of **Equation 5.12** at a constant strain rate with respect to the reciprocal of deformation temperature *(1/T)* yield **Equation 5.13**:

$$\left[\frac{\partial \ln \{ \sinh (\alpha \sigma_p) \}}{\partial (1/T)} \right]_{\dot{\varepsilon}} = \frac{Q}{nR} \tag{5.13}$$

Therefore, the activation energy can be defined as follows:

$$Q = R n S \tag{5.14}$$

where $S = \left[\dfrac{\partial \ln \{ \sinh (\alpha \sigma_p) \}}{\partial (1/T)} \right]_{\dot{\varepsilon}}$

which is determined by linear regression of the *(1000/T)* vs $\ln\left[\sinh\left(\alpha\sigma_p\right)\right]$ plots at constant strain rate, as shown in **Figure 5.13d**. Afterwards, the final value of *S* is an average of slop values obtained at different strain rates. By using the average value of *n* and *S* in **Equation 5.14**, final activation energy can be calculated.

Determination of A: The linear regression of the $\ln\dot{\varepsilon}$ vs $\ln[\sinh(\alpha\sigma_p)]$ plots from **Equation 5.11** at each temperature can provide the intercept value to calculate constant *A,* as shown in **Figure 5.13c.** Furthermore, *A* can be calculated by following equations.

$$\left(\ln\dot{\varepsilon}-\operatorname{int}erception\right)=\ln A-\frac{Q}{RT} \tag{5.15}$$

Simplifying **Equation 5.15** yield to **Equation 5.16**

$$A=\exp\left[\left(\ln\dot{\varepsilon}-\operatorname{int}erception\right)+\frac{Q}{RT}\right] \tag{5.16}$$

Since the value of *Q* is already obtained. *A* was determined using the intercept of the linear regression of the $\ln\dot{\varepsilon}$ vs $\ln[\sinh(\alpha\sigma_p)]$ plot at each temperature. Afterwards the average value of *A* for all range of deformation temperature was obtained.

5.3.1 Zr-1Nb alloy (extruded β quenched):

Constitutive equation or constitutive analysis of Zr-1Nb alloy (extruded β quenched condition) was developed in two different modes. Mode-1: by considering peak flow stresses at different strain rates for entire temperature range (no consideration for the phases present). This is the usual procedure followed in the reported literature. Mode-2: by considering peak flow stresses at different strain rates from different temperature ranges based on phases present i.e., individual constitutive equations for each phase or phase mixture.

Figure 5.13 illustrates calculation of materials constants, using peak flow stress of two phase region. Detailed procedure to develop constitutive equation is given in **Section 5.3**. **Figure 5.13a** and **Figure 5.13b** show the calculation of material constants n' and β, from the average slope of the best fit line in the plot between $\ln\dot{\varepsilon}\,vs\ln\sigma_p$ and $\ln\dot{\varepsilon}\,vs\,\sigma_p$, respectively. Similarly, the plots of $\ln\left(\sinh\left(\alpha\sigma_p\right)\right)vs\ln\dot{\varepsilon}$ **(Figure 5.13c)** and, $1/T\,vs\ln\left(\sinh\left(\alpha\sigma_p\right)\right)$ **(Figure 5.13d)** were used to calculate the values of material constants *n* and *S* respectively. It is worthwhile to mention here that all the lines in **Figure 5.13c** are almost parallel to each other. The parallelism of these lines confirms that the obtained value of stress multiplier (α) is accurate. The accurate value of stress multiplier (α) is highly desirable for correct calculation of stress exponent (*n*) and activation energy (*Q).* The calculation of stress multiplier (α) is rigorously analysed by Dipti et

al. [167] and it is reported that the α value plays significant role in the development of accurate constitutive equation.
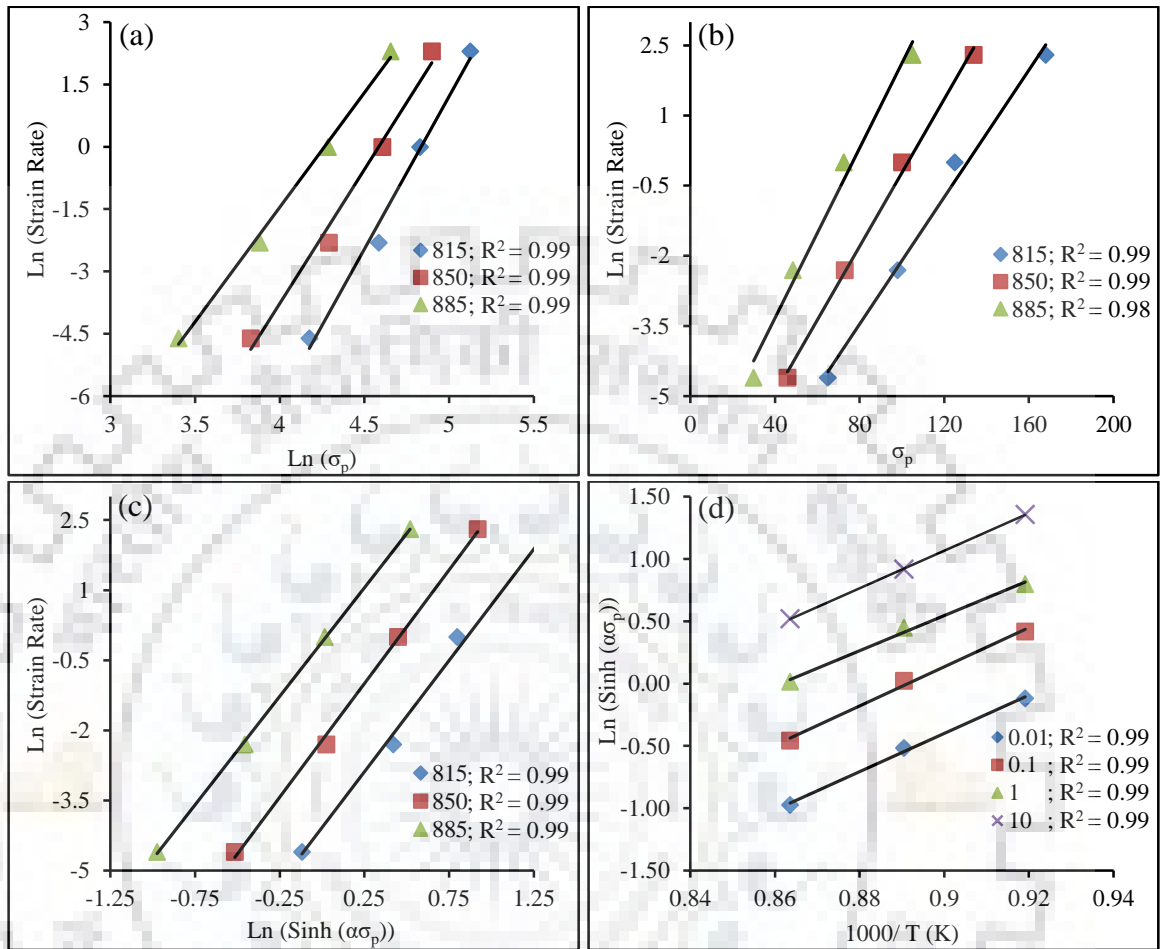
Figure 5.13: Relationship among stress, strain rate, and temperature to obtain the value of material parameters (a) n', (b) β, (c) n, and (d) S

The values of material constants and activation energy in all different modes are summarised in **Table 5.1**. From **Table 5.1**, it is clear that in Mode-1 (single calculation for entire deformation temperature range), the values of activation energy (Q) and stress exponent (n) are 491 kJ/mol and 4.5 respectively. In Mode-2, values of Q in α– phase is 333 kJ/mol, in β– phase is 293 kJ/mol and in two phase (α+β), it is 749 kJ/mol.

Table 5.1: Material constants and activation energies in different modes using peak flow stress values.

Parameters	Mode-1	Mode-2		
	All range temperature	α–Phase	Two Phase	β–Phase
α	0.01575	0.00534	0.01340	0.03150
n	4.5	6.2	5.2	4.9
s	13.1	6.5	17.4	7.2
Q	491	333	749	293
Ln A	53.07	38.83	77.96	25.86

Stress exponent values n in α–phase, β–phase and (α+β) phase are 6.2, 5.2, 4.9 respectively. The calculated values of stress exponent (n) in present study is in the range of 4–6, which is consistent with reported literature [58, 168-171]. The value of n in this range suggests that the dislocation climb could be deformation controlling mechanism.

The calculated value of Q, for entire temperature range of deformation (Mode-1) is quite different than the values obtained from different phases or phase mixture (Mode-2). The values of Q calculated in present work for different phases (Mode-2) are close to the reported values of Q for respective phases in Ti and Zr alloys [4, 53, 55, 58, 172-176].

Developed constitutive equations are shown in **Equations 5.17** and **5.18** for different modes of calculation.

$$\dot{\varepsilon}=1.12\times10^{23}\,[\sinh{(0.01575\times\sigma_p)}^{4.5}]\exp\left(-\frac{491000}{RT}\right) \quad (\textit{for All Temperature Range}) \quad (5.17)$$

$$\left.\begin{aligned}
\dot{\varepsilon}&=7.32\times10^{16}\,[\sinh{(0.00534\times\sigma_p)}^{6.2}]\exp\left(-\frac{333000}{RT}\right) \quad &(\textit{for Alpha Phase})\\[2mm]
\dot{\varepsilon}&=7.19\times10^{33}\,[\sinh{(0.01340\times\sigma_p)}^{5.2}]\exp\left(-\frac{749000}{RT}\right) \quad &(\textit{for Two Phase})\\[2mm]
\dot{\varepsilon}&=1.70\times10^{11}\,[\sinh{(0.03150\times\sigma_p)}^{4.9}]\exp\left(-\frac{293000}{RT}\right) \quad &(\textit{for Beta Phase})
\end{aligned}\right\} \quad (5.18)$$

5.3.1.1 Validation with Zener-Hollomon parameter: To check the validity of developed constitutive equations of Zr-1Nb alloy, Zener-Hollomon parameter (temperature-compensated strain rate parameter) is used [113], and defined as follows:

$$Z=\dot{\varepsilon}\exp(Q/RT)=A[\sinh(\alpha\sigma_p)]^n \quad (5.19)$$

The relationship between peak stress and Zener-Hollomon parameter for different modes are shown in **Figure 5.14**. It is clear from **Figure 5.14**, that the peak stress increases as Z increases, and the correlation coefficient (R^2) for the linear regression is varying from 0.97 to 0.99. The value of R^2 demonstrates the accuracy of **Equations 5.17** and **5.18** for the hot deformation behaviour of Zr-1Nb. It was found that the value of R^2 is high (i.e. 0.99) in Mode-2 (**Figures 5.14b-5.14d)** whereas, R^2 value is low i.e. 0.97 (**Figure 5.14a)** in Mode-1.
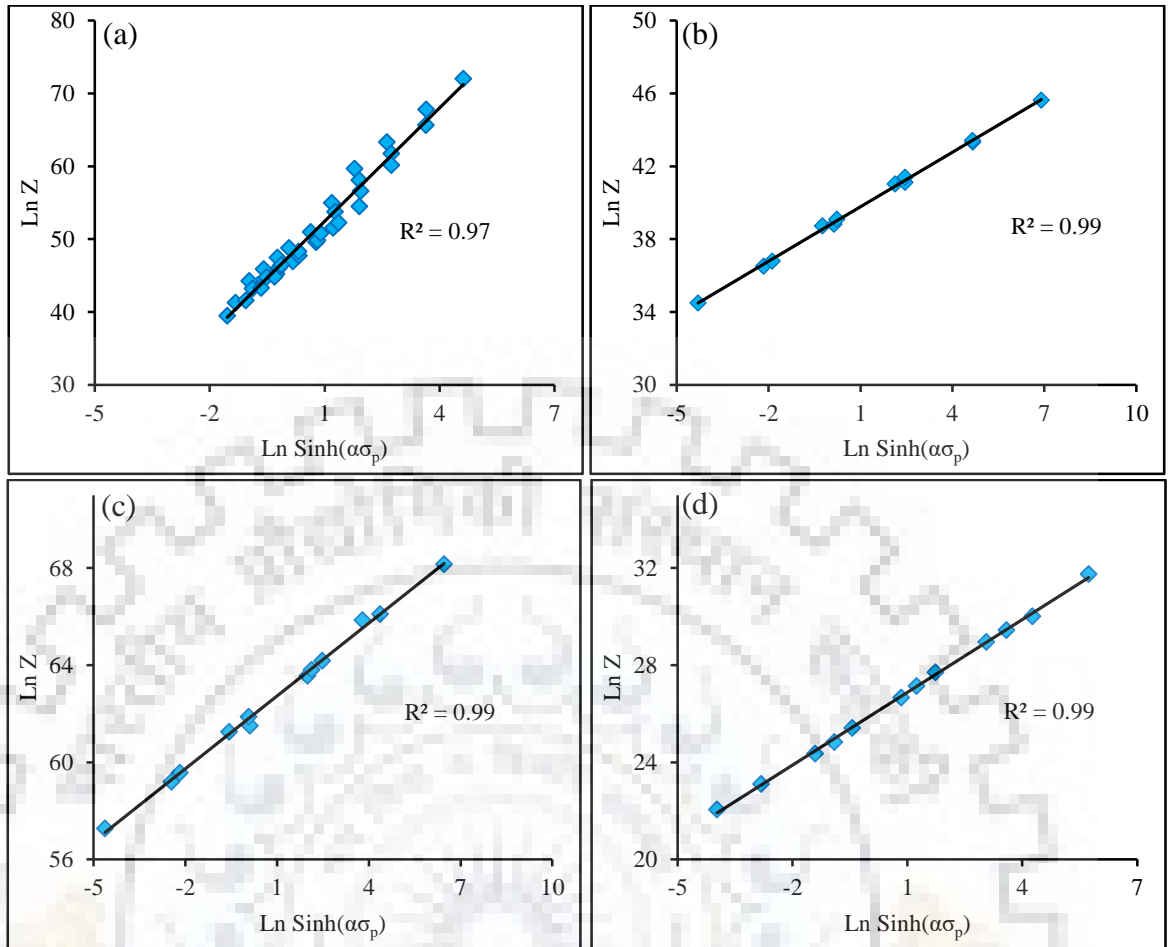
Figure 5.14: Plot of Ln Z vs Ln sinh($\alpha\sigma$); (a) for all temperature range, (b) α–phase, (c) two phase and (d) β–phase.

5.3.1.2 FEM simulation: An additional validation of developed constitutive equations for Zr-1Nb alloy was performed by FEM simulation of hot extrusion process. FEM simulation results were compared with real hot extrusion shop floor data. The shop floor hot extrusion data (DAS) were collected from Nuclear Fuel Complex (NFC), Hyderabad. The extrusion experiment was carried out by employing a 37.8 MN press operated under direct extrusion mode. The shop-floor data of physical extrusion was recorded by an electronic data acquisition system installed on the press. The data was obtained in terms of ram-force v/s speed of extrusion that was converted to ram force v/s ram displacement. The numerical simulation of hot extrusion was done using a 3–D finite element analysis (FEA) software HyperXtrude®. HyperXtrude is a commercial simulation software module dedicated to simulation of extrusion process using the ALE (Arbitrary Lagrangian and Eulerian) approach. The dimensions/ parameters of actual extrusion product generated from the physical experiments and FEA were kept similar. **Table 5.2** summarises the dimensions/ parameters used in the physical experiment and simulation.

The FEM extrusion models were prepared using a structured mesh with appropriate biasing to maintain accuracy and continuity across the faces of different elements. **Figure 5.15** shows the geometry of the FEM extrusion model. The various boundaries, interaction of the billet material with the surroundings was modelled using appropriate heat transfer and friction conditions as shown in **Figure 5.16**. The interaction of the billet material with the surroundings in terms of heat transfer and friction boundaries are given in **Table 5.3** and shown in the **Figure 5.16**. The details of the FE formulation have been documented elsewhere [42]. Only the details pertaining to this work have been included here.

The inputs to the HyperXtrude® FEA was introduced in two ways; i) flow stress- strain data obtained from the uniaxial hot compression tests in the form of look up table (LUT) and, ii) constants of constitutive equations developed using compression stress-strain data. The output of simulation was in terms of ram force as a function of ram displacement along with the temperature, strain rate distributions. The evolution of ram force during the actual physical extrusion was available and is used for comparison and validation of the FEA results.
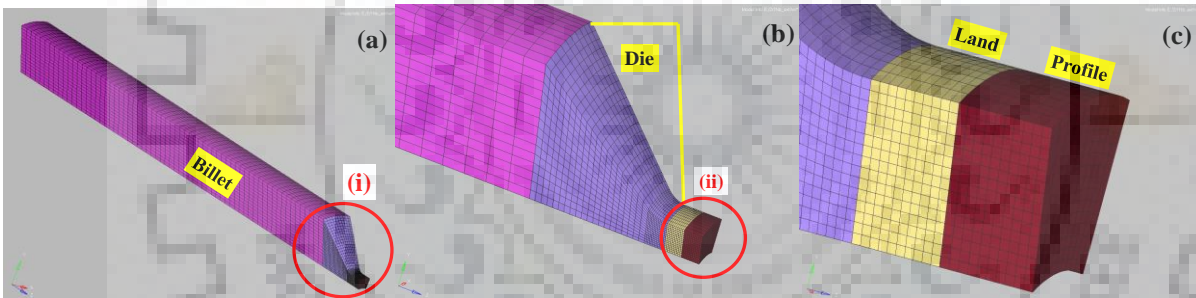
Figure 5.15: Simulation model developed using HyperXtrude software for extrusion process of Zr-1Nb showing different components, mashing, and geometry; (a) full frame model for the tube, (b) Expanded view of circle (i) to reveal die pattern, (c) Expanded view of circle (ii) to reveal land and profile pattern
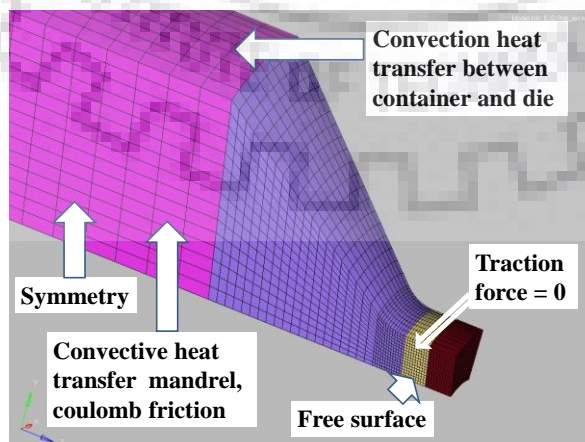
Figure 5.16: Extrusion model developed in HyperXtrude software showing interactions of the model with different boundary surfaces

Table 5.2: Process parameters used in FEA simulation and real extrusion

Parameters	FEA Simulation	Real extrusion
Billet Diameter (mm)	150	150
Billet length (mm)	500	500
Billet temperature (°C)	810	810
Fillet radius (mm)	10	10
Reduction ratio	5.41	5.41
Ram Speed (mm/s)	30	30
Friction factor at die- billet interface	0.3	-
Friction factor at container-billet interface	0.1	-
Step size for simulation (mm)	0.02	-

Table 5.3: Details of heat transfer and friction boundaries during simulation modelling

Free Surface Boundary	free surface boundary is assigned at profile surface. This boundary is assigned an insulated boundary, i.e., q (heat flux) = 0.
Friction Boundary	when shear stress over contact surfaces exceeds critical shear stress, material starts to flow
Convective Heat Transfer boundary	all tool face boundaries are assigned convective heat transfer boundary, i.e., heat removal from these faces is through convection
Inflow Boundary	a constant velocity and temperature boundary condition is assigned at billet ram face
Outflow Boundary	this boundary is assigned to profile face
Displacement	= 0 (as extrudate is free to expand)
Traction forces	= 0 (as the extrudate is not pulled out of the die)
heat flux	= 0
Symmetric Boundary	It is assigned to all symmetric faces

5.3.1.2.1 Material properties in simulations: The inputs to simulation of the extrusion process are material properties and boundary conditions. The material properties mainly consist of flow stress data as a function of strain, strain rate and temperature. In HyperXtrude software, the material properties can be included as "Look-Up Table" (LUT), which contain experimentally measured flow stress values from compression tests at various temperatures, strains and strain rates. An alternative approach is to use parameters/constants of constitutive equation as inputs to HyperXtrude in order to simulate extrusion process and predict ram force. The other material properties used for simulation are shown in **Table 5.4**.

Table 5.4: Materials properties used in FEA software [42, 177, 178]

Density (Kg/m^3)	6500
Specific heat (J/ Kg. K)	328
Conductivity (W/m. K)	20.8
Co-efficient of thermal expansion (1/K)	9.46 x 10^{-4}
Volumetric heat source (W/ m^3)	0
Reference temperature (K)	1083
Liquidus temperature (K)	2000
Solidus temperature (K)	1950
Young's Modulus (GN/m^2)	2.0 x 10^{10}
Poisson's ratio	0.35

In the earlier **Section 5.3.1**, the constitutive equations were developed in two modes; Mode-1 is for entire temperature range and Mode-2 is for temperature range corresponding to individual phases or phase mixture. Parameters of these constitutive equations were used for simulation. In case of Mode-2, parameters of the constitutive equation developed for two phase mixture were considered as input to the simulation. Since, physical extrusion occurs in two phase region (i.e. 810°C).
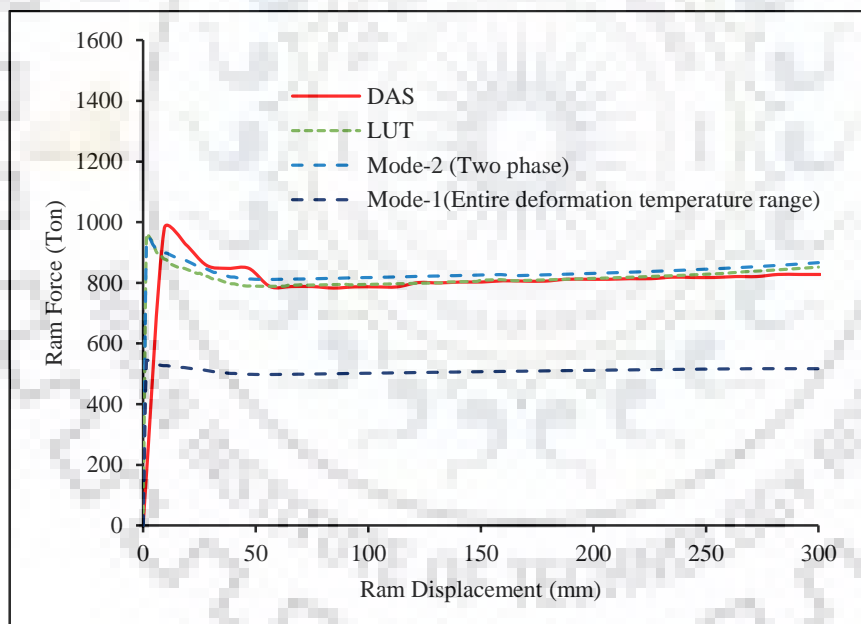
Figure 5.17: Comparison of ram force values obtained from simulation and real extrusion

5.3.1.2.2 Validation of constitutive equation and FEM simulation: Figure 5.17 shows plots of ram force v/s ram displacement. The plot of ram force v/s ram displacement from shop floor is compared with the simulated one using LUT, and constitutive equations parameters from Mode-1 and Mode-2. The experimentally measured ram force values (DAS data) are close to the values obtained from the simulations using LUT approach and parameters of constitutive equations developed using two phase flow stress data (Mode–2). However, simulation output

using parameters of constitutive equation developed using entire temperature range (Mode-1) are significantly lower than the experimental shop floor data. **Table 5.5** shows the error calculation between ram forces obtained using various inputs, i.e. LUT, parameters of both constitutive equations, DAS data. Comparison of simulated results using LUT and shop floor data (DAS) shows error of 1.9% in peak ram force and -2.2% in steady state ram force. This confirms that development of simulation model, materials properties used, boundary conditions and other parameters are acceptable. The error in prediction of ram force using constitutive equation parameters in two phase region (Mode-2) is 3.3% in peak ram force and -4% in steady state ram force. This confirms that the developed equation in two phase region is well suited to predict ram force. From **Table 5.5**, it is clear that the error in prediction of peak ram force and steady state ram force are 80.6% and 38.0% respectively with DAS data, when the input was constitutive equation parameters developed for the entire range of deformation temperature or considering all phases in a single calculation (Mode-1). It thus emerges that if the extrusion material has allotropic behaviour (i.e. undergoes phase transformation in the temperature domain of interest), then the development of constitutive equations should be according to the constituent phases, i.e. individual constitutive equation for each phase. The measured force versus displacement curve does show some oscillations during transition from the peak force to steady state force, mainly due to the variations introduced in the ram velocity under practical conditions of the extrusion which are rather difficult to incorporate in the simulations.

Table 5.5: Error calculation among experimental DAS data, simulation using the constitutive equation and simulation using the LUT.

Position	Error (%)			
	DAS vs. Mode-1	DAS vs. Mode-2	DAS vs. LUT	Mode-2 vs. LUT
Peak ram force	80.6	3.3	1.9	-1.4
Steady state ram force	38.0	-4.0	-2.2	1.7

From both the validation methods, it can be concluded that the development of single constitutive equation which covers different phases could produce erroneous results. Therefore, the development of a constitutive equation should be based on phases present. Similar observation for individual phase in two phase region is reported by Saxena et al. [232, 240].

5.3.2 Zr-2.5Nb-0.5Cu (ZNC):

Constitutive equations were developed using experimental flow stress data obtained from hot compression test of Zr-2.5Nb-0.5Cu. In the present work, different sets of peak flow stress data were considered to develop constitutive equations: one set belongs to experimental data, and another set of flow stress was calculated from the experimental values in a two phase range. Using each set of flow stress data, independent constitutive equations were developed for;

i) deformation temperature range 700°C to 815°C, related to *(α+β)* phase, ii) for deformation temperature 815°C to 925°C related to *β* phase, iii) entire range of deformation temperature i.e. 700°C to 925°C related to *(α+β)* and *β* phase (or complete data set irrespective of phases present) and, iv) the calculated flow stress values of individual phases (i.e. individual α and β phase) in (α+β) phase range. The calculation of different material parameters to develop constitutive equations are similar as defined in earlier **Section 5.3**. **Table 5.6** represents different material parameters calculated from the procedure defined in earlier **Section 5.3** for ZNC.

Table 5.6: Calculated material constants of ZNC for various sets

Deformation temperature (°C)	Relevant phase	α (MPa^{-1})	n	Q (kJ/mol)	A (s^{-1})
700-815 (α+β) phase	AE 1	0.0082	4.5	524	4.58×10^{25}
815-925 β phase	AE 2	0.01698	4.0	300	1.23×10^{13}
700-925 (α+β) and β phase	AE 3	0.01204	4.0	472	1.19×10^{22}
700-815 (two phase range for individual phase calculation)	AE 4	0.01015	4.6	$Q^c_{two\,phase\,range}$ = 477 Q^c_{α} = 532 Q^c_{β} = 373	2.01×10^{22}

5.3.2.1 Activation energies in different temperature domains: Phase diagram of the studied ZNC alloy is more or less similar to that of Zr-2.5Nb alloy. It's hexagonal closed packed (HCP) *α-Zr* phase is stable up to 630°C (± 10°C) and body centered cubic (BCC) phase *β–Zr* is stable at high temperatures above about 825°C (± 10°C). In the intermediate temperature range it has a two phase range i.e. (α+β) phase [14]. It is expected that the activation energy of hot deformation may show two entirely different values, depending upon the dominant phase in the two phase region. Therefore, in the present work, activation energy calculations were done according to the deformation temperature range (or domain). Thus, three different activation energies were calculated: AE1 for a deformation temperature range 700°C to 815°C, related to (α+β) phase, AE2 for deformation temperature 815°C to 925°C related to β phase, and AE3 is in the entire range of deformation temperature i.e. 700°C to 925°C related to (α+β) and β phase. Thus, the calculated activation energies using peak flow stress for different temperature ranges are as follows: AE1 is 524 kJ/mol, AE2 is 300 kJ/mol, and AE3 is 472 kJ/mol.

5.3.2.2 Validation of predicted peak stress: In order to validate the calculated material parameters, calculated peak flow stresses were compared with the experimental peak flow

stresses. Applying a sine-hyperbolic law equation **(Equation 5.5)**, a general expression to predict peak flow stress of a material can be obtained by using **Equation 5.20**.

$$\sigma_p = \frac{1}{\alpha}\sinh^{-1}\left[\frac{\dot{\varepsilon}\exp(Q/RT)}{A}\right]^{1/n} \tag{5.20}$$

As described earlier, constitutive analysis of hot deformation of Zr-2.5Nb-0.5Cu was performed in four modes: AE1, AE2, AE3 and AE4. Thus, four different constitutive equations were developed to predict peak flow stress as given below:

$$\sigma_{p(\alpha+\beta)\,phase}^{E} = \frac{1}{0.0082}\sinh^{-1}\left[\frac{\dot{\varepsilon}\exp(524000/RT)}{4.58\times10^{25}}\right]^{1/4.5} \tag{5.21}$$

$$\sigma_{p(\beta\,phase)}^{E} = \frac{1}{0.01698}\sinh^{-1}\left[\frac{\dot{\varepsilon}\exp(300000/RT)}{1.23\times10^{13}}\right]^{1/4.0} \tag{5.22}$$

$$\sigma_{p[(\alpha+\beta)\,and\,\beta\,phase)]}^{E} = \frac{1}{0.0121}\sinh^{-1}\left[\frac{\dot{\varepsilon}\exp(472000/RT)}{1.19\times10^{22}}\right]^{1/4.0} \tag{5.23}$$

$$\sigma_{p(two\,phase\,range)}^{c} = \frac{1}{0.01015}\sinh^{-1}\left[\frac{\dot{\varepsilon}\exp(477000/RT)}{2.01\times10^{22}}\right]^{1/4.6}$$

(5.24)

The predictability of a constitutive equation was also assessed by employing standard statistical parameter such as correlation coefficient (R) and average absolute relative error (AARE).

$$R = \frac{\sum_{i=1}^{n}(E_i - \bar{E})(P_i - \bar{P})}{\sqrt{\sum_{i=1}^{n}(E_i - \bar{E})^2 \sum_{i=1}^{n}(P_i - P)^2}} \tag{5.25}$$

$$AARE\,(\%) = \frac{1}{n}\sum_{i=1}^{n}\left|\frac{E_i - P_i}{E_i}\right|\times100 \tag{5.26}$$

In above **Equations 5.25 and 5.26**, P is predicted value obtained using the constitutive equation and E is experimental value obtained from compression test, whereas $\bar{P}$ and $\bar{E}$ are the mean values of P and E respectively. The total number of data employed during the investigation is represented by n.

The correlation coefficient (R) is a commonly used statistical tool and provides information about the goodness of fit of a model with experimental values. The value of R lies in the range of 0 to 1. R near 1 represents that the regression line fits well with experimental values. However, this is not always true because of the bias in the data [116, 179]. On the other

81

hand, AARE provides term by term relative error and therefore is considered an unbiased statistical tool [116, 180-182]. Thus, in this work, the verification of a constitutive equation was also performed using AARE. Thus, the minimum value of AARE will indicate that a particular constitutive equation is able to predict with more accuracy. The values of R and AARE obtained for different constitutive equations are listed in the **Table 5.7** and shown in **Figure 5.18**.

AARE found to be very high for AE3 and comparable values for AE1, AE2 and AE4. Interestingly, R values for all equations are very close to each other. Constitutive equations developed for a (α+β) range (AE1) and for a single β–phase (AE2) show good agreement with experimental values. On the other hand, a constitutive equation developed for the entire range of deformation temperature 700-925ºC (AE3) predicts significant variation in peak flow stress values at a higher strain rate and temperatures. This is due to clubbing of hot deformation data
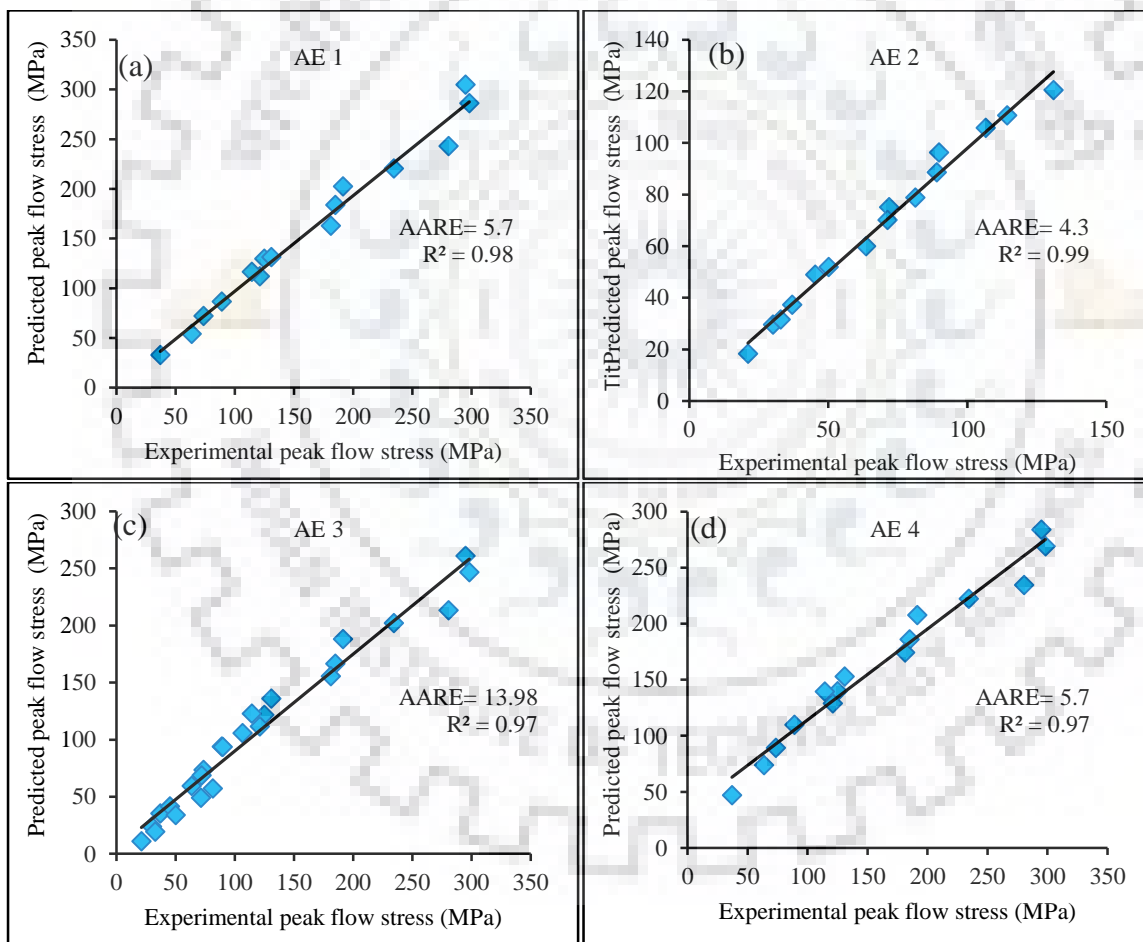
Figure 5.18: Plots to show the regression coefficient and AARE for; (a) AE1, (b) AE2, (c) AE3, and (d) AE4

Table 5.7: Values of R and AARE obtained for different constitutive equations

Statistical parameter	Constitutive equations			
	AE1	AE2	AE3	AE4
R	0.98	0.99	0.97	0.97
AARE	5.7	4.3	13.98	5.7

obtained from different phases. Therefore, it is interesting to note that the constitutive equation for (α+β) range (AE1) is able to predict peak stress though, the proportions of α and β– phase must be significantly different at different deformation temperatures. A constitutive equation developed using calculated stress values for α and β phases by applying the rule of mixture (AE4) clarify that variation in proportion of the two phases does not affect predictability of the equation developed.

5.4 MICROSTRUCTURAL FEATURES: Microstructures of different Zr-Nb alloys, before and after deformation are presented in this section. The effect of hot deformation conditions on microstructural evolution is presented to identify the deformation mechanism and to validate the processing map. The microstructural analysis was carried out for selected deformation conditions, where the processing map predicted either maximum power dissipation efficiency or instability.

5.4.1. Zr-1Nb Alloys:

5.4.1.1 Extruded β-quenched:

5.4.1.1.1: As received microstructure: Figure 5.19 shows microstructure of the as-received or undeformed sample of the Zr-1Nb alloy, which is in extruded β quenched condition. **Figure 5.19** reveals prior β grains which transformed to fully martensitic microstructure containing fine α plate morphology of martensite. The morphology of the transformed α plates inside the prior β grains is similar to the martensitic microstructure found in other Ti and Zr alloys [183]. The average grain size of the prior β grains was found to be approximately 350 μm.
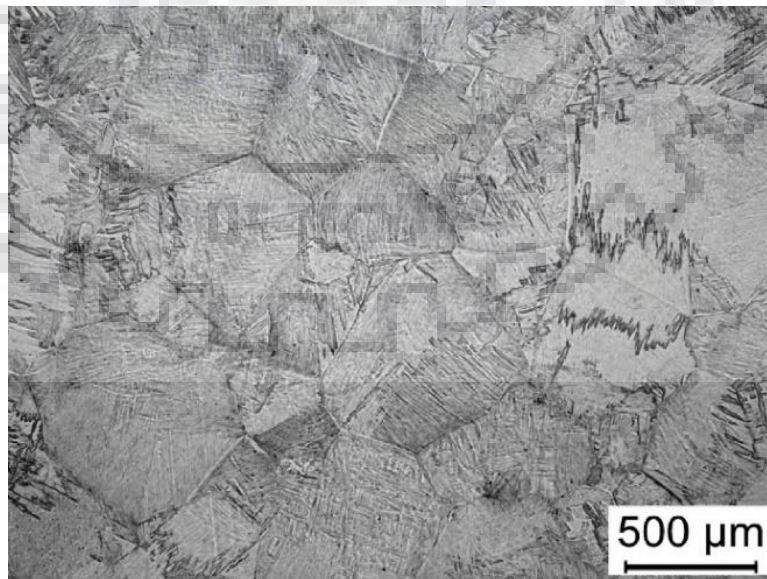
Figure 5.19: Microstructure of as-received Zr-1Nb alloy in extruded β quenched condition.

5.4.1.1.2: Deformed microstructure: Microstructures were taken from the samples deformed at specific deformation conditions. The specific deformation conditions were chosen from the processing map, where higher power dissipation efficiency or instability was predicted. In the processing map (DMM), **Figure 5.20 (reproduced here from Figure 5.9 for reference)**, maximum power dissipation efficiencies were observed at strain rate of 10^{-2} s^{-1} and, instabilities were predicted at higher strain rate of 10 s^{-1} for entire range of deformation temperatures.

Microstructures of the stable region:

Domain-1 (D-1): In the processing map, **Figure 5.20**, domain D-1 (670 – 750°C) is the stable region with high power dissipation efficiency of 0.44 lying in the α–phase region. The microstructures of two deformation conditions (i.e. 700 and 750°C at strain rate of 10^{-2} s^{-1}) were selected for microstructural analysis from D-1.
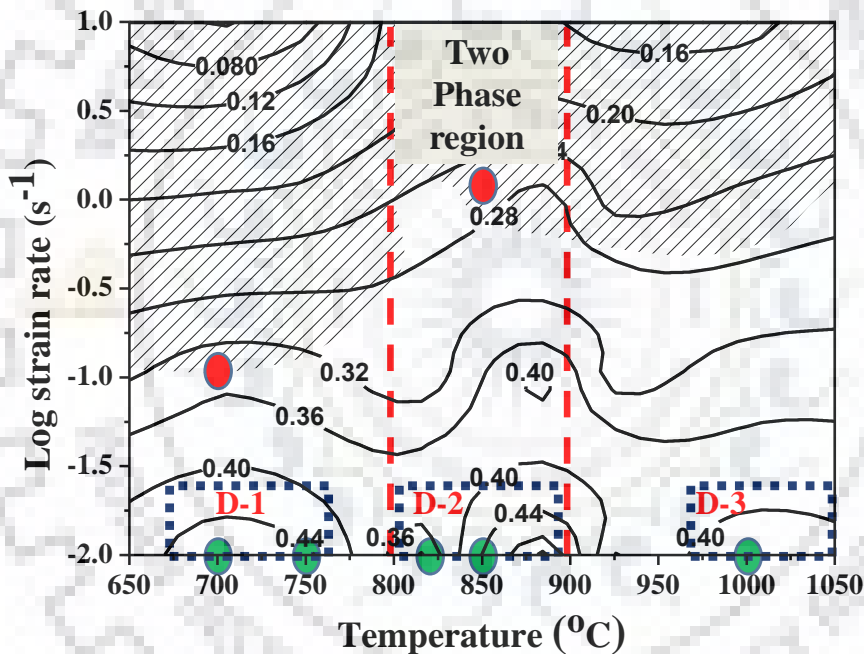
Figure 5.20: Processing map developed using DMM at true strain of 0.6 for Zr-1Nb alloy in extruded β quenched condition (**reproduction of Figure 5.9**). From each phase one domain was selected exhibiting high efficiency of power dissipation and marked as D-1, D-2, and D-3. Green and red circles show the deformation conditions at which microstructural analysis was performed

D-1, 700°C/ 10^{-2} s^{-1}: The microstructure obtained after deformation at 700°C/ 10^{-2} s^{-1} is shown in **Figure 5.21**. **Figure 5.21a** shows the optical microstructure, whereas **Figure 5.21b** is EBSD scan showing map of high angle grain boundaries to reveal the grain structure after deformation. The map of **Figure 5.21b** represents an area marked in **Figure 5.21a**. Analysis of optical micrograph in association with EBSD scan revealed that most of the α martensitic plates are fragmented and few are elongated. **Figure 5.21b** reveals significant structural modification

occurred due to hot deformation which may be termed as partial recrystallization. The HAGB fraction is found to be 0.61 at this deformation condition. The grain orientation spread (GOS) is shown in **Figure 5.21c** to identify the recrystallized grains. The grains having GOS<1° is considered as recrystallized one. **Figure 5.21c** reveals that recrystallization fraction is around 0.41 at this deformation conditions. Another observation is that the fine grains are showing lower GOS value (GOS<1°) whereas the elongated grains are showing higher GOS value of more than 2.5°. Interestingly, the initial criss-cross morphology (indicated by arrows in **Figure 5.21b**) of the α plates (β transformed) is still visible.

Figure 5.21: Zr-1Nb extruded β quenched condition deformed at 700°C / 10^{-2} s$^{-1,}$ wherein processing map (**Figure 5.20**) predicts high power dissipation efficiency of 0.44. The deformation temperature is in the single phase α region; (a) optical micrograph after deformation, (b) EBSD image showing high angle grain boundary map of the area encircled in **Figure 5.21a**, wherein criss-cross morphology is encircled and also indicated by arrows and (c) EBSD image showing grain orientation spread (GOS). Keys for GOS and HAGB are shown at right bottom. The compression axis is vertical to micrograph.

D-1, 750°C/ 10^{-2} s^{-1}: **Figure 22** show micrographs of the sample deformed at 750°C/10^{-2} s^{-1}. Microstructural features shown in **Figure 22a** and **b** are more or less similar to that of sample deformed at 700°C/10^{-2} s^{-1} (**Figure 5.21**). The fraction of HAGB is found to be 0.62, which is

more or less equal to the HAGB of sample deformed at $700^{\circ}C/10^{-2}$ s^{-1}. However, there is substantial difference in size of equiaxed grains and orientation of elongated plates. Fragmented α plates are finer in size and elongated plates are aligned in one direction and have serrated boundaries. The volume fraction of grains with GOS<1° is 0.49, as shown in GOS map (**Figure 5.22c**). From GOS map, it is evident that the elongated plates have GOS>2.5° which is an indication that the elongated plates contain higher dislocation density and substructure.

Figure 5.22: Zr-1Nb extruded β quenched condition deformed at $750^{\circ}C / 10^{-2}$ s^{-1}, wherein processing map (**Figure 5.20**) predicts high power dissipation efficiency of 0.44. The deformation temperature is in the single phase α region; (a) optical micrograph after deformation, (b) EBSD image showing high angle grain boundary map of the area encircled in **Figure 5.22a**, (c) EBSD image showing grain orientation spread (GOS), and (d) Inverse pole figure (IPF) map, wherein serrated grain boundaries are indicated by arrows and one magnified image is shown in the inset. Keys for GOS and HAGB are shown at right bottom. The compression axis is vertical to micrograph.

The **Figure 5.22d** represents the IPF map at deformation condition of $750^{\circ}C/10^{-2}$ s^{-1}. It is clear in IPF map (**Figure 5.22d**) that the criss-cross morphology (indicated by arrows in **Figure 5.21b**) of the α plates (β transformed) is disappeared and the grains got aligned in the direction of 45° to the compression direction, i.e. in the maximum shear stress direction. Similar to the deformation condition of $700^{\circ}C/10^{-2}$, at condition of $750^{\circ}C/10^{-2}$ s^{-1} also the microstructure showed partial

recrystallization with bands of coarse and fine grains. The coarse grains have serrated grain boundaries and contain sub-grains surrounded by low angle grain boundaries. Hua et al. [184] also reported similar features of serrated grain boundaries in deformation of near β Titanium alloy Ti-5553. To quantify the recrystallization fraction, the grains with GOS<1° are shown in **Figure 5.21c** and **5.22c** for deformation temperature of 700 and 750°C. The recrystallization fraction increased with deformation temperature - the fraction of grains with GOS<1° increased from 0.41 at 700°C to 0.49 at 750°C. Increase in temperature is expected to provide necessary activation energy for recrystallization and hence resulted in higher recrystallization fraction. Presence of bimodal grain size distribution and grain boundary serrations, which are clearly visible in the $(10\bar{1}0)$ oriented grains **(Figure 5.22d)**, may suggest that the recrystallization in single phase α region is through geometric dynamic recrystallization (GDRX) [185].

Domain-2 (D-2): It is clear from the dilatometry study that the two phase region in Zr-1Nb alloy exists in the temperature range of 791 – 899°C. D-2 was observed in the temperature range of 805 – 899°C around strain rate of 10^{-2} s^{-1}. For D-2, efficiency of power dissipation varied from 0.36 to 0.44 at the strain rate of 10^{-2} s^{-1}. The higher power dissipation efficiency of 0.44 suggests DRX/DRV. In this domain D-2, two deformation conditions are selected from microstructural analysis, where processing map shows higher efficiency of 0.44 (at 850°C/ 10^{-2} s^{-1}) and 0.36 efficiency (at 815°C/ 10^{-2}s^{-1}).

D-2, 815°C/ 10^{-2} s^{-1}: **Figure 5.23** show the micrographs of sample deformed in two phase range at temperature of 815°C and strain rate of 10^{-2} s^{-1}. **Figure 5.23a** represents the EBSD scan showing the high angle grain boundary map of the deformed sample. HAGB map reveals fine recrystallized grains with 0.79 fraction of high angle grain boundaries. The starting microstructure is completely modified at this deformation condition. At this deformation condition, recrystallization fraction is 0.62 (**Figure 5.23b**) with fraction of HAGB of around 0.79, which implies that microstructure is more or less fully recrystallized.

D-2, 850°C/ 10^{-2} s^{-1}: **Figure 5.24** shows the micrograph of the sample deformed in the two phase region at a strain rate of 10^{-2} s^{-1} and temperature of 850°C. This deformation condition was in the stable domain of processing map with an efficiency of 0.44. The microstructure after deformation at 850°C/10^{-2} s^{-1} condition **(Figure 5.24a)** appears quite different from the microstructure at 815°C/10^{-2} s^{-1} (**Figure 5.23a**). The microstructure in **Figure 5.24a** exhibits a mixture of two types of the grains. Some of them are coarse and elongated and few are fine in between the coarse grains. The coarse/elongated grains appear to be transformed from β phase, whereas band of fine grains are of α phase. The size of the transformed α (from β phase) and

prior α grains are larger than those in the microstructure of sample deformed at 815°C/10^{-2} s^{-1}. **Figure 5.24b** shows the GOS map at same deformation condition. GOS map clearly revealed that the fine grains have GOS<1° and hence considered to be recrystallized. The IPF map for same processing condition (i.e. 850°C/10^{-2} s^{-1}) are shown in **Figure 24c** to get more information about morphology. The IPF map **(Figure 5.24c)** after deformation at 850°C/10^{-2} s^{-1} also illustrates the two sets of grain structures – coarse/elongated grains with a large fraction of LAGBs and band of fine grains in between the coarse grains. In the microstructure **(Figure 5.24c)**, coarse/elongated grain are indicated by arrow and fine grains are encircled. The recrystallization fraction at 850°C/10^{-2} s^{-1} was 0.42 and fraction of HAGB was around 0.58.
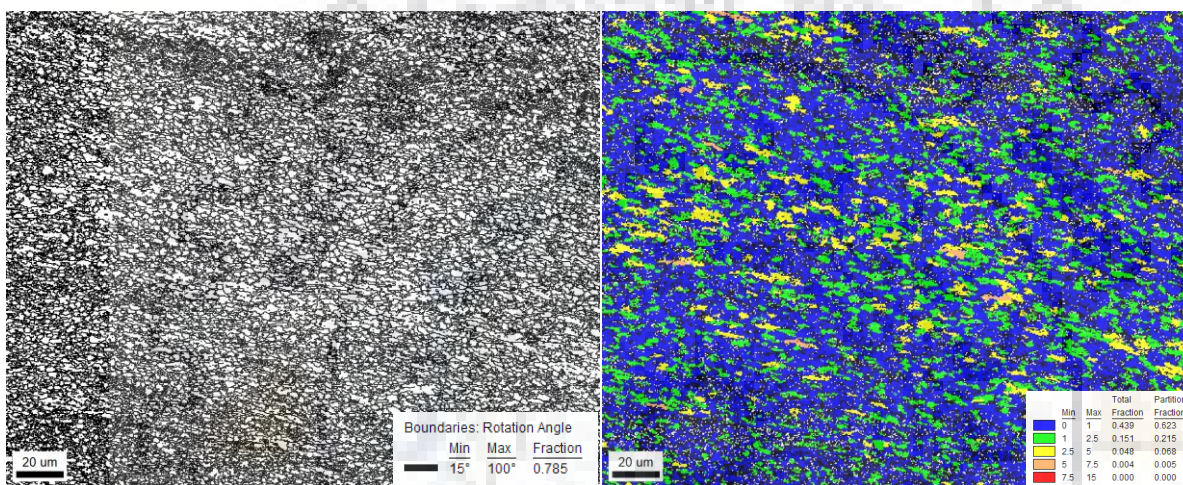
Figure 5.23: Zr-1Nb extruded β quenched condition deformed at 815°C / 10^{-2} s^{-1}, wherein processing map (**Figure 5.20**) predicts considerable high power dissipation efficiency of 0.36. The deformation temperature is in the two phase (α+β) region; (a) EBSD image showing high angle grain boundary map of the deformed sample, and (b) EBSD image showing grain orientation spread (GOS). Keys for GOS and HAGB are shown in inset. The compression axis is vertical to micrograph.

However, the power dissipation efficiency at the deformation condition of 815°C/10^{-2} s^{-1} is lower as 0.36 in comparison to 0.44 at 850°C/10^{-2} s^{-1}. Therefore, fine recrystallized microstructure with high recrystallization fraction and high fraction of HAGB at such lower efficiency does not support the processing map prediction.

Domain-3 (D-3): D-3 is in the safe region of single β–phase with the peak power dissipation efficiency value of 0.40 in the temperature range of 970 – 1050°C for strain rate of 10^{-2} s^{-1}. Two deformation conditions are selected for microstructural examination from D-3. The one is at 925°C and other is at 1000°C for strain rate of 10^{-2} s^{-1}.

D-3, 925°C/ 10^{-2} s^{-1}: The image quality (IQ) map of the sample deformed in single β–phase at the temperature of 925°C and strain rate of 10^{-2} s^{-1} is shown in **Figure 5.25a**. The prior

β grains as well as α plates are coarser than that obtained at lower temperatures. The prior β grain boundaries and plate like structure are clearer in the HAGB map (**Figure 5.25b**). The area for HAGB map is selected from **Figure 5.25a**. The GOS map shown in **Figure 5.25c** reveals that the recrystallization fraction of single β–phase at these deformation conditions is less as 0.19.
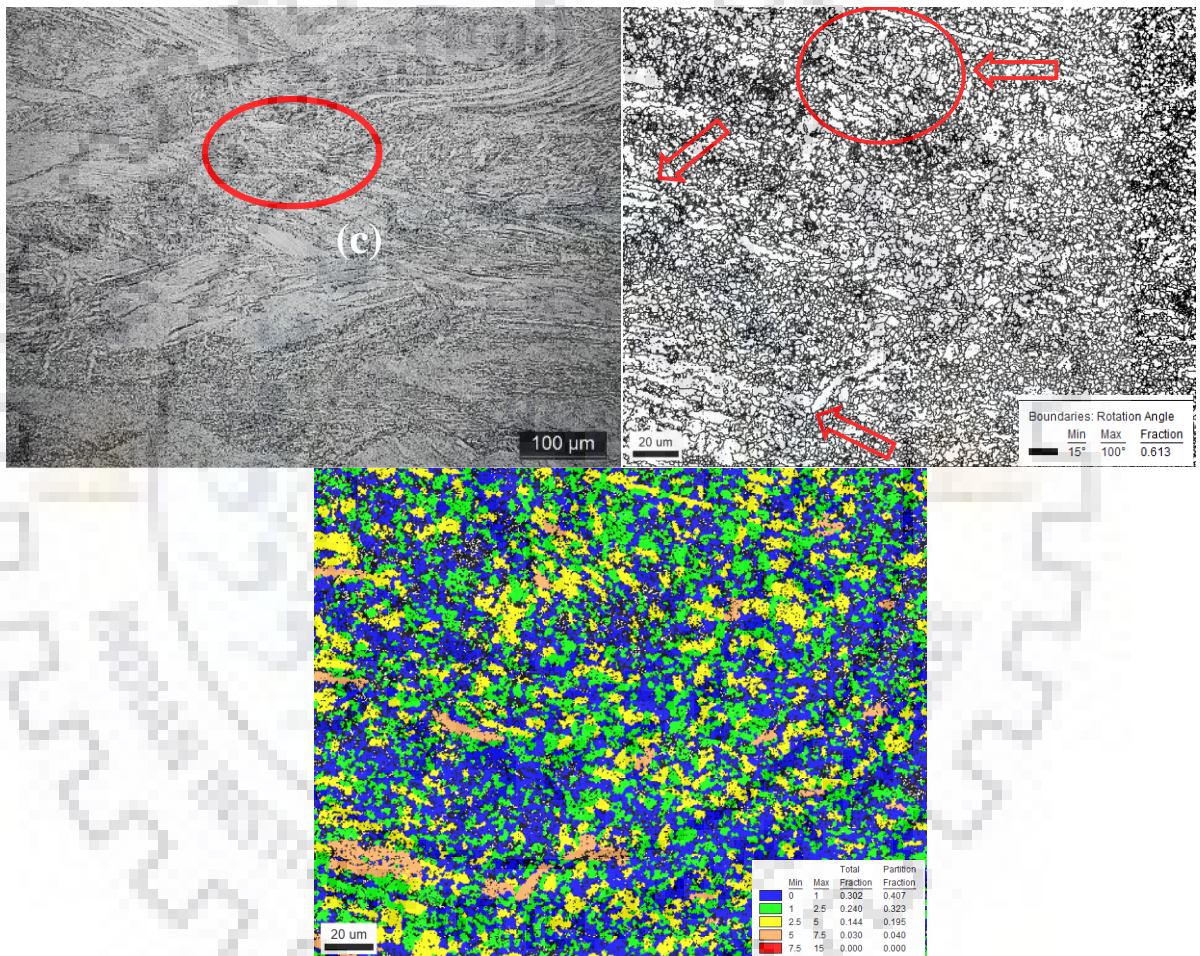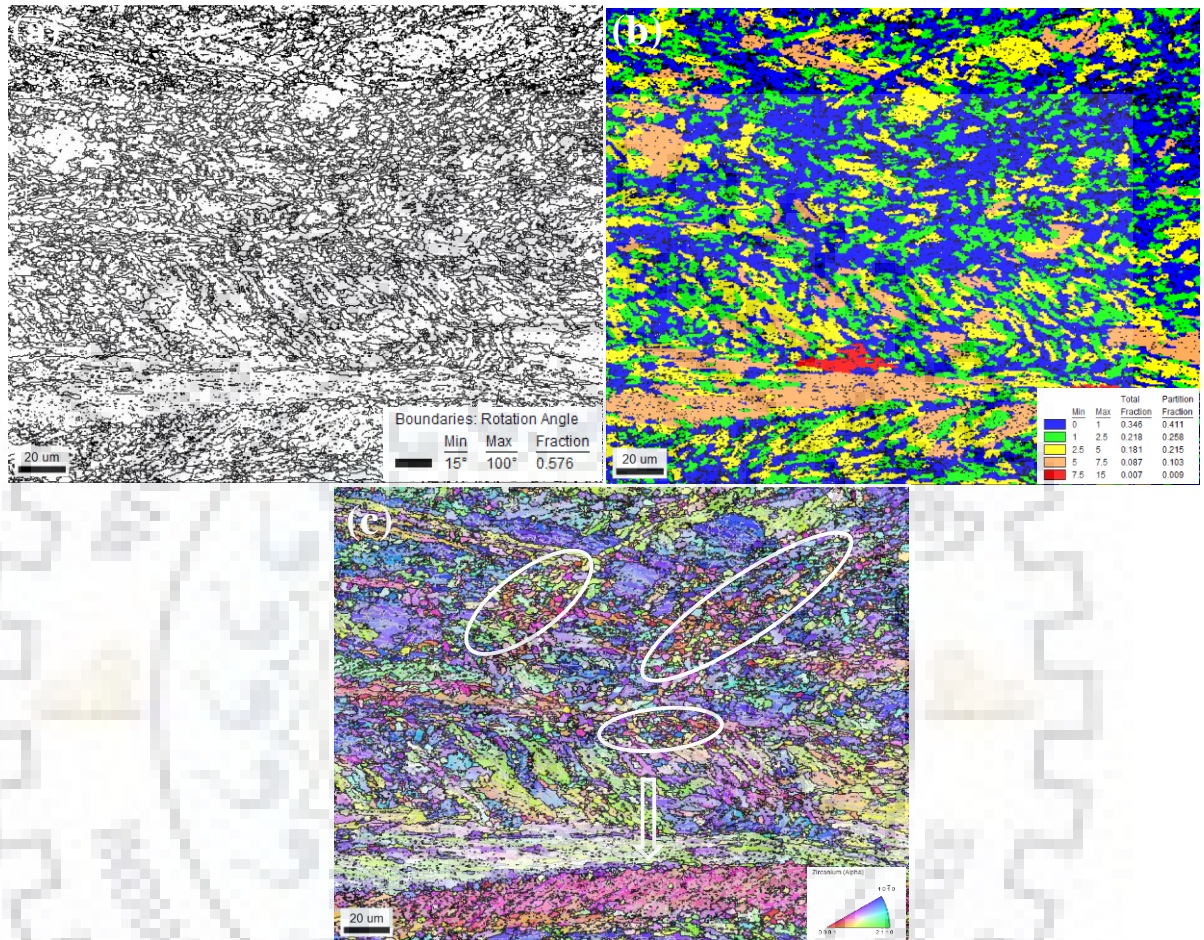

Figure 5.24: Zr-1Nb extruded β quenched condition deformed at 850°C / 10^{-2} s^{-1}, wherein processing map (**Figure 5.20**) predicts considerably high power dissipation efficiency of 0.44. The deformation temperature is in the two phase (α+β) region; (a) EBSD image showing high angle grain boundary map of the deformed sample, (b) EBSD image showing grain orientation spread (GOS), and (c) IPF map showing two sets of grain structure – band of fine grains (encircled) and coarse/elongated grains having fine α plates (indicated by arrow). Keys for GOS and HAGB are shown at right bottom. The compression axis is vertical to the micrographs.

D-3, 1000°C/ 10^{-2} s^{-1}: The image quality (IQ) map of the sample deformed in β–phase at the temperature of 1000°C at constant strain rate of 10^{-2} s^{-1} is shown in **Figure 5.26a**. The micrograph reveals more or less similar features obtained at deformation conditions of 925°C/ 10^{-2} s^{-1}. But it seems that the plates related features are different from lower temperature deformation. The prior β grain boundaries are also visible in deformed microstructure. The grain size and plate size is increasing as a function of deformation temperature in β–phase. For better visualization and understanding of morphology, IPF map of sample deformed at 1000°C/10^{-2} s^{-1}

is shown in **Figure 5.26d**. The analysis of recrystallized grain (GOS<1°) (**Figure 5.26c**) and HAGB (**Figure 5.26b**) revealed that the fraction of recrystallized grains at this condition was 0.58 and fraction of HAGB was 0.88. Unlike the transformed β grains in the two phase region, transformed β had multiple variants of α plates in the single β–phase region. According to crystallography of bcc-hcp transformation, 12 variants of α plates within a β grain are expected [4].
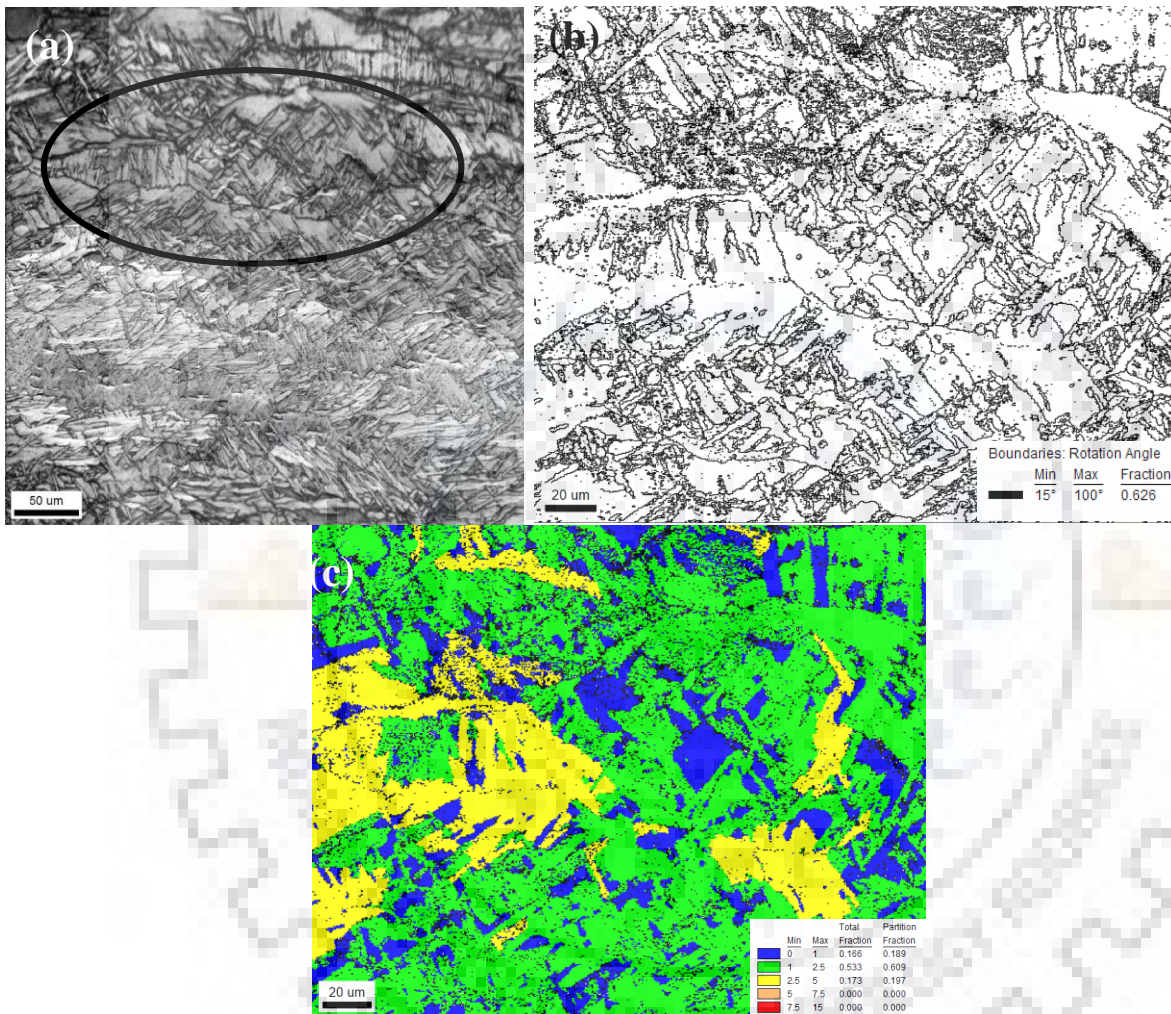
Figure 5.25: Zr-1Nb extruded β quenched condition deformed at 925°C / 10^{-2} s^{-1}, wherein processing map (**Figure 5.20**) predicts considerably high power dissipation efficiency of 0.40. The deformation temperature is in the single β–phase region; (a) Image quality map (b) EBSD image showing high angle grain boundary map from the encircled area in **Figure 5.25a** and (c) EBSD image showing grain orientation spread (GOS). Keys for GOS and HAGB are shown at right bottom. The compression axis is vertical to the micrographs.

Microstructures of unstable region: The processing map **(Figure 5.20)** exhibits a large domain of flow instability at strain rates higher than 10^{-1} s^{-1} in single α–phase and two phase (α+β) regions whereas, in the β–single phase region instability is observed above strain rates of 1.0 s^{-1}.

90

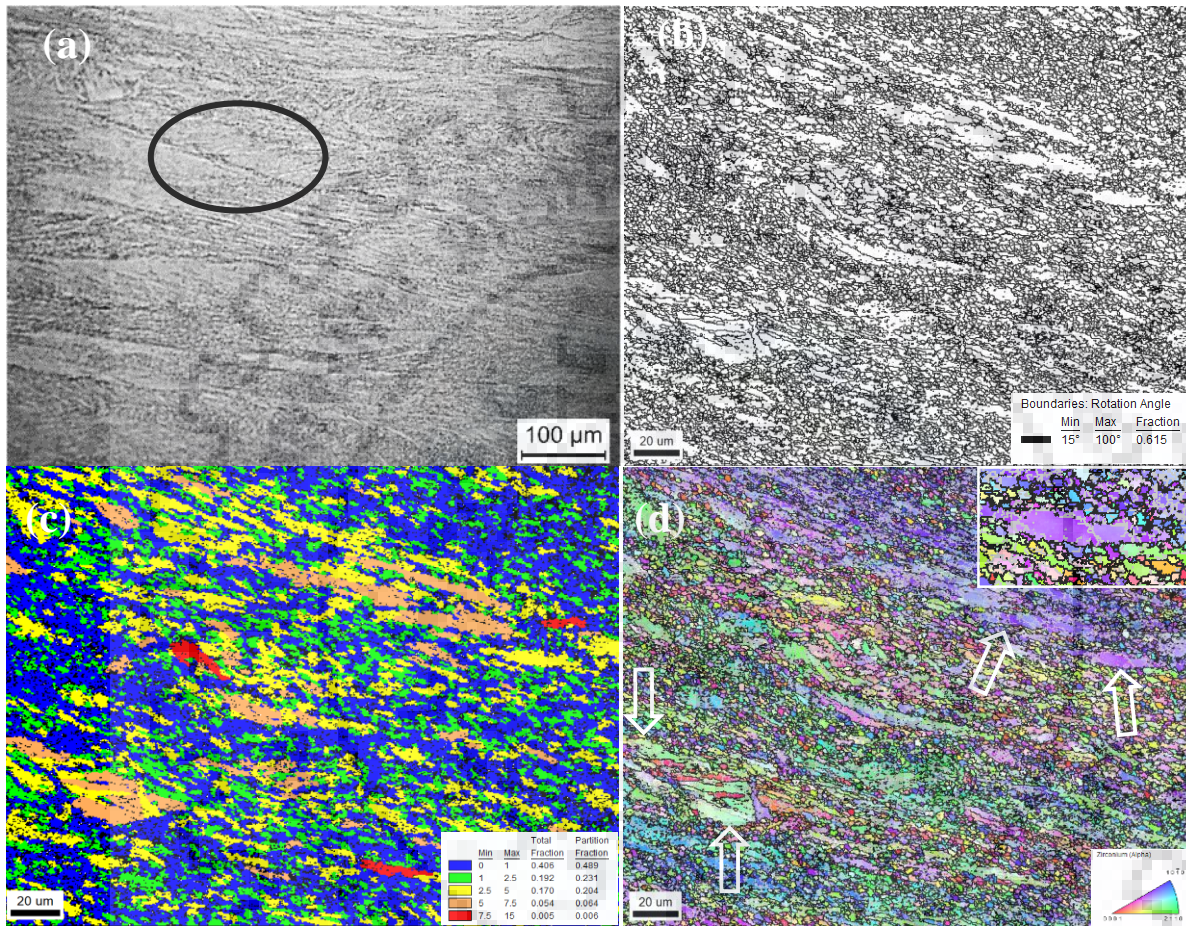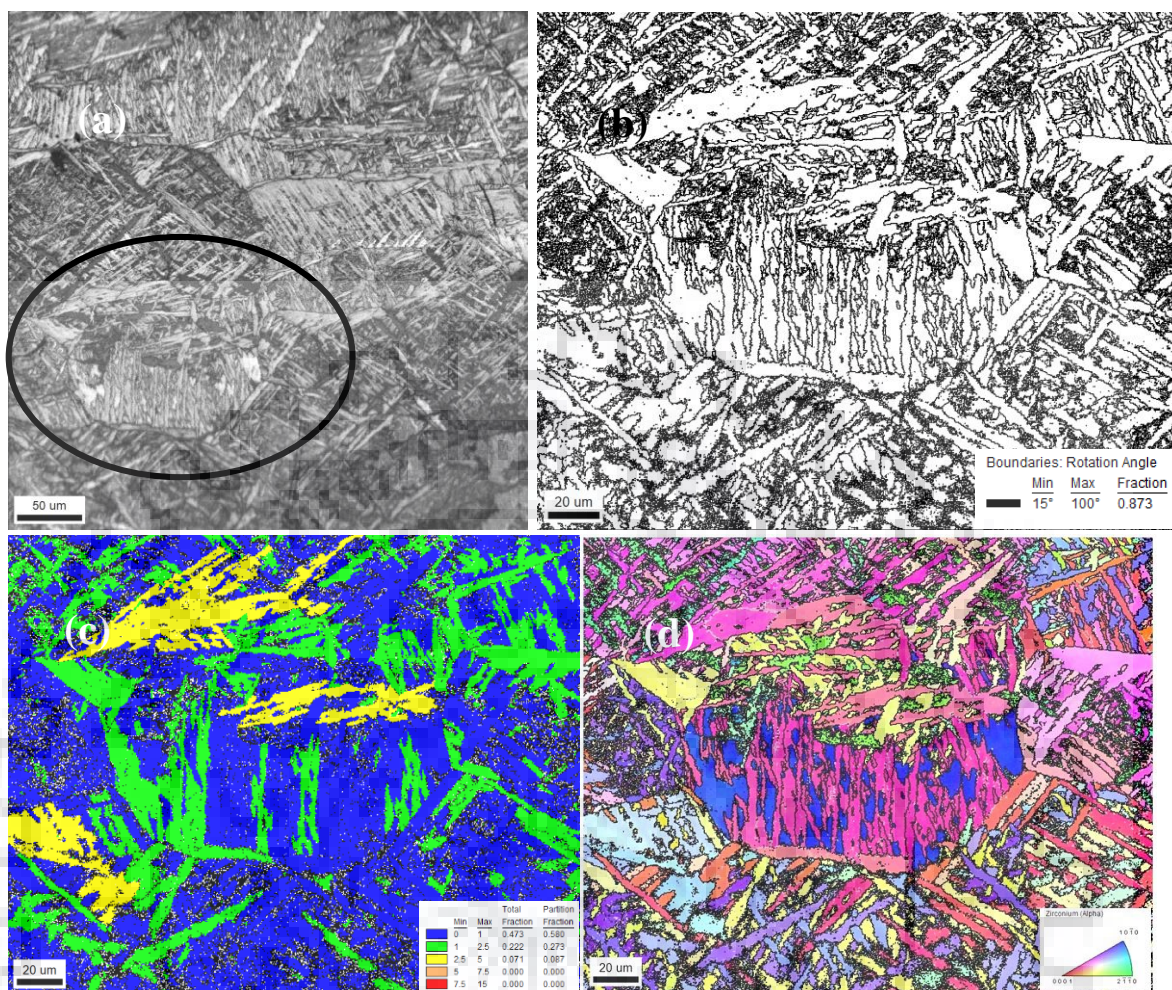**Figure 5.26**: Zr-1Nb extruded β quenched condition deformed at 1000°C / 10^{-2} s^{-1}, wherein processing map (**Figure 5.20**) predicts considerably high power dissipation efficiency of 0.40. The deformation temperature is in the single β phase region; (a) Image quality map (b) EBSD image showing high angle grain boundary map of the deformed sample, (c) EBSD image showing grain orientation spread (GOS) and (d) IPF map. Keys for GOS and HAGB are shown at right bottom. The compression axis is vertical to micrograph.

The optical micrograph **(Figure 5.27a)** revealed cracks and kinking of α plates, which are a sign of instability that was accurately predicted by the processing map **(Figure 5.20)**. It has been reported that in hot compression experiments, the direction of crack formation and shear band formation occurred at 45° to the compression direction [159]. Similar results of the kinking of α plate induced instability have been reported in the literature [157, 186, 187]. To understand the mechanism of kinking, IPF map was plotted for the sample of same deformation condition. **Figure 5.27b** presents the IPF map of the kinked α plates and illustrates the process of kinking. Kinking was a result of the strain build up from the corner of the grain to its centre, as revealed by the change in the orientation of the α plates. To clarify this observation, **Figure 5.27c** shows grain reference orientation deviation-angle (GROD) of the same region and we can see strain

accumulation at the centre, which is manifested by an increase in GROD. The GROD maps brings out distribution of local misorientation within a grain wherein smallest kernel average misorientation is taken as the reference orientation [188]. It appears that strain accumulation within the α plates reached a point where plates could not sustain the strain anymore and exhibited breaking of a large number of α plates in the form of a kink.
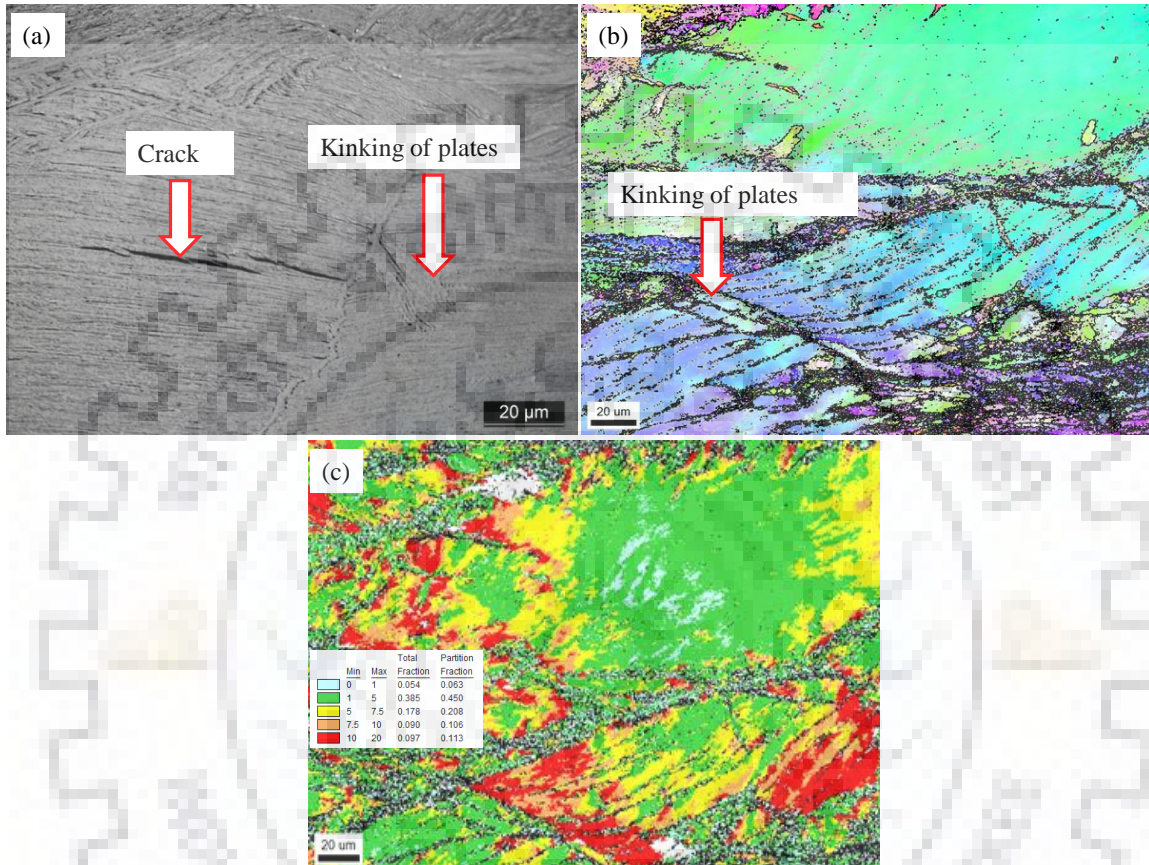
Figure 5.27: Inverse pole figure (IPF) map of the sample after deformation at 700°C / 10^{-1} s^{-1}. This deformation condition was in unstable region of the processing map (**Figure 5.20**). (a) Optical micrograph showing instability in the form of kink and crack, (b) IPF map showing kinking of α plates, (c) Grain reference orientation deviation-angle (GROD) map clearly bringing out the process of kinking by the accumulation of strain. The compression direction is vertical.

Figure 5.28 shows the microstructure of sample deformed at 850°C and strain rate of 1 s^{-1}, which belongs to two phase region of Zr-1Nb alloy. The deformation condition of 850°C/1 s^{-1} is in unstable domain of processing map **(Figure 5.20)**. The microstructure **(Figure 5.28)** revealed the formation of void in between the α plates. Void of similar shape was reported for Ti-6Al-4V alloy during hot deformation [189]. The formation of void can be attributed to deformation inhomogeneity between hard particles (i.e. α–phase) embedded in a soft matrix (i.e. β–phase). Moreover, hard particles do not deform at the same rate as does the matrix. Therefore, strain mismatch occurs around the hard particles, which may lead to cavity or void formation

92

[190]. The shape of void was reported to be spherical for smaller size and elliptical for larger ones [191].
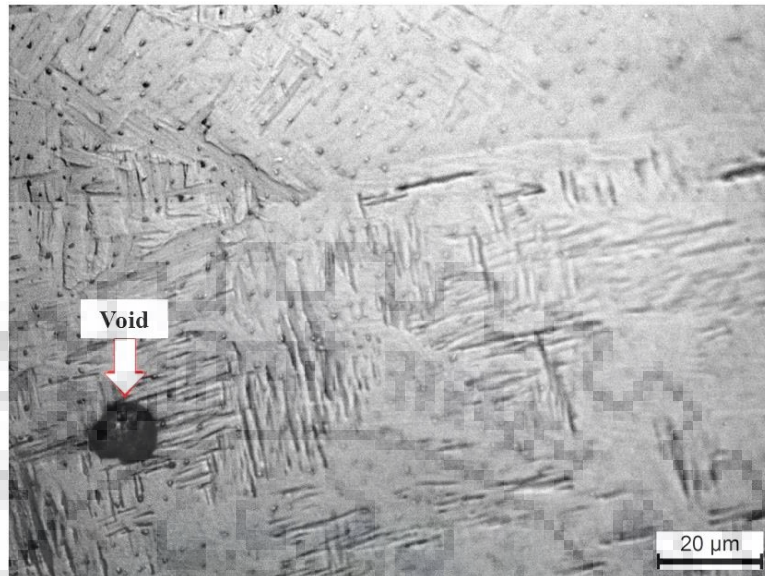
Figure 5.28: Optical microstructure of the sample deformed at 850ºC / 1 s⁻¹ showing void formation. The compression direction is vertical.

5.4.1.2 Swaged and annealed in α–phase region:

5.4.1.2.1: As received microstructure: Figure 5.29 shows microstructure of as-received or undeformed sample of the Zr-1Nb alloy swaged followed by annealing in single α–phase. Equiaxed α grains are clearly visible.
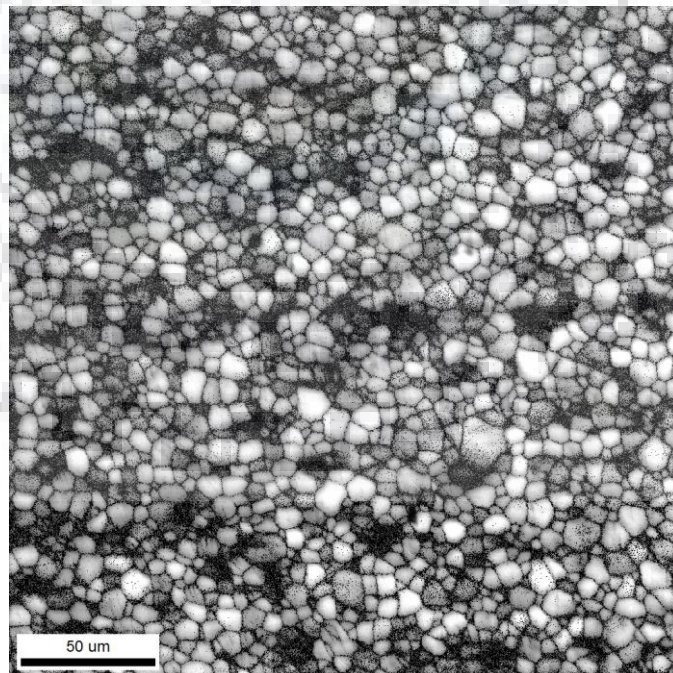
Figure 5.29: SEM micrograph (IQ map) showing as received microstructure of Zr-1Nb alloy swaged and annealed in single α–phase condition.

5.4.1.2.2: Deformed microstructure
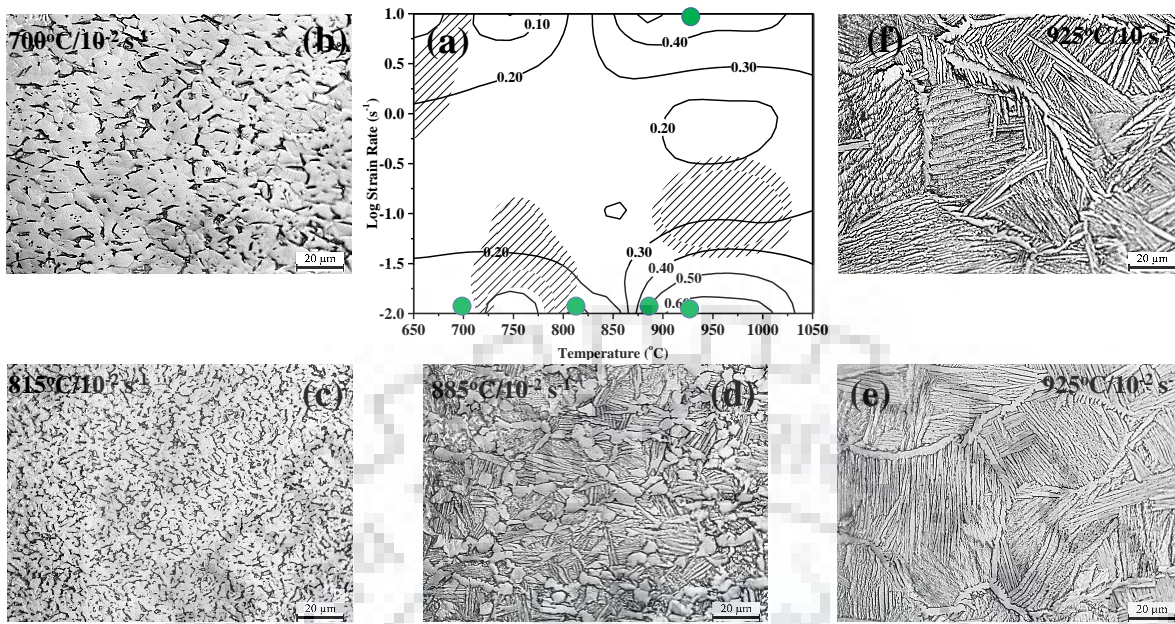
Figure 5.30: Processing map and selected deformed microstructures for Zr-1Nb alloy swaged and annealed condition; (a) processing map developed using DMM approach at true strain of 0.6 (reproduction of **Figure 5.10a**), (b) deformed microstructure at 700ºC/10^{-2} s^{-1}, (c) deformed microstructure at 815ºC/10^{-2} s^{-1}, (d) deformed microstructure at 885ºC/10^{-2} s^{-1}, (e) deformed microstructure at 925ºC/10^{-2} s^{-1} and (f) deformed microstructure at 7925ºC/10 s^{-1}. The dark etched network of β–phase after deformation in the Zr-1Nb alloy is clearly visible. Deformed samples were slow cooled from their corresponding deformation temperature. The compression axis is vertical.

In **Figure 5.30a**, processing map is reproduced from **Figure 5.10a** for the better understanding. From processing map, it is clear that the high efficiency domain lies around the temperature of 860 to 1050ºC at strain rate of 10^{-2} and 10 s^{-1}. In these domains the efficiency varies from 0.30 to 0.60. In single phase alpha region, although efficiency at 750ºC/10^{-2} s^{-1} (>0.30) is more than at 700ºC/10^{-2} s^{-1} (0.20-0.30), the sample deformed at 700ºC was preferred for microstructural analysis because at 750ºC processing map also predicted instability. In general, samples of high efficiency deformation conditions selected for microstructural characterizations.

The optical microstructure of the sample deformed at 700ºC / 10^{-2} s^{-1} is shown in **Figure 5.30b**. The deformation temperature of 700ºC lies in the single α–phase field. The microstructure at this deformation condition reveals deformed α grains surrounded by β–phase. The microstructure of sample deformed at 815ºC / 10^{-2} s^{-1} is shown in **Figure 5.30c**. This deformation temperature corresponds to start of two phase region. At this deformation condition, microstructure reveals fine α grains with higher fraction of β phase compared to the microstructure at 700ºC / 10^{-2} s^{-1}.

At deformation temperature of 885ºC and strain rate of 10^{-2} s^{-1}, the processing map (**Figure 5.30a**) reveals higher power dissipation efficiency of about 0.50. This deformation condition is

close to β transus temperature and has higher fraction of β–phase. The deformed microstructure (**Figure 5.30d**) exhibits primary α grains and α plates (transformed from β–phase). The microstructure (**Figure 5.30e**) of sample deformed at temperature of 925°C and strain rate of 10^{-2} s^{-1} reveals α plates and network of α phase at the prior β–phase grain boundaries. These plates are arranged in a parallel or near parallel fashion within the colony. In the prior β grain, many such colonies are observed. The deformation temperature of 925°C is in single β–phase and indicates that the growth of α plates (transformed from β–phase) is much faster in single β–phase compared to two phase region. The deformed microstructure at 925°C and strain rate of 10 s^{-1} is shown in **Figure 5.30f**. At this deformation condition, microstructure reveals similar features as observed at same deformation temperature but lower strain rate of 10^{-2} s^{-1}.

The processing map shown in **Figure 5.30a**, revealed small domains of unstable region compared to processing maps of other materials studied in this work. This could be due to the starting conditions of material. No evidence of instabilities was found in the deformed microstructures. It may be due to starting condition of material and the slow cooling after deformation.

To get the quantitative information such as volume fraction of α–phase and transformed β–phase (α plates), and the size of α plates, scanning electron microscopy (SEM) images were taken for the sample deformed in two phase region at selected strain rates. **Figure 5.31** shows scanning electron microscopy (SEM) images in backscattered mode of the selected deformation conditions in the two phase region. In SEM images, bright (white) portion represents the β–phase boundaries, whereas dark (black) portion is α–phase. The combined presence of the α–phase grains (primary α) and α plates (transformed from β–phase) are clearly visible in **Figure 5.31**, whereas a small fraction of β–phase along the grain boundaries of α and between inter-lamellar locations is also noticed.

Figure 5.31a clearly reveals very fine primary α with scattered β grain boundaries at a temperature that corresponds to start of two phase region and at lower strain rate (815°C/10^{-2} s^{-1}). At higher strain rate but same deformation temperature (i.e. 815°C/ $1s^{-1}$) in **Figure 5.31b**, microstructure reveals coarser primary α grains with fine features of α plates. At temperature of 850°C (**Figure 5.31c and 5.319d**), clear appearance of transformed β–phase into α plates and primary α at both the strain rates are visible. Microstructural morphology exhibited at temperature of 885°C (very close to β transus temperature) for both the strain rates (see **Figure 5.31e and 5.31f**) have similar features compared to the microstructure of sample deformed at 850°C, only the difference could be in shape and size of grains/plates. It seems that the grain size of primary α increases and the length and thickness of α plates decreases with increase in strain

rate, whereas on increasing deformation temperature length and thickness of α plates increases and primary grain size decreases, at least for samples deformed at 1 s^{-1}.
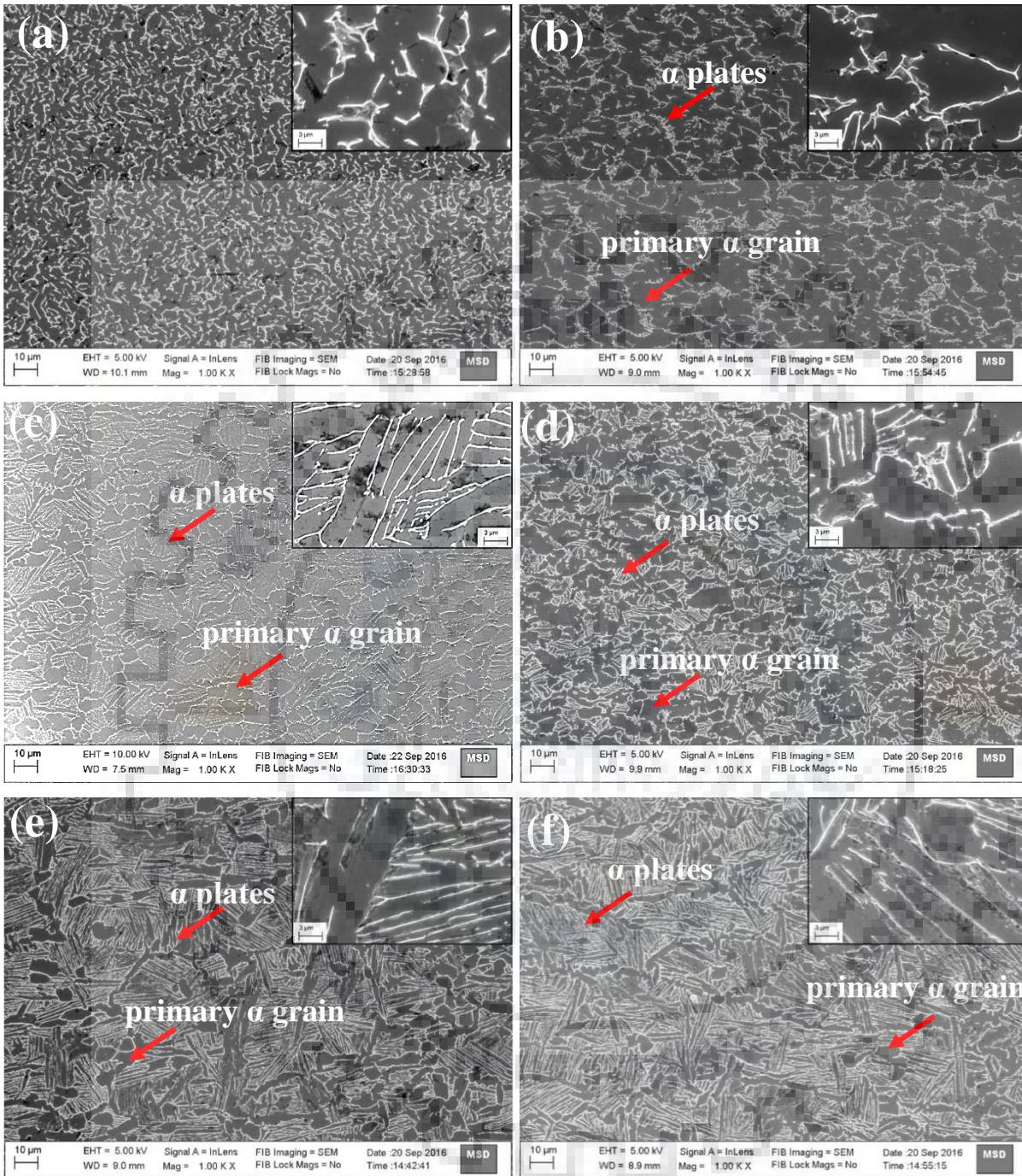
Figure 5.31: Backscatter electron images depicting the variation in microstructure at different deformation conditions in the two phase region: (a) 815°C/ 10^{-2} s^{-1}, (b) 815°C/ 1 s^{-1}, (c) 850°C/ 10^{-2} s^{-1}, (d) 850°C/ 1 s^{-1}, (e) 885°C/ 10^{-2} s^{-1} and (f) 885°C/ 1 s^{-1}. Higher magnification images are shown in the inset. The compression direction is vertical to image.

The scattering of β–phase and fine primary α–phase at 815°C/10^{-2} s^{-1} could have resulted from large strain partitioning to the softer β–phase, while the harder α–phase carries more stress. Owing to the bcc structure of β–phase, it is softer than the hcp structured α–phase. Due to the

soft nature of β–phase, it starts to deform more by accommodating most of the imposed strain in the initial stages of deformation. However, the low volume fraction of β–phase ensures that all the imposed strain cannot be accommodated by itself. With increasing plastic strain, as the β–phase strain hardens, the flow stress of both the phases may become comparable and strain could be partitioned by both the phases. The microstructure of the sample at the same temperature (815°C), but at higher strain rate (1 s^{-1}), is characterized by the presence of continuous β–phase. During high temperature deformation, with increase in strain rate the time available for recovery or recrystallization reduces and as a consequence, in spite of large of strain accommodated by the phases, they do not undergo substantial restoration processes. Such differences in the extent of DRV/DRX may explain the formation of fine features of β–phase at lower strain rate while continuous β–phase at higher strain rate [192, 193].

To understand the effect of deformation temperature on phase transformation, Radical$^®$ commercially available image analysis software is used for quantitative analysis to get the volume fractions of primary α–phase and transformed β and β–phase and this is shown in **Table 5.8**. It is clear from **Table 5.8** that the volume fraction of α–phase decreases as temperature increases and correspondingly volume fraction of α plates increases. At higher temperatures in two phase region (i.e. 850 and 885°C), strain rates have no significant influence on the phase transformation and shows more or less similar values of volume fractions.

The quantified results of α plate size are shown in **Table 5.9.** These are calculated using line intercept method from the SEM images. The fraction and the thickness of transformed α plates increases with deformation temperature, whereas the thickness of the plates is not much affected by the strain rate. It is worth to be mention that a constant soaking time of 5 mins was provided to all the samples. Therefore, there is no influence of soaking time on different deformation conditions. Only the soaking temperature is a parameter that affects the morphology of microstructure along with the rate of deformation. It is clear from **Figure 5.31** and **Table 5.9** that for two phase microstructure, decrease in α platelet thickness increases the peak stress (see **Figure 5.3d–5.3f**). Similar observation was reported by Semiatin and Bieler [253]. At lowest strain rate (10^{-2} s^{-1}), the same trend was observed in the microstructure of specimens deformed at 850°C and 885°C and the peak stress decreases with increase in the thickness of α plates. More clear morphology can be seen in the image quality map shown in **Figure 5.32**. It is reported that a higher soaking temperature (deformation temperature) increases the β–phase transformation and size of α–plates [41]. Only at the deformation conditions of 815°C/10^{-2} s^{-1}, microstructure seems to have negligible effects of transformation and is predominantly governed by the high

temperature deformation mechanisms. The volume fraction of transformed β–phase (α plate) affect the volume of α/β phase boundaries.

Table 5.8: Volume fractions (%) of primary α–phase and transformed β (α plate) and β–phase at different deformation conditions in the two phase region

Strain rate (s⁻¹)	10^{-2}		1	
Temperature (°C)	α–phase	Transformed β–phase (α plates) and β phase	α–phase	Transformed β–phase (α plates) and β phase
815	73	27	65	35
850	45	55	49	51
885	38	62	39	61
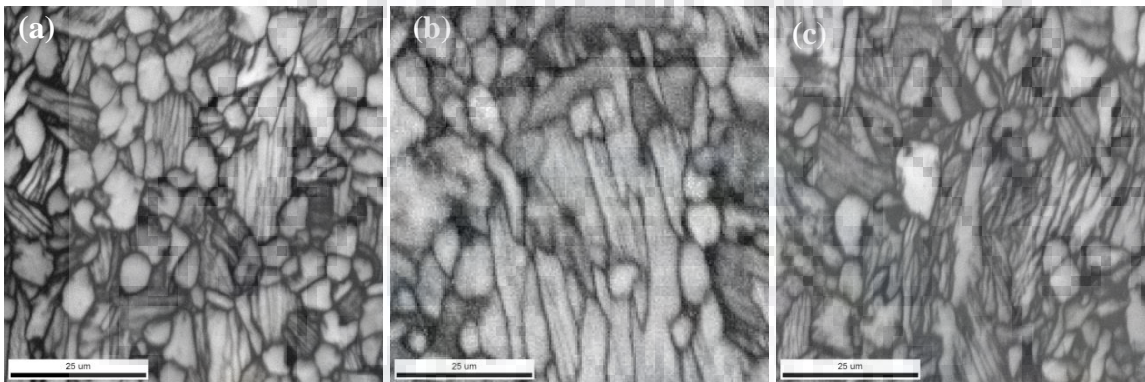
Figure 5.32: Image quality maps of specimens deformed using: (a) 850°C/ 10^{-2} s⁻¹, (b) 885°C/ 10^{-2} s⁻¹, and (c) 885°C/ 1 s⁻¹ conditions showing bimodal type microstructures consisting of primary α–phase and transformed α plates from β–phase

Table 5.9: Width of transformed β–phase (α plate) at different deformation conditions in the two phase region

Temperature (°C)\ Strain rate (s⁻¹)	Width of transformed β phase (α plate) (µm)	
	10^{-2}	1
815	No plate only serrated β phase boundaries	0.73
850	1.36	1.19
885	1.595	1.76

The trend of obtained results for volume fraction of each phase and the thickness of α plates obtained in this work is consistent with the reported work of Kulkarni et al. [126] for Zr-2.5Nb alloy. At 885°C, close to the β–transus, the microstructure has lower fraction of primary α–phase, as compared to other two temperatures of 815°C and 850°C. This effect can be attributed to the fact that closer to β transus temperature, the fraction of transformed microstructure increases with temperature [194].
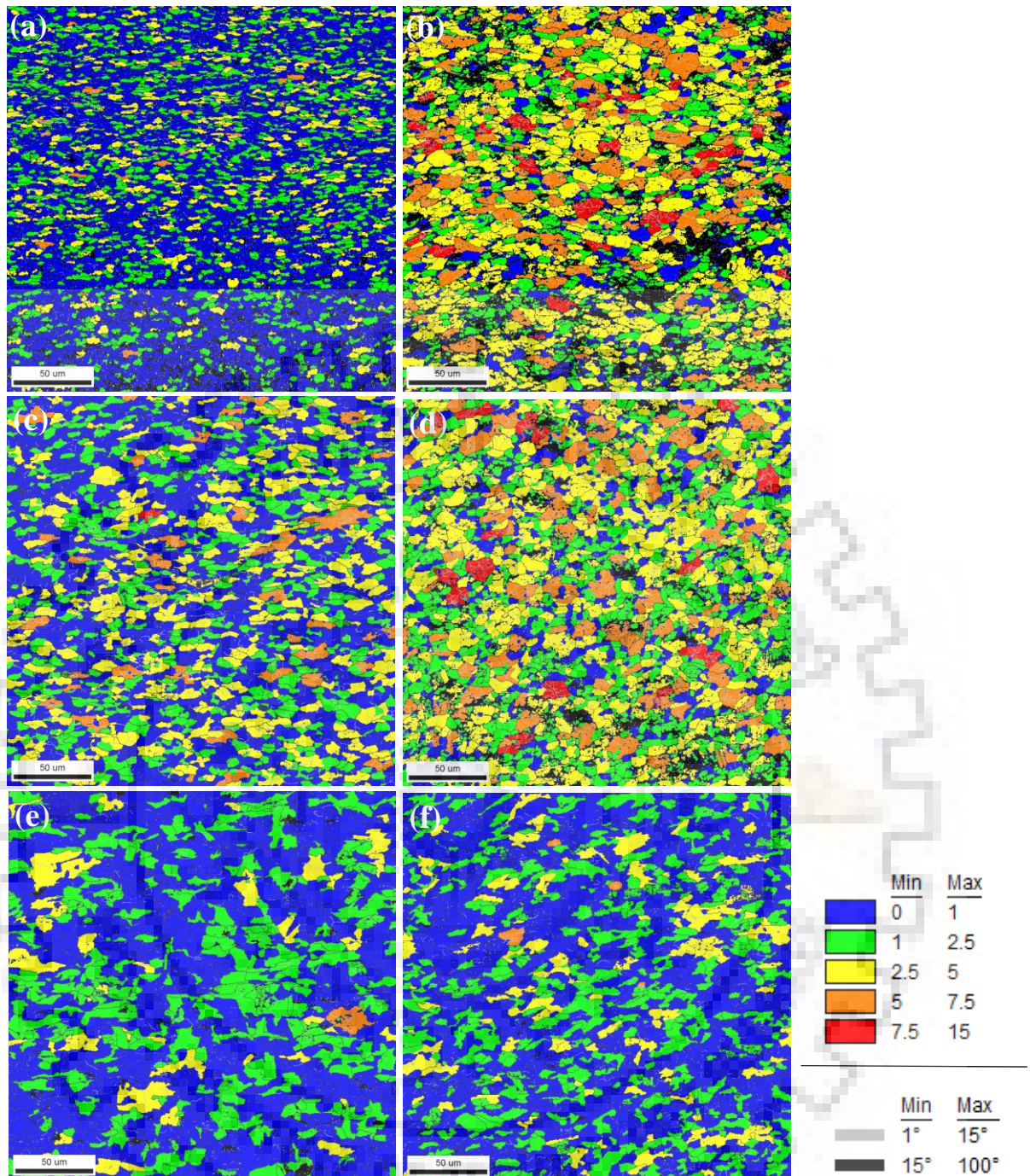
Figure 5.33: EBSD images showing grain orientation spread (GOS) along with high angle grain boundaries (HAGB) and low angle grain boundaries (LAGB) at different deformation conditions: (a) 815°C/ 10^{-2} s^{-1}, (b) 815°C/ 1s^{-1}, (c) 850°C/ 10^{-2} s^{-1}, (d) 850°C/ 1 s^{-1}, (e) 885°C/ 10^{-2} s^{-1} and (f) 885°C/ 1 s^{-1}. Keys for GOS, HAGB and LAGB are shown at the right bottom.

EBSD analysis: For better understanding of the occurrence of DRX, DRV and the evolution of deformation microstructure, the grain orientation spread (GOS) along with high and low angle grain boundaries at different deformation conditions in two phase region are presented in **Figure 5.33**. It is to be mentioned that the value of GOS is also an indicator for the intra-grain misorientation that could be directly correlated to the fraction of geometrically necessary

dislocations in a deformed sample [195, 196]. A higher GOS value is representative of deformed microstructure and a very low value that of recrystallized microstructure. The higher volume fraction of GOS<1º represents the dynamic recrystallization (DRX) in the microstructure, whereas GOS>2.5º represents only deformed microstructure after hot deformation. At strain rate of 10^{-2} s^{-1}, the volume fraction of grains with GOS<1º first decreases from 0.63 to 0.49 with increase in temperature from 815ºC (see **Figure 5.33a**) to 850ºC (see **Figure 5.33c**), and subsequently increased to 0.63 at 885ºC (see **Figure 5.33e**). Whereas at the strain rate of 1 s^{-1} it increases from 0.15 to 0.61 for temperatures of 815ºC (see **Figure 5.33b**) and 885ºC (see **Figure 5.33f**).

5.4.2 Zr-2.5Nb:

5.4.2.1 As received microstructure: **Figure 5.34** shows the microstructure of the as-received Zr-2.5Nb alloy in forged followed by β quenched condition. In **Figure 5.34**, very fine martensitic plates of α phase are surrounded by prior β grain boundaries. The average grain size of prior β grains is 350 μm.
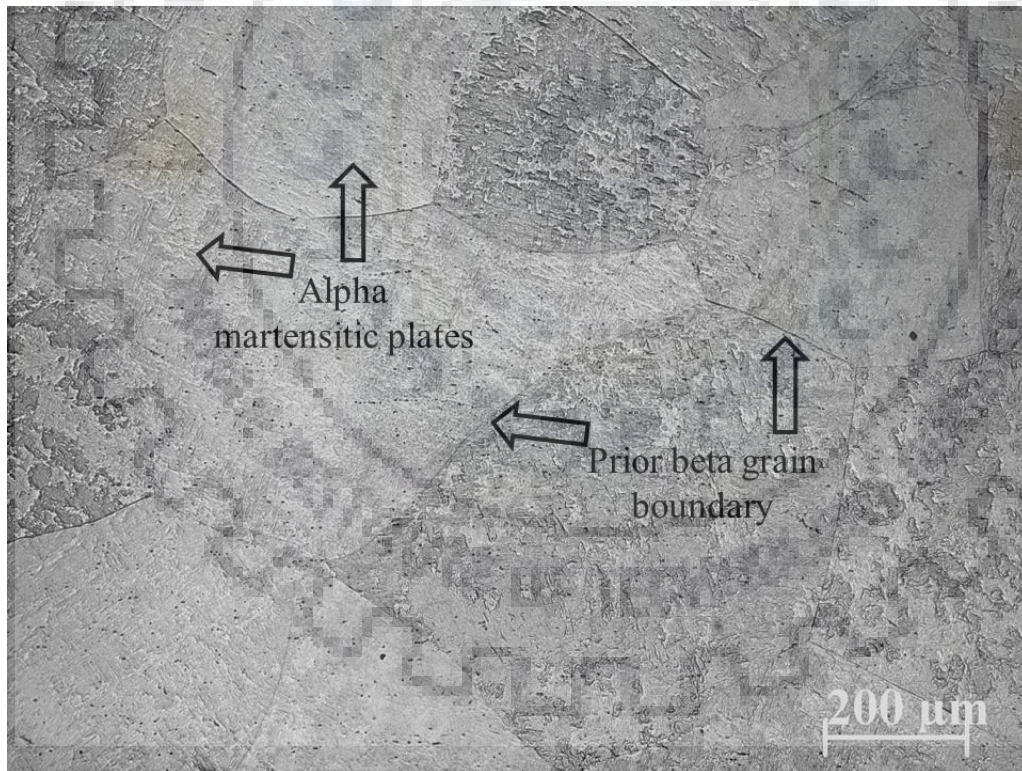
Figure 5.34: As received microstructure of Zr-2.5Nb alloy forged β–quenched condition. The average grain size is 350 μm. Very fine martensitic plates of α–phase are surrounded by prior β grain boundaries, as indicated by arrows.

5.4.2.2 Microstructure of deformed samples: Selected deformed samples were considered for microstructural observation from the deformation conditions predicted by processing maps (**Figure 5.11a**) developed using different materials models. The selected

deformation conditions were related to high dissipation efficiency and unstable regions of the processing maps. The microstructures are classified according to the dominant features observed.
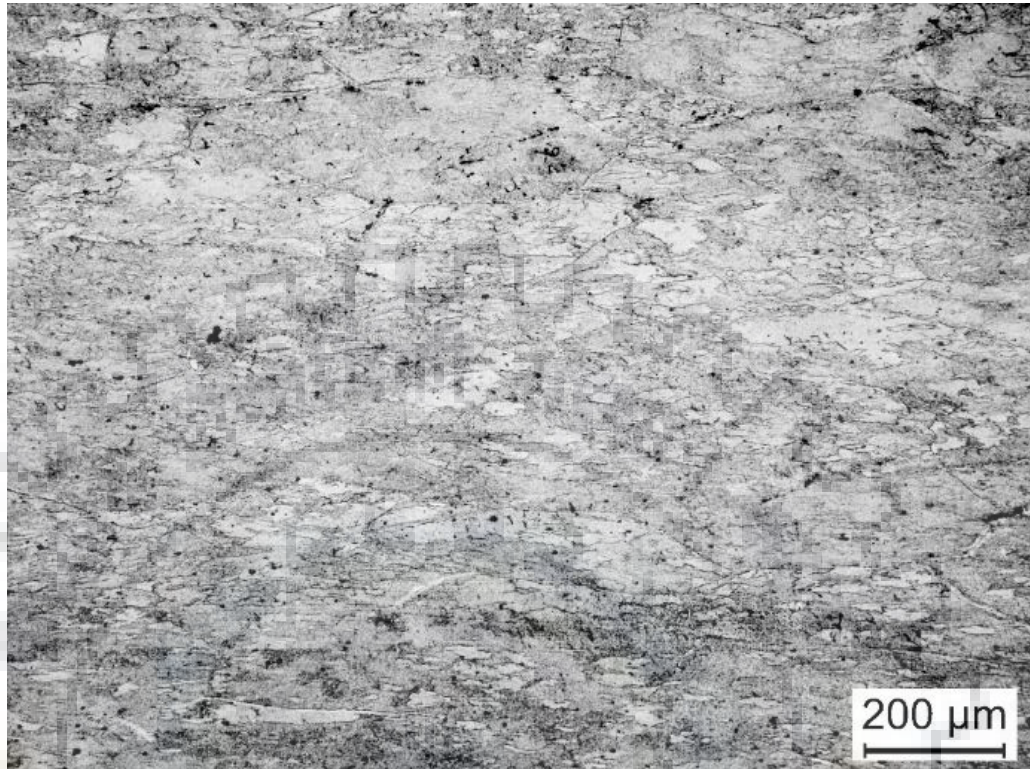
Figure 5.35: Optical micrograph of Zr-2.5Nb alloy, deformed at 700°C / 0.1s^{-1}. The axis of compression is vertical.
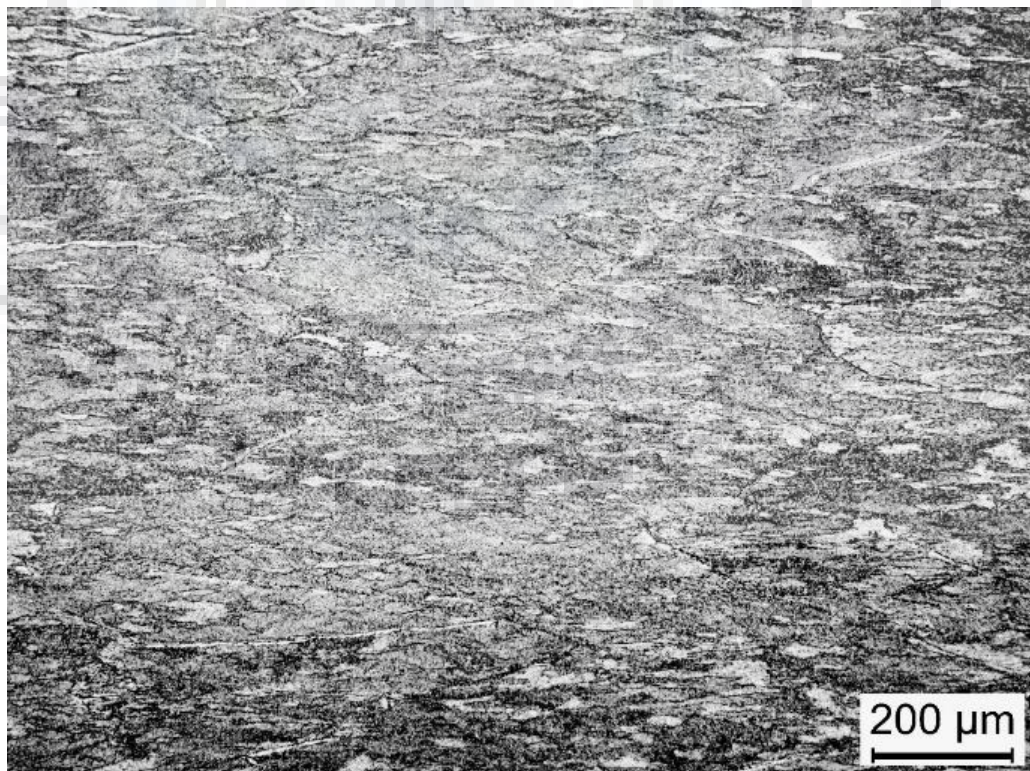
Figure 5.36: Optical micrograph of Zr-2.5Nb alloy, deformed at 750°C / 0.01s^{-1}. The axis of compression is vertical.
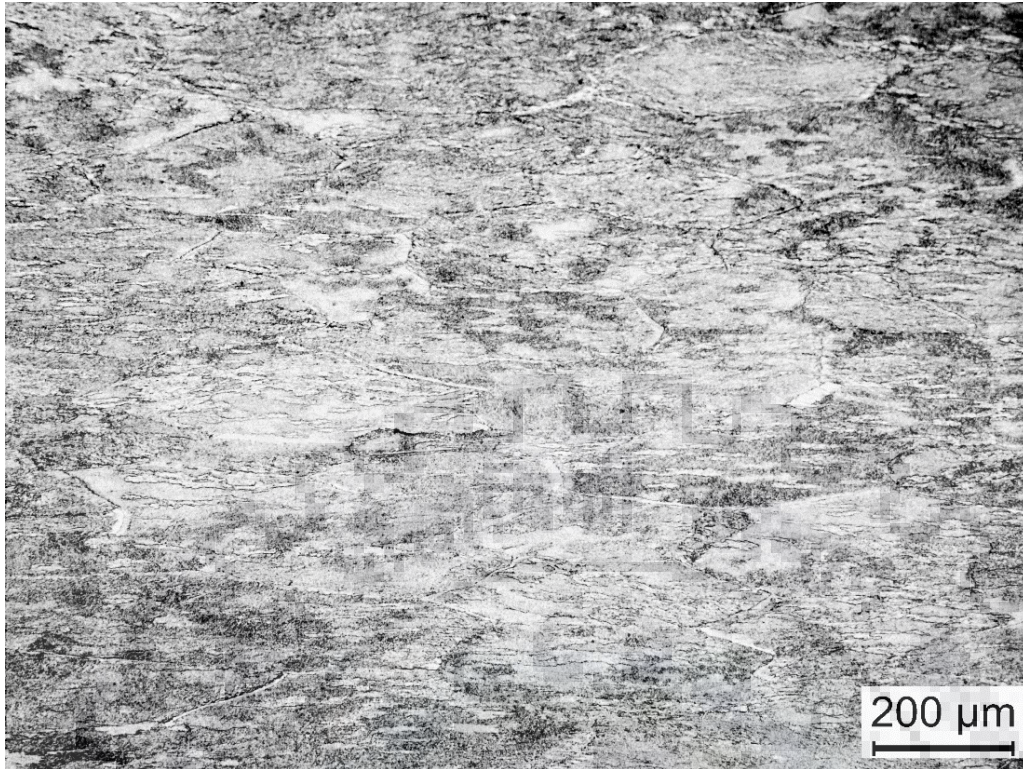
Figure 5.37: Optical micrograph of Zr-2.5Nb alloy, deformed at 750°C / 0.1s⁻¹. The axis of compression is vertical.
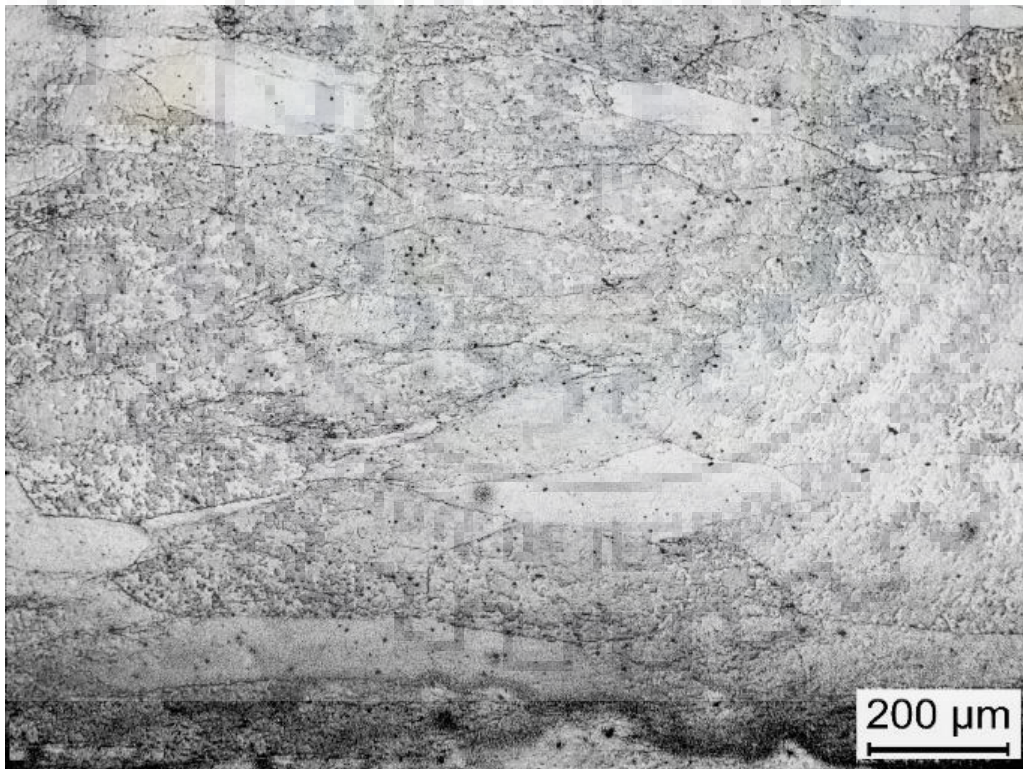
Figure 5.38: Optical micrograph of Zr-2.5Nb alloy, deformed at 925°C / 10s⁻¹. The axis of compression is vertical.

Dynamic recrystallization and dynamic recovery: **Figure 5.35-5.38** show the optical micrographs of samples after deformation at various deformation conditions. **Figure 5.35** shows recrystallized microstructure after deformation at the temperature of 700°C/ 10^{-1} s⁻¹ whereas,

Figures 5.36 and **5.37** show partially recrystallized microstructure after deformation at the conditions of 750°C/ 10^{-2} s^{-1}, and 750°C/ 10^{-1} s^{-1} respectively. DRX is a favorable condition for hot working since accompanied flow softening enhances the intrinsic workability.

For the above deformation conditions, power dissipation efficiency using DMM approach is found to be in the range of 35 – 45%. High efficiency in this range is reported to be associated with DRX in the Zr-2.5Nb alloy [67]. **Figure 5.38** shows the microstructure after deformation at the temperature of 925°C and strain rate of 10 s^{-1}. At this deformation condition, the grains appear elongated in the direction perpendicular to the compression axis. Although the models predict instability at this condition, no sign of instability was observed in the microstructure.

Flow localization / shear band formation: Microstructures shown in **Figures 5.39-5.41**, exhibit flow localization after deformation at conditions of 815°C/ 10 s^{-1}, 700°C/ 10 s^{-1} and 815°C/ 1 s^{-1}. The flow localization bands are lying at 30 – 45° to the direction of compression. Flow localization is usually associated with localized adiabatic heating at higher strain rates and is found to lie in the direction of maximum shear strain.

Void formation: **Figures 5.39-5.40, 5.42** show formation of void at the deformation condition of 815°C (10 s^{-1}), 700°C (10 s^{-1}) and 925°C (1 s^{-1}). The same deformation conditions have been reported by Raj maps for the formation of void [70]. Void formation is due to deformation inhomogeneity between hard particle (i.e. α–phase) embedded in a soft matrix (i.e. β–phase). Adiabatic heating during shear band formation also leads to the formation of void coalescence [197]. Shape of void was reported to be spherical for smaller size and elliptical for larger ones [191, 197].

Crack generation: Microstructure shown in the **Figure 5.43** exhibits cracks within a grain at the deformation condition of 850°C / 5 s^{-1}. The direction of this crack is in the direction of compression. At 850°C, the equilibrium structure consists of a large fraction of the β–phase and a very small fraction of α–phase. It has been reported that the α–phase is harder than β–phase, and the harder α–phase will essentially behave as second phase particles in the softer β–phase matrix [198]. Incompatibility in the strain between the soft matrix (β) and the hard phase (α) may nucleate a crack.
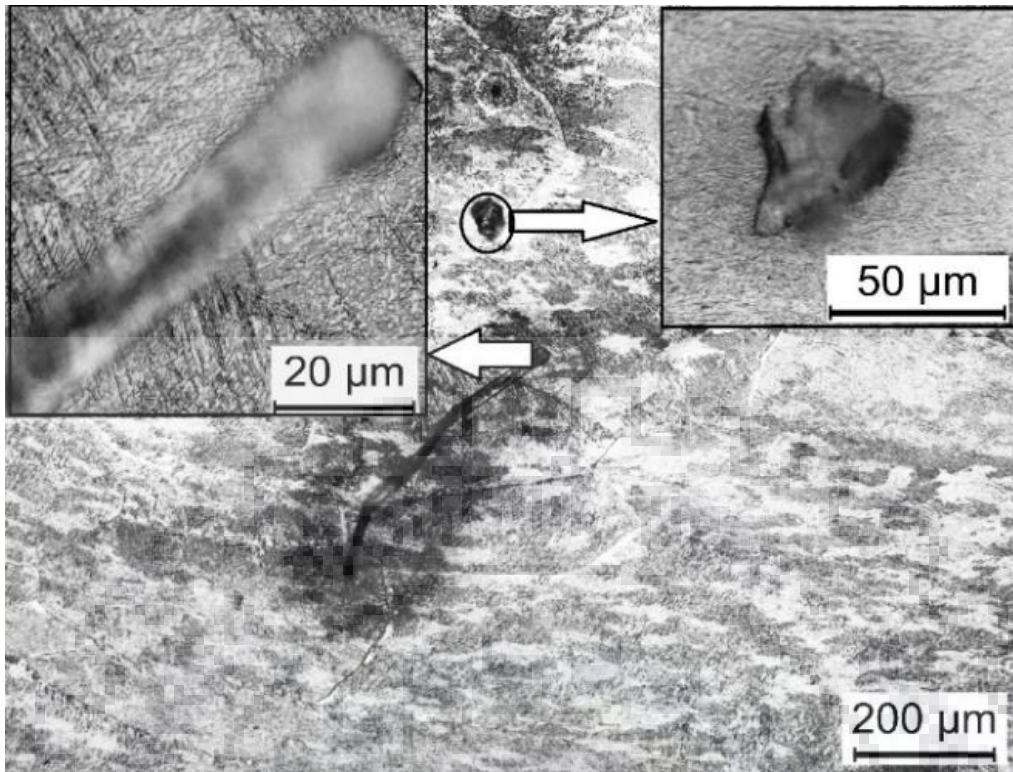
Figure 5.39: Optical micrographs of Zr-2.5Nb alloy after deformation exhibiting instabilities in the form of void and flow localization at 815°C and strain rate of 10 s⁻¹. Axis of compression is vertical.
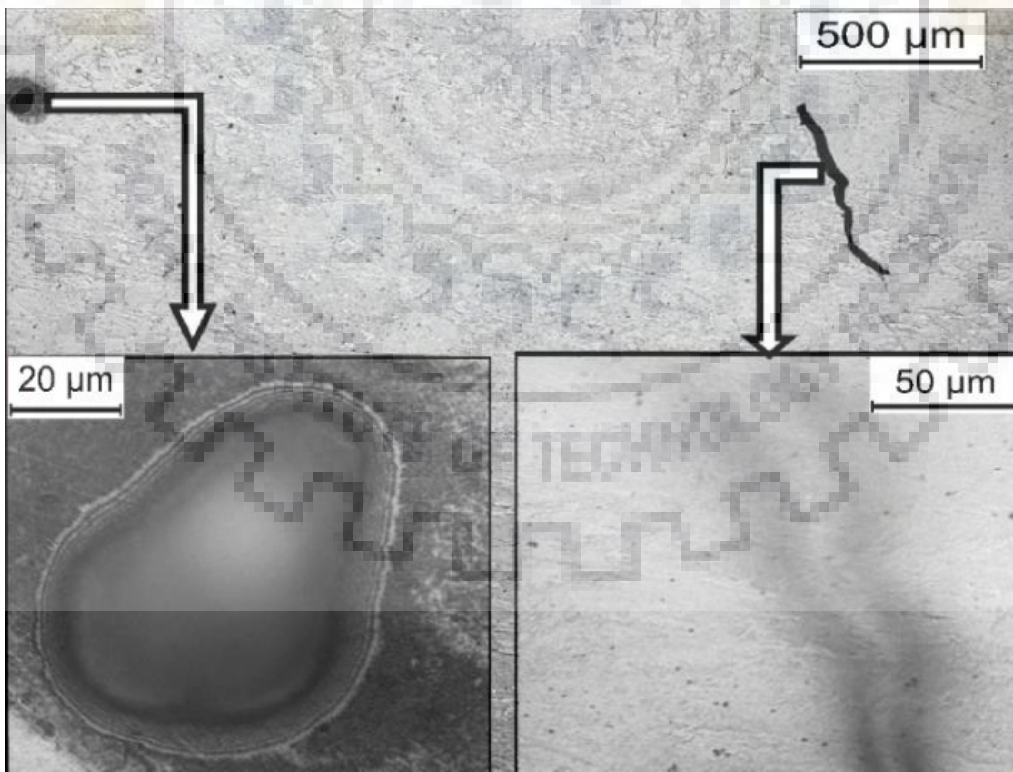
Figure 5.40: Optical micrographs of Zr-2.5Nb alloy after deformation at 700°C/ 10 s⁻¹ exhibiting instabilities in the form of void and flow localization. Axis of compression is vertical.
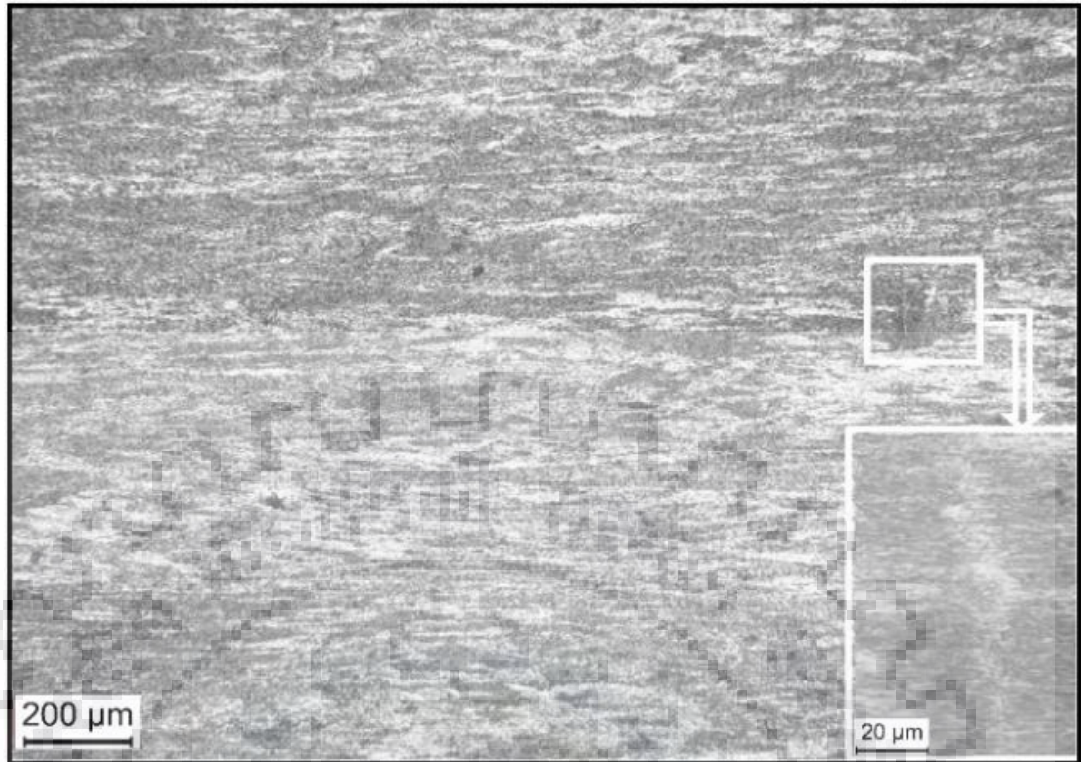
Figure 5.41: Optical micrographs of Zr-2.5Nb alloy after deformation at 815°C/ 1 s^{-1} exhibiting instabilities in the form of flow localization. Axis of compression is vertical.
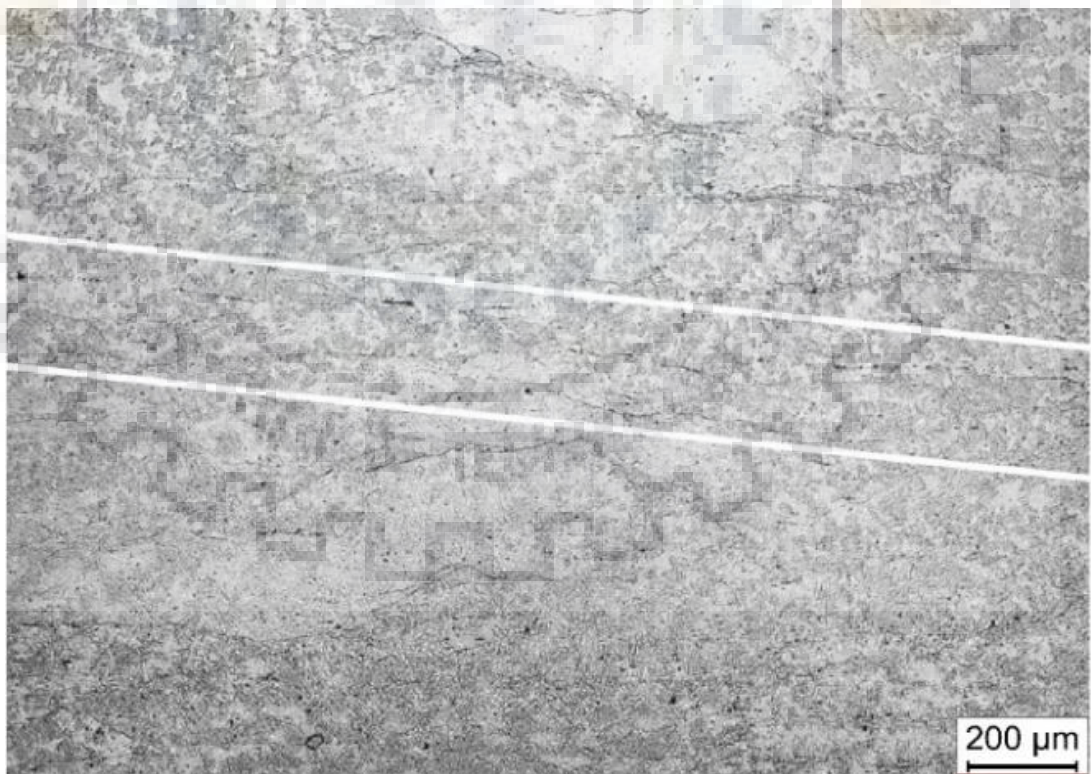
Figure 5.42: Optical micrographs of Zr-2.5Nb alloy after deformation at 925°C/ 1s^{-1} exhibiting instabilities in the form of cavity stringers (highlighted by two parallel lines) and elongated grains. Axis of compression is vertical.
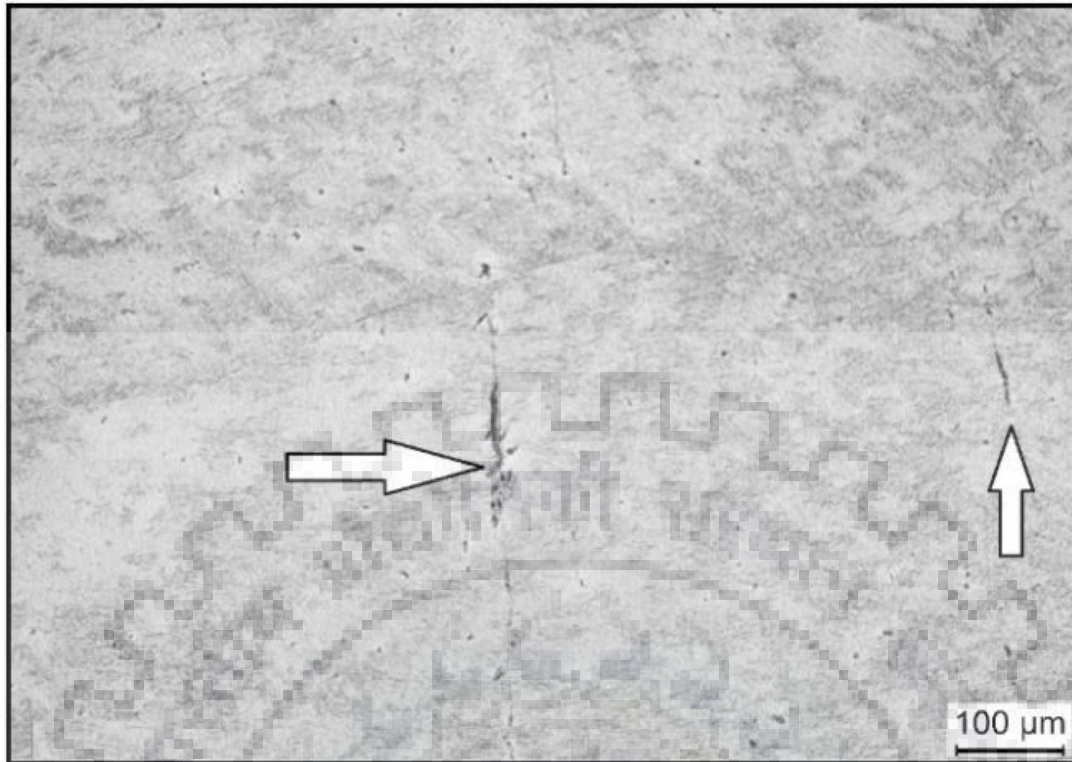
Figure 5.43: Optical micrographs of Zr-2.5Nb alloy after deformation at 850°C / 5 s^{-1} exhibiting instabilities in the form of intergranular cracks along compression axis. Axis of compression is vertical.

5.5 MECHANICAL PROPERTIES USING SMALL PUNCH TEST (SPT):

The small punch test was conducted at room temperature and Zr-1Nb alloy with swaged and annealed condition was considered as candidate material. For SPT, selected deformation strain rates were considered in the two phase region at all three different deformation temperatures. Out of four strain rates reported in the **Section 5.1.1.2**, two strain rates i.e. 10^{-2} and 1 s^{-1} were selected for further analysis of mechanical properties based on two considerations; (i) these two strain rates represent different deformation mechanisms as explained in **Section 5.1.1.2**, (ii) both the strain rates show efficiency of more than 30% in the processing map (**Figure 5.10a**).

The results of SPT are in terms of yield load (P_y) vs displacement (δ) and maximum load (P_m) vs displacement (δ), and are schematically shown in **Figure 4.8a**. Different yield load and maximum load values of sample tested were found based on their processing conditions and are presented in **Figure 5.44a** and **5.44b** respectively. Yield load of the undeformed (as received) sample was 38.33 N. The yield load value (**Figure 5.44a**) of hot deformed samples is increased for all deformation conditions except 815°C/ 10^{-2} s^{-1}, where this value reduced to 34.7N. An appreciably high value of yield (**Figure 5.44a**) and maximum load (**Figure 5.44b**) is obtained for the sample deformed at condition of 815°C/ 1s^{-1}. The sample deformed at other conditions

reveals moderate increment in the value of yield and maximum load compared to the as received sample. **Figures 5.44a** and **5.44b** reveal that as the temperature increases in two phase region, the value of yield load and maximum load decreases at the strain rate of 1 s^{-1}, whereas at the strain rate of 10^{-2} s^{-1} it increases. The yield load and maximum load is higher at strain rate of 1 s^{-1} as compared to strain rate of 10^{-2} s^{-1} for all the deformation temperatures, but at temperature of 885°C, lower strain rate (10^{-2} s^{-1}) shows higher value in yield and maximum load. Similar value of maximum load is observed for the samples deformed at 850°C and strain rates of 10^{-2} s^{-1} and 1s^{-1}.
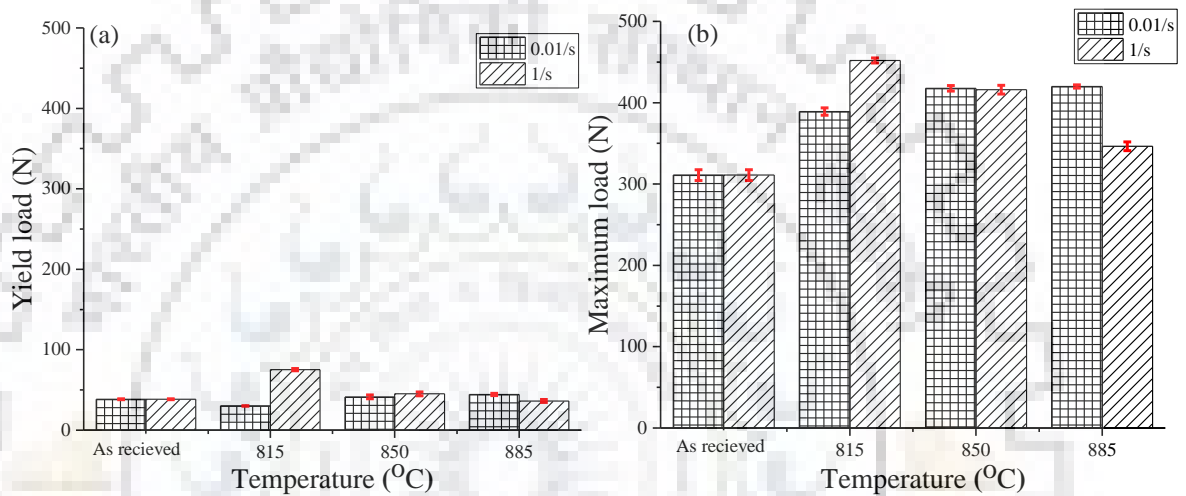
Figure 5.44: Small punch test (SPT) results of samples deformed at different processing conditions: (a) yield load, and (b) maximum load

6

DISCUSSION

6.1 PROCESSING MAP:

From the results presented in **Section 5.2**, it is quite clear that the predictions of processing maps developed using different materials models are not common for any of the Zr-Nb alloys. The efficiency values and unstable deformation conditions predicted by each model lie at different processing conditions. Moreover, the processing map approach is not able to provide complete information in the two phase region, i.e. which phase is dominating during the hot deformation. Therefore, discussion in this section is divided in two sub-sections. (i) **Section 6.1.1** deals with the determination of appropriate materials model/ approach for Zr-Nb alloys, taking Zr-2.5Nb as candidate material. (ii) **Section 6.1.2** deals with the identification of dominant phase during hot deformation in the two phase region for which Zr-1Nb was selected as candidate material.

6.1.1 Evaluation of various processing maps: To corroborate the observations obtained from processing maps **(Figure 5.11)**, microstructures of selected deformation condition were presented in **Section 5.4.2.2**. Deformation conditions were selected where the processing maps exhibit high efficiency of power dissipation or instabilities. The microstructures of material after deformation at 700°C and strain rate of 0.1 s^{-1} and, 750°C and strain rates of 0.01 and 0.1 s^{-1} were compared in **Figures 5.35-5.37**. The microstructure of the sample deformed at the temperature of 700°C and strain rate of 0.1 s^{-1} shows recrystallized grains whereas samples deformed at 750°C and strain rates of 0.01 – 0.1 s^{-1} show partially recrystallized equiaxed grains.

During high temperature deformation, instability occurs in the form of flow localization, shear band formation and adiabatic heating [199]. Identification of deformation conditions that lead to instability is important for materials processing. However, instability domains predicted by different material models does not agree with each other [200]. Most of the work reported on Zr-2.5Nb considered DMM to predict instability. In this work, instability criteria of different models are compared to understand their applicability to Zr-2.5Nb alloy. Comparison of instability regions obtained from different models suggests that MDMM is the most conservative model. The MDMM predicts flow instability domains at high strain rate range of 0.1 – 10 s^{-1} for all deformation temperatures. Further, it covers all instability domains suggested by DMM and *α–parameter* except a domain predicted by *α–parameter* at lower temperature.

Table 6.1: Comparative summary of the safe and unsafe domain predicted by different models along with the description of microstructure at the same deformation condition.

Deformation condition	DMM (Prasad et al.) Power efficiency	MDMM (Murty & Rao) Power efficiency	α-parameter (Jonas et al.)	Microstructure at the conclusion of deformation	Models with accurate prediction
700°C (0.1s⁻¹)	35% Stable region	41-45% Partially stable region	Unstable region	Recrystallization (Fig. 5.36) Safe	DMM
750°C (0.01s⁻¹)	40-45% Stable region	35-38% Stable region	Stable region	Partial Recrystallization (Fig. 5.37) Safe	DMM / MDMM / Alpha parameter
750°C (0.1s⁻¹)	35% Stable region	45-47% Stable region	Unstable region	Partial Recrystallization (Fig. 5.38) Safe	DMM
925°C (1s⁻¹)	30% Unstable region	45-48% Unstable region	Stable region	Cavity stringers and elongated grains (Fig. 5.43)	DMM / MDMM
925°C (10s⁻¹)	10% Unstable region	31% Unstable region	Unstable region	Elongated grains (Fig. 5.39) Safe	All models failed
700°C (10s⁻¹)	30% Unstable region	34% Unstable region	Unstable region	Void and flow localization (Fig. 5.41) Unsafe	DMM / MDMM / Alpha parameter
815°C (1s⁻¹)	30-35% Partially stable region	48-52% Unstable region	Stable region	Flow localization (Fig. 5.42) Unsafe	DMM / MDMM
850°C (10s⁻¹)	15-20% Unstable region	31-34% Unstable region	Stable region	Void and flow localization (Fig. 5.40) Unsafe	DMM / MDMM
850°C (5s⁻¹)	20-25% Unstable region	36-41% Unstable region	Stable region	Crack formation (Fig. 5.44) Unsafe	DMM / MDMM

To validate the instability suggested by different material models, microstructures of specific deformation conditions were selected for comparison. **Table 6.1** summarizes microstructural observations and predictions by different models for selected deformation conditions. It is clear that for some deformation conditions, predictions of different models are not corroborated by microstructural observations. Comparison between different models suggests that DMM however, predicted correctly for most of the selected deformation conditions. Interestingly deformation at the temperature of 925°C and strain rate of 10 s⁻¹ is predicted as unsafe by all the three models but microstructural observation suggests otherwise. It appears that it is difficult to capture local deformation peculiarities by any model. Still, we can say that for Zr-2.5Nb alloy, DMM is the most accurate model to predict safe deformation conditions.

6.1.2 Dominant phase in the two phase region:

In the **Section 5.4.1.1.2** titled as **deformed microstructure** of Zr-1Nb alloy extruded β quenched condition, the microstructural analysis was carried out for selected deformation conditions, where the processing map predicted either maximum power dissipation efficiency or instability. At deformation condition of 815°C/10^{-2} s⁻¹, analysis of processing map (**Section 5.2.1.1**) revealed lower power dissipation efficiency whereas, microstructural analysis (**Section 5.4.1.1.2**) showed fine recrystallized grains (**Figure 5.23**) with recrystallization fraction of around 0.62 (GOS < 1°). However, recrystallization belongs to the high efficiency domain of a processing map [62]. This is in direct disagreement with the prediction of the processing map (**Figure 5.9a**), which predicted lower efficiency at 815°C/10^{-2} s⁻¹. Thus, the processing map developed using experimental data was found to be deficient in the prediction of correct deformation mechanism at certain deformation conditions. Also, there is discontinuity in iso-efficiency contours at the temperatures where phase change is expected (or near the phase transus temperature). This is reported for other alloys as well [10, 58]. Since the processing maps were generated considering only the flow stress data without including any microstructural input, therefore, the discontinuity can be attributed to change in the phase fraction at different temperatures. To overcome the above mentioned deficiencies, the processing map in the present work was also developed using calculated flow stress data in the two phase region. The flow stress values were calculated by incorporating the information of the phase fractions of individual phases and their respective flow stress values. This is detailed in the following section.

6.1.2.1 Calculation of flow stress in the two phase region: Flow stress values of α–(σ_{α}^{c}) and β–(σ_{β}^{c}) phases in the two phase region were calculated by extrapolation of the flow stress values of the single phase regions in to the two phase region. Log transformed flow stress values

were plotted as a function of inverse of the temperature as, $\ln \sigma \ vs \ \dfrac{1}{T(K)}$ and a linear relationship was fit to obtain the extrapolated flow stress values. The general equation, which was used to extrapolate flow stress is shown in **Equation 6.1**, where C_1 and C_2 are the constants, unique to strain rates. The flow stress in the two phase region ($\sigma^{Cal}_{(\alpha+\beta)}$) was calculated according to **Equation 6.2.** For **Equation 6.1** to be valid, the deformation was assumed to be under equi-strain conditions. This assumption and the adopted procedure was validated by comparing the calculated values of the flow stress ($\sigma^{Cal}_{(\alpha+\beta)}$) with the experimental values in the two phase region (**Figure 6.1**). As is demonstrated by R^2 values in **Figure 6.1**, the flow stress values ($\sigma^{Cal}_{(\alpha+\beta)}$) calculated using extrapolated method are in agreement with the experimental data.

$$ln \ \sigma = C_1 \ \frac{1}{T} + C_2 \tag{6.1}$$

$$\sigma^{Cal}_{(\alpha+\beta)} = f_\alpha \sigma^c_\alpha + f_\beta \sigma^c_\beta \tag{6.2}$$
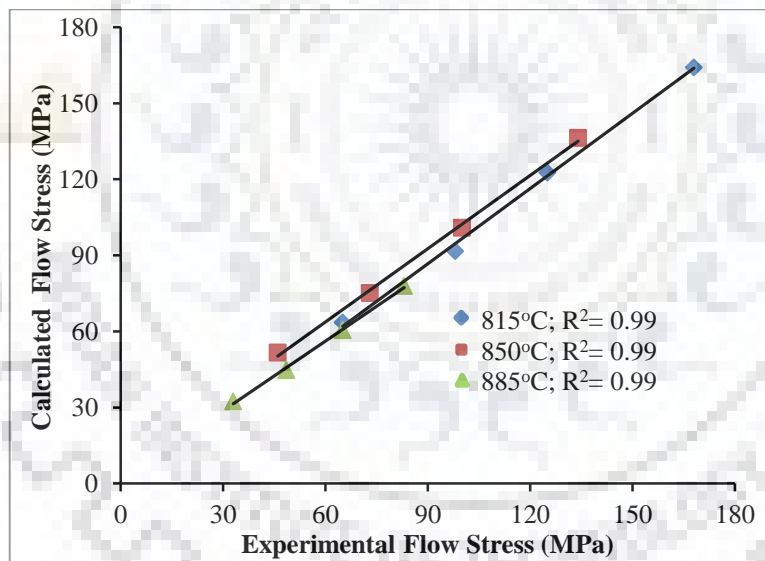
Figure 6.1: Comparison of experimental flow stress values with calculated flow stress values in the two phase region. Calculated flow stress values were obtained using **Equations 6.1** and **6.2.**

6.1.2.2 Development of processing map using calculated flow stress in the two phase region: The processing map developed using calculated flow stress data is shown in **Figure 6.2**. Single domain of highest efficiency of 0.44 was obtained in the temperature range of $670 - 860^oC$ and strain rate of $10^{-2} \ s^{-1}$, effectively combining the two domains (D-1 and D-2) of **Figure 5.9a**. The other domain (D-3) of high efficiency of 0.40 was observed in the temperature range of $970 - 1050^oC$ and strain rate of $10^{-2} \ s^{-1}$. In **Figure 6.2**, instability occurs in the entire range of

deformation temperature when the strain rate is 10^{-1} s^{-1} or greater. A comparison of **Figures 5.9a** and **6.2** leads to the following observations; (i) there is a discontinuity in the efficiency contours at the start of two phase region in **Figure 5.9**, which disappeared in **Figure 6.2**, (ii) the efficiency contours in the single phase regions are similar. Microstructural analysis in **Section 5.4.1.1.2** corroborates the above observations.
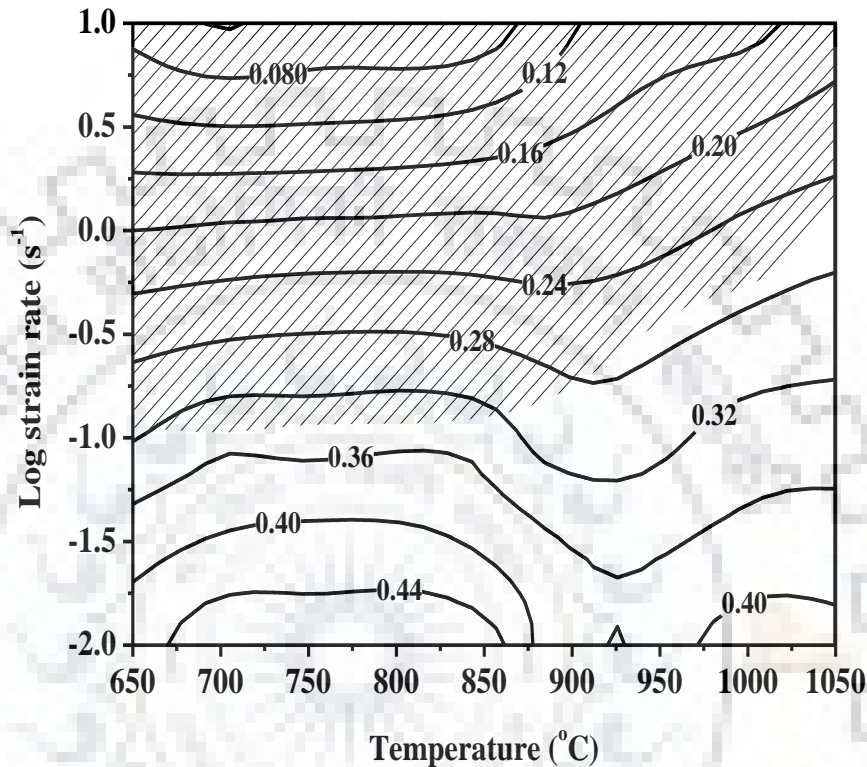
Figure 6.2: Processing map developed using calculated flow stress values obtained using **Equations 6.1 and 6.2**. Contours showing power dissipation efficiency, whereas shaded region represents instability. The high efficiency domain is extended from single phase to two phase region.

Thus, the processing map shown in **Figure 6.2** is more accurate in predicting processing conditions for efficient hot deformation processes than **Figure 5.9a**. However, both the processing maps (**Figures 5.9a and 6.2**) are not able to distinguish the contribution of the individual phases in the two phase region. For example, if a processing map exhibits high efficiency in the two phase region, then it is not clear which phase is undergoing high efficiency deformation processes (e.g. DRX). To address this, issue a different approach for plotting processing map is suggested in the following section.

6.1.2.3 Identification of dominant phase in the two phase region using processing maps approach: To understand the role of individual phases in the two phase region, flow stress values were extrapolated from each of the single phase regions into the two phase region, and were used. The extrapolated flow stress data of single phase α–phase and β–phase was then used

113

to develop the power dissipation map so as to distinguish the efficiency of individual phases in the two phase region.
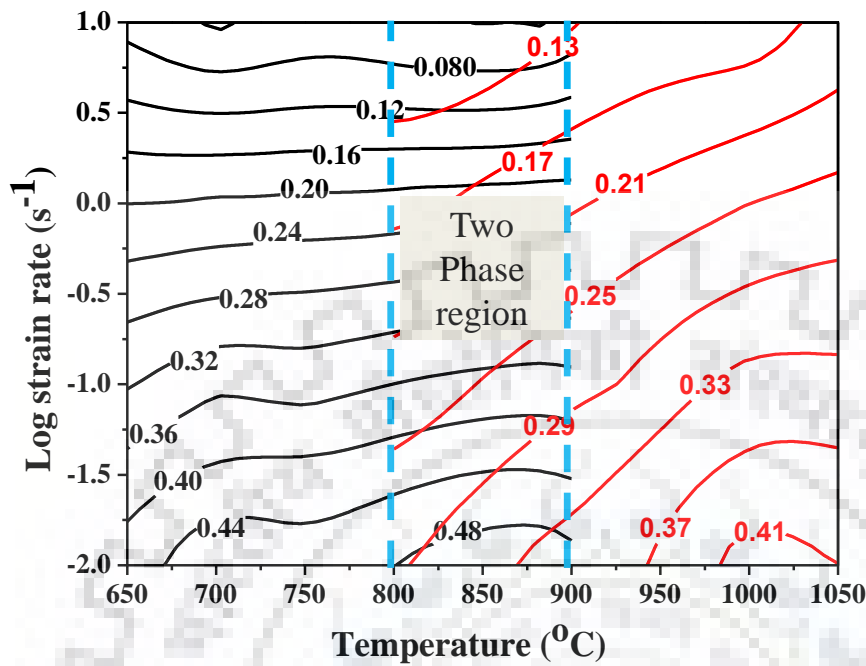
Figure 6.3: Superimposed power dissipation maps of α and β–phases in the two phase region. Black lines contours are showing the efficiency of α–phase, whereas red lines represent the efficiency of β–phase.

The superimposed power dissipation map of α–phase and β–phase, using extrapolated data of each phase (i.e. α–phase and β–phase) in the two phase region is shown in the **Figure 6.3**. The deformation conditions showing high efficiency of power dissipation in single phase regions are approximately similar to **Figures 5.9a** and **6.2**. However, in the two phase region, notably the power dissipation efficiency of the α–phase (0.48) is much higher than that of the β–phase (0.29). Therefore, based on higher power dissipation efficiency of α–phase, we can say that α–phase is the dominant phase in the two phase region during the hot deformation of the Zr-1Nb alloy. Thus, it is expected that the DRX will occur only in the α–phase and not in the β–phase. Microstructural analysis described in **Section 5.4.1.1.2**, also revealed that the α–phase experienced DRX, whereas the β–phase exhibited coarse elongated grains and possibly dynamic recovery.

6.1.3 Validation of the approach used in Section 6.1.2 through microstructural analysis:

To identify the dominating phase during the hot deformation in two phase region, deformation condition 850°C / 10^{-2} s^{-1} is selected. The deformation temperature 850°C is in two phase region, where the fraction of each phase (i.e. α phase and β phase) is nearly equal. The Zr-1Nb alloy extruded β quenched condition is considered as a candidate material for this analysis. Microstructure of deformed sample for the selected deformation condition (i.e. 850°C/ 10^{-2} s^{-1}),

was shown in **Figure 5.24.** The microstructure exhibited two kind of grain structures: band of fine grains and coarse/elongated grains having fine α plates. From the microstructural analysis, it was observed that the coarse/elongated grains had a large fraction of LAGBs. To calculate the fraction of recrystallized grains in the deformed microstructure and validate the recrystallized fine grains, grain orientation spread (GOS) values were used. In literature [151, 152], it is reported that GOS < 1° is a suitable criterion to identify DRX grains in the deformed matrix.
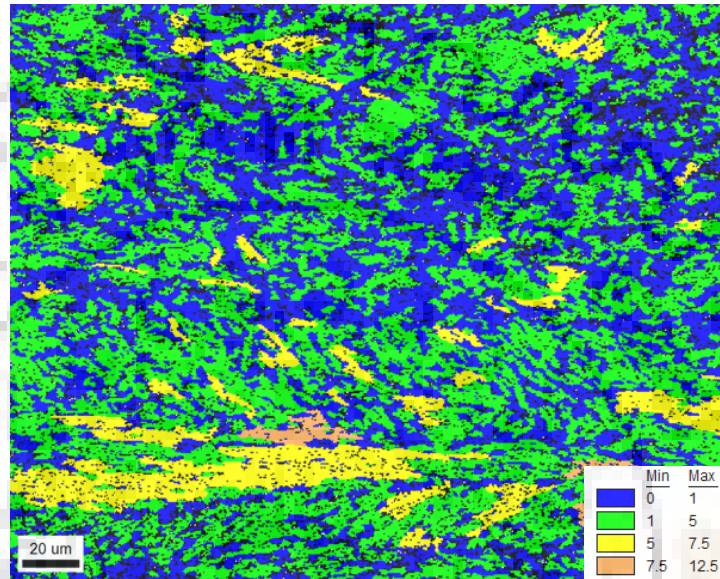
Figure 6.4: Grain orientation spread map (GOS) of sample deformed at 850°C and strain of 10^{-2} s^{-1}, showing that the fine grains have a low value of GOS. The compression direction is vertical.

Figure 6.4 presents the GOS map of the same area of sample deformed at **850°C / 10^{-2} s^{-1}**, and indicates that the fine grains are having low GOS (GOS < 1°) and hence are recrystallized whereas, coarse grains had high GOS (GOS > 2.5°). To segregate the band of fine recrystallized grains and coarse/elongated grains, image quality (IQ) is partitioned.
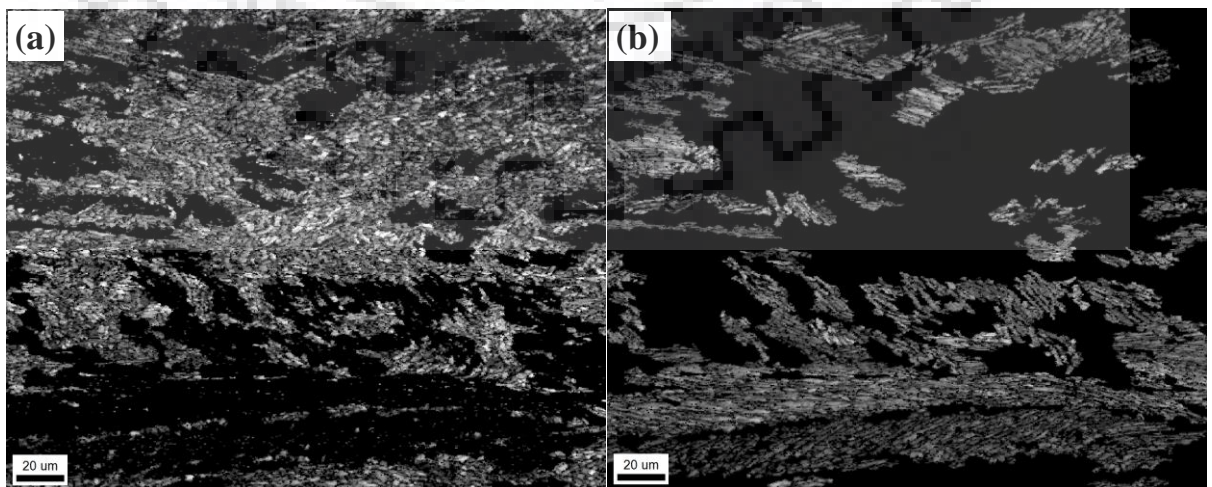
Figure 6.5: Image quality (IQ) maps of the sample deformed at 850°C and strain of 10^{-2} s^{-1}; (a) partitioned fine grain microstructure appear to be recrystallized/globular α grains, (b) partitioned coarse/elongated grains (of prior β– phase) containing fine α plates. The compression direction is vertical.

115

Figures 6.5a and **6.5b** present the image quality (IQ) maps of partitioned fine and coarse grain microstructures respectively. The recrystallization fraction in the fine grained region was 0.59 and the fraction of HAGBs was 0.69 whereas, in the coarse grain region recrystallization fraction was 0.16 and the fraction of HAGBs was 0.13. Microstructural analysis of sample deformed at 850°C posed a considerable challenge due to the equal fraction of β–phase, which after deformation and subsequent quenching transformed to α'. Since the initial condition of microstructure was also β quenched, hence it is difficult to understand whether recrystallization took place in α or β–phase. However, an attempt is made here to distinguish the two phases based upon their unique microstructural features. The original α plates after experiencing deformation are expected to show bending or fragmentation (globularization) whereas, the transformed α from deformed β grains is expected to show plate like morphology [206, 207]. Close inspection of coarse grain microstructure showed fine plates of α' aligned in a particular direction (e.g. elongated grains at the bottom of **Figure 5.24**). It appears that these coarse grains belonged to prior β–phase which transformed to α' after quenching. It is interesting to note that only one variant is observed, i.e. variant selection is taking place which was not present when deformation was performed in the fully β–phase region (**Figure 5.26**). It is likely that the applied stress and the constraint imposed by the hard α–phase around soft β–phase [208] resulted in stress assisted variant selection. On the other hand, the band of fine grained microstructure (**Figure 6.5a**) formed from the α–phase and its microstructure also looks similar to the one found in the material deformed at 815°C (**Figure 5.23**). Further, the fraction of fine grained microstructure was found to be 0.48 and this is close to the α–phase fraction expected at 850°C. Thus, it is highly probable that while the α–phase experienced dynamic recrystallization, β–phase showed dynamic recovery.

6.2 CONSTITUTIVE ANALYSIS:

In the **Section 5.3.2,** constitutive equation development was explained for extruded β quenched Zr-2.5Nb-0.5Cu alloy. From the hot compression stress strain data, peak flow stress was considered for constitutive equation development. Different sets of peak flow stress data were considered to develop constitutive equations. Using each set of flow stress data, independent constitutive equations were developed for; (i) deformation temperature range 700°C to 815°C, related to *(α+β)* phase, (ii) for deformation temperature 815°C to 925°C related to *β* phase, and (iii) entire range of deformation temperature i.e. 700°C to 925°C related to *(α+β)* and *β* phase (or complete data set irrespective of phases present). During the development of constitutive equations, various values of material constants and activation energies for different

sets were calculated and summarised in **Table 5.6**. The calculated value of Q, for entire temperature range of deformation (AE3) is quite different than the values obtained from different phases or phase mixture (AE1 and AE2). It did not reveal any information about deformation mechanism of individual phases. Therefore, activation energy values of individual phases are required for further analysis.

6.2.1 Activation energy of individual phases in the two phase range: Unlike single phase material, activation energy of a two phase material cannot be related directly to the operating deformation mechanism [201]. However, if the contribution of individual phases can be separated, one can estimate deformation parameters of the phases present. To determine the contribution of individual phases during hot deformation in the two phase range, it is necessary to calculate activation energies of individual phases. To obtain the flow stress of individual α phase (σ_α^c) and β phase (σ_β^c), flow stress values from single phase β (σ_β^E) were extrapolated in the two phase range. Assuming equi-strain rate condition, i.e. stress is distributed among their constituent phases according to their phase fraction [201], as expressed in **Equation 6.3**, flow stress values of α – phase were calculated.

$$f_\alpha \sigma_\alpha^c = \sigma_{(\alpha+\beta)}^E - f_\beta \sigma_\beta^c \tag{6.3}$$

In **Equation 6.3**, $\sigma_{(\alpha+\beta)}^E$ is an experimental flow stress in the two phase range; f_α, f_β and $\sigma_\alpha^c, \sigma_\beta^c$ are the fractions and calculated flow stresses of individual α and β phases in the two phase range respectively. After getting the stress values of individual α and β phases, Q_α^c and Q_β^c were calculated using the same procedure as described in earlier **Section 5.3**. After calculating activation energies of individual phases, the activation energy of the composite microstructure containing both the phases was calculated using analysis proposed by Briottet et al. [201] in the manner as described in **Equation 6.4**.

$$Q_{two\,phase\,range}^c = \frac{f_\alpha \sigma_\alpha^c m_\alpha Q_\alpha^c + f_\beta \sigma_\beta^c m_\beta Q_\beta^c}{f_\alpha \sigma_\alpha^c m_\alpha + f_\beta \sigma_\beta^c m_\beta} - RT^2 \frac{\left(\sigma_\alpha^c - \sigma_\beta^c\right)}{m\,\sigma} \frac{df}{dT} \tag{6.4}$$

where m and σ, are the average values of strain rate sensitivity and flow stress of individual phases. The first term on the right hand side of **Equation 6.4**, represents the weighted average of Q_α^c and Q_β^c, which is normalized by factor $f\sigma m$ of each phase. The second term on the right hand side is a product of two terms: one includes the difference between the flow stresses of individual phases at a particular temperature, and the other one is the first derivative of the fraction of any individual phase with respect to the temperature. The calculated activation

117

energies of Q_α^c and Q_β^c are 532 kJ/mol and 373 kJ/mol, whereas activation energy $Q_{two\,phase\,range}^c$ for a two phase range is 477 kJ/mol.

6.2.2 Significance of activation energy and stress exponent in the deformation behavior:
Apparent activation energy of hot deformation depends upon the rate controlling process, i.e. the slowest process. It is determined using peak stress as a function of temperature at a constant strain rate with the assumption that the microstructure remains unchanged. By comparing the apparent activation energy values with the true activation energy values of different diffusion processes, the dominant deformation mechanism can be predicted. Usually, the two activation energies are quite different since apparent activation energy depends upon alloying element, ease of dislocation glide or climb and grain size. The apparent activation energy calculated from hot deformation data is usually much higher than the true activation energy calculated from atomic diffusion mechanisms [162]. Dyment et al. [176] reported that the true activation energies are approximately half of that predicted by semi-empirical relations based on physical properties. For example, the apparent activation energy value calculated in this work is in the range of 300 – 524 kJ/mol whereas, true activation energy values were: 113 kJ/ mol for self-diffusion of pure Zr, 93 kJ/ mol for the diffusion of Zr in Zr-Nb alloys, while the activation energy for diffusion of Nb in Zr is 132 kJ /mol. Activation energies (AE4) calculated for individual phases in the two phase range suggests that the diffusion in α–phase is slower than in β–phase. Therefore, α–phase should dominate hot deformation in the two phase range. Additionally, the activation energy (Q_α^c) of individual α–phase, i.e. 532 (kJ/mol) is also very close to the activation energy (AE1) of the two phase range i.e. 524 kJ/mol determined from experimental data.

The values of stress exponent calculated in **Section 5.3.2** and shown in **Table 5.6** for different phases of calculation, brings out that the value of stress exponents lie in the range of 3.9 to 4.5. The value of the stress exponent less than or equal to 5 suggests that the deformation mechanism during the hot deformation of ZNC alloy is controlled by glide and climb of dislocations (climb controlled) [58, 68]. For climb controlled deformation mechanism the activation energy should be close to the activation energy of lattice diffusion [168, 202-207]. However, the values of activation energy determined from experimental data in present work are much higher than that of lattice diffusion. Therefore, we used experimentally determined activation energy values to develop constitutive equations instead of the activation energy value of lattice diffusion.

According to Briottet et al. [201], an alloy can be categorized as T-type (titanium) if it shows greater flow stresses for a lower temperature phase than the higher temperature phase over

the entire two phase range and the calculated activation energy $Q_{(two\ phase\ range)}$ should be greater than the weighted average of Q_α^c and Q_β^c. For the present alloy, Q_α^c and Q_β^c were obtained as 532 (kJ/mol) and 373 (kJ/mol) respectively and the weighted average of $Q_{two\ phase\ range}^c$ is 399 (kJ/mol), which is less than the calculated $Q_{two\ phase\ range}^c$ (477 (kJ/mol)) for the two phase range. This confirms that the hot deformation behavior of Zr-Nb alloy is similar to Ti alloys.

6.3 MECHANICAL PROPERTIES:

Results of mechanical properties obtained using small punch test were reported in **Section 5.5** and presented in **Figure 5.45**. From the **Figure 5.45**, it was observed that the yield load and maximum load was appreciably high for the sample hot deformed at 815°C/ 1s⁻¹. **Figure 5.45a** and **5.45b** reveals that as the temperature increases in two phase region, the value of yield load and maximum load decreases at strain rate of 1 s⁻¹, whereas at strain rate of 10⁻² s⁻¹ it increases. The strengthening of hot deformed samples compared to the as received condition might have attributes in different factors, such as grain size, strengthening from grain boundaries, dislocation density, morphology of α–phase, and crystallographic texture.

To understand the effect of grain size on mechanical properties, average grain size was calculated for all samples after hot deformation at different conditions. The influence of hot deformation at different processing conditions on grain size is shown in **Figure 6.6**. It is clear from **Figure 6.6** that the grain size monotonically increased with the temperature in two phase region at strain rate of 10⁻² s⁻¹. The influence of hot deformation on grain size at strain rate of 1 s⁻¹ was minimal in this temperature regime. Therefore, the changes in the average grain size after hot compression/deformation were negligible and do not seems to have significant impact on the mechanical properties.
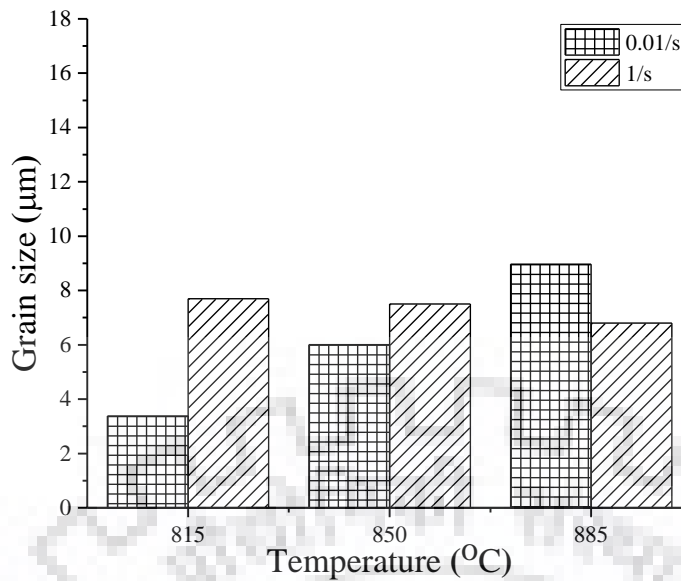
Figure 6.6: Average grain size at different deformation conditions.

Another reason for improved mechanical properties may be the recrystallization in the deformed microstructure. To determine extent of recrystallization, a bar graph representing number fraction of grains with GOS<1º is shown in **Figure 6.7a**. **Figure 6.7b** shows bar graph to represent the fractions of deformed regions (volume fraction of GOS>2.5º), which as expected is showing a reverse trend to the distribution of grain with GOS<1º. At deformation condition of 815ºC/1 s^{-1}, the volume fraction of GOS>2.5º (**Figure 6.7b**) is maximum (i.e. 0.60) and it decreases as the deformation temperature increases. At lower strain rate of 10^{-2} s^{-1}, it is maximum with value of 0.27 at 850ºC and for lower and higher temperatures it decreased to 0.12 and 0.08 respectively. Yield load and maximum load were found to increase with temperature at 0.01 s^{-1} and decrease with increase in temperature at 1 s^{-1}. Hence, at strain rate of 1 s^{-1} yield and maximum load were found to increase with decrease in recrystallization fraction. It implies that higher dislocation density and substructure are contributing to the mechanical properties. However, at strain rate of 0.01 s^{-1} no clear trend is noticed.
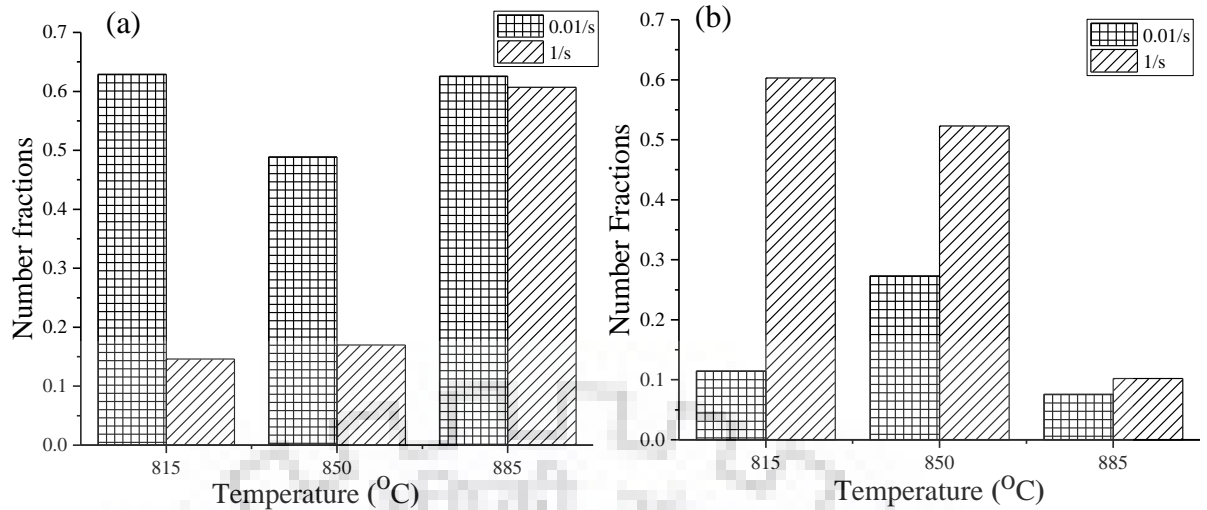
Figure 6.7: Number fraction of grain orientation spread (GOS) at different deformation temperatures in two phase region at strain rate of 0.01 and 1 s^{-1} (a) GOS<1°, (b) GOS>2.5°. GOS<1° is the representation of dynamic recrystallization (DRX), whereas GOS>2.5° represents neither DRX nor dynamic recovery in the microstructures.

Figure 6.8 shows the volume fraction of HAGB at different deformation temperatures and for the strain rates of 10^{-2} s^{-1} and 1 s^{-1}. In **Figure 6.8**, the nature of HAGB fraction at strain rates of 10^{-2} s^{-1} and 1 s^{-1} is similar to the nature of graph of GOS<1° (**Figure 6.7a**) at the same deformation condition. For strain rate of 10^{-2} s^{-1} lower value (i.e. 0.69) is observed at temperature of 850°C and higher values 0.75 and 0.82 are observed at 815°C and 885°C. Similarly, the volume fraction of HAGB at strain rate of 1 s^{-1} increases continuously from 0.45 at temperature of 850°C and 0.37 and 0.83 for temperature of 815°C and 885°C. At lower strain rate, the difference in the recrystallized fraction is only marginal with different deformation temperatures, while at higher strain rate, a sudden increase in the fraction of recrystallized grains at 885°C indicates a possibility for change in the mechanism of softening assisted by a high fraction of β–phase during deformation.
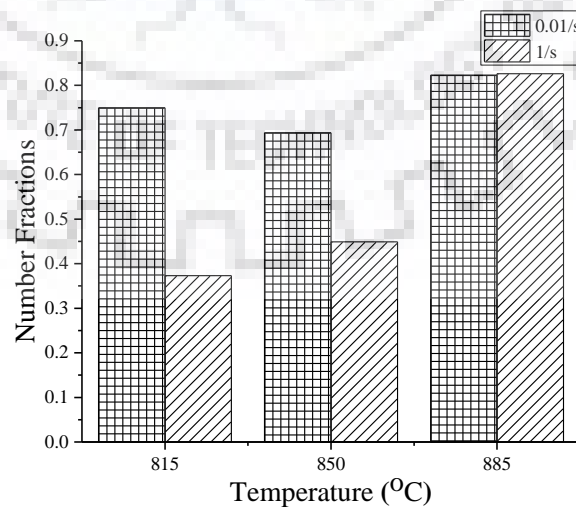
Figure 6.8: Number fraction of HAGB at different deformation conditions
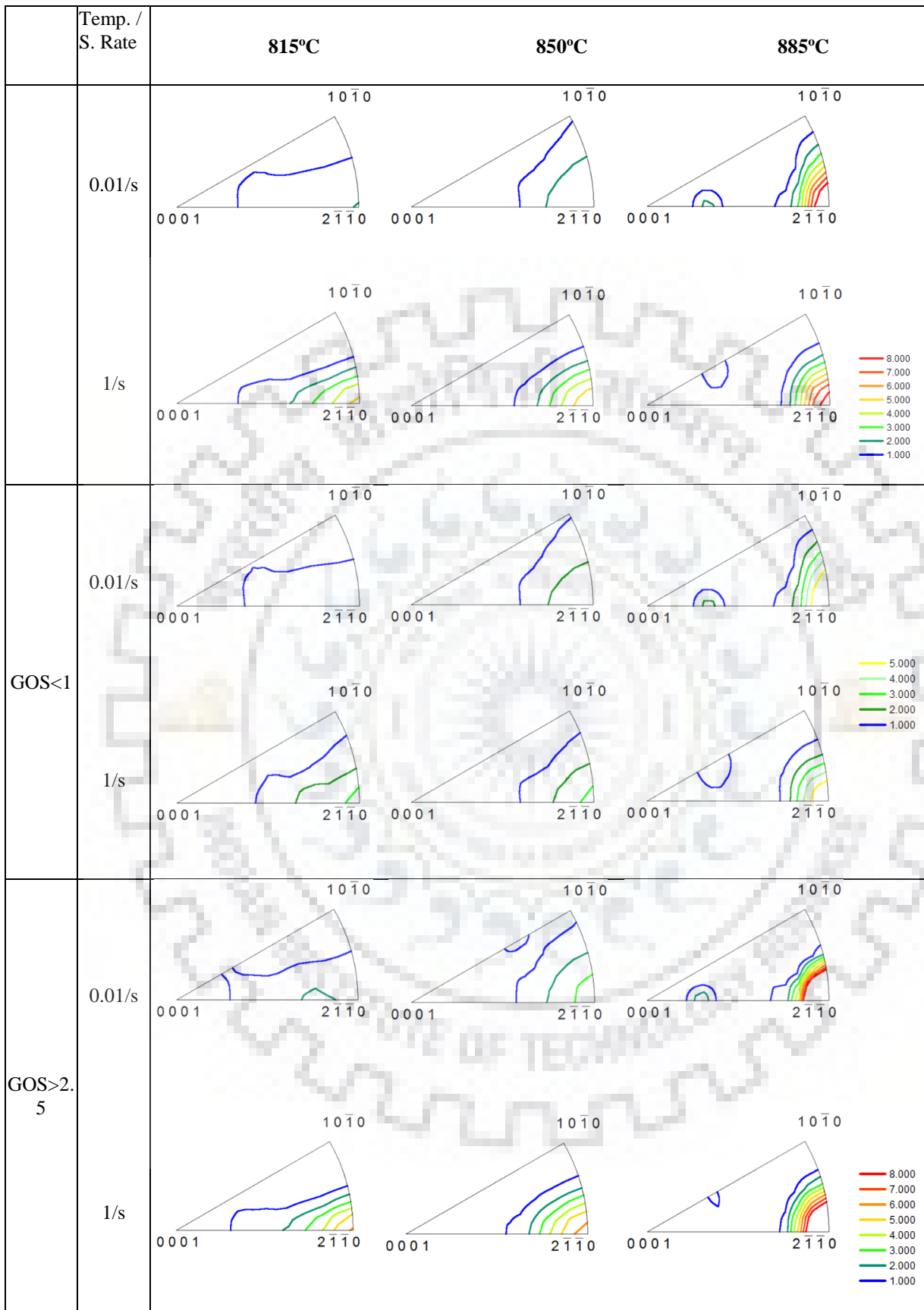
Figure 6.9: Inverse pole figures (IPF) images showing orientation of fiber in three different directions at **[001]** for different deformation temperature and strain rates. **GOS<1° represents** that the IPF image shows only the fibre having GOS <1°, and **GOS>2.5° represents** that the IPF image shows only the fibre having GOS >2.5°.

The other explanation for variation in mechanical properties could be given from the fiber direction or texture in the deformed microstructures. **Figure 6.9** shows the inverse pole figure (IPF) map of the sample compressed in the two phase region at different temperatures and strain rates, to show the fibre direction in different orientation along compression direction. It is clear from **Figure 6.9** that mostly the <11–20>||CD fiber is observed at all the deformation conditions. The tendency for the formation of <11–20>||CD fiber increases with temperature and strain rate which is demonstrated through the strengthening as well as decrease in the spread of the orientations and is clearly visible in **Figure 6.10**. The strengthening of the texture could arise from two factors, either through deformation and recrystallization or due to $\beta \rightarrow \alpha$ transformation. In order to identify the major source of strengthening of texture at high deformation temperatures, the EBSD data were partitioned based on the GOS values to represent deformed (GOS>2.5°) and recrystallized microstructures (GOS<1°) and texture of the corresponding regions were calculated. The texture of deformed and recrystallized fractions, irrespective of the deformation temperature and strain rate, are qualitatively similar in terms of formation of texture components, however, they exhibit drastic changes close to the transformation temperature in terms of quantitative description. The deformed regions demonstrate a formation of stronger <11-20>||CD fiber compared to recrystallized region and strength of this fiber drastically increases after deformation at 885°C.
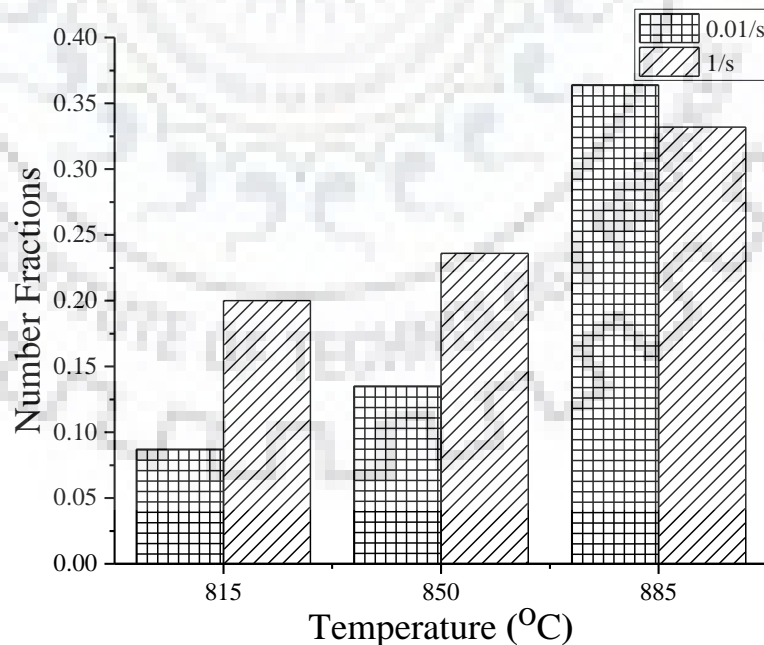
Figure 6.10: Number fraction of <11–20>||CD fiber at different temperatures and strain rates.

A weak contribution of <2-1-14>||CD fiber is also noticed at certain deformation conditions. With increase in temperature, the fraction of recrystallized grains is expected to

increase and the same is observed through the microstructural evidences. Albeit a concomitant strengthening of texture of the recrystallized regions, a sudden strengthening of texture of deformed regions at 885ºC is observed which suggest that transformation aspects and/or deformation in the β–phase field are playing a greater role in strengthening of texture. Strengthening of <111> β fiber is reported for hot deformation of two phase titanium alloys [208, 209], and which upon transformation is expected to transform to <11-20> α fiber. With increased volume fraction of transformed microstructures with temperature, fraction of grains following Burgers orientation relationship increases. Therefore, a direct correlation between textures of α and β–phases are possible. While at 815ºC, sufficiently below the β–transus temperature, only the deformation of α–phase is predominantly contributing to the texture of α, and at higher temperature, deformation within β and subsequent transformation to α contributes towards texture formation. The formation of weak texture at 815ºC could be attributed to multiple slip activity at high temperature. With increase in processing temperature, the difference between the critical resolved shear stresses of different slip systems are expected to reduce and as a result, different slip systems take part in deformation, which otherwise were restricted at low temperature. With the activation of multiple slip systems, texture migrates towards randomization, rather than towards a stable end orientation [210].

As noticed from **Figure 6.7a**, the fraction of grains with GOS<1º, is higher for all testing temperatures at 10^{-2} s^{-1} and indicate possible occurrence of DRX. Because of high fraction of DRX grains, the strengthening contribution from dislocation density for these samples is only moderate and only lamellar microstructures contribute towards strengthening, which is in accordance with the observed increase in strength. The remarkable increase in yield point at 815ºC and 1 s^{-1} could be attributed to the combined effect of high dislocation density and finer size of α lath. As noticed from **Figure 6.7b**, the highest fraction of grains with GOS>2.5º is observed for samples deformed at 815ºC and 1 s^{-1}, which could be directly correlated with the presence of GNDs. Further, this sample is characterized by finer α lath size (**Table 5.9**). The hardness of α with hcp structure is higher than that of β with bcc structure. The α plates tends to align parallel to the external force during mechanical testing such as tensile test. When the aspect ratio (the ratio of length to diameter) of the secondary α is higher than the critical aspect ratio, the load can be transferred to α through α/β interface according to shear lag theory. Moreover, the obstacle of α plates to dislocation slip is favorable for promoting the strength [211]. The strain partitioning between the two phases and the temperature of deformation decides the extent of DRV/DRX. At low temperature and high strain rate, the chances of restoration are always lower in both the phases. Because of high dislocation density in both the phases combined with finer

size of α lath, any slip transfer, during room temperature SPT, across the lamellar microstructure will be harder. While samples deformed at higher temperatures, have both higher β–phase fraction and sufficient thermal driving force for DRV/DRX. With sufficiently higher aspect ratio of α–phase and lower dislocation density, slip transfer becomes easier for other processed conditions.

The strengthening of hot deformed samples (especially 815°C/ 1 s^{-1}) compared to the as received condition was expected due to different factors, such as grain size, strengthening from grain boundaries, dislocation density, morphology of α–phase, and crystallographic texture. But, it was observed that the changes in the average grain size after hot compression was negligible and do not seems to have significant impact during SPT. The strengthening of texture fibers with respect to deformation temperature or strain rate is not as significant compared to the rise in the yield load of sample deformed at 815°C and 1 s^{-1} and due to this the texture strengthening might not be a major factor affecting the yield load during SPT. Among the different morphologies of Zr sample, fine lamellar structure provides higher strength compared to equiaxed grains. While the fraction of lamellar α that results from the transformed microstructure is higher after deformation at high temperature (885°C), the yield point increment was insignificant. Hence, a notable increase in the yield point of sample deformed at 815°C/ 1 s^{-1} was attributed to the combined effect of higher dislocation density of the material and finer α lath size.

<div align="right">**7**</div>

CONCLUSIONS AND SUGGESTIONS FOR FUTURE WORK

This chapter presents the summary of major findings of the research work and directions for the future work.

7.1 CONCLUSIONS

1) Dynamic materials model (DMM) was found to be the best approach to predict safe and unsafe processing conditions for hot deformation of Zr-Nb alloys. Different processing maps were developed to identify safe processing conditions without any instability. The predictions of different processing maps were validated with microstructural analysis.

2) The processing map developed using experimental flow stress data exhibited discontinuous contour near the phase transus temperature and predicted lower power dissipation efficiency around this temperature. Microstructural analysis showed that fully recrystallized fine grain microstructure exists at the α to (α+β) transus temperature. It implies that the processing map developed using experimental flow stress values was not able to predict accurately near transus temperature. Therefore, a novel approach was proposed to develop the processing map using calculated flow stress values in the two phase region. The calculated flow stress data was obtained after incorporating the information of the individual phases in the two phase region. Thereafter, processing map was developed using calculated flow stress data. This approach could delineate the high efficiency domain accurately in the two phase region. Moreover, processing map did not exhibit discontinuous contour near the phase transus temperature. Superimposed power dissipation efficiency maps of individual phases (i.e. α–phase and β–phase) in two phase region confirmed that the α–phase was the dominant phase during hot deformation of Zr-1Nb alloy. The observation was supported with microstructural analysis.

3) The constitutive equation developed using calculated flow stress values for α (σ_α^c) and β–phases (σ_β^c) in the two phase region, clarified that the variation in the proportion of the two phases did not affect the predictability of the developed equation. The activation energy of the two phase mixture was found to be close to that of the single α–phase, which

reinforced the earlier outcome that the dominant phase in the two phase region of Zr-Nb alloys was the α–phase.

4) Constitutive equations developed for single phase regions or two phase (α+β) region showed good agreement with experimental values whereas, the constitutive equation developed for the entire range of deformation temperature (combining data of all the phases) predicted significant variation in the values of flow stress at higher strain rates and temperatures. Therefore, each phase should have its individual constitutive equations to predict accurate results. FEM simulation also confirmed that the phase-wise constitutive equations predict same ram force as provided by flow stress data (LUT) and matched with the shop floor data. This shows that the phase-wise constitutive equation was quite accurate whereas, single constitutive equation for all phases predicted ram force far from the experimental shop floor data.

5) Characterization of the deformed samples to identify the influence on mechanical properties, revealed the formation of <11-20> fiber, volume fraction of which was found to increase with deformation temperature in two phase region. The strengthening of fiber was attributed to the transformation and deformation in the β–phase region. Recrystallized grains invariably found to have a weaker texture compared to deformed grains. Therefore, a notable increase in the yield strength of sample deformed at 815°C and 1 s^{-1} was attributed to the combined effect of higher dislocation density and finer α lath size.

7.2 SUGGESTIONS FOR FUTURE WORK

The following suggestions are proposed for the future work as an extension of the current work:

1. The novel approach for development of the processing maps can be extended to other alloys. Similar approach can be used for development of constitutive equations of different materials.

2. The limit to define safe processing condition using workability parameter (*α–parameter*) can be worked out for Zr-Nb alloys, for accurate prediction of processing conditions.

3. In-depth microstructural evolution using TEM ought to be carried out to identify the substructure development in the individual phases after deformation in two phase region of Zr-Nb alloys. This is required to verify or strengthen the observations made using EBSD analysis.

4. Phase-wise constitutive equation can be developed for other alloy systems. This will help in better prediction and simulation of industrial processes. Constitutive model can be modified to include effect of DRX, DRV and grain size on flow stress which will help in FEM simulation of hot deformation processes.

REFERENCES

[1] D.O. Northwood, The development and applications of zirconium alloys, Materials & Design, 6 (1985) 58-70.

[2] C. Lemaignan, A.T. Motta, Zirconium Alloys in Nuclear Applications, in: Materials Science and Technology, Wiley-VCH Verlag GmbH & Co. KGaA, 2006.

[3] H.G. Rickover, L.D. Geiger, B. Lustman, History of the development of zirconium alloys for use in nuclear reactors, in, Energy Research and Development Administration, , Washington, D.C. (USA). , 1975.

[4] R. Kapoor, J.K. Chakravartty, Characterization of hot deformation behaviour of Zr–2.5Nb in β phase, Journal of Nuclear Materials, 306 (2002) 126-133.

[5] J.K. Chakravartty, R.N. Singh, A. Sarkar, Assessment of Deformation Behavior of Zr-2.5Nb Alloy during Thermo-Mechanical Processing and under Service Condition, Procedia Engineering, 55 (2013) 685-692.

[6] N. Saibaba, K. Vaibhaw, S. Neogy, K.V. Mani Krishna, S.K. Jha, C. Phani Babu, S.V. Ramana Rao, D. Srivastava, G.K. Dey, Study of microstructure, texture and mechanical properties of Zr–2.5Nb alloy pressure tubes fabricated with different processing routes, Journal of Nuclear Materials, 440 (2013) 319-331.

[7] J.K. Chakravartty, R. Kapoor, A. Sarkar, V. Kumar, S.K. Jha, N. Saibaba, S. Banerjee, Identification of safe hot-working conditions in cast Zr-2.5Nb, in: P. Barberis, R.J. Comstock (Eds.) 17th International Symposium on Zirconium in the Nuclear Industry, ASTM International, 2015, pp. 259-281.

[8] J.K. Chakravartty, G.K. Dey, S. Banerjee, Y.V.R.K. Prasad, Characterization of hot deformation behaviour of Zr-2.5Nb-0.5Cu using processing maps, Journal of Nuclear Materials, 218 (1995) 247-255.

[9] S. Neogy, D. Srivastava, G.K. Dey, J.K. Chakravartty, S. Banerjee, Annealing Studies on Zr-1Nb and Zr-1Nb-1Sn-0.1Fe Alloys, Trans. Indian Inst. Met., 57 (2004) 509-519.

[10] S. Neogy , D. Srivastava, J.K. Chakravartty, G.K. Dey, S. Banerjee, Microstructural Evolution in Zr-1Nb and Zr-1Nb-1Sn-0.1Fe Alloys, Metallurgical and Materials Transactions A, 38 (2007) 485-498.

[11] W.W. Stephens, Extractive Metallurgy of Zirconium—1945 to the Present, in: Zirconium in the nuclear industry- Sixth International Symposium, American Society for Testing and Materials-ASTM Vancouver, Canada, 1984.

[12] V.P. Bobkov, L.R. Fokin, E.E. Petrov, V.V. Popov, V.N. Rumiantsev, A.I. Savvatimsky, Thermophysical properties of material for nuclear engineering: A tutorial and collection of data, in, International atomic energy agency, Vienna,, 2008.

[13] R.W.L. Fong, R. Miller, H.J. Saari, S.C. Vogel, Crystallographic Texture and Volume Fraction of α and β Phases in Zr-2.5Nb Pressure Tube Material During Heating and Cooling, Metallurgical and materials transctions A, 43 (2012) 806-821.

[14] Waterside corrosion of zirconium alloys in nuclear power plants, in, 1998.

[15] J.K. Mackenzie, J.S. Bowles, The crystallography of martensite transformations—IV body-centred cubic to orthorhombic transformations, Acta Metallurgica, 5 (1957) 137-149.

[16] J.B. Vander Sande, A.L. Bement, An investigation of second phase particles in Zircaloy-4 alloys, Journal of Nuclear Materials, 52 (1974) 115-118.

[17] E. Vitikainen, P. Nenonen, Transmission electron microscopy studies on intermetallics in some zirconium alloys, Journal of Nuclear Materials, 78 (1978) 362-373.

[18] Thermophysical properties of materials for water cooled nuclear reactors, in, International Atomic Energy Agency, Vienna, Austria, 1997.

[19] R. Krishnan, M.K. Asundi, Zirconium alloys in nuclear technology, Proceedings of the Indian Academy of Science, 4 (1981) 41-56.

[20] S.A. Aldridge, B.A. Cheadle, Age hardening of Zr-2.5 wt % Nb slowly cooled from the (α +β) phase field, Journal of Nuclear Materials, 42 (1972) 32-42.

[21] C.D. Williams, R.W. Gilbert, Tempered structures of a Zr-2.5 wt % Nb alloy, Journal of Nuclear Materials, 18 (1966) 161-166.

[22] T.R.G. Kutty, K. Ravi, C. Ganguly, Studies on hot hardness of Zr and its alloys for nuclear reactors, Journal of Nuclear Materials, 265 (1999) 91-99.

[23] M. Christensen, W. Wolf, C.M. Freeman, E. Wimmer, R.B. Adamson, L. Hallstadius, P.E. Cantonwine, E.V. Mader, Effect of alloying elements on the properties of Zr and the Zr–H system, Journal of Nuclear Materials, 445 (2014) 241-250.

[24] G.C. Weatherly, The precipitation of γ-hydride plates in zirconium, Acta Metallurgica, 29 (1981) 501-512.

[25] J.J. Kearns, C.R. Woods, Effect of texture, grain size, and cold work on the precipitation of oriented hydrides in Zircaloy tubing and plate, Journal of Nuclear Materials, 20 (1966) 241-261.

[26] J.S. Bradbrook, G.W. Lorimer, N. Ridley, The precipitation of zirconium hydride in zirconium and zircaloy-2, Journal of Nuclear Materials, 42 (1972) 142-160.

[27] A. Miquet, D. Charquet, C. Michaut, C.H. Allibert, Effect of Cr, Sn and O contents on the solid state phase boundary temperatures of Zircaloy-4, Journal of Nuclear Materials, 105 (1982) 142-148.

[28] D. Arias, J.P. Abriata, The Cr−Zr (Chromium-Zirconium) system, Bulletin of Alloy Phase Diagrams, 7 (1986) 237-244.

[29] G.T. Bereznai, G. Harvel, Introduction to Candu Systems and Operation, in: Workshop on Nuclear Power Plant Simulators University of Ontario Institute of Technology, Oshawa, Ontario, Canada Ontario, Canada 2011.

[30] R.W.L. Fong, Anisotropic deformation of Zr–2.5Nb pressure tube material at high temperatures, Journal of Nuclear Materials, 440 (2013) 467-476.

[31] H.H. Klepfer, Zirconium — niobium binary alloys for boiling water reactor service part I — corrosion resistance, Journal of Nuclear Materials, 9 (1963) 65-76.

[32] H.H. Klepfer, Zirconium-niobium binary alloys for boiling water reactor service part II - corrosion hydrogen embrittlement, Journal of Nuclear Materials, 9 (1963) 77-84.

[33] J.-Y. Park, B.-K. Choi, S.J. Yoo, Y.H. Jeong, Corrosion behavior and oxide properties of Zr–1.1 wt%Nb–0.05 wt%Cu alloy, Journal of Nuclear Materials, 359 (2006) 59-68.

[34] N. Saibaba, Studies on designing and optimization of hot deformation process for Zr-2.5%Nb alloy, in: Bhabha Atomic Research Centre, Homi Bhabha National Institute, Mumbai, India, Mumbai, India, 2014.

[35] A.R. Massih, T. Andersson, P. Witt, M. Dahlbäck, M. Limbäck, Effect of quenching rate on the β-to-α phase transformation structure in zirconium alloy, Journal of Nuclear Materials, 322 (2003) 138-151.

[36] A.R. Massih, M. Dahlbäck, M. Limbäck, T. Andersson, B. Lehtinen, Effect of beta-to-alpha phase transition rate on corrosion behaviour of Zircaloy, Corrosion Science, 48 (2006) 1154-1181.

[37] S. Banerjee, R. Krishnan, Martensitic transformation in zirconium-niobium alloys, Acta Metallurgica, 19 (1971) 1317-1326.

[38] C.S. Cramer S., Corrosion: Environments and Industries, ASM International., Ohio, Materials Park, 2006.

[39] S.E. Maussner G., Tenckhoff E., Nucleation and Growth of Intermetallic Precipitates in Zircaloy-2 and Zircaloy-4 and Correlation to Nodular Corrosion Behavior, in: Zirconium in the Nuclear Industry: Seventh International Symposium, American Society for Testing and Materials-ASTM STP 939, Strasbourg, France, 1987, pp. 307.

[40] S.N. R. V. Kulkarni, B. N. Rath, K. Manikrishna,, N.S. D. Srivastava, I. Samajdar, E. Ramadasan, , S.A. G. K. Dey, Microstructural and Textural Evolution in Heat Treated Zr-2.5%Nb Pressure Tube Material Subjected to Dilatometric Studies, Trans Indian Inst Met, 64 (2011) 395-399.

[41] R.V. Kulkarni, K.V. Mani Krishna, S. Neogy, D. Srivastava, E. Ramadasan, R.S. Shriwastaw, B.N. Rath, N. Saibaba, S.K. Jha, G.K. Dey, Mechanical properties of Zr–2.5%Nb pressure tube material subjected to heat treatments in α+β phase field, Journal of Nuclear Materials, 451 (2014) 300-312.

[42] N. Saibaba, N. Keskar, K. V. Mani Krishna, V. Raizada, K. Vaibhaw, S. K. Jha, D. Srivastava, G.K. Dey, A Numerical Study of the Effect of Extrusion Parameters on the Temperature Distribution in Zr–2.5Nb, in: Robert Comstock, P. Barberis (Eds.) Zirconium in the Nuclear Industry: 17th International Symposium, STP 1543, ASTM International, West Conshohocken, PA 2015.

[43] F.J. Humphreys, M. Hatherly, Recrystallization and related annealing phenomena, 2 ed., Pergamon, 2004.

[44] R.D. Doherty, D.A. Hughes, F.J. Humphreys, J.J. Jonas, D.J. Jensen, M.E. Kassner, W.E. King, T.R. McNelley, H.J. McQueen, A.D. Rollett, Current issues in recrystallization: a review, Materials Science and Engineering: A, 238 (1997) 219-274.

[45] S.E. Ion, F.J. Humphreys, S.H. White, Dynamic recrystallisation and the development of microstructure during the high temperature deformation of magnesium, Acta Metallurgica, 30 (1982) 1909-1919.

[46] R.E. Logé, J.W. Signorelli, Y.B. Chastel, M.Y. Perrin, R.A. Lebensohn, Sensitivity of α-Zy4 high-temperature deformation textures to the β-quenched precipitate structure and to recrystallization: application to hot extrusion, Acta Materialia, 48 (2000) 3917-3930.

[47] R.K. J. K. Chakravartty, A. Sarkar, and S. Banerjee, Dynamic Recrystallization in Zirconium Alloys, Journal of ASTM International, 7 (2010) 1-17.

[48] K. Huang, R.E. Logé, A review of dynamic recrystallization phenomena in metallic materials, Materials & Design, 111 (2016) 548-574.

[49] J.K. Chakravartty, G.K. Dey, S. Banerjee, Y.V.R.K. Prasad, Dynamic recrystallisation during hot working of Zr–2·5Nb: characterisation using processing maps, Materials Science and Technology, 12 (1996) 705-716.

[50] J.K. Chakravartty, Y.V.R.K. Prasad, M.K. Asundi, Processing Map for Hot Working of Alpha-Zirconium, Metallurgical Transaction A, 22A (1991) 829.

133

[51] J.K. Chakravartty, S. Banerjee, Y.V.R.K. Prasad, M.K. Asundi, Hot-working characteristics of Zircaloy-2 in the temperature range of 650–950°C, Journal of Nuclear Materials, 187 (1992) 260-271.

[52] O. Bocharov, Sergei Zavodchikov, V. Belov, A. Kabanov, V. Kotrekhov, V. Rozhdestvenski, V. Filippov, A. Losistskiy, A. Shikov, Temperature and Strain Rate Effects on Zr-1%Nb Alloy Deformation, Journal of ASTM International, 2 (2005) 1-15.

[53] J.K. Chakravartty, S. Banerjee, Y.V.R.K. Prasad, Superplasticity in β-zirconium: A study using a processing map, Scripta Metallurgica et Materialia, 26 (1992) 75-78.

[54] D.L. Douglass, The relative contributions of dispersion and solution strengthening in Zr-Sn-Nb alloys, Journal of Nuclear Materials, 9 (1963) 252-260.

[55] J.K. Chakravartty, R. Kapoor, S. Banerjee, Y.V.R.K. Prasad, Characterization of hot deformation behavior of Zr–1Nb–1Sn alloy, Journal of Nuclear Materials, 362 (2007) 75-86.

[56] P. Gaunt, J.W. Christian, The crystallography of the β-α transformation in zirconium and in two titanium-molybdenum alloys, Acta Metallurgica, 7 (1959) 534-543.

[57] J.S. Bowles, J.K. Mackenzie, The crystallography of martensite transformations I, Acta Metallurgica, 2 (1954) 129-137.

[58] A. Sarkar, J.K. Chakravartty, Hot deformation behavior of Zr–1Nb alloy: Characterization by processing map, Journal of Nuclear Materials, 440 (2013) 136-142.

[59] R. Kapoor, J.K. Chakravartty, C.C. Gupta, S.L. Wadekar, Characterization of superplastic behaviour in the (α+β) phase field of Zr–2.5wt.%Nb alloy, Materials Science and Engineering: A, 392 (2005) 191-202.

[60] P. Griffiths, C. Hammond, Superplasticity in large grained materials, Acta Metallurgica, 20 (1972) 935-945.

[61] H. K. Khandelwal, R. N. Singh, A. K. Bind, S. Sunil, B. N. Rath, J. B. Singh, S. Kumar, J.K. Chakravartty, Influence of Soaking Temperature and Time on Microstructure and Mechanical Properties of Water Quenched Zr–2.5Nb Alloy, Materials Performance and Characterization, 3 (2014) 216-238.

[62] Y.V.R.K. Prasad, T. Seshacharyulu, Modelling of hot deformation for microstructural control, International Materials Reviews, 43 (1998) 243.

[63] S.V.S.N. Murty, B.N. Rao, B.P. Kashyap, Development and validation of a processing map for zirconium alloys, Modelling and Simulation in Materials Science and Engineering, 10 (2002) 503-520.

[64] Dilek Halici, C. Poletti, Flow localization modelling in Ti alloys and Ti matrix composites, Key Engineering Materials, 651-653 (2015) 3-8.

[65] M. Dikovits, C. Poletti, F. Warchomicka, Deformation Mechanisms in the Near-β Titanium Alloy Ti-55531, Metallurgical and Materials Transctions A, 45 (2014) 1586-1596.

[66] Y. Xu, L. Hu, Y. Sun, Processing map and kinetic analysis for hot deformation of an as-cast AZ91D magnesium alloy, Materials Science and Engineering: A, 578 (2013) 402-407.

[67] Y.V.R.K. Prasad, S. Sasidhara, Hot Working Guide: A Compendium of Processing Maps, 1st ed., ASM International, materials Park, OH, 1997.

[68] S.K. Rajput, M. Dikovits, G.P. Chaudhari, C. Poletti, F. Warchomicka, V. Pancholi, S.K. Nath, Physical simulation of hot deformation and microstructural evolution of AISI 1016 steel using processing maps, Materials Science and Engineering: A, 587 (2013) 291-300.

[69] H.J. Frost, M.F. Ashby, Deformation-mechanism maps, Pergamon press, 1982.

[70] R. Raj, Development of a Processing Map for Use in Warm-Forming and Hot-Forming Processes, MTA, 12 (1981) 1089-1097.

[71] Y.V.R.K. Prasad, H.L. Gegel, S.M. Doraivelu, J.C. Malas, J.T. Morgan, K.A. Lark, D.R. Barker, Modeling of dynamic material behavior in hot deformation: Forging of Ti-6242, Metallurgical Transctions A, 15 (1984) 1883-1892.

[72] F. Montheillet, J.J. Jonas, K.W. Neale, Modeling of dynamic material behavior: A critical evaluation of the dissipator power co-content approach, Metallurgical and Materials Transactions A, 27 (1996) 232-235.

[73] S.V.S.N. Murty, B.N. Rao, Ziegler's criterion on the instability regions in processing maps, Journal of Materials Science Letters, 17 (1998) 1203-1205.

[74] S.V.S.N. Murty, B.N. Rao, B.P. Kashyap, On the hot working characteristics of 2014 Al–20 vol% Al_2O_3 metal matrix composite, Journal of Materials Processing Technology, 166 (2005) 279-285.

[75] Y. Sun, W.-D. Zeng, Y.-Q. Zhao, X.-M. Zhang, X. Ma, Y.-F. Han, Constructing processing map of Ti40 alloy using artificial neural network, Transactions of Nonferrous Metals Society of China, 21 (2011) 159-165.

[76] Y.V.R.K. Prasad, T. Seshacharyulu, Processing maps for hot working of titanium alloys, Materials Science and Engineering: A, 243 (1998) 82-88.

[77] S.V.S.N. Murty, B.N. Rao, Hot working characteristics of Zr-2.5Nb using processing maps, Materials Science and Technology, 14 (1998) 835-837.

[78] I. Kartika, Y. Li, H. Matsumoto, A. Chiba, Constructing Processing Maps for Hot Working of Co-Ni-Cr-Mo Superalloy, Materials Transactions, 50 (2009) 2277-2284.

[79] J.J. Jonas, R.A. Holt, C.E. Coleman, Plastic stability in tension and compression, Acta Metallurgica, 24 (1976) 911-918.

[80] S.V.S.N. Murty, B.N. Rao, On the development of instability criteria during hotworking with reference to IN 718, Materials Science and Engineering: A, 254 (1998) 76-82.

[81] S.V.S.N. Murty, B.N. Rao, On the flow localization concepts in the processing maps of titanium alloy Ti–24Al–20Nb, Journal of Materials Processing Technology, 104 (2000) 103-109.

[82] S.V.S.N. Murty, B.N. Rao, B.P. Kashyap, Identification of flow instabilities in the processing maps of AISI 304 stainless steel, Journal of Materials Processing Technology, 166 (2005) 268-278.

[83] E.W. Hart, Theory of the tensile test, Acta Metallurgica, 15 (1967) 351-355.

[84] Y.C. Lin, Y.C. Xia, X.M. Chen, M.S. Chen, Constitutive descriptions for hot compressed 2124-T851 aluminum alloy over a wide range of temperature and strain rate, Computational Materials Science, 50 (2010) 227-233.

[85] S.R. Bodner, Y. Partom, Constitutive equations for elastic-viscoplastic strain-hardening materials, Journal of Applied Mechanics, 42 (1975) 385-389.

[86] A. Rusinek, J.R. Klepaczko, Shear testing of a sheet steel at wide range of strain rates and a constitutive relation with strain-rate and temperature dependence of the flow stress, International Journal of Plasticity, 17 (2001) 87-115.

[87] F.J. Zerilli, R.W. Armstrong, Dislocation- mechanics- based constitutive relations for material dynamics calculations, Journal of Applied Physics, 61 (1987) 1816-1825.

[88] T. Mirzaie, H. Mirzadeh, J.-M. Cabrera, A simple Zerilli–Armstrong constitutive equation for modeling and prediction of hot deformation flow stress of steels, Mechanics of Materials, 94 (2016) 38-45.

[89] H. Zhang, W. Wen, H. Cui, Y. Xu, A modified Zerilli–Armstrong model for alloy IC10 over a wide range of temperatures and strain rates, Materials Science and Engineering: A, 527 (2009) 328-333.

[90] D.L. Preston, D.L. Tonks, D.C. Wallace, Model of plastic deformation for extreme loading conditions, Journal of Applied Physics, 93 (2003) 211-220.

[91] G.Z. Voyiadjis, A.H. Almasri, A physically based constitutive model for fcc metals with applications to dynamic hardness, Mechanics of Materials, 40 (2008) 549-563.

[92] Z.-Y. Jin, J. Liu, Z.-S. Cui, D.-L. Wei, Identification of nucleation parameter for cellular automaton model of dynamic recrystallization, Transactions of Nonferrous Metals Society of China, 20 (2010) 458-464.

[93] R.L. Goetz, V. Seetharaman, Modeling dynamic recrystallization using cellular automata, Scripta Materialia, 38 (1998) 405-413.

[94] U.F. Kocks, Laws for work-hardening and low-temperature creep, Journal of Engineering Materials and Technology, 98 (1976) 76-85.

[95] G.R. Johnson, W.H. Cook, Constitutive model and data for metals subjected to large strains, high strain rates and high temperatures, in: The Seventh International Symposium on Ballistic, The Hague, The Netherlands, 1983, pp. 541–547.

[96] A.S. Khan, H. Zhang, L. Takacs, Mechanical response and modeling of fully compacted nanocrystalline iron and copper, International Journal of Plasticity, 16 (2000) 1459-1476.

[97] B. Farrokh, A.S. Khan, Grain size, strain rate, and temperature dependence of flow stress in ultra-fine grained and nanocrystalline Cu and Al: Synthesis, experiment, and constitutive modeling, International Journal of Plasticity, 25 (2009) 715-732.

[98] A. Molinari, G. Ravichandran, Constitutive modeling of high-strain-rate deformation in metals based on the evolution of an effective microstructural length, Mechanics of Materials, 37 (2005) 737-752.

[99] A. Marchattiwar, A. Sarkar, J.K. Chakravartty, B.P. Kashyap, Dynamic recrystallization during hot deformation of 304 austenitic stainless steel, Journal of Materials Engineering and Performance, 22 (2013) 2168-2175.

[100] J. Li, X. Xia, Modeling high temperature deformation behavior of large-scaled Mg-Al-Zn magnesium alloy fabricated by semi-continuous casting, Journal of Materials Engineering and Performance, 24 (2015) 3539-3548.

[101] H. Mirzadeh, A simplified approach for developing constitutive equations for modeling and prediction of hot deformation flow stress, Metallurgical and Materials Transaction A, 46A (2015) 4027-4037.

[102] N. Kotkunde, H.N. Krishnamurthy, P. Puranik, A.K. Gupta, S.K. Singh, Microstructure study and constitutive modeling of Ti–6Al–4V alloy at elevated temperatures, Materials & Design, 54 (2014) 96-103.

[103] C.M. Sellars, W.J. McTegart, On the mechanism of hot deformation, Acta Metallurgica, 14 (1966) 1136-1138.

[104] J.J. Jonas, C.M. Sellars, W.J.M. Tegart, Strength and structure under hot-working conditions, Metallurgical Reviews, 14 (1969) 1-24.

[105] Y.C. Lin, X.-M. Chen, A critical review of experimental results and constitutive descriptions for metals and alloys in hot working, Materials & Design, 32 (2011) 1733-1759.

[106] A. Cingara, H.J. McQueen, New formula for calculating flow curves from high temperature constitutive data for 300 austenitic steels, Journal of Materials Processing Technology, 36 (1992) 31-42.

[107] C. Phaniraj, M. Nandagopal, S.L. Mannan, P. Rodriguez, The relationship between transient and steady state creep in AISI 304 stainless steel, Acta Metallurgica et Materialia, 39 (1991) 1651-1656.

[108] D. Samantaray, C. Phaniraj, S. Mandal, A.K. Bhaduri, Strain dependent rate equation to predict elevated temperature flow behavior of modified 9Cr-1Mo (P91) steel, Materials Science and Engineering: A, 528 (2011) 1071-1077.

[109] Z.H.A. Kassam, Z. Wang, E.T.C. Ho, Constitutive equations for a modified Zr-2.5wt.%Nb pressure tube material, Materials Science and Engineering: A, 158 (1992) 185-194.

[110] H. Mirzadeh, Constitutive description of 7075 aluminum alloy during hot deformation by apparent and physically-based approaches, Journal of Materials Engineering and Performance, 24 (2015) 1095-1099.

[111] H. Mirzadeh, J.M. Cabrera, A. Najafizadeh, Constitutive relationships for hot deformation of austenite, Acta Materialia, 59 (2011) 6441-6448.

[112] D. Samantaray, S. Mandal, A.K. Bhaduri, P.V. Sivaprasad, An overview on constitutive modelling to predict elevated temperature flow behaviour of fast reactor structural materials, Trans Indian Inst Met, 63 (2010) 823-831.

[113] C. Zener, J.H. Hollomon, Effect of strain rate upon plastic flow of steel, Journal of Applied Physics, 15 (1944) 22-32.

[114] J.H. Kim, S.L. Semiatin, C.S. Lee, Constitutive analysis of the high-temperature deformation of Ti–6Al–4V with a transformed microstructure, Acta Materialia, 51 (2003) 5613-5626.

[115] N. Kotkunde, A.D. Deole, A.K. Gupta, S.K. Singh, Comparative study of constitutive modeling for Ti–6Al–4V alloy at low strain rates and elevated temperatures, Materials & Design, 55 (2014) 999-1005.

[116] Z. Yuan, F. Li, H. Qiao, M. Xiao, J. Cai, J. Li, A modified constitutive equation for elevated temperature flow behavior of Ti–6Al–4V alloy based on double multiple nonlinear regression, Materials Science and Engineering: A, 578 (2013) 260-270.

[117] C. Zhang, X.-Q. Li, D.-S. Li, C.-H. Jin, J.-J. Xiao, Modelization and comparison of Norton-Hoff and Arrhenius constitutive laws to predict hot tensile behavior of Ti–6Al–4V alloy, Transactions of Nonferrous Metals Society of China, 22 (2012) 457-464.

[118] G. Chen, C. Ren, X. Qin, J. Li, Temperature dependent work hardening in Ti–6Al–4V alloy over large temperature and strain rate ranges: Experiments and constitutive modeling, Materials & Design, 83 (2015) 598-610.

[119] G.-B. Wei, X.-D. Peng, F.-P. Hu, A. Hadadzadeh, Y. Yang, W.-D. Xie, M.A. Wells, Deformation behavior and constitutive model for dual-phase Mg–Li alloy at elevated temperatures, Transactions of Nonferrous Metals Society of China, 26 (2016) 508-518.

[120] C. Qin, Z.-k. Yao, Y.-q. Ning, Z.-f. Shi, H.-z. Guo, Hot deformation behavior of TC11/Ti–22Al–25Nb dual-alloy in isothermal compression, Transactions of Nonferrous Metals Society of China, 25 (2015) 2195-2205.

[121] I. Balasundar, T. Raghu, B.P. Kashyap, Modeling the hot working behavior of near-α titanium alloy IMI 834, Progress in Natural Science: Materials International, 23 (2013) 598-607.

[122] P. Wanjara, M. Jahazi, H. Monajati, S. Yue, J.P. Immarigeon, Hot working behavior of near-α alloy IMI834, Materials Science and Engineering: A, 396 (2005) 50-60.

[123] T. Seshacharyulu, S.C. Medeiros, W.G. Frazier, Y.V.R.K. Prasad, Hot working of commercial Ti–6Al–4V with an equiaxed α–β microstructure: materials modeling considerations, Materials Science and Engineering: A, 284 (2000) 184-194.

[124] J. Porntadawit, V. Uthaisangsuk, P. Choungthong, Modeling of flow behavior of Ti–6Al–4V alloy at elevated temperatures, Materials Science and Engineering: A, 599 (2014) 212-222.

[125] G. Lütjering, Influence of processing on microstructure and mechanical properties of (α+β) titanium alloys, Materials Science and Engineering: A, 243 (1998) 32-45.

[126] R.V. Kulkarni, K.V. Mani Krishna, S. Neogy, D. Srivastava, E. Ramadasan, G.K. Dey, N. Saibaba, S.K. Jha, R.S. Shriwastaw, S. Anantharaman, Determination of correlation parameters for evaluation of mechanical properties by Small Punch Test and Automated Ball Indentation Test for Zr–2.5% Nb pressure tube material, Nuclear Engineering and Design, 265 (2013) 1101-1112.

[127] W.J. Evans, Optimising mechanical properties in alpha+beta titanium alloys, Materials Science and Engineering: A, 243 (1998) 89-96.

[128] R.A. Holt, In-reactor deformation of cold-worked Zr–2.5Nb pressure tubes, Journal of Nuclear Materials, 372 (2008) 182-214.

[129] A.K. Dureja, S.K. Sinha, A. Srivastava, R.K. Sinha, J.K. Chakravartty, P. Seshu, D.N. Pawaskar, Flow behaviour of autoclaved, 20% cold worked, Zr–2.5Nb alloy pressure tube material in the temperature range of room temperature to 800°C, Journal of Nuclear Materials, 412 (2011) 22-29.

[130] R. Kondo, N. Nomura, Suyalatu, Y. Tsutsumi, H. Doi, T. Hanawa, Microstructure and mechanical properties of as-cast Zr–Nb alloys, Acta Biomaterialia, 7 (2011) 4278-4284.

[131] S.X. Liang, M.Z. Ma, R. Jing, C.L. Tan, R.P. Liu, Structural evolution and mechanical properties of Zr–45Ti–5Al–3V alloy by heat treatments, Materials Science and Engineering: A, 541 (2012) 67-72.

[132] S.X. Liang, L.X. Yin, X.Y. Liu, R. Jing, Y.K. Zhou, M.Z. Ma, R.P. Liu, Effects of annealing treatments on microstructure and mechanical properties of the Zr345Ti35Al33V alloy, Materials Science and Engineering: A, 582 (2013) 374-378.

[133] R. Filip, K. Kubiak, W. Ziaja, J. Sieniawski, The effect of microstructure on the mechanical properties of two-phase titanium alloys, Journal of Materials Processing Technology, 133 (2003) 84-89.

[134] C.J. Bennett, A comparison of material models for the numerical simulation of spike-forging of a CrMoV alloy steel, Computational Materials Science, 70 (2013) 114-122.

[135] L.X. Li, K.P. Rao, Y. Lou, D.S. Peng, A study on hot extrusion of Ti–6Al–4V using simulations and experiments, International Journal of Mechanical Sciences, 44 (2002) 2415-2425.

[136] Z. Wang, L. Qi, G. Wang, H. Li, M.S. Dargusch, Constitutive equation for the hot deformation behavior of Csf/AZ91D composites and its validity for numerical simulation, Mechanics of Materials, 102 (2016) 90-96.

[137] W. Zhang, Y. Liu, L. Wang, B. Liu, Numerical simulation and physical analysis for dynamic behaviors of P/M TiAl alloy in hot-packed forging process, Transactions of Nonferrous Metals Society of China, 22 (2012) 901-906.

[138] L. Li, J. Zhou, J. Duszczyk, Determination of a constitutive relationship for AZ31B magnesium alloy and validation through comparison between simulated and real extrusion, Journal of Materials Processing Technology, 172 (2006) 372-380.

[139] Z. Wang, L. Qi, J. Zhou, J. Guan, J. Liu, A constitutive model for predicting flow stress of Al18B4O33w/AZ91D composite during hot compression and its validation, Computational Materials Science, 50 (2011) 2422-2426.

[140] J. Zhou, L. Li, J. Duszczyk, Computer simulated and experimentally verified isothermal extrusion of 7075 aluminium through continuous ram speed variation, Journal of Materials Processing Technology, 146 (2004) 203-212.

[141] Y.-S. Jang, D.-C. Ko, B.-M. Kim, Application of the finite element method to predict microstructure evolution in the hot forging of steel, Journal of Materials Processing Technology, 101 (2000) 85-94.

[142] C. Liang, C. Hui, T. Bin, K. Hongchao, L. Jinshan, Simulation of Microstructure for Hot Pack-Forging of a High Nb Containing TiAl Alloy, Rare Metal Materials and Engineering, 43 (2014) 36-41.

[143] X. Li, L. Duan, J. Li, X. Wu, Experimental study and numerical simulation of dynamic recrystallization behavior of a micro-alloyed plastic mold steel, Materials & Design, 66, Part A (2015) 309-320.

[144] https://gleeble.com/support/training.html, in.

[145] T.S. Hideaki Takahashi, Xinyuan Mao, Yoshikazu Hamaguchi, Toshihei Misawa, Masahiro Saito,, T.K. Tatsuo Oku, Kiyoshi Fukaya, Hiroshi Nishi, Masahide Suzuki, Recommended Practice for Small Punch (SP) Testing of Metallic Materials, in, Japan Atomic Energy Research Institute, 1988.

[146] X. Mao, H. Takahashi, T. Kodaira, Supersmall punch test to estimate fracture toughness JIc and its application to radiation embrittlement of 2.25Cr-1Mo steel, Materials Science and Engineering: A, 150 (1992) 231-236.

[147] X. Mao, H. Takahashi, T. Kodaira, Estimation of mechanical properties of irradiated nuclear pressure vessel steel by use of subsized CT specimen and small punch specimen, Scripta Metallurgica et Materialia, 25 (1991) 2487-2490.

[148] X. Mao, M. Saito, H. Takahashi, Small punch test to predict ductile fracture toughness JIC and brittle fracture toughness KIC, Scripta Metallurgica et Materialia, 25 (1991) 2481-2485.

[149] X. Mao, H. Takahashi, Development of a further-miniaturized specimen of 3 mm diameter for tem disk (ø 3 mm) small punch tests, Journal of Nuclear Materials, 150 (1987) 42-52.

[150] Adam J. Schwartz, Mukul Kumar, Brent L. Adams, D.P. Field, Electron Backscatter Diffraction in Materials Science, Second Edition ed., Springer, 2009.

[151] S. Mandal, A.K. Bhaduri, V.S. Sarma, A Study on Microstructural Evolution and Dynamic Recrystallization During Isothermal Deformation of a Ti-Modified Austenitic Stainless Steel, Metallurgical and Materials Transaction A, 42A (2011) 1062-1072.

[152] K.A. Babu, S. Mandal, A. Kumar, C.N. Athreya, B. de Boer, V.S. Sarma, Characterization of hot deformation behavior of alloy 617 through kinetic analysis, dynamic material modeling and microstructural studies, Materials Science and Engineering: A, 664 (2016) 177-187.

[153] A. Gholamzadeh, A. Karimi Taheri, The prediction of hot flow behavior of Al–6%Mg alloy, Mechanics Research Communications, 36 (2009) 252-259.

[154] J.L.a.X.-G.C. Cangji Shi, Microstructural Evolution and Dynamic Softening Mechanisms of Al-Zn-Mg-Cu Alloy during Hot Compressive Deformation, Materials, 7 (2014) 244-264.

[155] A.N. Behera, A. Chaudhuri, R. Kapoor, J.K. Chakravartty, S. Suwas, High temperature deformation behavior of Nb–1 wt.%Zr alloy, Materials & Design, 92 (2016) 750-759.

[156] X.G. Fan, H. Yang, P.F. Gao, Prediction of constitutive behavior and microstructure evolution in hot deformation of TA15 titanium alloy, Materials & Design, 51 (2013) 34-42.

[157] A.B. Li, L.J. Huang, Q.Y. Meng, L. Geng, X.P. Cui, Hot working of Ti–6Al–3Mo–2Zr–0.3Si alloy with lamellar α + β starting structure using processing map, Materials & Design, 30 (2009) 1625-1631.

[158] S.L. Semiatin, V. Seetharaman, I. Weiss, Flow behavior and globularization kinetics during hot working of Ti–6Al–4V with a colony alpha microstructure, Materials Science and Engineering: A, 263 (1999) 257-271.

[159] K.K. Saxena, S. Sonkar, V. Pancholi, G.P. Chaudhari, D. Srivastava, G.K. Dey, S.K. Jha, N. Saibaba, Hot deformation behavior of Zr-2.5Nb alloy: A comparative study using different materials models, Journal of Alloys and Compounds, 662 (2016) 94-101.

[160] K.K. Saxena, S.D. Yadav, S. Sonkar, V. Pancholi, G.P. Chaudhari, D. Srivastava, G.K. Dey, S.K. Jha, N. Saibaba, Effect of Temperature and Strain Rate on Deformation Behavior of Zirconium Alloy: Zr-2.5Nb, Procedia Materials Science, 6 (2014) 278-283.

[161] S.L.Semiatin, T. Altan, Measurement and Interpretation of Flow Stress Data for the Simulation of Metal-Forming Processes, in, AIR FORCE RESEARCH LABORATORY, MATERIALS AND MANUFACTURING DIRECTORATE WRIGHT-PATTERSON AIR FORCE BASE, OH 45433-7750, 2010.

[162] N.D. Ryan, H.J. McQueen, Mean pass flow stresses and interpass softening in multistage processing of carbon-, HLSA-, tool- and γ-stainless steels, Journal of Mechanical Working Technology, 12 (1986) 323-349.

[163] W.-F. Zhang, W. Sha, W. Yan, W. Wang, Y.-Y. Shan, K. Yang, Constitutive modeling, microstructure evolution, and processing map for a nitride-strengthened heat-resistant steel, Journal of Materials Engineering and Performance, 23 (2014) 3042-3050.

[164] S. Banerjee, P.S. Robi, A. Srinivasan, L. Praveen Kumar, High temperature deformation behavior of Al–Cu–Mg alloys micro-alloyed with Sn, Materials Science and Engineering: A, 527 (2010) 2498-2503.

[165] H.J. McQueen, N.D. Ryan, Constitutive analysis in hot working, Materials Science and Engineering: A, 322 (2002) 43-63.

[166] H. Mirzadeh, A. Najafizadeh, M. Moazeny, Flow curve analysis of 17-4 PH stainless steel under hot compression test, Metallurgical and Materials transactions A, 40 (2009) 2950-2958.

[167] D. Samantaray, S. Mandal, A.K. Bhaduri, Constitutive analysis to predict high-temperature flow stress in modified 9Cr–1Mo (P91) steel, Materials & Design, 31 (2010) 981-984.

[168] T.G. Langdon, An analysis of flow mechanisms in high temperature creep and superplasticity, Materials Transactions, 46 (2005) 1951 -1956.

[169] R. Mahmudi, A. Rezaee-Bazzaz, H.R. Banaie-Fard, Investigation of stress exponent in the room-temperature creep of Sn–40Pb–2.5Sb solder alloy, Journal of Alloys and Compounds, 429 (2007) 192-197.

[170] T.G. Langdon, Identifiying creep mechanisms at low stresses, Materials Science and Engineering: A, 283 (2000) 266-273.

[171] W. Peng, W. Zeng, Q. Wang, H. Yu, Comparative study on constitutive relationship of as-cast Ti60 titanium alloy during hot deformation based on Arrhenius-type and artificial neural network models, Materials & Design, 51 (2013) 95-104.

[172] R. Kapoor, D. Pal, J.K. Chakravartty, Use of artificial neural networks to predict the deformation behavior of Zr–2.5Nb–0.5Cu, Journal of Materials Processing Technology, 169 (2005) 199-205.

[173] Y.B. Tan, L.H. Yang, C. Tian, R.P. Liu, X.Y. Zhang, W.C. Liu, Hot deformation behavior of ZrTiAlV alloy with a coarse grain structure in the β phase field, Materials Science and Engineering: A, 577 (2013) 218-224.

[174] X. Yang, H. Guo, H. Liang, Z. Yao, S. Yuan, Flow Behavior and Constitutive Equation of Ti-6.5Al-2Sn-4Zr-4Mo-1W-0.2Si Titanium Alloy, Journal of Materials Engineering and Performance, 25 (2016) 1347-1359.

[175] J. Cai, F. Li, T. Liu, B. Chen, M. He, Constitutive equations for elevated temperature flow stress of Ti–6Al–4V alloy considering the effect of strain, Materials & Design, 32 (2011) 1144-1151.

[176] F. Dyment, C.M. Libanati, Self-diffusion of Ti, Zr, and Hf in their hcp phases, and diffusion of Nb95 in hcp Zr, Journal of Materials Science, 3 (1968) 349-359.

[177] H.E. Rosinger, D.O. Northwood, The elastic properties of zirconium alloy fuel cladding and pressure tubing materials, Journal of Nuclear Materials, 79 (1979) 170-179.

[178] D.O. Northwood, I.M. London, L.E. Bähen, Elastic constants of zirconium alloys, Journal of Nuclear Materials, 55 (1975) 299-310.

[179] P. Zhang, C. Hu, Q. Zhu, C.-g. Ding, H.-y. Qin, Hot compression deformation and constitutive modeling of GH4698 alloy, Materials & Design, 65 (2015) 1153-1160.

[180] J. Cai, K. Wang, C. Miao, W. Li, W. Wang, J. Yang, Constitutive analysis to predict high-temperature flow behavior of BFe10-1-2 cupronickel alloy in consideration of strain, Materials & Design, 65 (2015) 272-279.

[181] J. Zhao, H. Ding, W. Zhao, M. Huang, D. Wei, Z. Jiang, Modelling of the hot deformation behaviour of a titanium alloy using constitutive equations and artificial neural network, Computational Materials Science, 92 (2014) 47-56.

[182] M.R. Rokni, A. Zarei-Hanzaki, C.A. Widener, P. Changizian, The strain-compensated constitutive equation for high temperature flow behavior of an Al-Zn-Mg-Cu alloy, Journal of Materials Engineering and Performance, 23 (2014) 4002-4009.

[183] Chapter 4 - Martensitic Transformations, in: S. Banerjee, P. Mukhopadhyay (Eds.) Pergamon Materials Series, Pergamon, 2007, pp. 257-376.

[184] K. Hua, X. Xue, H. Kou, J. Fan, B. Tang, J. Li, Characterization of hot deformation microstructure of a near beta titanium alloy Ti-5553, Journal of Alloys and Compounds, 615 (2014) 531-537.

[185] M.T. Pérez-Prado, S.R. Barrabes, M.E. Kassner, E. Evangelista, Dynamic restoration mechanisms in α-zirconium at elevated temperatures, Acta Materialia, 53 (2005) 581-591.

[186] T. Seshacharyulu, S.C. Medeiros, W.G. Frazier, Y.V.R.K. Prasad, Microstructural mechanisms during hot working of commercial grade Ti–6Al–4V with lamellar starting structure, Materials Science and Engineering: A, 325 (2002) 112-125.

[187] X. Ma, W. Zeng, K.L. Wang, Y. Lai, Y. Zhou, The investigation on the unstable flow behavior of Ti17 alloy in α+β phase field using processing map, Materials Science and Engineering: A, 550 (2012) 131-137.

[188] S.I. Wright, M.M. Nowell, P.F. David, A Review of Strain Analysis Using Electron Backscatter Diffraction, Microscopy and Microanalysis, 17 (2011) 316-329.

[189] N.-N. Sia, W.-G. Guo, V.F. Nesterenko, S.S. Indrakanti, Y.-B. Gu, Dynamic response of conventional and hot isostatically pressed Ti–6Al–4V alloys: experiments and modeling, Mechanics of Materials, 33 (2001) 425-439.

[190] S. Roy, S. Suwas, The influence of temperature and strain rate on the deformation response and microstructural evolution during hot compression of a titanium alloy Ti–6Al–4V–0.1B, Journal of Alloys and Compounds, 548 (2013) 110-125.

[191] S.V. Shukla, C. Chandrashekharayya, R.N. Singh, R. Fotedar, R. Kishore, T.K. Sinha, B.P. Kashyap, Effect of strain rate and test temperature on superplasticity of a Zr–2.5 wt% Nb alloy, Journal of Nuclear Materials, 273 (1999) 130-138.

[192] S.L. Semiatin, F. Montheillet, G. Shen, J.J. Jonas, Self-Consistent Modeling of the Flow Behavior of Wrought Alpha/Beta Titanium Alloys under Isothermal and Nonisothermal Hot-Working Conditions, Metallurgical and Materials Transctions A, 33 (2002) 2719-2727.

[193] P. Vo, M. Jahazi, S. Yue, P. Bocher, Flow stress prediction during hot working of near-α titanium alloys, Materials Science and Engineering: A, 447 (2007) 99-110.

[194] E.B. Shell, S.L. Semiatin, Effect of Initial Microstructure on Plastic Flow and Dynamic Globularization during Hot Working of Ti-6Al-4V, Metallurgical and Materials Transctions A, 30 (1999) 3219-3229.

[195] M. Calcagnotto, D. Ponge, E. Demir, D. Raabe, Orientation gradients and geometrically necessary dislocations in ultrafine grained dual-phase steels studied by 2D and 3D EBSD, Materials Science and Engineering: A, 527 (2010) 2738-2746.

[196] K.S. Suresh, N.P. Gurao, S. Singh D, S. Suwas, K. Chattopadhyay, S.V. Zherebtsov, G.A. Salishchev, Effect of equal channel angular pressing on grain refinement and texture evolution in a biomedical alloy Ti13Nb13Zr, Materials Characterization, 82 (2013) 73-85.

[197] F.-L. Sui, L.-X. Xu, L.-Q. Chen, X.-H. Liu, Processing map for hot working of Inconel 718 alloy, Journal of Materials Processing Technology, 211 (2011) 433-440.

[198] H.E. Roslnger, A.E. Unger, The superplastic and strain-rate dependent plastic flow of zirconium-2.5 wt% niobium in the 873 to 1373 K temperature range, in, Whiteshell Nuclear Research Establishment, 1979.

[199] T. Seshacharyulu, S.C. Medeiros, J.T. Morgan, J.C. Malas, W.G. Frazier, Y.V.R.K. Prasad, Hot deformation and microstructural damage mechanisms in extra-low interstitial (ELI) grade Ti–6Al–4V, Materials Science and Engineering: A, 279 (2000) 289-299.

[200] J. Zhang, H. Di, K. Mao, X. Wang, Z. Han, T. Ma, Processing maps for hot deformation of a high-Mn TWIP steel: A comparative study of various criteria based on dynamic materials model, Materials Science and Engineering: A, 587 (2013) 110-122.

[201] L. Briottet, J.J. Jonas, F. Montheillet, A mechanical interpretation of the activation energy of high temperature deformation in two phase materials, Acta Materialia, 44 (1996) 1665-1672.

[202] A.K. Mukherjee, An examination of the constitutive equation for elevated temperature plasticity, Materials Science and Engineering: A, 322 (2002) 1-22.

[203] H. Mirzadeh, Constitutive analysis of Mg–Al–Zn magnesium alloys during hot deformation, Mechanics of Materials, 77 (2014) 80-85.

[204] H. Mirzadeh, Constitutive behaviors of magnesium and Mg–Zn–Zr alloy during hot deformation, Materials Chemistry and Physics, 152 (2015) 123-126.

[205] S. Saadatkia, H. Mirzadeh, J.-M. Cabrera, Hot deformation behavior, dynamic recrystallization, and physically-based constitutive modeling of plain carbon steels, Materials Science and Engineering: A, 636 (2015) 196-202.

[206] H. Mirzadeh, Quantification of the strengthening effect of reinforcements during hot deformation of aluminum-based composites, Materials & Design, 65 (2015) 80-82.

[207] H. Mirzadeh, Simple physically-based constitutive equations for hot deformation of 2024 and 7075 aluminum alloys, Transactions of Nonferrous Metals Society of China, 25 (2015) 1614-1618.

[208] A.W. Bowen, D.S. McDarmaid, P.G. Partridge, Effect of high-temperature deformation on the texture of a two-phase titanium alloy, Journal of Materials Science, 26 (1991) 3457-3462.

[209] S. Banumathy, R.K. Mandal, A.K. Singh, Phase Transformation Textures in Hot-Rolled Binary Ti-Nb Alloys, Metallurgical and Materials Transctions A, 44 (2013) 2499-2511.

[210] B. Beausir, L.S. Tóth, K.W. Neale, Ideal orientations and persistence characteristics of hexagonal close packed crystals in simple shear, Acta Materialia, 55 (2007) 2695-2705.

[211] S. Shuyu, L. Weijie, Microstructure and Mechanical Properties of TC18 Titanium Alloy, Rare Metal Materials and Engineering, 45 (2016) 1138-1141.

Appendix-A

Processing map (DMM approach)

The total power, P dissipated by a unit volume of a visco-plastic material specimen may be distributed into two parts. One part of the power is dissipated in deformation work, G, and other part of power is dissipated in microstructural change, J. G and J can be represented by following equations:

$$P_{T,\varepsilon} = G + J = \sigma\dot{\varepsilon} = \int_0^{\dot{\varepsilon}} \sigma\,d\dot{\varepsilon} + \int_0^{\sigma} \varepsilon\,d\sigma$$

where (1-A)

$$G = \int_0^{\dot{\varepsilon}} \sigma\,d\dot{\varepsilon} \quad and \quad J = \int_0^{\sigma} \varepsilon\,d\sigma$$

Efficiency of power dissipation, η and instability parameter, ξ can be described on the basis of power partition. Power partitioning between G and J is decided by the strain rate sensitivity parameter, m.

$$\frac{\partial J}{\partial G} = \frac{\dot{\varepsilon}\,\partial\sigma}{\sigma\,\partial\dot{\varepsilon}} = \frac{\partial(\ln\sigma)}{\partial(\ln\dot{\varepsilon})} = m$$

(2-A)

m at each strain rate was calculated by taking derivative of 2nd order polynomial curve between $\ln\dot{\varepsilon}$ and $\ln\sigma$ at constant strain and temperature.

In case of ideal linear power dissipater, strain rate sensitivity parameter m becomes unity. Therefore, J acquires its maximum value, J_{max} and can be represented as:

$$J_{max} = \frac{\sigma\dot{\varepsilon}}{2} = \frac{P}{2}$$

(3-A)

The efficiency of power dissipation, η is:

$$\eta_{Prasad} = \frac{J}{J_{max}} = \frac{2J}{P} = \frac{2m}{m+1}$$

(4-A)

For efficiency contour maps, discrete values of $\frac{2m}{m+1}$ were interpolated using cubic spline function in to a matrix of 30×30 and then plotted as a function of temperature (X axis) and strain rate (Y axis).

Instability can be calculated according to the following procedure:

$$\xi_{Prasad} = \frac{\partial\ln(m/m+1)}{\partial\ln\dot{\varepsilon}} + m < 0$$

(5-A)

145

The term $\dfrac{\partial \ln(m/m+1)}{\partial \ln \dot{\varepsilon}}$ was calculated from the derivative of 2nd order polynomial fit between

$\ln \dot{\varepsilon}$ and $\ln(m/m+1)$ at constant strain and temperature. The instability value is sum of

$\dfrac{\partial \ln(m/m+1)}{\partial \ln \dot{\varepsilon}}$ and m values. Discrete values of instability were interpolated using cubic spline

function in to a matrix of 30×30 and then plotted as a function of temperature (X axis) and strain rate (Y axis). The instability values less than zero ($\xi < 0$) were identified with a hatched region in the map.

Thus, at constant strain (ε), the variation of efficiency (η) and instability (ξ) as a function of T and $\dot{\varepsilon}$, provides power dissipation map and instability map respectively. Superimposition of power dissipation map and instability map gives processing map.

Appendix-B

In this appendix procedure for calculation of stresses experienced by individual phases in two phase region is explained. The stresses were calculated by extrapolating the stress values from single phase region to two phase region. For the present alloys system, calculation of stress in alpha phase was carried out by extrapolating single phase data from low temperatures (where single phase alpha exist) to high temperatures (where two phases exist). Similarly, in case of beta phase extrapolation will be at lower temperatures. It was assumed that activation energy for individual phases remains same in the temperature range of interest.

Calculation of flow stress from experimental flow stress data

The Zenner-Hollomon parameter (Z) is expressed as follows:

$$Z = \dot{\varepsilon} \exp(Q/RT) \tag{1-B}$$

where R is the universal gas constant (8.31 J mol^{-1} K^{-1}) and Q is apparent activation energy for the deformation.

Flow stress can be expressed in terms of Z as follows;

$$Z = A F(\sigma) \tag{2-B}$$

where $F(\sigma)$ is a stress function and A is a constant. Therefore, equation 1-B and 2-B can be rewritten as

$$F(\sigma) = \dot{\varepsilon} \exp(Q/RT) \tag{3-B}$$

From equation 3-B, it is clear that at constant strain rate, if it is assumed that activation energy remains constant, then stress will be inversely proportional to temperature. Therefore, plot of $\ln \sigma$ vs $\dfrac{1}{T(K)}$ follow linear relationship which can be extrapolated to get flow stress values at lower or higher temperatures. The general equation which was used to extrapolate flow stress is shown in **Equation 4-B**, where C_1 and C_2 are the constants for a given strain rate. The flow stress in the two phase region ($\sigma_{(\alpha+\beta)}^{Cal}$) was calculated according to **Equation 5-B.** For **Equation 5-B** to be valid, the deformation was assumed to be under equi-strain condition.

$$ln\,\sigma = C_1 \frac{1}{T} + C_2 \tag{4-B}$$

$$\sigma_{(\alpha+\beta)}^{Cal} = f_\alpha \sigma_\alpha^c + f_\beta \sigma_\beta^c \qquad\qquad\qquad\qquad (5\text{-}B)$$
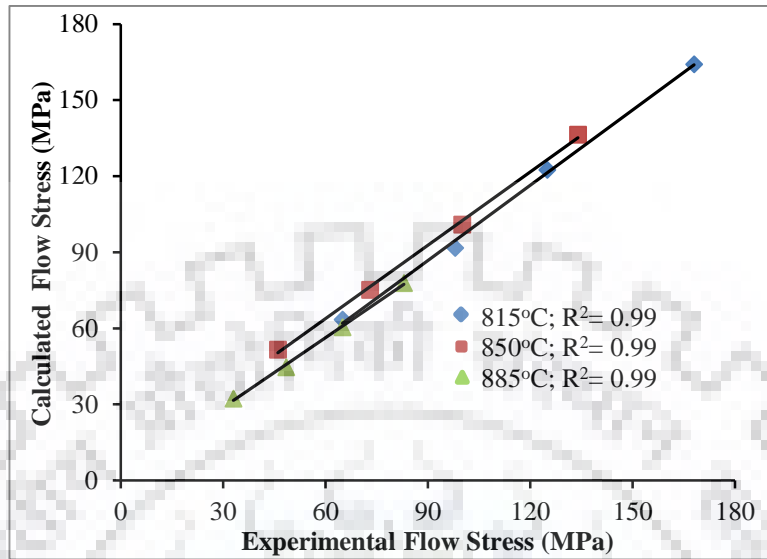

Figure 1-B: Comparison of experimental flow stress values with calculated flow stress values in the two phase region. Calculated flow stress values were obtained using **Equations. 4-B** and **5-B.**

This assumption and the adopted procedure was validated by comparing the calculated values of the flow stress ($\sigma_{(\alpha+\beta)}^{Cal}$) with the experimental values in the two phase region (**Figure 1-B**). As is demonstrated by R^2 values in **Figure 1-B**, the flow stress values ($\sigma_{(\alpha+\beta)}^{Cal}$) calculated using extrapolated method are in agreement with the experimental data.

List of Journal Publications Arising from The Thesis

1. **K.K. Saxena**, K.S. Suresh, R.V. Kulkarni, K.V. Mani Krishna, V. Pancholi, D. Srivastava; *Hot deformation behavior of Zr-1Nb alloy in two-phase region – microstructure and mechanical properties*, Journal of Alloys and Compounds, **741 (2018) 281-292**.

2. **K.K. Saxena**, V. Pancholi, S.K. Jha, G.P. Chaudhari, D. Srivastava, G.K. Dey; *A novel approach to understand the deformation behavior in two phase region using processing map*, Journal of Alloys and Compounds, *706 (2017) 511-519*

3. **K. K. Saxena**, S. K. Jha, V. Pancholi, G. P. Chaudhari, D. Srivastava, G. K. Dey, N. Saibaba; *Role of activation energies of individual phases in two phase range on constitutive equation of Zr-2.5Nb-0.5Cu,* Transactions of Nonferrous Metals Society of China, 27**(2017)** 172−183.

4. **K. K. Saxena**, S. Sonkar, V. Pancholi, G. P. Chaudhari, D. Srivastava, G. K. Dey, S. K. Jha, N. Saibaba; *Hot Deformation Behavior of Zr-2.5Nb Alloy: A Comparative Study Using Different Materials Models,* Journal of Alloys and Compounds, 662(**2016**), pp. 94-101.

5. **Kuldeep K. Saxena**, Vivek Pancholi, Dinesh Srivastava, G. K. Dey, Sanjay K. Jha, Nudurupati Saibaba; *Determination of Instability in Zr-2.5Nb-0.5Cu Using Lyapunov Function*, Materials Science Forum Vols. 830-831 (2015) pp 329-332.

6. **K.K. Saxena**, S. Sonkar, R. Kumar, V. Pancholi, G.P. Chaudhari, D. Srivastava, G.K. Dey, S.K. Jha, N. Saibaba; *Effect of Temperature and Strain Rate on Deformation Behavior of Zirconium Alloy, Zr-2.5Nb-0.5Cu"* Procedia Materials Science, 6, **2014**, Pages 188–193.

7. **K.K. Saxena**, S.D. Yadav, R. Kumar, V. Pancholi, G.P. Chaudhari, D. Srivastava, G.K. Dey, S.K. Jha, N. Saibaba; *Effect of Temperature and Strain Rate on Deformation Behavior of Zirconium Alloy: Zr-2.5Nb*, Procedia Materials Science, 6, **2014**, Pages 278–283.

8. **K. K. Saxena**, K. Chetan, S.K. Jha, K.V. Mani Krishna, V. Pancholi, D. Srivastava; *Experimental investigation, mathematical modelling and numerical simulation of Zr-1Nb alloy during hot compression and extrusion test,* Communicated to Journal of Materials Processing Technology.